Ultrafast dynamics and energy loss channels at a hybrid organic inorganic interface

vorgelegt von
Diplom-Physikerin
Laura Foglia
aus Savona, Italien

von der Fakultät II – Mathematik und Naturwissenschaften
der Technischen Universität Berlin
zur Erlangung des akademischen Grades
Doktor der Naturwissenschaften
Dr. rer. nat.

genehmigte Dissertation

Promotionsausschuss:

Vorsitzende: Prof. Dr. Andreas Knorr

Gutachter: Prof. Dr. Martin Wolf

Gutachterin: Prof. Dr. Ulrike Woggon

Gutachterin: Dr. A. Julia Stähler

Tag der wissenschaftlichen Aussprache: 08. Dezember 2015

Berlin 2015

[...]

Genova nera e bianca.

Cacumine. Distanza.

Genova dove non vivo,

mio nome, sostantivo.

[...]

Giorgio Caproni - Litanìa

Abstract

Laura Foglia
Ultrafast dynamics and energy loss channels at a hybrid organic inorganic interface

Hybrid inorganic organic systems (HIOS) promise to lead to a new generation of light-harvesting and emitting devices that combine high carrier mobilities and charge injection (or ejection) efficiency with strong light matter coupling and wide tunability. The efficiency of hybrid devices relies on the occurrence of charge or energy transfer processes at the interface before a significant amount of excess energy is lost in competing processes. The understanding of the relative balance of energy loss mechanisms and their timescales is thus a fundamental aspect in the design of such heterojunctions. This thesis investigates these relaxation mechanisms in the model HIOS formed by the spirobifluorene derivative 2,7-bis(biphenyl-4-yl)-2',7'-ditert-butyl-9,9'-spirobifluorene (SP6) and the inorganic semiconductor ZnO with complementary time-resolved optical techniques, time-resolved photoluminescence (tr-PL) and time-resolved excited state transmission (tr-EST), that access the excited state dynamics in the bulk of the system on a femtosecond timescale. Additionally, a novel non-linear optical technique, time-resolved electronic sum-frequency generation (tr-eSFG) spectroscopy, is applied, for the first time, to the study of a solid state system. tr-eSFG is based on a second order optical effect that arises where inversion symmetry is broken. Therefore, it is potentially an *interface-specific* technique that allows for the spectroscopy of interfacial electronic states in real devices, in which the active interface is buried under layers of matter.

This study shows that at high excitation densities, the transient optical properties of ZnO are strongly affected by the photoinduced depletion of in-gap states (IGS) which act as traps for excited electrons in the conduction band (CB), leading to ultrafast decay of the photoluminescence (PL) response. Since the trapping mechanism is a second order process, i.e. it requires the absorption of two photons to occur, lower excitation density reduces the influence of IGS on the charge carrier lifetime and dynamics and, indeed, exciton formation is observed within hundreds of picoseconds.

The tr-EST of SP6 shows the formation of two excitonic states of comparable lifetime localized on the two π-systems of the molecule, X_{6P} and X_{2P}, which are populated after the initial vibrational relaxation. Additionally, a triplet state is efficiently populated by intersystem crossing (ISC). Only the X_{6P} excitons decay via radiative recombination and charge separation (CS). The CS efficiency decreases with increasing temperature due to exciton scattering events that reduce the exciton lifetime and thus shorten the diffusion length. The X_{2P} excitons, instead, which are identified as intramolecular charge transfer excitons, decay exclusively via ISC and constitute the main loss channel in the hybrid system.

The presented results show that the dominant energy loss channels in both semiconductors and at the hybrid interface are related to the presence of long-lived, strongly-localized excited states, such as defect-related IGS or charge transfer and triplet excitons. These states act as electron or exciton traps and limit the probability of radiative recombination or charge separation at the interface. Remarkably, despite the long lifetime of these trap states, the respective relaxation pathway is determined by *ultrafast* processes, either already during the photoexcitation or the initial vibrational relaxation phase. These findings suggest that alternative excitation schemes are likely to increase the efficiency of the hybrid system.

Deutsche Kurzfassung

Laura Foglia
Ultrafast dynamics and energy loss channels at a hybrid organic inorganic interface

Auf anorganisch-organische Halbleiter basierende Hybridsysteme sind vielversprechende Kandidaten für eine neue Generation von Solarzellen und LEDs, die sich durch die Kombination höher Ladungsträgermobilität und effizienter Ladungsträgerinjektion (bzw. -extraktion) mit starker Kopplung zwischen Licht und Materie sowie durch eine breite spektralen Durchstimmbarkeit auszeichnet. Die Effizienz solcher Systeme beruht auf Ladungs- bzw. Energietransferprozessen an ihren Grenzflächen bevor die Überschussenergie durch konkurrierende Relaxationsprozesse verlorengeht. Sowohl die relative Verhältnisse der unterschiedlichen Energieverlustmechanismen als auch ihre Zeitskalen sind somit fundamentale Aspekte bei der Entwicklung solcher Hybridsysteme. Diese Dissertation untersucht solche Mechanismen anhand eines Modellsystems bestehend aus dem Spirobifluorenderivat 2,7-Bis(Biphenyl-4-yl)-2',7'-Ditertbutyl-9,9'-Spirobifluoren (SP6) und dem anorganischen Halbleiter ZnO mit komplementären zeitaufgelösten optischen Methoden: Photolumineszenzspektroskopie (PL) und transiente Transmission. Diese haben Zugang zur femtosekunden Dynamik der angeregten Zustände. Darüberhinaus wurde einer neue nicht-lineare optische Methode, zeitaufgelöste elektronische Summenfrequenzerzeugungsspektroskopie (eSFG), zum ersten Mal zur Untersuchung eines Festkörpers angewendet. eSFG basiert auf optischen Prozessen zweiter Ordnung, die bei gebrochene Inversionssymmetrie entstehen. Daher ist sie potentiell *grenzflächenspezifisch* und wird zukünftig die Spektroskopie von Grenzflächenzuständen in funktionellen Bauelementen, in denen die aktive Grenzfläche durch Materialschichten begraben ist, erlauben.

Diese Arbeit zeigt, dass, bei hoher Anregungsdichte, die transienten optischen Eigenschaften von ZnO stark von der photoinduzierten Depopulation von Defektzuständen beeinflusst sind. Diese Zustände dienen als Falle für Leitungsbandelektronen und führen zu einer Abnahme der PL-Wahrscheinlichkeit. Da der Einfangmechanismus ein Prozess zweiter Ordnung ist, verringert einer geringe Anregungsdichte den Einfluss der Defekte auf die optischen Eigenschaften: Der Exzitonengrundzustand entsteht innerhalb weniger hundert Pikosekunden.

Die transiente Transmission von SP6 zeigt die Bildung zweier vergleichbar langlebiger Zustände, X_{6P} und X_{2P}, welche in den zwei π-Systemen des Moleküls lokalisiert sind und bereits während der anfänglichen Schwingungsrelaxation besetzt werden. Darüberhinaus werden auch Tripletzustände effizient besetzt. Nur die X_{6P} Exzitonen zerfallen über radiative Rekombination und Ladungstransfer. Die Ladunsgstransfereffizienz nimmt mit steigender Temperatur durch Streuungsprozesse ab, welche die Diffusionslänge verringern. Die X_{2P} Exzitonen zerfallen dagegen ausschließlich in den Tripletzustand und stellen damit den primären Verlustpfad im Hybridsystem dar.

Die hier dargestellten Ergebnisse zeigen, dass die Hauptverlustpfade in beiden Halbleitern des Hybridsystems mit langlebigen, stark-lokalisierten Zuständen, wie Störstellen oder Ladungstransfer- und Tripletexzitonen, zusammenhängen. Diese Zustände wirken als Senke für die Anregung und reduzieren die Wahrscheinlichkeit der radiativen Rekombination oder des Ladungstransfers an der Grenzfläche. Darüber hinaus, trotz ihrer langen Lebensdauer, ist der jeweilige Relaxationspfad durch ultraschnelle Prozesse bestimmt, entweder bereits während der Anregung oder der anfänglicher Schwingungsrelaxation. Dieses Resultat legt nahe, dass alternative Anregungsmechanismen die Effizienz von Hybridsystemen wohlmöglich noch steigern könnten.

Contents

IV

List of Figures

Acronyms

6P   sexiphenyl.

AFM   atomic force mycroscopy.

AMOLED   active matrix organic light emitting device.

AP   acoustical phonon.

CAL   charge accumulation layer.

CB   conduction band.

CCD   charge coupled device.

CMOS   complementary-metal-oxide-semiconductor.

CS   charge separation.

CT   charge transfer.

DM   deformable mirror.

EHP   electron-hole-plasma.

EMCCD   electron multiplying charge coupled device.

ESA   excited state absorption.

eSFG   electronic sum-frequency generation.

EST   excited state transmission.

FRET   Förster resonant energy transfer.

FWHM   full width half maximum.

FX   free exciton.

GD   group delay.

GVD   group velocity dispersion.

HIOS   hybrid inorganic organic system.

HOMO   highest occupied molecular orbital.

IC   internal conversion.

iCCD   intensified charge coupled device.

IGS	in-gap states.
IR	infrared.
ISC	intersystem crossing.
IVR	intramolecular vibrational relaxation.
LED	light emitting device.
LOP	longitudinal optical phonon.
LUMO	lowest unoccupied molecular orbital.
MBE	molecular beam epitaxy.
MOCVD	metalorganic chemical vapor deposition.
NMR	nuclear magnetic resonance.
OBE	optical Bloch equations.
OPA	optical parametric amplifier.
PL	photoluminescence.
SF	self focusing.
SFG	sum-frequency generation.
SHG	second-harmonic generation.
SNR	signal-to-noise ratio.
SP6	2,7-bis(biphenyl-4-yl)-2',7'-ditertbutyl-9,9'-spirobifluorene.
SPM	self phase modulation.
SX	surface exciton.
tr-T	time-resolved transmission.
tr-eSFG	time-resolved electronic sum-frequency generation.
tr-EST	time-resolved excited state transmission.
tr-PL	time-resolved photoluminescence.
UHV	ultra high vacuum.
UV	ultraviolet.
VB	valence band.
VIS	visible.
WLC	white-light continuum.

Introduction

The first thing most of us do in the morning is turning off the alarm clock and many have taken the habit of doing it by sweeping the screen of a smartphone. Currently, the leading technology in mobile screens, the so-called active matrix organic light emitting device (AMOLED), is based on hybrid inorganic organic systems (HIOS). In an AMOLED, organic light emitting devices are controlled by an active matrix of inorganic thin film transistors, that determine the current injected in each pixel of the screen. Excitons, i.e. electron-hole pairs bound by Coulomb attraction, are formed upon electron-hole injection in the molecular units and the light produced by their radiative recombination forms what we perceive as image on the screen. AMOLED has outdone the performance of liquid crystal displays with conventional light emitting device (LED) back-illumination, because only the pixels that need to be illuminated are powered. Nevertheless, the screen remains one of the largest power drains on mobile devices, consuming on average 20 % of battery power, due to typical efficiency values around 25 to 30 %. Even worse efficiencies are achieved when HIOS are used for light harvesting. The national center for photovoltaic (NCPV) of the United States of America quotes laboratory efficiencies of 10 to 12 % [1] while the market leader Heliatek claims the efficiency of standard production to be about 8 % [2]. Clearly, there is still room for improvement.

The efficiency of HIOS depends on several factors. HIOS combine the advantages of organic and inorganic semiconductors into one single device in order to overcome some of the current limitations: the former provides strong light-matter coupling, i.e. high light emission or absorption yields, and the flexible tuning of optical properties through chemical structure, while the latter provides high charge carrier and exciton mobilities and low carrier injection and ejection barriers. Still, the two materials have to be chosen carefully, since the energy level alignment at the interface influences both device efficiency and functionality, favoring the transfer of energy and charges from organic to inorganic semiconductor or vice versa.

Additionally, multiple dynamic aspects affect the excitations lifetime in these semiconductors, and consequently the HIOS efficiency. Consider the example of a HIOS-based light harvest-

ing device. Its working principle is fairly simple: excitons are created in the molecules, diffuse to the interface with the inorganic substrate, are separated by electron (or hole) transfer to the conduction band (CB) (or valence band (VB), respectively) and the charge carriers are extracted from the device. Clearly, the largest amount of energy is harvested if, in the first place, the excitons reach the interface without decaying. In an organic semiconductor, for example, they can scatter with vibrations, transform into triplet excitons after a spin flip process or radiatively recombine. Secondly, they need to overcome the electron-hole Coulomb attraction and separate at the interface. Here, it is largely debated if efficient charge separation requires the formation of intermediate charge transfer excitons with or without excess electronic or vibrational energy [3, 4]. Finally, the charge carriers need to be efficiently extracted without undergoing previous scattering or trapping events in the inorganic semiconductor, which are often caused by the presence of structural or chemical impurities. Clearly, the discernment and control of energy loss pathways is of great relevance for the development of new functional interfaces.

The full comprehension of energy loss is also a stimulating goal for fundamental science. Aspects such as (1) how and on which extent defect related in-gap states (IGS) affect the exciton (or charge) relaxation pathways and dynamics in inorganic semiconductors, (2) how the existence of long-lived excited states, e.g. intramolecular charge transfer excitons or triplet states, influence the efficiency of charge and energy transfer processes at hybrid interfaces and (3) how the relative balance between different relaxation channels is modified by external factors, as, for example, temperature and layer thickness, are, yet, largely unanswered questions.

In this thesis, I address these aspects by investigating the excited state dynamics of the HIOS constituted by the spirobifluorene derivative 2,7-bis(biphenyl-4-yl)-2',7'-ditertbutyl-9,9'-spirobifluorene (SP6) and the inorganic semiconductor ZnO. The wide band gap, large exciton binding energy and metallic surface of ZnO makes it the ideal material for transparent electrodes and substrates for optoelectronic applications, while SP6 exhibits strong light-matter coupling and is therefore a good candidate as emitter, even for lasing applications, in the near ultraviolet [5, 6]. When combined, they form a type II interface, where both charge separation (CS) and resonant energy transfer have been previously observed [7, 8], thus making this a model HIOS for the study of loss channels affecting the efficiency of HIOS-based devices.

As stated above, all relaxation processes are *dynamic* and occur on timescales ranging from tens of femtoseconds up to microseconds. Their investigation, therefore, requires time-resolved

experimental techniques that allow to access these ultrafast timescales. Here, they are investigated by looking at changes either in the photoluminescence yield (time-resolved photoluminescence (tr-PL)) or in light absorption (time-resolved excited state transmission (tr-EST)) as a function of elapsed time from the excitation. Tr-PL and tr-EST are complementary linear optical techniques sensitive to the dynamics of the excited states in the *bulk* of the semiconductor. The former measures the radiative recombination of excitons in the lowest excited state, while the latter, instead, looks at higher excited state transitions that are activated after photoexcitation. In addition, in this thesis, I demonstrate the first application of time-resolved electronic sum-frequency generation (tr-eSFG) spectroscopy to a solid state material, a non-linear optical technique which, until now, had been applied only at liquid interfaces [9]. Even though, here, tr-eSFG is demonstrated for the bulk of non-centrosymmetric ZnO, it bases on a second order optical non-linearity and thus has the potential for being *interface specific*, in presence of centrosymmetric materials. This will allow the direct spectroscopy of interface and charge transfer states, even for realistic devices where the active interface is sometimes buried under thick material layers. This combination of complementary techniques provides a comprehensive picture of the exciton and charge carrier pathways in both constituents of the hybrid system and disentangles several loss channels that undermine the efficiency of CS, as summarized in the following.

Outline of the thesis: The first chapter discusses the processes that occur in semiconductors after photoexcitation, with particular attention to the differences between organic and inorganic semiconductors and how they are exploited in HIOS, and introduces the investigated SP6/ZnO system. The theoretical fundament of optical spectroscopy, both linear and non-linear, is resumed in chapter 2, while chapter 3 describes the experimental setup for linear optical spectroscopy (sec. 3.1 and 3.2) and the sample preparation (sec. 3.3). The newly developed non-linear optical setup is described and characterized in chapter 4.

The results on ZnO are presented in chapter 5. The IGS-related dynamics have been tackled by comparison of the optical response of a single crystal with the one of a thin film deposited by molecular beam epitaxy (MBE). For both samples, the spectroscopic characterization reveals occupied IGS between 1.7 eV and 2.7 eV below the onset of the CB. Their photoinduced optical response dominates the tr-EST at high excited electron densities, where screening prevents

exciton formation. Moreover, after pump-induced depletion, the IGS are found to act as traps for the excited electrons in the CB an lead to an ultrafast (ps) decay of the photoluminescence (sec. 5.2). Also in the low excitation regime, IGS substantially affect the optical properties of ZnO by acting as intermediate states in a double resonant transition to the exciton-polariton levels. Only at low excitation density, tr-eSFG detects the formation of bound excitons on a 100 to 200 ps timescale (sec. 5.3.3).

Chapter 6 reports the results on the SP6 and at the hybrid interface, where several relaxation pathways are found to compete with CS. After an initial fast intramolecular vibrational relaxation (IVR), two distinct excited states form, localized in the two π-systems of the molecule and decoupled by the spiro-link. Both levels have comparable lifetimes of hundreds of ps and efficiently decay via intersystem crossing (ISC), leading to the formation of a triplet state having a microsecond lifetime. Despite comparable lifetimes, *only* the lowest energetic level is found to radiatively recombine and efficiently charge separate at the hybrid interface. Consequently, the other excited state, which is identified as an intramolecular charge transfer (CT) exciton across the two π-systems, constitutes an important loss channel for the charge separation process.

Finally, chapter 7 summarizes the results to draw a comprehensive picture of the energy loss channels at this hybrid interface, where it becomes clear that the HIOS efficiency is severely affected by the existence of multiple long-lived excited states that compete with those involved in the CS process. The design of HIOS-based devices thus requires the optimization of the excited states to the desired functionality and the quenching of non-relevant excited states (both the CT exciton in the organic dye and the IGS in the ZnO) or triplet excitons.

1. The main players
Investigated processes and systems

The interaction of a semiconductor with light of sufficient photon energy leads to the promotion of an electron to higher energy level while a hole is left behind. These electron and hole can feel a Coulomb attraction and bind in a quasiparticle called exciton. The strength of the interaction and the degree of delocalization of the exciton in the crystal depend on the screening by other charge carriers and on the electronic structure of the material, such that inorganic semiconductors are characterized by weakly bound and highly delocalized excitons while the excitations of organic semiconductors are mostly localized and strongly bound. These differences, which are summarized in the first section of this chapter (1.1), naturally influence energy and charge carrier transport and relaxation mechanisms and, in turn, affect the efficiency of either class of semiconductors when used for light harvesting or emission applications. On the other hand, the differences can be exploited if organic and inorganic compounds are combined in an hybrid structure, where the optoelectronic properties can eventually go beyond a mere superposition of the single material properties, as discussed in section 1.2. This work employs various time-resolved all-optical techniques (cf. chapter 2) to investigate the interplay of the multiple energy and charge relaxation pathways that determine the dynamics of the excited state population in ZnO, in the organic dye 2,7-bis(biphenyl-4-yl)-2',7'-ditertbutyl-9,9'-spirobifluorene (SP6) and at their hybrid interface. The two materials and why they represent a model system for hybrid inorganic organic systems (HIOS) are discussed in sections 1.3 and 1.4.

1.1 Excitations in semiconductors

In inorganic solids the distinction between metals and insulators arises from band theory at zero temperature. The ground state of a metal possesses at least one partially empty band, with electrons that can conduct if an electric field is applied. In an insulator, instead, the valence electrons completely fill the bands, such that no conduction is possible. The highest energy

of the valence band (VB) is separated from the lowest energy of the first empty band, the conduction band (CB), by a band gap of energy E_g. At a finite temperature there is a non-zero probability that an electron is excited thermally from the valence to the conduction band and the number of thermally excited electrons depends on the gap energy as $\exp(-E_g/2k_BT)$. A crystal where E_g is small enough to guarantee a thermally excited electron density leading to a macroscopic current is defined as *semiconductor* and its conductivity increases with increasing temperature, opposite to what occurs for metals [10]. Analogously, an organic semiconductor has electronic properties between those of the metal and the insulator. Typical values for the band gap range from few hundreds of meV to some eV, both for the inorganic and the organic compounds. This section reviews the electronic and optical properties as well as the relaxation processes after photoexcitation in both classes of semiconductors, with particular attention to the differences between them.

The electronic properties of an inorganic semiconductor are determined by its band gap energy and the position of the Fermi level E_F within it. A semiconductor is said to have a *direct* band gap if the top of the VB and the bottom of the CB are at the same point of the Brillouin zone, i.e. have the same momentum $\mathbf{k}$, and an *indirect* one when the emission or absorption of a phonon is required for an optical transition at the band gap energy. The energetic position of the Fermi level within the band gap is determined by the presence of structural and chemical impurities creating additional energy levels in the band gap and in an ideally pure crystal the Fermi energy lies in the middle of the band gap [10, 11]. If these defect levels are located a few tens of meV away from the band edges and the associated wave function is extended as far as the Coulomb potential, one speaks of shallow defects. Otherwise, if the wave function is rather localized and the associated energy level is deep in the band gap, they are named deep defects. Shallow defects can be thermally ionized, thus adding extra electrons (holes) to the CB (VB) and significantly affecting the conductivity. A controlled introduction of defects is called doping and can be achieved with concentrations up to $10^{20}\,\mathrm{cm}^{-3}$. A semiconductor with a prevalence of electron donor (acceptor) doping is said to be *n*- (*p*-) doped [12]. Typical values of the mobility in inorganic semiconductors range from $600\,\mathrm{cm^2\,V^{-1}\,s^{-1}}$ of PbS to $77\,000\,\mathrm{cm^2\,V^{-1}\,s^{-1}}$ in InSb for the electrons, while are maximum $1800\,\mathrm{cm^2\,V^{-1}\,s^{-1}}$ for the holes in Ge. Deep level defects, instead, do not relevantly contribute to the overall conductivity but can influence the optical properties of a semiconductor quite dramatically, acting as carrier generation and recombination

centers, thus potentially decreasing the carrier lifetime and concentration [13].

Organic semiconductors are usually formed by sp^2-hybridized carbon atoms, aligned in an alternated configuration of single and double bonds, the conjugation backbone, which normally assumes planar configuration. The unhybridized p_z orbitals, below and above the backbone, overlap and form shared molecular orbitals, the π-system. The electrons in these orbitals are delocalized over the whole conjugated system. In such molecules, the lowest excitation is given by the $\pi - \pi^*$ transitions and the energy width of the band gap can be controlled by extending the π-system, with the gap energy decreasing for bigger conjugated systems [14]. This way, chemistry directly offers a tool to continuously tune the gap. Organic semiconductors form weakly van der Waals bonded solids. As a consequence, the excitations are much more localized than in inorganic semiconductors and the optical properties of the ensemble, both for the absorption and the emission, retain characteristics of the molecules in the gas phase, such as the vibronic progressions. Another important consequence of the higher localization is that two well-defined spin states, singlet and triplet, persist in the molecular ensemble. Both these characteristics strongly affect the mobility of the carriers, the energy transport and the decay of the excitations, as will be discussed in the following [15]. The absorption and emission spectrum, the relaxation pathways and the mobility are also influenced by the degree of ordering of the molecular crystal.

The next sections compare photoexcitation mechanisms and relaxation pathways for the two classes of semiconductors, which differ substantially due to the intrinsically different electronic structure of inorganic crystals and amorphous organic films.

1.1.1 Relaxation pathways in inorganic semiconductors

Photoexcitation of an inorganic semiconductor promotes an electron to the CB, leaving an unoccupied state, the hole, in the VB. The free electron and hole pair relax to the edge of their respective band by dissipating the excess energy through several scattering processes. The most relevant are: (1) scattering with phonons, both acoustical and optical, (2) scattering with electrons or other electronic excitations and (3) scattering with defects. In the case of weak excitation and low defect densities, the intraband relaxation occurs mostly by scattering with phonons, while electron-electron scattering dominates for high excitation densities [16, 17]. Scattering with longitudinal optical phonons (LOPs) prevails for values of electron excess energy with re-

spect to the bottom of the CB larger than $\hbar\omega_{\mathrm{LO}}$, where ω_{LO} is the lowest LOP frequency. This holds especially for polar semiconductors, where LOPs induce a macroscopic polarization that couples efficiently with the electron in a mechanism called Frölich interaction [16, 17]. LOP scattering occurs usually on timescales of hundreds of fs to few ps and, due to the typical LOP energies of tens of meV, leads to a substantial decrease in energy. For lower excess energies, the scattering must occur by emission or absorption of acoustical phonons. This process, that becomes slower and slower with decreasing energy due to a reduction of the phonon phase space, undergoes usually on timescales of 1 to 100 ps.

Excitons in inorganic semiconductors: The Wannier-Mott picture

Similar timescales of hundreds of picoseconds have been observed by THz transmission spectroscopy for the transition from a photoexcited electron-hole gas to an insulating quantum state, indicative of the formation of excitons [18, 19]. When the electron is photoexcited to the CB, it feels the Coulomb attraction to the hole left behind in the VB and they form a bound pair: the exciton. Since inorganic semiconductors have large dielectric constants, usually this electrostatic interaction is screened by the remaining valence electrons and the resulting weakly-bound electron-hole pairs are called Wannier-Mott excitons [20, 21]. They can be described theoretically within the effective mass approximation, where the electron and the hole have the effective mass m_C and m_V of the conduction and valence band, respectively [17].

The Hamiltonian of the system reduces to

$$-\left(\frac{\hbar^2}{2m_{\mathrm{CB}}}\right)\nabla^2_{\mathbf{R}_e} - \left(\frac{\hbar^2}{2m_{\mathrm{VB}}}\right)\nabla^2_{\mathbf{R}_h} - \frac{e^2}{4\pi\epsilon_0^2|\mathbf{R}_e - \mathbf{R}_h|}, \tag{1.1}$$

and is equivalent to the one of an hydrogen atom of reduced mass $\frac{1}{\mu} = \frac{1}{m_{\mathrm{CB}}} + \frac{1}{m_{\mathrm{VB}}}$ and Bohr radius $a_{ex} = \epsilon\frac{m_0}{\mu}a_0$, where m_0 is the free electron mass and a_0 the Bohr radius of the Hydrogen atom. Usually, due to the large ϵ, Wannier-Mott excitons have Bohr radii on the order of tens of lattice constants.

As it is common for a two particle system, the exciton equation of motion can be divided into the motion of the center of mass and the relative motion of electron and hole. The center of mass follows the equation of motion

$$\left(\frac{-\hbar^2}{2M}\right)\nabla^2 R\psi(R) = E_R\psi(R) \quad \text{and} \quad E_R = \frac{\hbar^2 K^2}{2M}.$$

Therefore, the exciton can be seen as a free particle of mass $M = m_C + m_V$ transporting energy but not charge. The equation for the relative motion of electron and hole

$$\left(\frac{-\hbar^2}{2\mu} \nabla^2 r - \frac{e^2}{4\pi\varepsilon^2 r} \right) \phi(r) = E_r \phi(r)$$

leads, for the approximation of isotropic masses, i.e. parabolic dispersion in all directions, to

$$E_r = E_g - \left(\frac{\mu}{m_0 \varepsilon^2} \right) \frac{R}{n^2} \quad \text{where} \quad R = 13.6 \, \text{eV is the Rydberg constant.} \tag{1.2}$$

Thus, similarly to the hydrogen atom there are bound and continuum states quantized with principal quantum number $n = 1, 2, \ldots$ and angular momentum $l = 0, \hbar, 2\hbar, \ldots$. This hydrogen-like series of excitonic peaks characterizes the onset of absorption in most semiconductors. Elliot [22] calculated the imaginary part of the dielectric function, associated with the absorption as discussed in chapter 2, in presence of excitons to be:

$$\varepsilon_i(\hbar\omega) = \frac{\mu^3 |\langle \psi_{\mathbf{k}}^c | \hat{e} \cdot \mathbf{p} | \psi_{\mathbf{k}}^v \rangle|^2}{8\pi^2 \varepsilon^6 \omega^2} \sum_1^\infty \frac{1}{n^3} \delta(\omega - \omega_n),$$

with the previously imposed condition that only excitons with $l = 0$, i.e. excitons with s symmetry can absorb or emit in the dipole interaction. The oscillator strength of the excitonic bound states decreases as n^{-3} and as $\omega \to \omega_g$, and thus the states merge into the continuum, the imaginary part of the dielectric function approaches $\varepsilon_i(\hbar\omega) = \frac{2\mu^2 |\langle \psi_{\mathbf{k}}^c | \hat{e} \cdot \mathbf{p} | \psi_{\mathbf{k}}^v \rangle|^2}{\omega_g^2 \varepsilon^2}$. Figure 1.1 shows the absorption coefficient as a function of photon energy for a direct band gap with excitonic effects, in green, and without them, in blue. Clearly, the presence of the excitonic resonances does not only alter the absorption below the band gap energy but also enhances the absorption above it. The image was adapted from [17].

Wannier-Mott excitons can recombine either radiatively or not. The radiative recombination, occurring predominantly from the 1-s ground state, is measured in photoluminescence (PL) spectra and gives direct information about the exciton binding energy. Additionally, due to the low binding energy, Wannier-Mott excitons can be easily thermally ionized and separate into free carriers in the CB and VB that contribute to the charge carrier mobility. Moreover, free Wannier-Mott excitons can get trapped by weakly binding to defect states. These strongly localized defect-bound excitons loose their Wannier-Mott character and their emission appears as additional lower energy lines in the PL spectrum of the semiconductor. Furthermore, they efficiently decay by Auger recombination mechanisms.
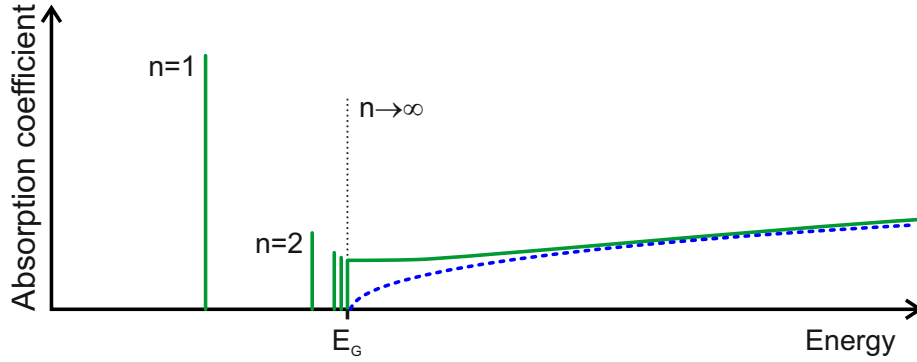
Figure 1.1: Comparison of the absorption coefficient of a direct band gap semiconductor with (green) and without (blue) excitonic absorption. The presence of excitonic absorption affects not only below the band gap energy but also affects the continuum absorption.

The free-exciton emission lineshape and the exciton-polariton.

As it will be discussed in section 2.1, any dipole-allowed transition between two electronic states is associated to a microscopic polarization field in the lattice and, in turn, an oscillating polarization emits an electromagnetic wave. This holds also for the dipole allowed exciton transitions and one can define a coupled state of the exciton and the photon: the exciton-polariton. Its eigenstates are a linear combination of the wavefunctions of exciton and photon and a splitting arises at the crossing point of their dispersion curves, as depicted in figure 1.2. The magnitude of this splitting, i.e. the difference $\omega_L - \omega_T$, depends on the coupling strength. The exciton-polariton dispersion curves are thus divided into a lower (LPB) and an upper branch (UPB). The first starts with a photon-like linear slope and goes over to an exciton-like dispersion at $E = \hbar\omega_T$. The upper branch instead is mostly photon-like, with slope dictated by the dielectric function in the energy region of the excitonic resonances. Furthermore, for anti-parallel electric field and polarization, there can be a fully exciton-like band called *longitudinal exciton* (L) [23].

Neglecting the exciton-photon coupling, radiative recombination is allowed only for excitons at the Γ point (i.e. $\mathbf{k} \simeq 0$) and the shape of the spectrum is Lorentzian and centered at the energy of the exciton 1-*s* ground state. However, most semiconductors exhibit an asymmetric emission lineshape for the free exciton (FX) [17]. In order to explain it, Toyozawa [24] proposed the interpretation of emission lineshapes in terms of exciton-polaritons. Indeed, if the coupling is considered, the polaritons in the lower branch having energy higher than $\hbar\omega_T$ scatter with phonons through their excitonic component, which results in a short lifetime. For energies lower
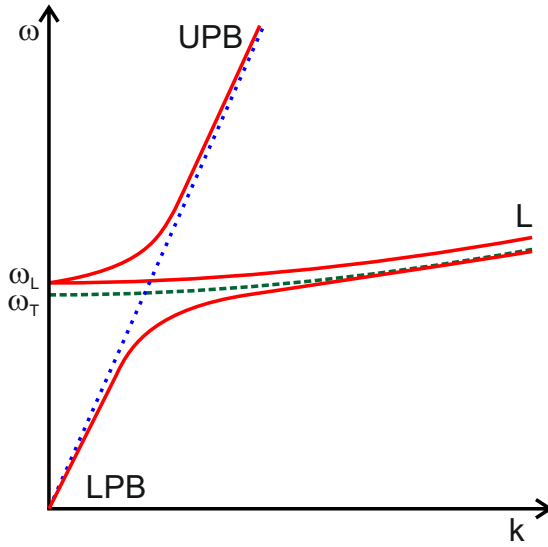
Figure 1.2: Dispersion curve of the exciton-polariton in red, of the bare photon in blue and of the bare exciton in green. At the crossing point between the dispersion curves of photon and exciton a splitting $\omega_L - \omega_T$ occurs in case of coupling and the exciton-polariton dispersion relation can be divided in two branches: lower (LPB) and upper (UPB) polariton branch, showing mixed photon (steep slopes) and exciton (small slope) character.

than $\hbar\omega_T$ they change their character from exciton-like to photon-like and again have short lifetime due to the high group velocities, defined as the slopes of the dispersion relation, and can efficiently leave the sample in form of light. In the crossing region, instead, their lifetimes are maximum and the distribution function peaks. Thus, the emission spectrum, which results from the product of the distribution function and the transmission function of the polaritons escaping the sample as photons, shows a maximum near the transverse energy and a tail extending until the longitudinal energy.

Electron-hole plasma and the Mott density

The optical properties of a semiconductor are determined by single electron-hole pairs (either in the form of free carriers or of excitons) only in the regime of low excitation. If the excitation density is increased such that the amount of created excitons is high enough for their average distance to be comparable with their Bohr radius, the electron-hole pairs loose their quasiparticle character due to screening and a new collective phase is formed: the electron-hole-plasma (EHP). The critical density at which this transition occurs is called the Mott density n_M and is crudely approximated by $n_M = 0.2 a_{ex}^{-3}$ [25]. In the intermediate regime, where the density in one of the bands is approaching the Mott density, for example due to high n-doping, the excitons assume the Mahan character [26] and can be viewed as a hole interacting with a Fermi sea of electrons. Mahan excitons have been predicted to occur for example in ZnO [27] and have been observed in InN [28].

11

Excitonic resonances or populations?

The absorption coefficient written above for the excitonic series indicates the presence of excitonic resonances even in the linear regime, where no real populations can be created but only a polarization. Excitation of a semiconductor above the band gap creates a complicated interplay of polarization, EHP, bound excitons and other higher order many-body interactions within the excited state population. Kira et al. showed with a microscopic model that a sharp emission line at the exciton energy does not necessarily imply the presence of a bound exciton population but it can also be due to the free electron-hole recombination, with the strong non-linearity in the dielectric function acting as a dielectric transmission filter and enhancing the transmission at the exciton energy [29]. The theory, summarized in references [30, chapter 2] and [31], was experimentally confirmed in GaAs quantum wells [32, 33] and has triggered large effort towards the identification of the characteristic signatures of bound excitonic population and free carrier emission in PL spectra (see for example references [29, 34–37]) as well as towards the development of direct probes of bound excitonic populations, such as employing laser pulses in the THz frequency range to look at the 1-*s* to 2-*s* excitonic transition [19, 38–40].

1.1.2 Photoexcitation of an organic semiconductor

A molecule can undergo an electronic transition by absorbing a photon if the energy of the photon is matching the energy difference between the initial and final state $\hbar\omega = E_f - E_i$ and if [41]:

1. the probability of the transition $|M_{if}^{\mathrm{el}}|^2 = |\langle f|\mu|i\rangle|^2$ is not zero. This probability depends on the wavefunction overlap, their symmetry and the electric dipole transition moment μ.

2. the spin quantum number is conserved, i.e. the optical transitions in a molecule occur only within states of the same spin multiplicity. Since the ground state S_0 of a molecule is usually a singlet state, i.e. of net spin zero, absorption of light is mostly observed only between singlet levels. Transitions between singlet and triplet states, the so-called intercombination bands, are observed only when the spin-orbit coupling is significant.

3. the Franck-Condon factor, corresponding to the square of the overlap integral of the vibrational wavefunctions of initial and final state has a finite value. Nuclear masses are larger than electron masses and in the Born-Oppenheimer approximation, the nuclear wavefunction
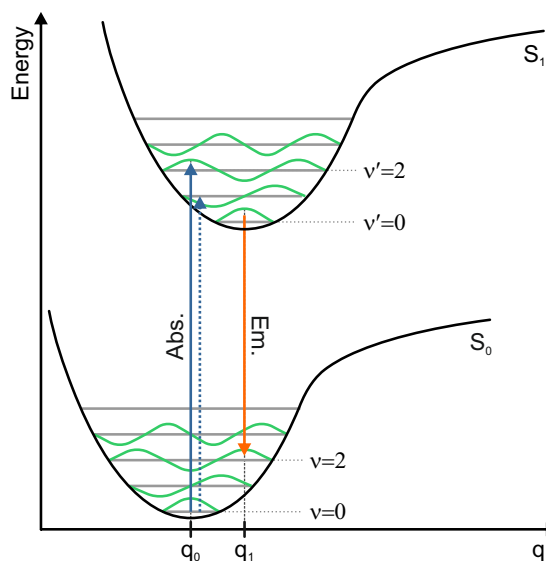
Figure 1.3: The Franck-Condon principle for optical transitions between the electronic ground and first excited state of a molecule. The transition, blue arrow, occurs vertically with respect to the nuclear coordinates to a vibronic level which wavefunction best overlaps with the ground state wavefunction. Transitions to other vibronic levels are possible (dashed arrow) and the probability is given by the square of the overlap integral: the Franck-Condon factor. Similarly for the emission. The shift between the maximum of the emission and absorption spectrum, the Stoke's shift, indicates the amount of geometrical reorganization in the excited state.

remains unchanged during an electronic transition. Therefore, the electronic transition occurs vertically along the nuclear coordinates axis and to a vibrational level with such a wavefunction that the overlap, i.e. the Franck-Condon factor is maximized, as depicted by the blue filled arrow in figure 1.3. Moreover, as demonstrated by the blue dashed arrow, there will be other vibrational levels ν' for which the Franck-Condon factor is non zero. The absorption spectrum will show a maximum corresponding to the vertical transition and several replica for all the levels that have non-zero overlap integral.

If the vibrational energies and their coupling to electronic transitions in the ground and electronic excited state are similar, the absorption and emission spectra are the mirror-image of each other. The shift of the maximum, called Stoke's shift, is an indication of the amount of reorganization that a molecule undergoes after excitation or, in other words, how the equilibrium geometry of the excited state differs from the one of the ground state [14]. In figure 1.3 this shift is given by the difference between the length of the blue and orange arrows and is due to the shift of the molecular coordinates from q_0 to q_1.

Once the molecule has been photoexcited, the excitation can undergo multiple relaxation processes, both radiative and non-radiative. These processes are shown in figure 1.4 in form of a so-called Jablonsky diagram. Usually, after photoexcitation the molecule starts, as seen in figure 1.3, from being in both a vibronically and electronically excited state and the first step
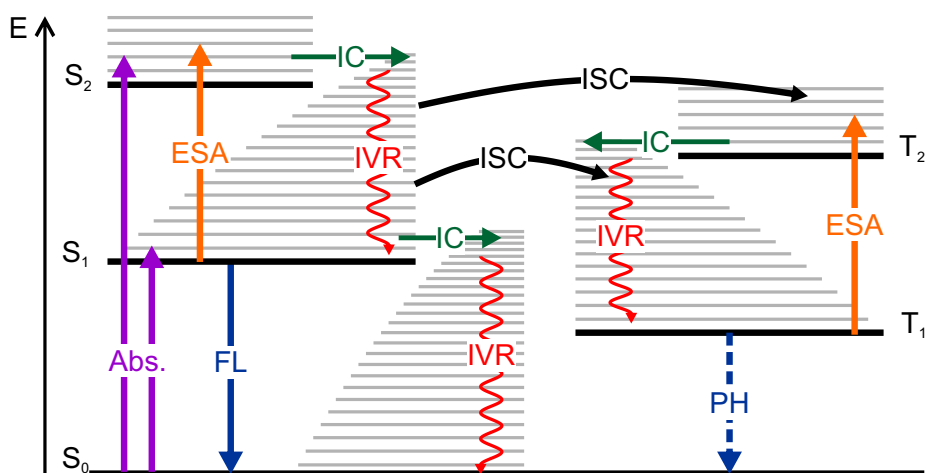
Figure 1.4: Jablonsky diagram of the relaxation processes in organics: the violet arrow represents the absorption (Abs.), that can occur only within singlet levels. After photoexcitation to a higher singlet state the molecule undergoes internal conversion (IC, green) and intramolecular vibrational relaxation (IVR, red), until it reaches the lowest singlet state, from which the electron can relax to S_0 either radiatively by fluorescence (FL, blue) or again by IC and intramolecular vibrational relaxation (IVR). If the spin-orbit coupling is sufficiently high the molecule can undergo intersystem crossing (ISC, black) to a triplet state, from which again can eventually relax to the ground state by phosphorescence (PH, dashed blue arrow).

is the relaxation to the vibrational ground state $\nu' = 0$ by intramolecular vibrational relaxation (IVR), depicted as a red arrow. Eventually, non-radiative relaxation can occur within electronic levels of the same spin multiplicity. This process is called internal conversion (IC) and is depicted in green. If the transition to another electronic level involves a spin-flip, the process is called intersystem crossing (ISC) and is indicated by the curved black arrow. Finally radiative recombination can occur either by fluorescence (FL) if it occurs between two singlet levels (blue filled arrow) or by phosphorescence (PH) if occurs from a triplet to the singlet ground state. Both processes together are called photoluminescence (PL).

The prevalence of one process with respect to the other is determined by the different rates. Due to the smaller energy separation among vibrational levels, compared to the one between electronic levels, usually IC and ISC occur much faster than fluorescence, with timescales respectively in the order of hundreds of fs to ps for the first two and hundreds of ps to ns for the latter. As a consequence, the excitation will always relax to the lowest excited state, both electronic and vibrational, of a given spin multiplicity before radiative recombination occurs.

This is the formulation of the spectroscopic rule by Kasha, which states that the measured PL spectrum in a molecule is always the same, independently of the excitation energy [42].

Phosphorescence, since it involves a spin-flip process, occurs on even longer timescales, which are determined by the strength of the spin-orbit coupling. An additional decay channel available for triplet state population and not shown in figure 1.4, is thermally-activated ISC: the electron is excited thermally to a vibrational level of the triplet from which it is possible for it to undergo ISC in the opposite direction to the singlet. This process leads to the observation of delayed fluorescence.

If the molecules are not isolated, processes involving two singlet or two triplet states are also possible: singlet fission and triplet-triplet annihilation. In the first case, a singlet excited state of one molecule interacts with the ground state of another molecule to form a triplet exciton in both. The second process is exactly the opposite and involves the annihilation of two triplet states into an excited and a relaxed singlet state [14].

Excitons in organic semiconductors: the Frenkel picture

The electronic structure of a molecular solid with weak intermolecular interactions is similar to the one of the molecule in the gas phase and the molecular orbitals overlap weakly. The electronic structure can be described within the framework of a tight binding model of molecular wavefunctions and the excitation is localized mostly on one molecule [43, chapter 15]. This corresponds to the Frenkel formalism for excitations in a monoatomic, weakly interacting gas and the excitations in a molecular solid are called *Frenkel excitons* [44, 45]. The binding energy E_{B} of a Frenkel S_1 exciton can be defined as:

$$IP - EA = E_{\mathrm{B}} + E_{\mathrm{opt}} \tag{1.3}$$

where IP is the ionization potential of the molecule and corresponds to the energy needed to extract an electron from the highest occupied molecular orbital (HOMO) in vacuum, EA is the electron affinity and is the energy needed to bring an electron from the vacuum into the lowest unoccupied molecular orbital (LUMO) and E_{opt} is the optical gap of the molecule, defined as the energy of the transition between the vibrationally relaxed levels of the two electronic levels involved, the so-called $0 \rightarrow 0$ transition in optical spectra. A molecule can have different kind of

excitons depending on the levels involved, e.g. singlet [1] excitons ($S_1, S_2, \cdot, S_n$) or triplet excitons ($T_1, \cdot, T_n$) and the formula above can be generalized by saying that the exciton binding energy is the energy difference between having two independent charges in two molecular units of the crystal, one in the electronic ground state and the other in the given energy level, and a bound electron-hole pair in one single molecule. Typical binding energies range from 0.2 to 1.6 eV [46].

In a regime of low interaction among the monomers the excitons transfer from one molecule to the other via an incoherent hopping process, described by the theory of Förster. The Förster mechanism, also called Förster resonant energy transfer (FRET), is based on a dipole-dipole interaction of the two monomers and depends on the overlap of the emission spectrum of the donor and the absorption spectrum of the acceptor, as well as on the inverse sixth power of the distance between them [47].

In the opposite limit of strong near-field interaction between the excitations in multiple monomers the theory of Förster cannot be applied. Molecules in these structures, called molecular aggregates, absorb light collectively and the exciton is delocalized over multiple lattice sites in the form of *excitation waves*. The energy transfer rates in aggregates can be as fast as fractions of fs and scale with the inverse of the cube of the intramolecular distance [48]. The absorption and emission spectra are characterized by the appearance of a narrow absorption band which is red-shifted in the case of J-aggregates [49, 50] and blue shifted for H-aggregates [51] with respect to the monomer absorption. The Stoke's shift in aggregates is usually smaller than in the corresponding monomers, indicating that they couple less to the environment [52]. Consequently, the emission band of J-aggregates appears blue-shifted with respect to the monomer emission and the one of H-aggregates well within the monomer spectrum. Furthermore, the intensity and width of the aggregate emission depends on the degree of exciton delocalization in the film [53], which rapidly decreases with increasing temperature due to an increased exciton-phonon coupling and disorder effects [54, 55]. Thus, aggregate emission exhibits a strong temperature dependence, that differs from the one of the monomer emission, allowing their identification.

In order to generate a separate electron-hole pair from an exciton, the binding energy needs

---

[1]Due to the similarity with the electronic structure of isolated molecules, excitonic states of the solid retain the same nomenclature as molecular electronic levels.

to be overcome and a radical cation and anion need to be generated in the ensemble, i.e. $M^* \rightarrow M^+ + M^-$. Due to the low dielectric constant of organic semiconductors, the electron-hole pair across the interface between the ionized molecules can still feel the mutual Coulomb attraction and remain bound in a so-called charge transfer (CT) exciton. It is an intermediate case of exciton between the delocalized Wannier-Mott exciton and the localized Frenkel exciton where the electron and the hole are localized on two neighboring lattice sites. Sometimes, CT excitons can form across one single molecule if, for example, the electron and the hole are spatially localized in two molecular sub-groups. Estimated binding energies for CT excitons are of few hundreds of meV [56]. CT excitons, especially in their vibrational excited "hot" form, are considered the precursor step for charge separation [57].

The free charge carrier transport through a molecular film involves ionic molecular states and, depending on the crystallinity of the solid, its mechanism falls between the limit of hopping and band transport. Still, considering the higher localization, the mobilities in molecular crystals are in the range 1 to $10 \, \mathrm{cm^2 \, V^{-1} \, s^{-1}}$, thus at least one order of magnitude smaller than in the inorganic counterpart [15].

Efficient optoelectronic and light harvesting devices require high charge carrier mobilities, low injection and ejection barriers, high light-matter coupling and the possibility of covering the broadest spectral range with elementary electronic transitions. Current commercial optoelectronic devices are mostly based on inorganic semiconductor technology, which satisfies the first two requirements. However, their band gap is not easily tuned and their light matter interaction usually lower than for organic compounds. The latter, despite constant technological progress, are still limited to low-performance applications, due to the low mobilities and the high injection and ejection barriers at the interface to metallic electrodes. In particular, this is the case when organic semiconductors are used in device designs that conceptually resemble the traditional ones. A different approach is to exploit the resonant interactions that can potentially arise at an inorganic/organic hybrid interface, as will be described in the next session.

1.2 Hybrid inorganic organic systems: a joint effort towards efficient optoelectronics

One of the first suggestions to combine organic and inorganic semiconductors was presented by Dexter in 1979 [58]. Here, he proposed to sensitize and thereby increase the efficiency of an inorganic solar cell with organic molecules, thus theoretically overcoming the Shockley and Queisser limit [59]. This limit sets the theoretical prediction of the maximum efficiency for a solar cell based on a inorganic semiconductor p-n junction to 33 % and has among the factors that determine it the loss of all solar energy larger than the semiconductor band gap. Dexter's idea was to efficiently absorb the solar light in molecules with appropriate optical gap rather than in the inorganic semiconductor. The excitons would then diffuse to the interface with the inorganic semiconducting substrate, where they would create e-h pairs by charge separation (CS) across the interface. The quantum yield could even be potentially doubled if triplet excitons would be created in the organic film by singlet fission. Indeed, this futuristic idea finds nowadays increasing experimental realization. Exemplary studies follow different approaches that include for example the resonant coupling of the excitations [60–63], the charge separation [64–66] or the formation of charge transfer excitons [67–69] at the interface between an organic and an inorganic semiconductor. They are stimulated by the vision of combining the advantageous properties of both organic and inorganic materials to overcome the respective limitations discussed above [70].

Hybrid inorganic/organic systems can exist either in the strong or in the weak excitation coupling regime. The first case, discussed extensively in theory [70–72] but not demonstrated yet in experiments, has been predicted to occur in quantum well structures and microcavities and would lead to a strong enhancement of optical nonlinearities and a non-zero second order susceptibility even for separately centrosymmetric inorganic and organic quantum wells. In this regime the excitations would assume an hybrid character given by the linear combination of the wavefunctions characteristic of both Frenkel and Wannier-Mott excitons. According to Agranovich et al. "these hybrid electronic excitations will be characterized by a radius dominated by their Wannier component and by an oscillator strength dominated by their Frenkel component". Therefore, such systems promise to obtain "qualitatively new physical effects" [71]. However, due to the large width of excitonic resonances in organic semiconductors, the weak coupling

regime is more common and the exchange of energy occurs via a FRET mechanism rather than by hybrid electronic states. In this regime one can think about light emitting devices where the charge is electrically injected in an inorganic quantum well and the energy is transferred to the organic dye, where electron and hole recombine radiatively. Alternatively, as Dexter suggested in 1979, a solar cell where the light is absorbed in the organic material and the current extracted from the inorganic after charge separation at the interface [70].

The functionality of a device working in the weak coupling regime, i.e. whether it is suited for light emission or harvesting, is determined by the energy level alignment at the interface.

(a) Type I: Energy transfer

(b) Type II: Charge separation
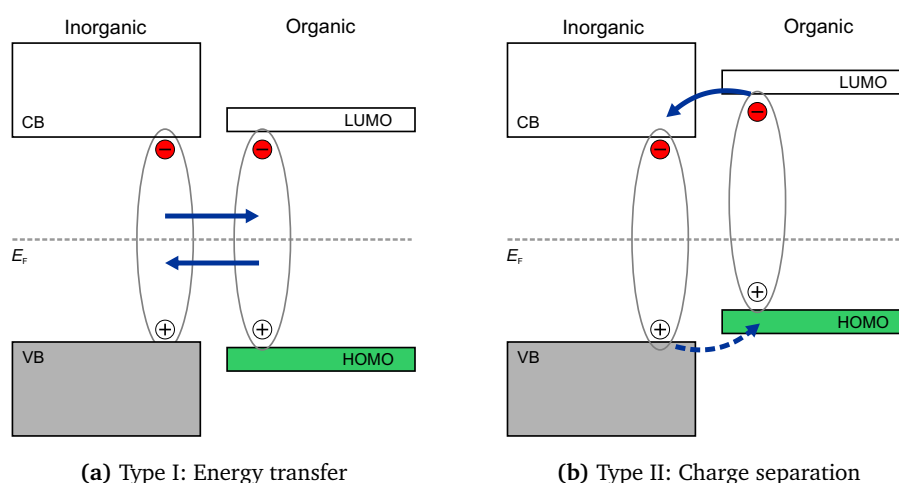
Figure 1.5: (a) The excitons in the organic and the inorganic semiconductors are resonant: this situation is favorable for FRET.(b) The LUMO of the molecules is resonant with the conduction band (CB) of the inorganic semiconductor: this situation is favorable for charge separation and electron injection from the molecules to the substrate (or hole injection in the opposite direction).

Figure 1.5 shows the two most relevant energy level alignments for technological applications. The first, depicted in (a), is the energy level alignment required for exploiting the high mobilities of inorganic semiconductors and the emission yield of organic compounds in efficient light emission devices. Here, excitons are generated in the inorganic substrate either by electrical charge injection at a p-n junction (not shown) or by photoexcitation and can transfer via Förster resonant energy transfer, thanks to the resonant overlap of the excitonic levels, to the organic semiconductor, where they can radiatively recombine. When the aim is to harvest light, then the energy level alignment depicted in (b) is the goal. The light is absorbed in the organic semiconductor generating excitons. The LUMO lies energetically resonant with the conduction

band, which grants a high density of states for the electron to tunnel into. On the other hand the hole is trapped in the HOMO and charge separation can occur at the interface. This configuration is fundamental for providing the force to overcome the Frenkel exciton binding energy and separate the charges generated by photoexcitation in the organic.

The energy level alignment is not the only factor affecting the efficiency of charge or energy transfer at an hybrid interface. As discussed in section 1.1.1 and 1.1.2, the excitation can decay efficiently via multiple relaxation pathways, both in inorganic and organic semiconductors. In the example of figure 1.5(b), the excitation generated in the organic film needs to diffuse to the interface before decaying. Therefore, diffusion needs to occur on timescales competitive with the ones of other relaxation processes such as (non-)radiative recombination or ISC, which, if the triplet level lies below the CB minimum, can also become a source of energy loss. Furthermore, the diffusion length of singlet excitons, ranging from 3 to 60 nm [73], dictates the limit for the thickness of the organic layer necessary to achieve maximum energy to charge conversion. The situation of figure 1.5(a) is similar. Here the diffusion length of the Wannier-Mott exciton in the inorganic crystal plays the main role and the excitons need to reach the interface as bound quasiparticles in order to undergo resonant energy transfer. Finally, in either case, charge transfer excitons at the interface can also be an energy loss channel if recombination or ionization occurs with higher probability than charge separation, as discussed in [67–69].

Clearly several factors need to be fully understood at a fundamental level in order to be able to design an efficient HIOS, as for example:

(1) What determines the rates of relaxation processes in organic films?

(2) Which mechanisms lead to exciton ionization and trapping in inorganic semiconductors and on which timescales do they happen?

(3) What are the spectral signatures of charge transfer excitons and their recombination mechanisms?

This work addresses the first two questions for a model hybrid inorganic-organic system composed of ZnO and a spirobifluorene derivative, SP6. The two materials are presented in detail in section 1.3 and 1.4, respectively.

1.3 Zinc Oxide

ZnO is a wide band gap semiconductor. Its direct band gap of 3.44 eV at 2 K [74] and of 3.365 eV at 300 K [75] makes it an interesting candidate for various applications in the realm of optoelectronics in the visible and near UV photon energy range. Furthermore ZnO crystals are natively *n*-type doped [76], which makes it a suitable compound as transparent conductor, for example in light harvesting applications. This section reviews the current understanding of the crystal and electronic band structure of ZnO, the role of defects in the energetic landscape and the carrier and exciton dynamics. A fast search in the web of science for publications on ZnO in the last 15 years leads to over 120 000 results only in the field of physics, chemistry, material science and optics. This huge number of publications on the one hand reflects the revived interest in understanding and controlling the optoelectronic properties of ZnO and on the other hand makes it almost impossible to gain a comprehensive picture. Moreover, the conductivity and optoelectronic properties are strongly influenced by the presence of in-gap states (IGS), in a way that is still far from being completely understood [76]. This, in addition to the challenges in growing samples with controlled properties, leads to literature values for the most relevant physical properties, e.g. linear and nonlinear susceptibilities, Mott density and Bohr exciton radius, ranging sometimes over orders of magnitude.
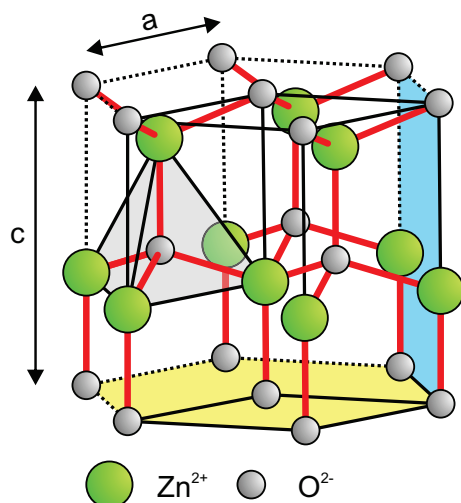
Figure 1.6: Hexagonal wurtzite structure of ZnO . In gray the oxygen anions and in green the zync cations. Each of them is surrounded by four atoms of the other specie in a tetrahedral coordination. The polar, oxygen terminated $(000\bar{1})$ surface is indicated in yellow and the $(10\bar{1}0)$ mixed-terminated in light blue.

The thermodynamically stable ZnO crystal structure at ambient conditions is wurtzite, as depicted in figure 1.6, where each anion is surrounded by four cations at the corner of a tetrahedron, and vice versa. The unit cell of the wurtzite structure is hexagonal, defined by the lattice

parameters a and c, and belongs to the space group C_{6v}^4 if $C/a = \sqrt{8/3}$. Therefore ZnO is non-centrosymmetric in the bulk. The structure results from two interpenetrating hexagonal-close-packed lattices, respectively for the oxygen and the zinc, displaced along the threefold c-axis [77]. The two surfaces perpendicular to the c axis (yellow in 1.6), (0001) and (000$\overline{1}$) are the polar zinc and oxygen terminated surfaces respectively. The non polar mix-terminated surface is the (10$\overline{1}$0) and is parallel to the c-axis (blue in 1.6). The crystal symmetry of ZnO leads to many interesting optical and electronic properties such as uniaxial birefringence, i.e. two different refractive indexes for polarization parallel and perpendicular to the c-axis, piezoelectricity, pyroelectricity and high second order nonlinear optical susceptibility $\chi^{(2)}$ for the bulk [78]. The susceptibility tensor of ZnO is calculated in appendix A and, for example, the values of $\chi_{ccc}^{(2)}$ at a wavelength of 1064 nm reported in literature range from -83.7 to 7 pm V^{-1} [79, 80], for thin films deposited by molecular beam epitaxy (MBE) and metalorganic chemical vapor deposition (MOCVD).

One of the advantages of ZnO when compared to other application-relevant semiconductors, e.g. GaN, is that is available as large single crystals that can be used as substrate for further homoepitaxial growth of thin films or for heterostructures. The ability of homoepitaxy can potentially prevent substrate contamination and reduce the concentration of extended defects, thus obtaining the high quality films required for optoelectronic applications where the crystalline quality of the films is fundamental. Bulk growth of ZnO is achieved with several methods, as for example gas or vapor transport [81], hydrothermal [82] and pressurized melt growth [83]. Thin films have been successfully deposited on both non-native substrates, such as sapphire, GaAs or GaN and on ZnO itself by pulsed laser deposition, chemical vapor deposition, MOCVD [84] and MBE [85].

The potential functionality of a semiconductor is to some extent determined by its band structure. In ZnO at the Γ point the conduction band is originating from the empty 4s Zn orbitals, while the valence band has prevalently p character and results from the occupied 2p oxygen orbitals. It is split by spin-orbit coupling and crystal field splitting into three very closely spaced bands usually called A,B and C. The splitting energies of $E_{\mathrm{AB}} = 9.5$ meV and $E_{\mathrm{BC}} = 39.7$ meV have been measured by emission and reflection spectra [74] and are in agreement with theoretical calculations [86]. The optical spectra across the band gap are dominated by transitions from the three VBs. The first excitonic spectrum of ZnO was measured with absorption and re-

flection by Thomas and is plotted in figure 1.7(a) (please note the decreasing energy axis). He observed three distinct resonances, one for $E \parallel c$ at 3.418 eV and two for $E \perp c$ at 3.378 eV and 3.371 eV respectively, and proposed the transitions visible when the electric field polarization is perpendicular to the c-axis to result from the valence band A and B and the transition for $E \parallel c$ from C. This assignment leads to an inverted VB ordering with respect to usual wurtzite symmetries [87]. Park et al., instead, interpreted the spectrum with the usual ordering and attributed the line of the ground state A exciton-polariton transition to an ionized donor-bound exciton [88]. The extensive debate on the assignment of band symmetries and allowed transitions is still ongoing, with the inverted ordering being mostly adopted [75], and results in different assignments of the transition energies found in the literature [77]. Figure 1.7(b) shows the PL spectrum of ZnO in the region of the FX emission at a temperature of 10 K and with electric field perpendicular to the c-axis, as reported by Teke et al.. The inset expands on the region of the maximum emission. The authors assign the peaks considering a non-inverted band ordering and find the ground state emission of the FX-A at an energy of 3.377 eV and 3.376 eV, depending on the symmetry, and the ground state emission of the FX-B at 3.39 eV, about 12.7 meV apart. Furthermore, they observe additional fine structure, such as the appearance of the LPB and UPB related to exciton A respectively 2.9 meV and 3.6 meV below or above the pure exciton emission.

(a)   (b)
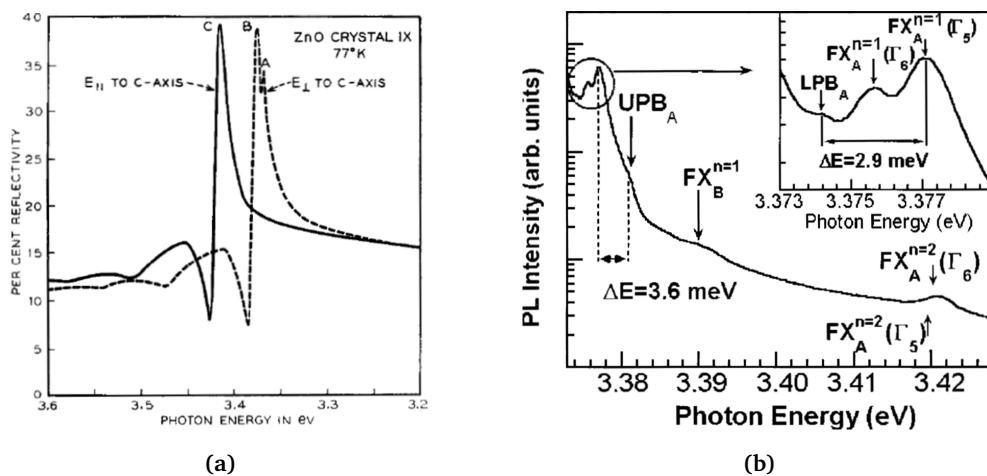
Figure 1.7: (a) Reflectivity spectra at 77 K for $E \parallel c$ (full line) and $E \perp c$ (dashed line), from ref. [87] (Please note the decreasing energy axis). (b) PL spectrum at 10 K in the energy region of FX emission for $E \perp c$, from reference [89]. See text for discussion.

Teke et al. traced the PL signatures of the A and B free excitons from 10 to 300 K and stated that they can be distinguished until about 160 K. For even higher temperatures the two excitons and the LOP replica all converge to a single broad peak. A similar trend is observed in reference [90], where the authors report a red shift of 60 meV from liquid helium to room temperature that is attributed to a combination of band gap narrowing and increased phonon-assisted recombination. Similar values for the band gap shift are measured in reference [91]. The band gap narrowing with increasing temperature is a common observation in semiconductors and is attributed mainly to an increase in carrier-phonon coupling and to the change in the lattice constants [16].

For energies below the emission of the free exciton A, phonon replica are observed in the PL spectra [23] with an energy separation of about 70 meV. Group theory predicts for a C_{6v}^4 crystal symmetry with 4 atoms in the unit cell the existence of 12 phonon modes, 9 optical and 3 acoustical. Among the optical phonons, the A_1 and E_1 branches are both Raman and infrared active. Raman scattering determines the existence of two LOPs of symmetry A_1 and E_1 at 583 cm^{-1} and 574 cm^{-1} respectively, corresponding to 71 meV and 72 meV [92]. Thus the phonon replica are attributed to the exciton scattering with one of the two LOPs.

Many donor-bound excitons are also observed in the PL spectra for energies below the FX emission, as for example the A excitons bound to neutral donor, with energies and line-widths depending on the sample [93, 94]. Figure 1.8 shows a schematic representation of the energy regions of the near band-edge transitions as presented in reference [94]. The black region indicates the free exciton (FX) energy region, in blue are represented the transitions associated to ionized (D$^+$X) and neutral (D^{0}X) donor bound excitons and their two electron satellites (TES), in orange the theoretically predicted acceptor bound excitons (A^{0}X) and in green the deeply bound excitons (Y) and their TES. The vertical lines mark the position of the most prominent lines in the emission spectra. These near band-edge defects usually play a relevant role in the optical and electronic properties of ZnO only at low temperatures, since for higher temperatures they can be easily released back as free excitons.

Analogously to other wide band gap semiconductors, ZnO has numerous other defect levels deeper in the band gap, which emission and absorption bands can be associated to. Mostly, these bands in the visible region are related to extrinsic substitutionals such as copper and lithium on the zinc site, responsible of a green and red emission band respectively. However, the green
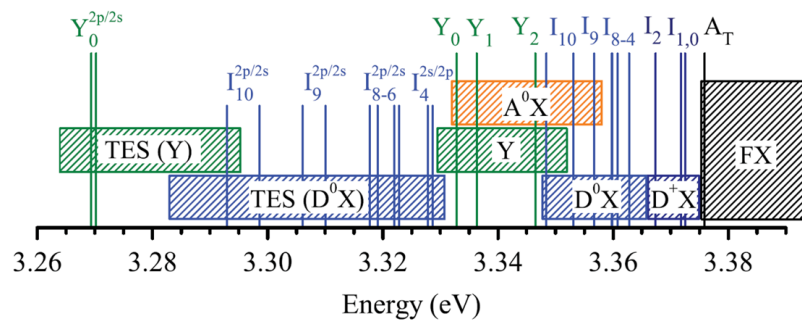
(a)
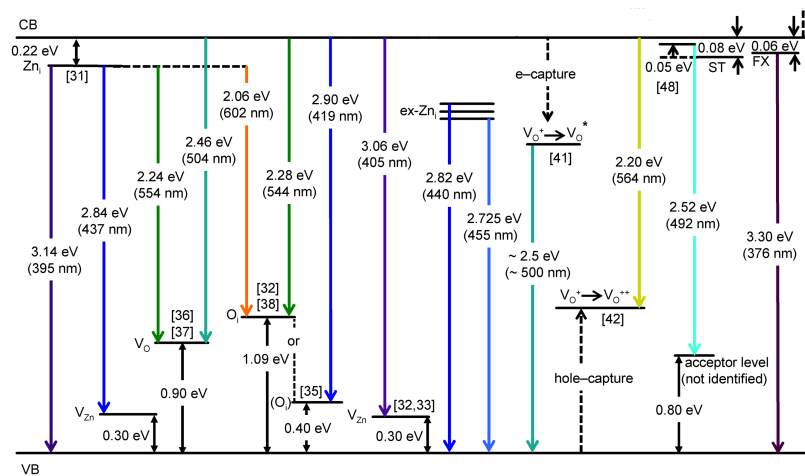
(b)

Figure 1.8: Scheme of the emission energies of the most important free and bound excitons in ZnO from ref. [94] and [95]. See text for details.

emission band is characteristic of most ZnO samples, also those where the presence of Cu can be excluded and has been attributed both to oxygen [96, 97] and zinc vacancies [98, 99]. Vempati et al. [95] present an extensive review of all the emission energies of the most relevant IGS in ZnO of intrinsic origin, which is summarized in panel (b) of figure 1.8. In addition references [100, 101] observe an emission line centered at 1.8 eV, which has been associated with defect complexes involving oxygen excess.

As discussed in section 1.1, defects also influence the electrical properties of a semiconductor. The prevalence of n-type conductivity in most ZnO samples was historically associated with intrinsic defects, such as oxygen vacancies and zinc interstitials [76]. Again, the assignment of the shallow donor character to a given kind of defect is controversial and is mostly related to

the calculation of formation enthalpies of intrinsic defects [102, 103]. The currently accepted theory is that *n*-type conductivity is instead related to an extrinsic defect: hydrogen. It is either necessary for or unintentionally present in most growth techniques, even under ultra high vacuum (UHV) conditions, and thus almost impossible to avoid. In most semiconductors, hydrogen compensates the prevailing conductivity, i.e. it is a so-called *amphoteric* defect, while in ZnO it occurs always as H^+ and therefore always acts as a donor [104]. Hydrogen is present on ZnO in two forms, both with low formation energies [76]: it can either intercalate as interstitial and bind strongly to oxygen or it can substitute on O sites.

The donor character of H *on* ZnO is also responsible for the occurrence of a charge accumulation layer (CAL) when it is adsorbed on the polar oxygen- and the non-polar mixed-terminated surfaces [105–107]. It induces a downward surface band bending which leads to a crossing of the CB with the Fermi energy. This results in a partial filling of the CB in the surface region ($\sim 1\,\text{nm}$) and, consequently, a strongly confined CAL is created. Simultaneously, the work function is reduced due to a change of the net surface dipole moment. Deinert et al. showed that this effect occurs already for very low hydrogen coverages, such as those present in an UHV environment [107].

Charge carrier and exciton dynamics

Excitation relaxation pathways play a central role in determining if a material is suitable for optoelectronic applications such as, for example, photodetection, optical switching or lasing. Furthermore, as discussed in section 1.1.2, the excitation density affects the shape of the optical spectra due to screening, band-gap renormalization or band-filling. Finally, the transition from a low density, excitonic regime to a EHP is continuous and the literature values for the Mott density at room temperature span two orders of magnitude: from 3×10^{17} to $3.7 \times 10^{19}\,\text{cm}^{-1}$ [108, and references therein]. Therefore, caution is required when assigning and interpreting the spectroscopic results. As discussed in section 1.1.1, this holds especially when treating optical spectroscopy data, where the existence of populations is deduced from changes in the optical resonances. Again, the ZnO literature on carrier relaxation and lifetimes is vast and the assignment and values reported often conflicting. This results in a variety of timescales seemingly associated to the same physical process, as well as a variety of processes related to the same timescale. Table 1.1 tries to order the literature values for the most relevant timescales,

as a function of excitation density. The abbreviations used therein are: X indicates the exciton in general, with FX the free exciton, AX and BX the excitons related to A and B valence band, DBX defect bound excitons and SX the surface exciton. The first column lists the process and the second the technique used. For each process the results are sorted for increasing excitation density. Great extent of the literature reports time-resolved photoluminescence (tr-PL) experiments, where the emission at the exciton energy is measured as a function of time. In all the publications listed the results are discussed in terms of excitonic processes, even if the excitation density used is above the nominal Mott density, where excitonic populations should not exist. Exciton formation and relaxations timescales are reported to be hundreds of ps to tens of ns. Details about the charge carrier dynamic and trapping, as well as the experiments performed above the Mott density, are mostly obtained with transient reflectivity and absorption experiments. The charge carrier thermalization in the CB is established to occur in fs to ps, depending on the excess energy above the CB minimum. Direct probes, such as photoemission spectroscopy or THz-spectroscopy, are best-suited to observe electronic and excitonic populations. The formation of the bulk exciton is investigated in reference [19] by looking at the changes in the THz conductivity and they establish the formation of an insulating gas of bound quasiparticles to occur in 100 to 200 ps. Reference [109] directly observes in a photoemission experiment the increase of electronic population *below* the Fermi energy in 200 fs, which is attributed to the formation of "hot" surface excitons. Both results are in good agreement with first-principle calculations [110].

From this comparison it becomes clear that parameters so important for technology as charge carrier and exciton lifetimes are still not established. This work contributes to the identification of charge carrier and exciton relaxation pathways and the corresponding time constants by applying complementary static and time-resolved optical techniques such as time-resolved photoluminescence, time-resolved transmission (tr-T) and the newly developed time-resolved electronic sum-frequency generation. The resonances associated to the three VB are identified in the spectra as well as a defect band going from 1.7 to 2.7 eV. The charge carrier dynamics in the CB are investigated using both the linear optical techniques for excitation densities above the average Mott density ($\sim 3 \times 10^{18}$ cm^{-3}). The linear-optical response, however, is dominated by defect dynamics which are compared for two different ZnO samples. Finally, for excitation densities below the Mott density the exciton formation dynamics are observed both directly as a

time-resolved electronic sum-frequency generation (tr-eSFG) decrease at the resonance energy or indirectly over the onset of stimulated emission.

Process	Note	Technique	T (K)	E_{pump}(eV)	Excitation density	Timescale (ps)	Reference
Carrier thermalization in CB		THz-spectroscopy	30	3.1	$2 \times 10^{16}\,cm^{-3}$	4	Hendry et al. [19]
		2PPE	120	4.4	$5 \times 10^{16}\,cm^{-3}$	0.05	Tisdale et al. [111]
		Absorption	300	4.05	$4.0 \times 10^{19}\,cm^{-3}$	1	Yamamoto et al. [112]
	via LOP scattering	2PPE	50–300	4.19	$1.45 \times 10^{18}\,cm^{-3}$	0.02–0.04	Deinert et al. [109]
	"	Theory	0	0.01 above CBM	below Mott	fs	Zhukov et al. [110]
	via AP scattering	"	"	0–0.01 above CBM	"	ps	"
	Auger recombination	THz-spectroscopy	30	4.6	$2 \times 10^{19}\,cm^{-3}$	1.5	Hendry et al. [19]
Exciton formation	FX	THz-spectroscopy	30	3.1	$2 \times 10^{16}\,cm^{-3}$	200	Hendry et al. [19]
	SX	Tr-PL	2–4	4	below Mott	18	Travnikov et al. [113]
	"	2PPE	50–300	4.19	$1.45 \times 10^{18}\,cm^{-3}$	0.2	Deinert et al. [109]
Exciton lifetime and recombination	FX	THz-spectroscopy	30	3.1	$2 \times 10^{16}\,cm^{-3}$	> 1000	Hendry et al. [19]
	"	Tr-PL	293	3.42	–	970	Koida et al. [114]
	"	"	6	3.84	$3.56 \times 10^{17}\,cm^{-3}$	60–80	Kuehn et al. [115]
	FX (radiative)	"	2	3.48	–	1350	Wagner et al. [94]
	"	"	300	3.81	$8.7 \times 10^{19}\,cm^{-3}$	863.9	Teke et al. [89]
	AX	Tr-Catodoluminescence	5	–	–	95	Bertram et al. [116]
	AX and BX	Tr-reflectivity	4	3.36 and 3.39	–	50–100	Cook et al. [117]
	DX	Tr-PL	6	3.84	$3.56 \times 10^{17}\,cm^{-3}$	200 and 2100	Kuehn et al. [115]
	"	"	2	3.48	–	570–1600	Wagner et al. [94]
	SX	"	6	3.84	$3.56 \times 10^{17}\,cm^{-3}$	130 and 2200	Kuehn et al. [115]
	"	"	2–4	4	below Mott	60	Travnikov et al. [113]

Process	Note	Technique	T (K)	E_{pump}(eV)	Excitation density	Timescale (ps)	Reference
	Non-radiative rec.	Tr-PL	2	3.48	–	200	Wagner et al. [94]
	"	"	300	~ 3.43	–	3800	Chichibu et al. [118]
	"	"	300	3.81	$8.7 \times 10^{19}\,cm^{-3}$	170	Teke et al. [89]
Exciton and carrier trapping	e^- defect trapping	2PPE	120	4.4	$5 \times 10^{16}\,cm^{-3}$	100s of fs	Tisdale et al. [111]
	carrier trapping	Tr-Reflectivity	300	1.5	both	2–6	Versteegh et al. [108]
	"	Absorption @ > 500 nm	–	3.1	$2.30 \times 10^{20}\,cm^{-3}$	400	Bauer et al. [119]
	trapping and emission	Tr-PL	293	3.42	–	14000	Koida et al. [114]
	DX trapping	Tr-PL	2	3.48	–	230–375	Wagner et al. [94]
carrier diffusion to bulk		Tr-reflectivity	4	3.36 and 3.39	–	2–5	Cook et al. [117]
X-X scattering		Tr-PL	300	3.2	$2.0 \times 10^{19}\,cm^{-3}$	instantaneous	Takeda et al. [120]
		Absorption @ > 500 nm			$2.30 \times 10^{20}\,cm^{-3}$	12	Bauer et al. [119]
		Tr-PL	300	3.2	$2.0 \times 10^{19}\,cm^{-3}$	4.2 (rise)	Takeda et al. [120]
BG renormalization		Absorption	300	4.05	$4.0 \times 10^{19}\,cm^{-3}$	> 10	Yamamoto et al. [112]
EHP	optical gain	"	"	"	"	30–200	"
	decay	THz-spectroscopy	30	4.6	$2 \times 10^{19}\,cm^{-3}$	1500	Hendry et al. [19]
Defect recombination		Tr-PL @ 500 nm	–	3.1	$6.10 \times 10^{19}\,cm^{-3}$	340; 2110; 18 800	Bauer et al. [119]
	deeply trapped hole	Absorption @ > 500 nm	–	"	$2.30 \times 10^{20}\,cm^{-3}$	400	"

Table 1.1: Timescales for exciton and charge transfer dynamics in ZnO . The table is sorted by processes and within each process the data are sorted by excitation density, when given.

1.4 SP6

An organic molecule with a resonant optical gap of about 3.4 eV is required in order to form an hybrid system with ZnO, where the energy can be efficiently transferred via a resonant energy transfer mechanism from one semiconducting compound to the other. Furthermore, an efficient HIOS requires the organic compound to have a high absorption cross section and/or high emission yield.

One candidate model system is represented by the spirobifluorene derivative 2,7-bis(biphenyl-4-yl)-2',7'-ditertbutyl-9,9'-spirobifluorene (SP6). Its structure, both as structural formula and tridimensional sketch, is depicted in figure 1.9. It is formed by a sexiphenyl backbone spiro-
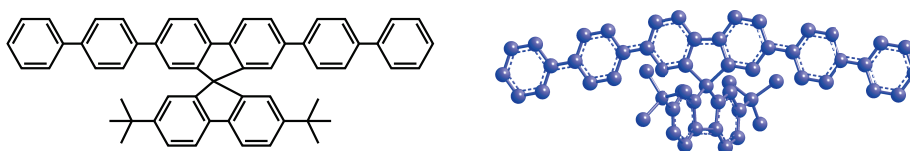
Figure 1.9: Structural formula (left) and tridimensional sketch (right) of SP6

linked to a tertbutyl-decorated biphenyl. The tridimensionality of the spiro-linkage gives the molecule its characteristic propeller-like shape. The sexiphenyl chain is slightly bent due to the linkage and the length of the molecule is of 25.8 Å, while the width is calculated to be 13.6 Å [6]. As shown in reference [121], this shape prevents crystallization of the solid phase by minimizing the packing. The amorphous growth of SP6 films on quartz glass and on $Zn_{0.86}Mg_{0.14}O$ is confirmed by the atomic force mycroscopy (AFM) images shown in reference [6] and [7], respectively.

Figure 1.10[2] shows the Kohn-Sham orbital shape of the frontier orbitals HOMO and LUMO as well as the LUMO+1 and +2. The electron density of the highest occupied molecular orbital is distributed over the whole molecule while the lowest unoccupied molecular orbitals are strongly localized on the two parts of the molecule. The existence of localized states in molecules consisting of conjugated segments separated by non-conjugated bridges has been investigated both theoretically in spiro-linked polyfluorenes [122] and experimentally on stilbene, naphthylene, and anthrylene derivatives [123]. This excited state localization leads to excited states with comparably long lifetimes, but, nevertheless, radiative recombination is observed to occur only

---

[2]Calculations shown by courtesy of Oliver Hofmann, TU Graz (Austria).

HOMO   LUMO   LUMO+1   LUMO+2
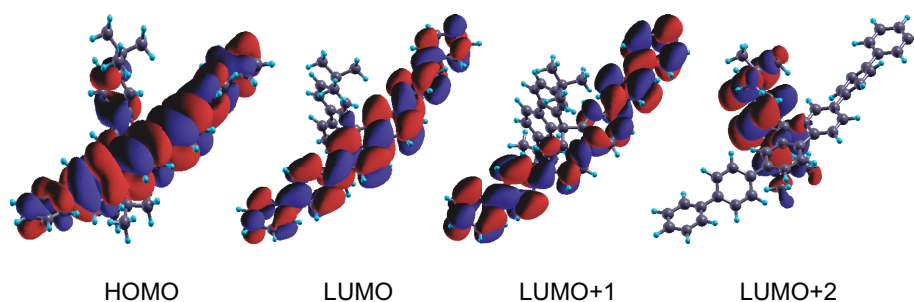
Figure 1.10: Kohn-Sham frontier orbitals of SP6. Clearly, while the HOMO is distributed over the whole molecule, the LUMO and LUMO+1 are localized on the sexiphenyl backbone and the LUMO+2 on the biphenyl group.

from the lowest excited state in all compounds, as expected from Kasha's rule.

The absorption spectrum of SP6 is structureless, as it is typical for phenylenes [124, 125]. It starts at 3.2 eV and peaks at 3.6 eV, thus overlapping with the absorption of ZnO. The absorption coefficient is $\alpha_{SP6} = 4 \times 10^5$ cm^{-1} at the peak energy. The first emission line is observed at 3.14 eV and the PL spectrum is maximum at 2.95 eV, where also an amplified spontaneous emission band appears [5], with an excitation threshold of 111 μJ cm^{-2}. SP6 also exhibits lasing in distributed-feedback (DFB) resonators. DFB resonators are used with organic semiconductors since they require low lasing thresholds. They incorporate a periodic modulation of the refractive index in the cavity that leads to Bragg reflection and laser emission occurs near the Bragg wavelength, which can be varied by changing the modulation period. In SP6 threshold behavior is observed at 166 kW cm^{-2} and no saturation before a minimum output power of 3 W. In the experiments the emission wavelength was tuned in the range between 401.5 nm and 434.2 nm (2.86 to 3.09 eV) by pumping different grating sections [5, 6].

SP6 also exhibits extraordinarily high Raman scattering cross section, which allowed Stähler et al. to perform non-resonant and non-enhanced Raman spectroscopy of SP6 films deposited on ZnO (000$\bar{1}$), ZnMgO(000$\bar{1}$) and sapphire. Their spectra are dominated by a band between 1285 cm^{-1} and 1480 cm^{-1}, associated with CC stretching modes, and a peak at 1600 cm^{-1}, related with the symmetric ring stretch. Furthermore, they showed that the change of substrate does not affect the vibrational modes of the electronic ground state, leading to the conclusion that the molecules adsorb without strong interactions with the substrates. This is further supported by the excellent agreement with density functional theory calculations of the gas phase spectrum [126].

The overlap of the absorption spectrum of SP6 with the one of ZnO, favoring the resonant coupling between the two semiconducting materials, together with the strong light-matter coupling of SP6 evidenced by the high emission and Raman scattering cross-sections, make SP6 the ideal candidate to form a model hybrid inorganic organic system with ZnO.

Furthermore, the frontier orbitals form, when SP6 is deposited on ZnO , a type II energy level alignment with the ZnO energy levels at the zinc terminated $(000\bar{1})$ surface, such as the one depicted in figure 1.5(b). Blumstengel et al. calculate a LUMO offset of 1.0 eV with respect to the CB minimum, from photoemission spectra and gas phase optical gap measurements [7, 8]. This kind of alignment favors electron transfer from the organic to the ZnO, which is indeed observed to occur very efficiently, with transfer times as short as 10 ps, once the excitons have reached the interface. Indeed, the photoluminescence lifetime measured as a function of organic film thickness demonstrates that the charge separation efficiency is limited by the diffusion of the excitons to the hybrid interface. Figure 1.11 shows the CS efficiency η_{CT} as a function of film thickness for two different temperatures (5 K and 280 K), as presented in reference [7]. η_{CT} was fitted with the one dimensional diffusion model setting the PL lifetime to 300 ps and from which the exciton diffusion length was estimated to be 3.7 nm at 5 K and 10 nm at 300 K.
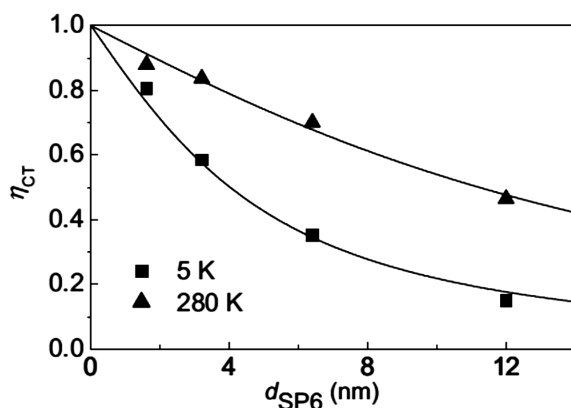
Figure 1.11: Film thickness dependence of the charge separation efficiency at the SP6/ZnO interface for two different temperatures. The higher efficiency at higher temperatures is attributed to the better diffusion of the excitons from the surface of the organic film to the hybrid interface [7].

By using a ZnO/ZnOMgO quantum well structure with a 3.5 nm ZnO quantum well, capped with a ZnMgO barrier of variable thickness, Blumstengel et al. were also able to demonstrate Förster resonant energy transfer from the quantum well to the molecule. This transfer results in the appearance of the quantum well emission peak in the luminescence spectrum of SP6. Furthermore, from the change in the lifetime of the quantum well excitons they established that 75 % of the Wannier-Mott excitons transfer to the organic to generate Frenkel excitons [7].

Both the experiments from Blumstengel et al. demonstrate efficient coupling between SP6

and ZnO [7, 8]. Nevertheless, luminescence spectroscopy directly addresses only the lowest excited state, due to Kasha's rule, and is only indirectly sensitive to higher excited states or to other decay channels that affect the S_1 population but do not lead to emission. These "dark" states, however, can act as traps for excitonic population, and thus strongly affect the efficiency of the hybrid system. Aim of the experiments presented in chapter 6 is to specifically investigate the lifetimes of the excited states by using time-resolved excited state transmission experiments, which are presented in section 3.1. These experiments measure the absorption of the excited state population in transitions to higher excited states S_n, and allow to directly look at all those excited states that have an absorption transition in the energy range of the probe pulse. Identifying the excited states that do not contribute to luminescence permits to tackle the multiple decay channels limiting the efficiency of energy or charge coupling between the two semiconducting materials. Finally, the experiments aim to further understand the mechanisms that are behind exciton diffusion in the SP6 bulk, which has been identified as the limiting factor for the charge separation mechanism.

2. Optical spectroscopy: shed light on matter

Spectroscopy   spec/tros/co/py [spek'träskəpē], *n.*

    The branch of science concerned with the investigation and measurement of spectra produced when matter interacts with or emits electromagnetic radiation.

Spectrum   spec/tum [ˈspɛktrəm], *n.* (*pl.* **spectra**)

    A characteristic series of frequencies of electromagnetic radiation emitted or absorbed by a substance.

This is how the Oxford dictionary [127] defines spectroscopy. But what does a spectrum tell us about the microscopic properties of matter? The answer to this question is the aim of the first section (2.1) of this chapter, which recalls the theoretical formalism connecting the macroscopic observables of an optical experiment, the spectrum, with the microscopic description of matter in terms of response functions. The second section (2.2) builds on the previously introduced definitions to elaborate on the interpretation of time-resolved optical experiments in terms of electronic populations and introduces the rate-equation analysis of optical transients, while the coherent effects visible in ultrafast optical spectroscopies are briefly discussed in its last part (cf. sec. 2.2.2). When the intensity of the light is comparable to the atomic fields, the response of matter is no longer linear with respect to the electric field and nonlinear effects arise, as described in section 2.3. Of particular interest are second order processes, which occur only for broken inversion symmetry, and therefore are powerful tools for interface specific investigations. Among them, sum-frequency generation is specifically relevant for this work and is given most attention. When not otherwise explicitly stated, sections 2.1 and 2.2 are based on references [128], [129] and [130]. The section on nonlinear optics, bases on [128],[131] and [132].

2.1 The observable of an optical experiment: the susceptibility

Matter can be thought as a collection of charged particles: the positive nuclei and the negative electrons. When an electric field is applied, these charged particles move accordingly. In metals the presence of the field leads to a net displacement of the free electrons, the current, while in insulators and semiconductors it produces a collection of oscillating dipoles. The displacement $\mathbf{r}$ of the electron of charge e from the nucleus is governed by the following equation of motion

$$\frac{m}{e}\left[\frac{d^2\mathbf{r}}{dt^2} + 2\Gamma\frac{d\mathbf{r}}{dt} + \Omega^2\mathbf{r} - \left(\chi^{(2)}\mathbf{r}^2 + \chi^{(3)}\mathbf{r}^3 + \cdots\right)\right] = -\mathbf{E}(t) \tag{2.1}$$

with resonant frequency Ω and damping constant Γ.

For an electric field $\mathbf{E}(t) = \frac{1}{2}\mathbf{E}\left[\exp(-i\omega t) + \exp(i\omega t)\right]$ and neglecting anharmonicity, the solution is given by

$$\mathbf{r}(t) = \frac{-e\mathbf{E}_0}{2m}\frac{\exp(-i\omega t)}{\Omega^2 - 2i\Gamma\omega - \omega^2} + c.c. \tag{2.2}$$

and the resulting dipole moment is $\mathbf{p} = -e \cdot \mathbf{r}$

If the medium is treated as an ensemble of N atoms, each with f_i dipoles oscillating with frequency Ω_i and with $\sum_i f_i = Z$ the number of electrons in the atom, then the overall effect of the electric field on the medium is to generate a time-dependent polarization $\mathbf{P}(t) = -eN\sum_i f_i \langle \mathbf{r(t)} \rangle$. It's Fourier transform $\mathbf{P}(\omega) = \varepsilon_0 \chi(\omega)\mathbf{E}(\omega)$ leads to the definition of the *linear susceptibility*, i.e. the linear response function, in the frequency domain, of the medium to a perturbing field of frequency ω:

$$\chi(\omega) = \frac{Ne^2}{\varepsilon_0 m}\sum_i\frac{f_i}{\Omega_i^2 - \omega^2 - 2i\Gamma_i\omega} \quad . \tag{2.3}$$

The fundamental physical meaning of (2.3) is that the dipoles are set to oscillate at the same frequency of the incident field and in turn radiate into the medium and modify how the electric field propagates. The overall electric field is then given by the incident and the induced components. Another common way of expressing the response is in terms of the of the complex dielectric function $\varepsilon(\omega) = \varepsilon_1 + i\varepsilon_2$, connected to the susceptibility by $\varepsilon(\omega) = 1 + \chi(\omega)$.

A linear optical experiment ultimately measures the amount of incident light that is transmitted and reflected by a sample. These macroscopic quantities are related to the microscopic properties of matter respectively via the index of refraction and the absorption coefficient, expressed as the real and imaginary part of the complex index of refraction $\tilde{n}(\omega) = n + ik = (\varepsilon)^{1/2}$.

Therefore, they can be determined from the linear susceptibility as

$$\Re(\chi) = n^2 - 1 = \frac{Ne^2}{\varepsilon_0 m} \sum_i f_i \frac{\Omega_i^2 - \omega^2}{\left(\Omega_i^2 - \omega^2\right)^2 + (2\Gamma\omega)^2} \tag{2.4}$$

and

$$\Im(\chi) = 2nk = \frac{Ne^2}{\varepsilon_0 m} \sum_i f_i \frac{2\Gamma\omega}{\left(\Omega_i^2 - \omega^2\right)^2 + (2\Gamma\omega)^2} \tag{2.5}$$

Since $\Re(\chi)$ and $\Im(\chi)$ are connected to each other by the Kramers-Kronig relations, measuring the reflectivity and the transmission of a sample over the whole frequency spectrum in principle allows the extraction of the full information on the linear susceptibility.

In order to solve (2.1) exactly, it is necessary to neglect anharmonicity, which is possible if the displacement $\mathbf{r}$ is small. This holds only for electric fields, both incident and induced, that are negligible when compared with interatomic fields, typically on the order of 10^{10} to $10^{11}\,\mathrm{V\,m^{-1}}$. If the overall field intensity becomes comparable, then anharmonic components to the displacement need to be taken into account and the solution of the equation of motion is no longer exact. However, if anharmonicity can still be considered as a perturbation, being small with respect to the linear term in $\mathbf{r}$, the resulting polarization can be expressed as a power series of the electric field

$$\mathbf{P} = \varepsilon_0\left(\chi^{(1)}\mathbf{E} + \chi^{(2)}\mathbf{E}^2 + \chi^{(3)}\mathbf{E}^3 + \cdots\right) = \mathbf{P}^{(1)} + \mathbf{P}_{NL} \quad, \tag{2.6}$$

where $\chi^{(2)}$ and $\chi^{(3)}$ are respectively the second and third order nonlinear susceptibility tensors. Nonlinear terms give rise to wave mixing phenomena, such as harmonic generation, as well as controlling the interaction between matter and multiple electric fields.

Before moving on to discuss the nonlinear interactions, it is instructive to deeper understand the connection between the linear response function, $\chi^{(1)}$, and the microscopic structure of matter. This is best achieved in a quantum-mechanical treatment.

2.2 Susceptibility and electronic populations

When a solid is perturbed by an external electrical potential $\Phi_a(\mathbf{r}, t)$ the overall potential is given by

$$V(\mathbf{r}, t) = V_0(\mathbf{r}, t) + e\left[\Phi_a(\mathbf{r}, t) + \Phi_i(\mathbf{r}, t)\right] \quad,$$

where $\Phi_i(\mathbf{r}, t)$ is the induced potential due to the reaction of the electron distribution to the applied electric field. The potentials are connected to the charge densities by Poisson equations of the form $\nabla^2 \Phi = 1/\varepsilon_0 \cdot \rho$ and the total potential $\Phi_{tot} = \Phi_a + \Phi_i$ to the applied external potential by the dielectric function as $\Phi_{tot} = \varepsilon^{-1} \Phi_a$ [133]. The dielectric constant, and in turn the susceptibility, can be determined in the linear response theory framework if the dependence of the external potential and the induced charge density on space and time are written as $\exp\{i[\mathbf{q} \cdot \mathbf{r} - (\omega + i\delta)\,t]\}$, where $\mathbf{q}$ is the momentum of the photon. The term $e^{\delta t}$ ensures that the perturbation goes to zero for long negative delays. The complex susceptibility is then proportional to

$$\chi(\mathbf{q}, \omega) \propto \frac{1}{V} \sum_{\mathbf{k}\mathbf{k}'nn'\sigma} |\langle n\mathbf{k}|e^{i\mathbf{q}\cdot\mathbf{r}}|n'\mathbf{k}'\rangle|^2 \frac{f(E_n(\mathbf{k})) - f(E_{n'}(\mathbf{k}'))}{E_{n'}(\mathbf{k}') - E_n(\mathbf{k}) - \hbar\omega + i\delta} \tag{2.7}$$

Since photons only transfer small momenta, the formula can be expanded for $\mathbf{q}$:

$$\begin{aligned}
\chi(\mathbf{q} \to 0, \omega) \propto {} & \frac{e^2}{Vq^2} \sum_{\mathbf{k}n\sigma} \frac{f(E_n(\mathbf{k} + \mathbf{q})) - f(E_n(\mathbf{k}))}{E_n(\mathbf{k} + \mathbf{q}) - E_n(\mathbf{k}) - \hbar\omega + i\delta} \\
& + \frac{1}{Vq^2} \sum_{\substack{\mathbf{k}nn'\sigma \\ n \neq n'}} \left|e^2 \langle n'\mathbf{k}'|\mathbf{r}|n\mathbf{k}\rangle\right|^2 \frac{f(E_{n'}(\mathbf{k})) - f(E_n(\mathbf{k}))}{E_{n'}(\mathbf{k}) - E_n(\mathbf{k}) - \hbar\omega + i\delta}
\end{aligned} \tag{2.8}$$

This expression highlights the contributions to the susceptibility due to *intra-* (first addend on right hand side) and *inter*-band (second addend on right hand side) transitions. Interband transitions occur only for a photon energy $\hbar\omega = E_{n'}(\mathbf{k}) - E_n(\mathbf{k})$ that matches an optical transition and are weighted by the occupation of the initial and final states as well as the matrix element

$$\left|e^2 \langle n'\mathbf{k}'|\mathbf{r}|n\mathbf{k}\rangle\right|^2 \tag{2.9}$$

proportional to the dipole operator between the final and the initial state. These matrix elements are commonly called the *oscillator strength* of the transitions.

From equation (2.7) and (2.8) it is clear that changes in the populations of the states due to the effect of a perturbation field result in changes of the optical properties of the material,

which can be indirectly measured through absorption and reflection experiments. If the optical properties at a given frequency are monitored as a function of the time since the electronic density has changed, then it is possible to infer the time evolution of electronic populations. This is at the basis of optical pump-probe experiments, where a perturbation field, the *pump*, is used to transiently modify the electronic populations and a second field, the *probe*, is used to measure the pump-induced changes on the dielectric function. The measurement of the probe transmission or reflection as a function of pump-probe delay is called a kinetic trace.

2.2.1 Pump-probe experiments and rate equations

In order to understand the kinetic traces observed in time-resolved spectroscopy it is useful to start by considering the simplest possible quantum mechanical system interacting with radiation: the two-level system. This problem was addressed by Einstein in 1917, when he postulated the existence of stimulated emission [134].

Two energy levels E_1 (ground state) and E_2 (excited state) of a system of N identical and non-interacting atoms in a cavity, which are separated by the energy $\hbar\omega$ and have a thermal population $N = N_1 + N_2$, are coupled radiatively by three possible transitions: spontaneous emission, absorption and stimulated emission. As long as there is population N_2 in the excited state an electron can spontaneously relax to E_1 with a probability per unit time A_{21}, the probability of spontaneous emission. The two other processes require the presence of external sources of electromagnetic radiation, with total energy $\langle W(\omega) \rangle = \langle W_T(\omega) \rangle + \langle W_E(\omega) \rangle$ given by the sum of thermal and external energy. The probability of absorption is then $B_{12} \langle W(\omega) \rangle$ and the one of stimulated emission $B_{21} \langle W(\omega) \rangle$.

The time evolution of the population in the states is described by the rate equation

$$\frac{dN_2}{dt} = -\frac{dN_1}{dt} = B_{12} \langle W(\omega) \rangle N_1 - (A_{21} + B_{21} \langle W(\omega) \rangle) N_2 \tag{2.10}$$

If at the time where the external field is turned on all the atoms are in the ground state, i.e. $N = N_1$, then the population in the excited state evolves as

$$N_2(t) \propto [1 - \exp(-A_{21}t)] \quad . \tag{2.11}$$

Although this approach can seem rather simplistic, since it does not take into account coherences between the two quantum mechanical states, rate equations can be used to describe the

dynamical evolution of electronic populations, as demonstrated in the following with a quantum mechanical approach [135].

If an atom interacts with an electric field of frequency ω the main contribution to the interaction is given by the dipole-dipole interaction, which Hamiltonian is defined as $\hat{H}_i = -e\mathbf{D} \cdot \mathbf{E}$, where $\mathbf{D}$ is the total dipole moment of the atom. If $|1\rangle$, $|2\rangle$ and $|3\rangle$ are three eigenstates of the non-interacting system, the eigenstates of the interacting system are a linear combination defined by the coefficients C_1, C_2 and C_3. Consider a pump-probe experiment performed on the three-level system depicted in figure 2.1. The pump beam creates a population in state $|2\rangle$ by promoting electrons from the ground state $|1\rangle$. These electrons decay back to $|1\rangle$ with the rate Γ_R. The population in $|2\rangle$ is monitored by the probe beam, delayed by a time τ, which induces a coherence ρ_{23} between state $|2\rangle$ and $|3\rangle$ that irradiates the signal. Thus, the pump-probe intensity I_{PP} is given by [136]

$$I_{PP} \propto \int_{-\infty}^{+\infty} E_{probe}(t,\tau)\rho_{23}(t)dt \quad . \quad (2.12)$$
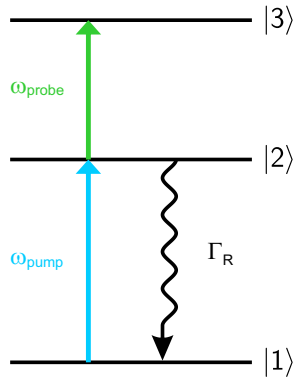
Figure 2.1: Three level system interacting with a pump and probe laser beam. T_R indicates the relaxation time of the intermediate state.

The three level system interacting with the pump and probe electric fields is best described within the density matrix formalism

$$\rho = \begin{pmatrix} |C_1|^2 & C_1 C_2^* & C_1 C_3^* \\ C_2 C_1^* & |C_2|^2 & C_2 C_3^* \\ C_3 C_1^* & C_3 C_2^* & |C_3|^2 \end{pmatrix} \quad (2.13)$$

where the diagonal elements $\rho_{ii} = |C_i|^2 = \frac{N_i}{N}$ are the population densities in the states $|1\rangle$, $|2\rangle$ and $|3\rangle$ and ρ_{ij} is the coherence between states $|i\rangle$ and $|j\rangle$.

The time evolution of the density matrix elements is given by the *optical Bloch equations (OBE)*

$$\dot{\rho}_{ij} = -\frac{i}{\hbar} \sum_a \left(\mu_{ia} E \tilde{\rho}_{aj} + \mu_{aj} E \tilde{\rho}_{ia} \right) + \Gamma_{diss} \rho_{ij} \quad (2.14)$$

where Γ_{diss} is a phenomenological dissipation rate of the population or coherence. For the levels

in the picture this results in the following system of coupled equations:

$$\dot{\rho}_{11} = \frac{i\mu_{12}E_{\text{pump}}(t-\tau)}{2\hbar}(\rho_{21}-\rho_{12}) + \Gamma_R\rho_{22}$$

$$\dot{\rho}_{22} = \frac{i\mu_{12}E_{\text{pump}}(t-\tau)}{2\hbar}(\rho_{12}-\rho_{21}) + \frac{i\mu_{23}E_{\text{probe}}(t)}{2\hbar}(\rho_{32}-\rho_{23}) - \Gamma_R\rho_{22}$$

$$\dot{\rho}_{33} = \frac{i\mu_{23}E_{\text{probe}}(t)}{2\hbar}(\rho_{23}-\rho_{32})$$

$$\dot{\rho}_{12} = \frac{i\mu_{12}E_{\text{pump}}(t-\tau)}{2\hbar}(\rho_{11}-\rho_{22}) - \left(\Gamma_{12}^{\star}+\frac{\Gamma_R}{2}\right)\rho_{12}$$

$$\dot{\rho}_{23} = \frac{i\mu_{23}E_{\text{probe}}(t)}{2\hbar}(\rho_{22}-\rho_{33}) - \left(\Gamma_{23}^{\star}+\frac{\Gamma_R}{2}\right)\rho_{23}$$

$$\rho_{21} = \rho_{12}^{*}$$

$$\rho_{32} = \rho_{23}^{*}$$

(2.15)

The dissipation rates are defined as $\Gamma_R = 1/\tau_R$ for the decay of the intermediate state population and $\Gamma_{12}^{\star}$, $\Gamma_{23}^{\star}$ for the pure dephasing of the coherences. $E_{\text{pump}}(t-\tau)$ and $E_{\text{probe}}(t)$ are the envelopes of the pump and probe pulse. The only assumptions made for writing the equations are that ω_{pump} and ω_{probe} are well separated spectrally, such that the only interactions possible are the ones depicted in figure 2.1, and that the lifetime of $|3\rangle$ is much longer than the duration of the probe pulse. These are plausible assumptions in the experiments performed in this work. The equations reduce to the form of the rate equation (2.10) for infinitely short dephasing times ($\Gamma_{ij}^{\star} \to \infty$), at least for times larger than the duration of the pulses and the coherences are expected to become more and more relevant for dephasing times that approach in order of magnitude the relaxation times. In order to get further insight on how strongly the optical transients are affected by the coherences the OBE are solved numerically for three different sets of parameters. The pulse durations are of 40 fs and 20 fs for the pump and probe respectively and the intensity of the pump is 100 times larger than the one of the probe. Since the dephasing time in molecules can vary from tens of femtoseconds to picoseconds depending on the size of the molecules and lacking a literature value for the dephasing in the specific case of SP6, the pure dephasing time is kept fixed to 10 fs for computational costs. The relaxation time $\tau_R = 1/\Gamma_R$ is varied over three orders of magnitude from 30 fs to 3 ps. The coherences are found to affect mostly the onset of the optical transient, as exemplary shown in figure 2.2 for a relaxation time of 300 fs. The figure compares the optical transient with the calculated pump-

Figure 2.2: Comparison of the calculated ρ_{22} and the optical transient for a relaxation time of 300 fs and a pure dephasing time of 10 fs. The presence of the coherences leads to a retarded maximum in the transient signal compared with the population.
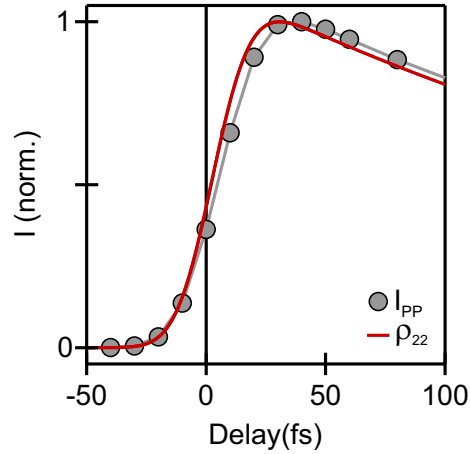
induced population density in level $|2\rangle$ and clearly shows that the effect of the coherences is to shift the maximum of the transient to larger positive delays.

How this transient shift affects the evaluation of the relaxation times in a rate equation picture is discussed in figure 2.3, where the optical transients obtained for relaxation times of 30 fs, 300 fs and 3000 fs are depicted (gray dots) from top to bottom and compared with the best fits for five fitting procedures that differ on how the transient is treated.

A (green): Given the expression for the population $N(t)$ obtained from the rate equations, the intensity of the pump-probe signal results from its convolution with the cross-correlation of pump and probe intensities [137]

$$I_{PP} = \int_{-\infty}^{+\infty} N(t) \int_{-\infty}^{+\infty} I_{\text{probe}}(t' - \Delta t) I_{\text{pump}}(t' - t) dt' dt \quad . \tag{2.16}$$

The cross correlation of two Gaussian pulses is again a Gaussian pulse and this fitting method fixes its FWHM to the addition in quadrature of the FWHM of pump and probe and the time zero of the onset of the population to $\Delta t = 0$ as dictated by the simulations. The only fitting parameter is the relaxation time τ_R

B (yellow): The function used is the same as in A but time zero is allowed to freely vary.

C (red): Same fit function as in A and B but the FWHM is also considered as free parameter.

D (dark red): The convolution of a step-like function with a Gaussian curve, which would correspond to equation (2.16) in absence of recombination, results in the error function $\text{erf}\left[(t - t_0)/\tau_p\right]$, where τ_p takes into account the width of the pulses. The optical transients can thus be fitted by the product of an error function with the exponential decay obtained from the rate equations. In this case, time zero is fixed to $\Delta t = 0$, while τ_p is a free parameter.

E (violet): In this case the same error function approach as above is used but both t_0 and τ_p are left as free parameters.

F (light blue): Here the onset is ignored and the transients are fitted with a simple exponential decay starting at the maximum intensity and with $t_0 = 0$.

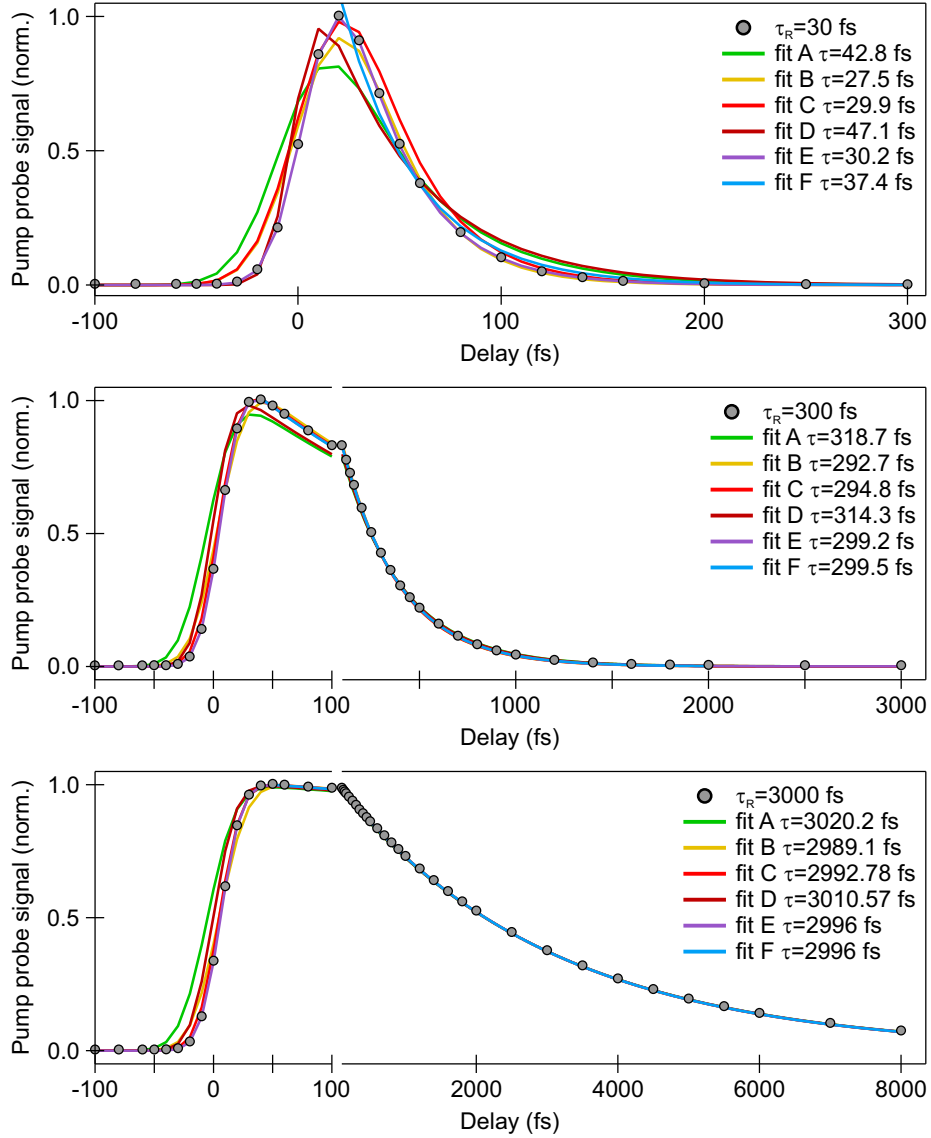**Figure 2.3:** *From top to bottom*: comparison of the theoretical pump-probe transients calculated from the OBE for three relaxation times 30 fs, 300 fs and 3000 fs with fits resulting from different methods as discussed in the text.

The resulting relaxation times τ are reported in the legend of the figure, while table 2.1 reports the relative error with respect to the expected theoretical value of $\tau_R = 30, 300$ or 3000 fs.

Table 2.1: Errors introduced in by fitting optical transients with the rate equations, and thus ignoring the coherences, instead of using the full Bloch equations treatment.

Method	Relaxation time (fs)		
	30	300	3000
A	42 %	6.2 %	0.6 %
B	8.3 %	2.4 %	0.4 %
C	0.1 %	1.7 %	0.2 %
D	57 %	4.8 %	0.35 %
E	0.6 %	0.3 %	0.1 %
F	25 %	0.2 %	0.1 %

The results evidence several aspects. First, the error introduced increases drastically with decreasing relaxation time, i.e. when relaxation and dephasing times become comparable as it was qualitatively expected from the equations. Second, the error increases for methods where time-zero is kept fixed such as A, D and F. For example, despite methods D and E use the same fit function, the introduced error in the case of the fastest relaxation time goes from 57 to 0.6 %. Finally, the more accurate convolution methods A,B and C do not improve significantly the errors compared with the other two methods, which are computationally less expensive. This comparison allows to conclude that fitting approaches based on rate equations describe sufficiently well the optical transients, even when dephasing and relaxation times are comparable, as long as time zero is allowed to be a free parameter. Moreover, the temporal shift of the transients with respect to the center of the pump and probe cross-correlation, could in principle contain information about the pure dephasing time [138]. This however requires the precise experimental determination of the pump-probe cross-correlation at the sample position.

Based on these results the transients presented in chapter 5 and 6 have been generally fitted with method E or F, depending on whether or not the transient presented effects due to higher order interactions such as those presented in the next section.

2.2.2 Higher order interactions: coherences in time-resolved spectroscopies

Until now only the classical description of pump-probe experiments was treated, where pump and probe interact sequentially. It means that the pump interacts with the sample first and the effects, both on the populations and coherences, are subsequently monitored by the probe. This

approach is definitely valid when pump and probe pulses are separated in time. With pulses of finite duration, however, it is natural to imagine scenarios where pump and probe do not interact sequentially but are mixed in time.

A full analytical description requires to treat pump and probe fields symmetrically and thereby consider all possible time orderings of the interactions between the two fields and matter. Calculating the response of the medium at the probe frequency ω_{probe} in the presence of the pump electric field corresponds to calculate the polarization at ω_{probe} and the pump induced correction to the linear response is given by the third order nonlinear response $\chi^{(3)}(\omega_{probe})$ [136, 139].

The detection scheme of a linear optical pump-probe experiment, such as time resolved transmission or reflection, is normally homodyne, i.e. the intensity of the signal field is detected without retaining any phase information. As a consequence, such experiments do not allow the detection of the evolution of the coherences, which nevertheless affect to some extent the transient signals at early pump-probe delays. Sequential coherences, such as the ones discussed in the previous section, have been shown to vary the onset of the transient. However, as long as the time zero is a free fit parameter, the rate equation description reproduces the full treatment [137]. Non-sequential contributions, instead, can strongly affect the early-time dynamics, especially if one of the fields has a broadband spectral distribution. Mixed terms, indeed, lead to effects such as two-photon absorption, stimulated Raman amplification and, mostly relevant for this work, cross-phase modulation [140]. This, similar to the case of self-phase modulation discussed in appendix B, arises when the intense pump beam modulates the real part of the refractive index in time. This modulation, in turn, generates a time-dependent modulation of the phase of the probe pulse, which leads to a redistribution of energy over the different frequencies. The effects, which depend on the temporal distribution of the different wavelengths in the probe spectrum (the *chirp*) [141], are detected as wavelength dependent oscillations around the time origin [142] and can severely affect the interpretation of early dynamics in weak transient spectra [138]. Nevertheless, such effects are present only for times where the pump and the probe electric field are simultaneously interacting with the sample, i.e. within their temporal cross-correlation. For any time before and after the time interval around the origin, the kinetic traces reflect the dynamics of the electronic populations.

2.3   Second-order phenomena as spectroscopic tools

When the amplitude of the applied electric field becomes of the order of the atomic electric field the lowest-order correction term $\mathbf{P}^{(2)} = \chi^{(2)}\mathbf{E^2}$ becomes comparable to the first order response. This induced second order polarization, in turn, acts as a source term for an electric field E^{NL}

$$\nabla \times \nabla \times \mathbf{E}^{NL} + \frac{1}{c^2}\frac{\partial^2}{\partial t^2}\mathbf{E}^{NL} = -\frac{1}{\varepsilon_0 c^2}\frac{\partial^2}{\partial t^2}\mathbf{P}^{NL}$$

Considering an incident field containing two different frequencies

$$\mathbf{E}(\mathbf{r},t) = E(t)\hat{e} = [E_1\exp(-i\omega_1 t) + E_2\exp(-i\omega_2)t]\hat{e}\,,$$

the induced second order polarization $P^{(2)}(t) = \varepsilon_0\chi^{(2)}E^2(t)$ takes the form

$$
\begin{aligned}
P^{(2)}(t) = \varepsilon_0\chi^{(2)}\Big[\quad & 2E_1^*E_1 + 2E_2^*E_2 + && \text{(OR)}\\
& +E_1^2 e^{-i(2\omega_1)t} + E_2^2 e^{-i(2\omega_2)t} + c.c.+ && \text{(SHG)}\\
& +2E_1 E_2 e^{-i(\omega_1+\omega_2)t} + c.c.+ && \text{(SFG)}\\
& +2E_1 E_2^* e^{-i(\omega_1-\omega_2)t} + c.c.\Big] && \text{(DFG)}
\end{aligned}
\tag{2.17}
$$

In general, the two different frequencies do not have to be in the same electric field but there can be two fields $\mathbf{E_1}$ and $\mathbf{E_2}$, each with its own propagation direction. This means that $\mathbf{P}^{(2)}$, $\mathbf{E_1}$ and $\mathbf{E_2}$ are vector quantities that can have components in each of the three space dimensions and $\chi^{(2)}$ is a third rank tensor with 27 elements. The most general formulation for the polarization is thus

$$P_i(\omega_n + \omega_m) = \varepsilon_0\sum_{jk}\sum_{(nm)}\chi_{ijk}^{(2)}(\omega_n+\omega_m,\omega_n,\omega_n)E_j(\omega_n)E_k(\omega_m) \tag{2.18}$$

where i, j, k are the Cartesian coordinates of the fields and the notation (nm) indicates that the sum $\omega_n + \omega_n$ is fixed while both the frequencies are allowed to vary and can take both positive and negative values.

Before discussing the properties of the tensor $\chi^{(2)}$, it is interesting to inspect equation (2.17) in detail. The second order polarization accounts for four different processes:

Optical rectification (**OR**): the generation of dc field by an intense optical beam.

second-harmonic generation (SHG): generation of a field at the doubled fundamental frequencies

Sum-frequency generation (SFG): generation of a field at the sum of the incoming frequencies

Difference-frequency generation **(DFG):** generation of a field at the difference of the incoming frequencies

Energy needs to be conserved in all these processes. This implies that, in the particular case of DFG, the mixing of a field of frequency ω_1 with one of frequency ω_2 to generate $\omega_3 = \omega_1 - \omega_2$ requires the annihilation of a photon at ω_1 and the creation of one at ω_2. This effective amplification of the field oscillating at ω_2 is called *optical parametric amplification* and is the working principle of the optical parametric amplifier (OPA) introduced in section 3.2.

Symmetry requirements of the $\chi^{(2)}$ tensor

The second-order susceptibility tensor $\chi^{(2)}$ determines the amplitude of the second order process. Furthermore, the susceptibility must satisfy symmetry requirements that have important practical consequences: reality, permutation and spatial symmetry. They are reviewed in this section, starting from the latter.

The spatial symmetry of the susceptibility tensor reflects the structural properties of the medium. Each medium belongs to a point symmetry group defined by symmetry operations S under which it is invariant and the spatial symmetry implies that $\chi^{(2)}$ also remains unchanged. The symmetry operation is a second-rank tensor and the spatial symmetry requirement can be written as

$$(\hat{i} \cdot \mathbf{S}^{\dagger}) \cdot \chi^{(2)} : (\mathbf{S} \cdot \hat{j})(\mathbf{S} \cdot \hat{k}) = \chi^{(2)}_{ijk} \; . \tag{2.19}$$

There are as many equations like the one above as the number of symmetry operations in the group and they can be used to reduce the number of independent tensor elements in $\chi^{(2)}$. The most important consequence of equation (2.19) occurs for *centrosymmetric* materials, i.e. those possessing an inversion symmetry. If the symmetry operation of the inversion is $\mathbf{S} \cdot \hat{e} = -\hat{e}$ then eq. (2.19) results in $\chi^{(2)}_{ijk} = -\chi^{(2)}_{ijk} = 0$.

A second order effect can only arise when inversion symmetry is broken.

Besides being forbidden in 11 crystal classes out of 32, those which are centrosymmetric, second-order effects also do not arise in amorphous solids. Indeed, even if the constituent molecules are lacking inversion symmetry, their dipole oscillations would interfere destructively due to the lack of long-range order. Inversion symmetry, however, is definitely broken at a surface or an interface. Therefore, second-order nonlinear effects are extensively used to study interfacial properties.

Both the polarization and the electric field are real, being physically measurable quantities, such that

$$P_i(-\omega_n - \omega_m) = P_i(\omega_n + \omega_m)^* \quad \text{and} \quad E_j(-\omega_n) = E_j(\omega_n)^* , E_k(-\omega_m) = E_k(\omega_m)^*$$

This is the reality condition that links the positive and negative frequency components of the susceptibility:

$$\chi_{ijk}^{(2)}(-\omega_n - \omega_m, -\omega_n, -\omega_m) = \chi_{ijk}^{(2)}(\omega_n + \omega_m, \omega_n, \omega_m)^* \tag{2.20}$$

Finally, the intrinsic permutation symmetry is a consequence of i, j, k, n and m being dummy indices and therefore:

$$\chi_{ijk}^{(2)}(\omega_n + \omega_m, \omega_n, \omega_m) = \chi_{ikj}^{(2)}(\omega_n + \omega_m, \omega_m, \omega_n)$$

For a lossless medium, i.e. far away from resonances, there is also *overall* permutation symmetry. If it applies, then all the frequency arguments can be freely exchanged as long as the corresponding Cartesian indices are exchanged as well.

2.3.1 Sum-frequency generation spectroscopy

From the discussion above, second-order optical phenomena are clearly useful to generate different frequencies starting from the fundamental of a laser or to get insight on the symmetry of a crystal, but it is their resonant nature that makes them really powerful.

The general expression of the second-order susceptibility for sum-frequency generation is given by [131]

$$\chi_{ijk}^{(2)}(\omega_3 = \omega_1 + \omega_2) = -\frac{N}{2\varepsilon_0 \hbar^2} \sum_{a,b,c} \rho_{aa}^{(0)} \frac{\langle a|\mu_i|b\rangle\langle b|\mu_j|c\rangle\langle c|\mu_k|a\rangle}{[\omega_3 - \omega_{ab} + i\Gamma_{ab}][\omega_2 - \omega_{ca} + i\Gamma_{ca}]} +$$

$$+ \frac{\langle a|\mu_i|b\rangle\langle b|\mu_k|c\rangle\langle c|\mu_j|a\rangle}{[\omega_3 - \omega_{ab} + i\Gamma_{ab}][\omega_1 - \omega_{ca} + i\Gamma_{ca}]} + \frac{\langle a|\mu_k|b\rangle\langle b|\mu_j|c\rangle\langle c|\mu_i|a\rangle}{[\omega_3 + \omega_{ab} + i\Gamma_{ab}][\omega_2 + \omega_{ca} + i\Gamma_{ca}]} +$$

$$+ \frac{\langle a|\mu_j|b\rangle\langle b|\mu_k|c\rangle\langle c|\mu_i|a\rangle}{[\omega_3 + \omega_{ab} + i\Gamma_{ab}][\omega_1 + \omega_{ca} + i\Gamma_{ca}]} - \frac{\langle a|\mu_j|b\rangle\langle b|\mu_i|c\rangle\langle c|\mu_k|a\rangle}{[\omega_3 - \omega_{bc} + i\Gamma_{bc}][\omega_2 + \omega_{ca} + i\Gamma_{ca}]} + \tag{2.21}$$

$$- \frac{\langle a|\mu_j|b\rangle\langle b|\mu_i|c\rangle\langle c|\mu_k|a\rangle}{[\omega_3 - \omega_{bc} + i\Gamma_{bc}][\omega_1 - \omega_{ba} + i\Gamma_{ba}]} - \frac{\langle a|\mu_k|b\rangle\langle b|\mu_i|c\rangle\langle c|\mu_j|a\rangle}{[\omega_3 - \omega_{bc} + i\Gamma_{bc}][\omega_2 - \omega_{ba} + i\Gamma_{ba}]} +$$

$$- \frac{\langle a|\mu_k|b\rangle\langle b|\mu_i|c\rangle\langle c|\mu_k|a\rangle}{[\omega_3 + \omega_{bc} + i\Gamma_{bc}][\omega_1 - \omega_{ca} + i\Gamma_{ca}]}$$
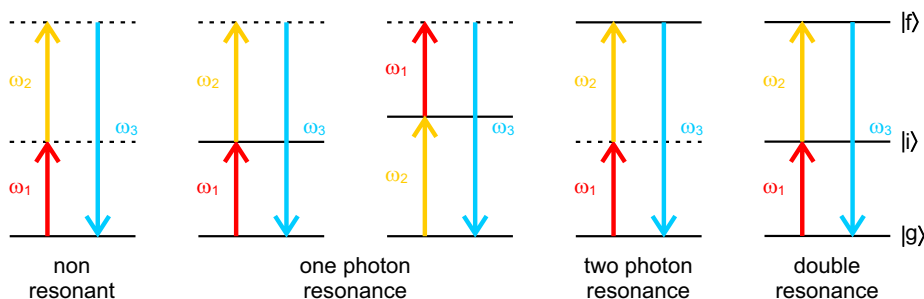
Figure 2.4: Possible resonances in a SFG experiment: *non resonant*, *one photon resonance*: either $\hbar\omega_1$ or $\hbar\omega_2$ are resonant with a transition, *two photons resonance*: the sum frequency $\hbar\omega_3$ is resonant with a transition, *double resonance*: all the photon energies are resonant with a transition. The ground, intermediate and final levels are labeled $|g\rangle$, $|i\rangle$ and $|f\rangle$ respectively. Dashed lines indicate virtual levels

where a, b and c are dummy indices indicating the states, $\rho_{aa}^{(0)}$ is the population density in state $|a\rangle$ at equilibrium and μ_ξ is the dipole operator along the ξ-axis. $\hbar\omega_{ab}$, $\hbar\omega_{bc}$ and $\hbar\omega_{ca}$ are the transition energies between the states and Γ is the linewidth of the transition. As in the case of the linear susceptibility, $\chi^{(2)}$ is resonantly enhanced if the photon energy of at least one of the fields matches the energy of an electronic transition. There are three different classes of possible resonances in a sum-frequency generation (SFG) experiment, which are depicted in figure 2.4. *One-photon resonances* arise when the photon energy of one of the incoming waves matches a transition and is also called intermediate state resonance. *Two-photon resonances* require the sum of the two incoming photon energies to match the transition and are therefore also called final state resonances. *Double resonances* occur when all the photon energies match an electronic transition. In this latter case both denominators of the corresponding term in equation (2.21) are resonant and the signal is doubly enhanced [143]. The output photon energy of one- and two-photon resonances is the same and they can not be distinguished for two fixed values of the incoming wave frequencies. A typical experimental scheme for SFG uses one tunable (or broadband) beam to match the resonances (the resonant beam) and a second beam, commonly called the upconverting beam, at a fixed frequency. Identification of intermediate or final state processes is possible by using different fixed frequencies for the upconverting beam.

Since its first application in 1988 [144], SFG is extensively used to probe vibrations of molecules at interfaces [145–147]. Here, one of the two incoming beams is a broadband infrared (IR) beam, being resonant with the vibrational transitions, while the upconverting beam

is a narrowband visible (VIS) beam. If one of the frequencies contained in the IR field matches a vibrational transition Ω_i^{vib}, the resulting SFG spectrum is enhanced at $\omega = \omega_{\text{upconv.}+\Omega_i^{\text{vib}}}$.

This work instead presents SFG as a suitable technique for the spectroscopy of *electronic* transitions in solids. The scheme is depicted in figure 2.5. A visible beam of frequency $\omega_1 = 800\,\text{nm}\,(=1.5\,\text{eV})$ is used to upconvert a broadband white-light continuum (WLC) ranging from 480 to 700 nm, corresponding to 1.8 to 2.6 eV. Such a broadband spectrum has the advantage over the fixed photon energy of resonant SFG that tuning of the frequency is not required for mapping the whole resonant density of states (DOS), thereby substantially simplifying the experiment (cf. chapter 4). The photon energies of the
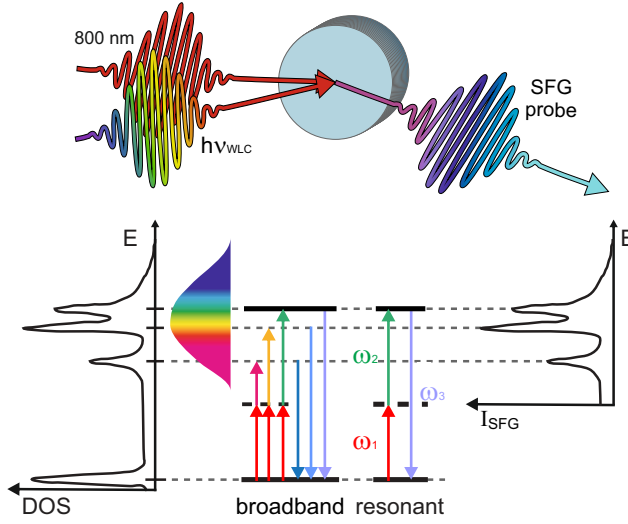

Figure 2.5: (*Top*) Beams used in the electronic SFG experiment. (*Bottom*) Energy scheme and relevant transitions for a broadband and a resonant SFG experiment

beams are such that a two-photon resonance is expected, for the materials used in this work, as depicted. To the best of my knowledge a similar scheme has never been used before for the spectroscopy of solids and only once for molecules in solution [148].

Finally, the spectral intensity of a SFG spectrum is given by

$$I \propto \left| [F(\omega_3) \cdot \hat{e}_3] \cdot \chi^{(2)} : [F(\omega_2) \cdot \hat{e}_2] \cdot [F(\omega_1) \cdot \hat{e}_1] \right|^2 \tag{2.22}$$

where $F(\omega_i)$ is the tensorial Fresnel coefficient relating the incoming field at frequency ω_i with the effective field inside the crystal and $\hat{e}_i$ is the polarization vector. The propagation direction of the generated SFG is defined by momentum conservation $\mathbf{k}_{SFG}^{\parallel} = \mathbf{k}_1^{\parallel} + \mathbf{k}_2^{\parallel}$. A detailed treatment for the determination of the Fresnel coefficients and the effective fields, as well as the SFG geometry is given in reference [149].

3. Worktools
Experimental details

A common characteristic of the excitation relaxation processes discussed in chapter 1, both for excitons or free carriers, is that they occur on ultrafast timescales ranging from few femtoseconds (fs) to hundreds of picoseconds (ps). Investigating processes on such short timescales requires techniques, the so-called pump-probe spectroscopies, that make use of short laser pulses of few tens of femtoseconds. While section 2.2.1 introduced their theoretical background, section 3.1 discusses their practical aspects by focusing on time-resolved excited state transmission spectroscopy, one of the complementary techniques used in this work. The time-resolved electronic sum-frequency generation (tr-eSFG) setup, developed and firstly demonstrated in the context of this thesis, will be extensively explained in a dedicated chapter (cf. chapter 4). Both experiments require a laser system that provides pulses of well defined intensity and temporal, spectral and spatial distribution, such as those provided by a femtosecond pulsed laser. Moreover, both experiments are based on the ability of generating and compressing a white-light continuum (WLC). Both the laser system and the WLC compression setup used in this work are presented in section 3.2. Section 3.3 describes the preparation of the ZnO, SP6/Glass and SP6/ZnO samples investigated in the experiments. Finally, section 3.4 briefly illustrates the optical cryostat used to keep the sample in a well defined environment in terms of temperature and pressure.

3.1 Probing ultrafast processes: pump-probe spectroscopies

Ultrafast processes are to a spectroscopist the analog of fast moving objects to a photographer. As the latter can acquire sharp and detailed pictures only by using an exposition time that is shorter than the movement, so the spectroscopist needs to use an exposition time that matches the time scale of the processes of interest. Only so is it possible to obtain a spectrum that constitutes a well defined temporal snapshot of the process and does not integrate over multiple timescales. A series of snapshots taken at different times then allows to determine the temporal

evolution of the system. However, the analogy ends here because the physical processes relevant to this work happen on timescales on the order of hundreds of picoseconds at most. To date, the record-holding integrated circuit operates at a frequency of 1 THz [150], corresponding to time intervals of 1 ps, but more common scientific instruments operate in the MHz to GHz regime, making it impossible to use electronics to achieve the required time resolution. A way to reach temporal resolution in the femtosecond regime is to make use of ultrashort laser pulses, as short as a few tens of femtoseconds, in a so-called pump-probe experiment. A first laser pulse, the "pump", is used to perturb the system, e.g. by exciting electrons or phonons, and thereby inducing a change in its optical and electronic properties. These changes are monitored by a second laser pulse, the "probe", for example by measuring the reflection or the transmission of the sample at the probe wavelength. The probe pulse needs to be significantly weaker than the pump to avoid further changes to the measured quantities. Varying the time delay Δt between pump and probe pulses allows to resolve the dynamics in time. The temporal overlap between the maxima in time of pump and probe pulses defines $\Delta t = 0$ and is called time zero (t_0). Typically, each acquired delay point averages over thousands of pump-probe pairs. During the time interval between two subsequent pairs of pump-probe pulses, i.e. the inverse repetition rate of the laser, the system is required to relax to its equilibrium conditions, such that every new pulse pair can again induce and probe the dynamics in a repeatable manner. Thus, the signal at negative delays, i.e. when the probe pulse reaches the sample *before* the pump pulse, coincides with the static signal acquired in absence of the pump. If the system does not relax, i.e. if at least one process lasts longer than the inverse repetition rate of the laser, they do not coincide and the measurements are affected by a quasi-stationary background. The time resolution of the experiment is given by the duration of the pulses and, usually, the measured response is given by the convolution of the system response with the cross correlation of pump and probe pulses, defined as

$$A_{XC}(\tau) = \int_{-\infty}^{+\infty} I_{pump}(t) I_{probe}(t - \tau) \, .$$

3.1.1 Time-resolved excited state transmission spectroscopy

Time-resolved excited state transmission (tr-EST) spectroscopy is an example of a pump-probe technique. Its mechanism is schematized in the inset of figure 3.1. Here, the pump excites the sample with photon energies exceeding the optical bandgap energy and creates an electronic
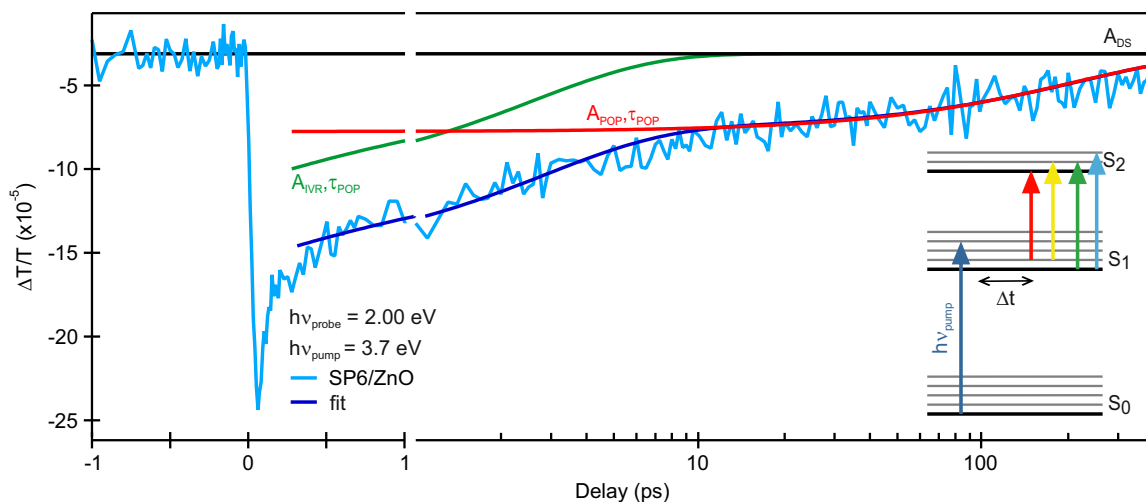
Figure 3.1: Exemplary tr-EST trace for a 25 nm thick film of SP6 on ZnO measured with 3.7 eV pump and 2.0 eV probe photon energy. A sudden drop in the transmission is observed for $\Delta t = 0$ as well as a subsequent double exponential recovery that reflects the dynamics of relaxation of the excited electronic population. The offset is due to dynamics exceeding the inverse repetition rate of 5 µs. Inset: schematics of the technique.

population in the previously unoccupied states. The probe photon energy is chosen to be smaller than the optical bandgap but resonant to transitions from the transiently excited states to unoccupied states even higher in energy. In this work, a WLC (see section 3.2.1) ranging from 480 to 700 nm, corresponding to 1.8 to 2.6 eV, is used to probe the transmission through the sample as a function of pump-probe delay. Figure 3.1 depicts an exemplary tr-EST trace measured for 25 nm of SP6 on ZnO with a pump photon energy of 3.7 eV and 2.0 eV probe. The plot shows the measured relative change of transmission $\Delta T/T$ as a function of the delay Δt. A sudden drop of the transmission is observed at the time zero t_0. This change is due to the onset of absorption at the probe photon energy, due to the electronic population created in the excited states by the pump pulse. At positive delays ($\Delta t > 0$) this population can relax via the multiple channels described in section 1.1.1 and section 1.1.2, which influence the optical properties of the system measured by the probe pulse. In fact, as explained in chapter 2, the matrix elements of an optical transition depend not only on the transition dipole moment, i.e. how good two energy levels couple with the probe beam, but also on the population of the involved initial and final states. The measured temporal evolution depends strongly on the relative importance of the relaxation processes and how they affect these electronic populations. At negative delays

the probe reaches the sample before the pump and no intensity change is expected. However, the trace plotted in figure 3.1 shows a non-zero intensity for $\Delta t < 0$. As explained before, this is due to a process that survived the inverse repetition rate of $\Delta t = 5\,\mu s$. In other words, the system exhibits dynamics that have been triggered by one pump pulse and measured by one probe pulse reaching the sample at least one inverse repetition rate later.

3.2 The femtosecond laser system

Both tr-EST and tr-eSFG experiments require not only ultrashort laser pulses, but also the ability of tuning the central wavelength of pump and probe pulses as well as generating the WLC. Both can be achieved via non-linear optical processes for which pulses of high peak power are needed. Laser pulses with these characteristics are obtained in the used setup by regenerative amplification of the output pulses of a Ti:Sapphire mode-locked oscillator. The employed laser setup, a commercial tunable femtosecond laser system from the company Coherent, is depicted in figure 3.2. It is based on the fully automated, hands-free oscillator *Vitara T* and the regenerative amplifier *RegA*. In both cases the laser active-medium is a Sapphire crystal doped with Titanium atoms, whose absorption and emission range from 400 to 600 nm and 680 to 1100 nm, respectively, with an emission maximum at 790 nm. Both the *Vitara* and the *RegA* are pumped by continuous wave optically pumped semiconducting lasers (CW-OPSL) emitting at 532 nm, with 5 or 12 W power respectively (Verdi G5 and G15). The pump laser of the oscillator is integrated in the box.

The cavity of the *Vitara* is sealed to guarantee highest stability. Its working principle is similar to the one of the Coherent *Micra* previously installed in the laboratory and explained in detail in [151]. Modelocking is achieved in a passive way, by exploiting the electro-optical Kerr effect that occurs when the refractive index of the medium is dependent on the intensity (see appendix B), i.e.

$$n(r,t) = n_0 + n_2 I(r,t) \,, \tag{3.1}$$

where n_0 is the linear refraction index, $n_2 \propto \chi^{(3)}$ is the first non-linear perturbation of the refractive index in centrosymmetric materials and $I(r,t)$ is the space and time dependent intensity of the laser pulse. The *spatially* non-uniform intensity of the laser pulse leads to the formation of a refractive index gradient lens that focuses more strongly the most intense part
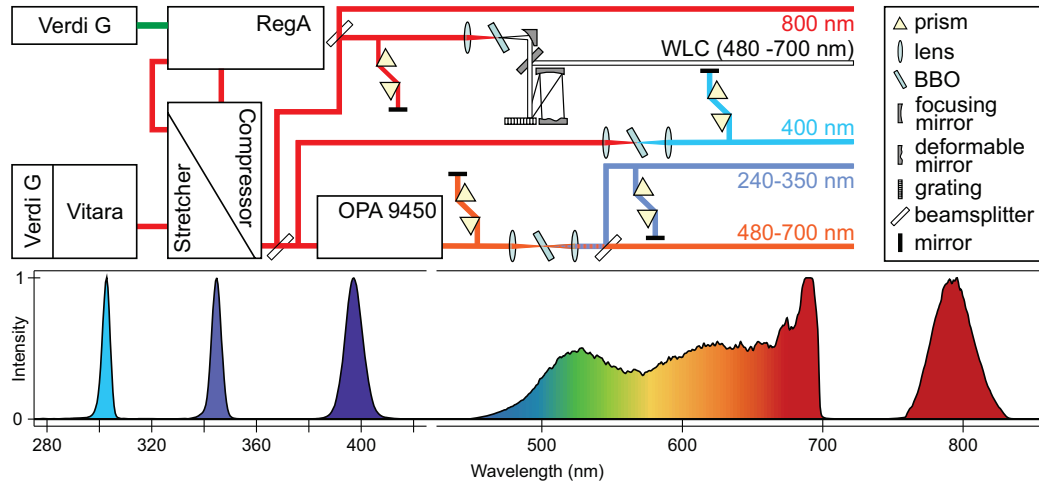
Figure 3.2: Schematic overview of the used commercial Coherent tunable femtosecond laser system: it consists of a Ti:Sa oscillator (*Vitara*), a regenerative amplifier (*RegA*) pumped by a CW-OPSL (*Verdi G*) and a collinear optical parametric amplifier (*OPA 9450*). The *RegA* output is split by a 50-50 beamsplitter (BS). One half is used to drive either the *OPA* or doubled to 400 nm, to generate the pump beam in the UV. 10 % of the remaining half generates the WLC. Bottom: spectra of the pulses used in this work.

of the beam in a self-sustained way. This allows to cut the less intense parts and the continuous wave emission with a slit in the cavity. The activation of the Kerr-lens is obtained by intensity fluctuations in the cavity, induced by a movable mirror that modifies the resonator length. Furthermore, the *temporal* intensity variations lead to another non-linear optical process, called self phase modulation (SPM), that widens the frequency spectrum of the pulse and leads to the emission bandwidth needed to support ultrashort laser pulses. Indeed, in the case of Gaussian pulses, the bandwidth and temporal duration are related as $\Delta t \Delta \nu \geq \frac{1}{\pi} 2 \ln 2$. To compensate for the positive group velocity dispersion (GVD) induced by self-phase modulation and pulse propagation, the pulses are compressed down to 20 fs by a prism compressor in the cavity [152]. A deeper analysis of GVD is given in appendix B.

The *Vitara T* emits 6.25 nJ pulses centered at 800 nm (1.55 eV) with a bandwidth of 60 nm and a repetition rate of 80 MHz, defined by the length of the resonator. A regenerative amplifier *RegA* is used to amplify the *Vitara* output, whose pulse energy is not sufficient to efficiently drive the non-linear optical processes required for wavelength conversion or WLC generation. *Chirped pulse amplification* is used in order to avoid damages to the *RegA* active medium by the high

peak energies obtained during the amplification. Before entering the cavity, the *Vitara* output is thus stretched, i.e. the frequency components are separated in time while going through a specific arrangement of dispersive gratings [153]. The stretched pulses are then coupled into the amplifier cavity with a tunable repetition rate by a high-speed acousto-optic modulator made of Tellerium Dioxide (TeO$_2$), the cavity dumper. They are then amplified for approximately 20 round trips (depending on the repetition rate), after which the population inversion of the Ti:Sa crystal is completely depleted and the cavity dumper ejects the beam from the cavity. Another acousto-optical modulator, the Q-switch, degrades the quality of the cavity during around 3 µs, to restore the population inversion before the next pulse is coupled in. The output of the *RegA* is compressed down to 40 fs by a second set of dispersive gratings, this time set to introduce negative group velocity dispersion [154].

For the experiments presented here the repetition rate of the *RegA* was tuned either to 40 or 200 kHz and the pulse energy reaches values of 10 µJ.

As depicted in figure 3.2 the *RegA* output is split in two by a 50-50 beamsplitter (BS) after compression. One half is used to generate the pump pulses either via second-harmonic generation (SHG) to generate 400 nm photons or by driving an optical parametric amplifier (Coherent *OPA 9450*). The theory behind both processes was developed in section 2.3 and the working principle of an OPA has been extensively explained in [155] and [156]. The output is compressed making use of prism compressors. Of the remaining 50 % of the *RegA* output, 10 % is used to generate the white-light continuum (WLC), as elucidated in section 3.2.1. Temporally matching the optical paths of all the different beams at the sample requires the remaining 800 nm pulses to travel for additional 6 m. Therefore, a dedicated prism compressor has been installed to compensate for the acquired temporal dispersion before generating the WLC.

3.2.1 Broadband white-light continuum for optical probing and electronic sum-frequency generation.

Optical experiments, whether linear or non-linear, probe inter-state transitions as resonances. The photon energy at which these resonances occur is, in most cases, unknown before the experiments are performed and photoinduced relaxation mechanisms may involve multiple resonances in a broad energy range [157]. Furthermore, in many cases, the effect of photoexcitation is to broaden and shift the resonances, e.g. by inducing bandgap renormalization [158, 159]. It

is therefore of great advantage to simultaneously probe as many resonances as possible, using a broadband continuum combined with energy-dispersive detection, instead of a tunable narrowband source. Additionally, broadband pulses can support shorter temporal durations than the narrowband counterpart and thus improve experimental time resolution. The latter is only possible if the temporal shape of the pulse as a function of frequency is well-known and controllable. For this purpose the setup developed by Wegkamp et al. and described in [160] and [161] is used.

The mechanism leading to WLC generation by focusing intense laser pulses in transparent media [162] is a delicate interplay of higher order non-linear optical effects such as self focusing (SF), self phase modulation (SPM), plasma and shock wave formation [163]. The simplest model considers only the interplay of SF and SPM. Here SF creates a positive lens in the material that leads to beam collapse and filament formation, such that the threshold intensities for SPM can be obtained. Due to the rapidly changing intensity in time and the consequent changing refractive index (cf. eq. (3.1)), the leading edge of the pulse generates red-shifted spectral weight and the trailing edge blue-shifted one, such that a broad continuum is generated. Given a fixed pulse energy, the total frequency shift is inversely proportional to the pulse duration, increasing for shorter incident pulses [128]. Another consequence of SPM is that the instantaneous frequency is time dependent, in other words the pulse is chirped and reaches time durations in the picosecond time scale for a 3 mm thick crystal. This GVD increases even further due to propagation of such a broadband pulse through dispersive media, as for example the windows of the cryostat or air itself. An algebraic description of SPM and its effects to the pulse duration is given in appendix B.

In the current setup a white-light continuum is generated by focusing with a 50 mm focal length lens 5 % of the *RegA* output intensity, corresponding to 20 pJ pulse energy, in a 3 mm thick sapphire plate with its optical axis perpendicular to the surface, i.e. in the so called C- or Z-cut. Sapphire has been chosen instead of a YAG crystal to extend the generated photon energy range further in the UV, even though it requires an higher input power [164][1]. The beam is then recollimated using an off-axis parabolic mirror with 2" diameter and a focal length of

---

[1]The use of CaF_2 has been considered. However its much lower damage threshold leads to WLC intensity fluctuations, even if the crystal is constantly moved, that can be detrimental for experiments where long integration times are required, such as tr-eSFG.

50.8 mm.

The setup is schematized in figure 3.3. After recollimation, the WLC beam enters a pulse shaper consisting of a dispersive grating (G - Richardson Gratings, 600 g/mm, blazed at 500 nm), a focusing mirror (FM - focal length 250 mm) and a deformable mirror (DM) in a configuration such that both the dispersive element and the DM are at a focal distance f from the FM. The DM [2] consists of an aluminum coated polymeric membrane which can be uni-directionally displaced by electrostatic forces generated by 30 metallic electrodes placed behind it. Situated in the Fourier plane of the compressor, it acts as a folding mirror and is vertically tilted such that
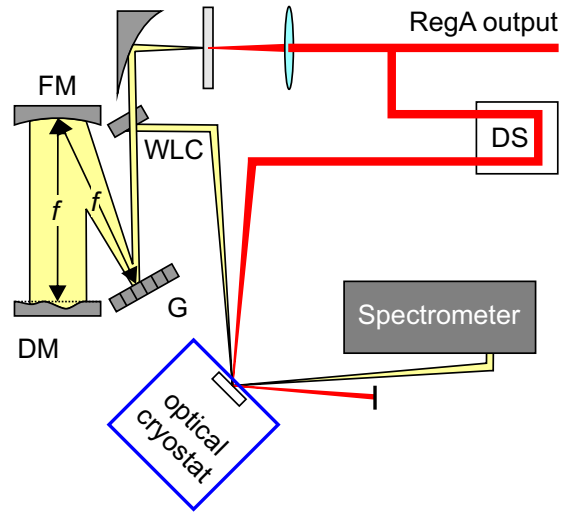

Figure 3.3: Schematic representation of the white-light continuum setup with the generation and the compression stages as described in the text.

the light travels back and is picked by a lower planar mirror after which it is guided and focused to the sample. It was shown by Martinez that this particular configuration of a pulse shaper, also known as 4f-compressor, does not introduce any phase shift due to the traveled distance [165]. However, this holds only if the grating is working in Luttinger configuration, since otherwise third- and higher-order dispersion is introduced. Furthermore, a slight detuning of the DM position from the Fourier plane can be used to best adapt to the shape of the GVD to the shape of the deformable membrane, such that optimum compression is achieved, as explained below. 45 % of the RegA output travels over a motorized delay stage (DS) before being focused to the sample and use as pump pulse for the WLC characterization described below. This DS allows to control the optical path, and thus the temporal delay, with respect to the WLC.

To characterize the temporal shape of the continuum we use a solid-state ultrafast optical switching, i.e. the pump-induced changes of optical properties of a material, as gating element, following the approach of [160] and [166]. They corresponds to the gate function $G(t - t')$ in

---

[2]The deformable mirror is manufactured by ADAPTICA Srl, Padova, Italy.

the spectrogram expression

$$S(\omega, t) = \left| \int_{-\infty}^{\infty} E(t')G(t-t')e^{-i\omega t'}dt' \right| \text{, where } E(t') \text{ is the electric field of the WLC.}$$

Compared to the usual non-linear gating techniques, such as frequency-resolved optical gating (FROG) [167], this approach does of not require phase matching conditions over the whole spectral range and can be realized in reflection or transmission in the optical cryostat with the same setup of a time-resolved pump-probe experiment. Consequently, it provides pulse characterization with the very same experimental conditions and allows the compensation of GVD generated by the WLC generation process and by all the optical media in the beam path (e.g. lenses and cryostat windows). For best pulse characterization it is required that the pump-induced transient variation of the optical properties of the gating medium occurs over the whole wavelength range of the continuum and that it is instantaneously triggered (within the pump pulse duration). Cilento et al. and Wegkamp et al. have shown that these conditions are hold for both VO_2 and LSMO [160, 166]. Here the pump induces an instantaneous step-like variation of the optical properties that lasts for times much longer than the duration of the WLC. Tuning the pump-WLC delay as in a normal transient transmission/reflection experiment corresponds to changing the delay $(t - t')$ of the gate function. In this work both VO_2 thin films and LSMO bulk crystals have been used routinely, depending on the experimental configuration. The first provides a smaller contrast, i.e. a smaller amplitude change, but allows for measurement in transmission if thin films are used, while the latter can be only used in reflection.

The top panel of figure 3.4 (a) shows the time- and wavelength-resolved transient transmission change $\Delta T/T$ of a 20 nm film of VO_2 measured with the uncompressed WLC probe, which was sent through the switched-off $4f$-compressor. The group delay (GD) is extracted as a polynomial fit of the time-zero response vs. wavelength, i.e. the wavelength dependent group delay $\tau_G(\lambda)$, and is plotted as a white line. Several procedures can be applied to extract the t_0 response: a) the data is smoothed and the half maximum of the rise is extracted, b) the derivative is calculated to find the maximum and c) the rising edge is fitted with a normalized error function $I(t) = 1/2\big[(t - \tau_G(\lambda))/\tau_{rise} + 1\big]$. Method c) gives the most accurate results but requires high signal-to-noise ratios. For routine compression method a) is used since it gives the best trade-off between accuracy and speed. The extracted GD shape differs from the one expected for a WLC propagating through normally dispersive media. Indeed it exhibits a
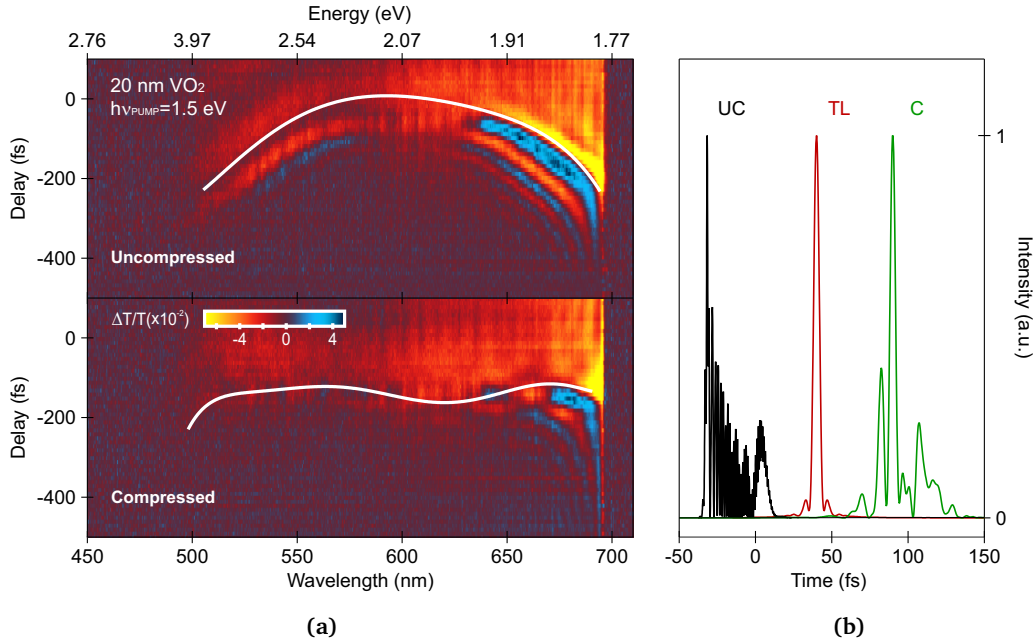
Figure 3.4: (a) Time and wavelength resolved transmission change of VO_2 measured with the uncompressed (top) and with the compressed (bottom) WLC. (b) Corresponding reconstructed intensity envelopes compared to the transform-limited pulse. The curves are shifted along the time axes for clarity.

parabolic shape with maximum at 580 nm, instead of peaking at the red extreme. This can have multiple reasons, as explained in [168]. The interplay of grating angle and the distances of grating or DM to focusing mirror play a subtle role in the ratio between the introduced second and third order GVD and lead to an overall phase shift even for switched-off DM. Furthermore, the mirror membrane is fixed only at the two extremities, such that a residual deformation can be expected for its center. The reconstructed intensity envelope shown in black in figure 3.4 (b) exhibits the oscillations typical of third and higher order terms in the GVD (see simulated spectra in appendix B).

The intensity envelopes $I(t)$ are reconstructed with the knowledge of the spectral intensity $I(\omega)$ and the spectral phase $\Phi(\omega)$, calculated as the integral of the extracted $\tau_G(\omega)$

$$\Phi(\omega) = \int_0^\omega \tau_G(\omega')d\omega' \tag{3.2}$$

which leads, by Fourier transformation, to

$$I(t) \propto \left| \int_{-\infty}^{\infty} \sqrt{I(\omega)} e^{i\Phi(\omega)} e^{-i\omega t} d\omega \right|^2 \tag{3.3}$$

Once the spectral phase is known it is possible to calculate the deformation $\Delta z(\omega)$ of the mirror membrane necessary to compensate for it [169]

$$\Delta z(\omega) = \Phi(\omega) \frac{c}{2\omega} \text{ , where } c \text{ is the speed of light.} \tag{3.4}$$

The longitudinal position of the different frequencies on the mirror membrane is measured by acquiring a calibration spectrum with a slit mask placed in front of the mirror, to allow for mapping of $\Delta z(\omega)$ in $\Delta z(x)$. An algorithm implemented in IGOR Pro containing the manufacturer calibration allows to transform the desired deformation into the voltage applied to the corresponding actuators. Usually few iterations of spectrogram acquisition, GD extraction, phase and deformation calculation are needed to achieve best results. The residual non-linear phase (a linear phase is equivalent to adding a constant $\tau_G(\omega)$ that corresponds to moving the arbitrary t_0) extracted in each cycle is added to the previous ones to achieve pulses close to the transform limited.

The bottom panel of figure 3.4 (a) shows the group delay obtained after two iterations of the algorithm. The corresponding intensity envelope is plotted in green in panel (b) together with the transform limited, in red. It can be clearly seen, that the compression works best for the central wavelengths, while it almost does not act on the extremities due to the fixed membrane ends. Figure 3.4 (b) compares the reconstructed temporal intensity envelops of the uncompressed (UC), compressed (C) and transform-limited (TL) pulses. Although the main peak of the compressed pulse coincides in FWHM with the transform-limited pulse, it still shows strong oscillations due to higher-order dispersion which do not allow to define a pulse duration. Finally, the replica shown in the 2D plots at negative delays arise from cutting the red side of the spectrum at the mirror edge and also influence the temporal envelope, as demonstrated by the wings visible in the transform-limited $I(t)$.

For the experiments presented in this work it is finally relevant to discuss the effects of the compressor on the spatial shape of the WLC. Figure 3.5 (a) shows the fits of the spot profiles measured with a CCD camera with 2 by 2 μm size pixels for seven different wavelengths, selected by inserting the calibration mask in front of the DM and opening one slit at a time.
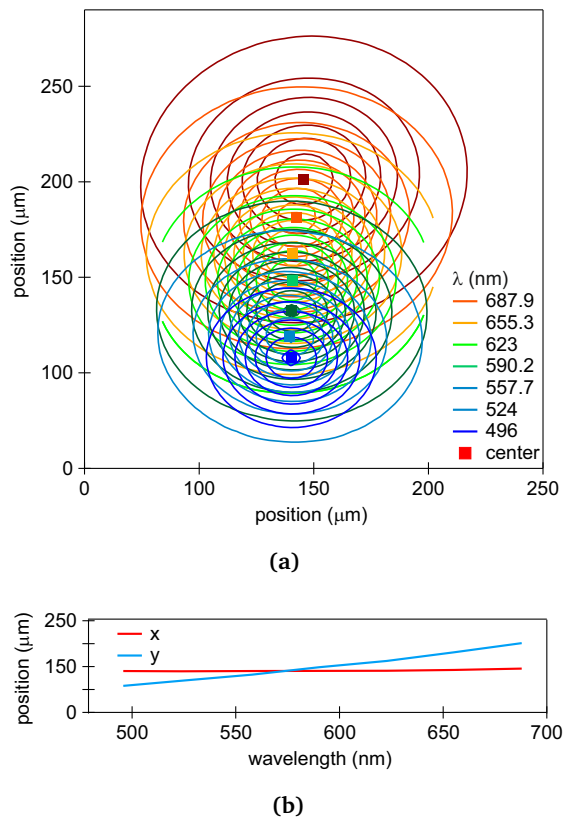
(a)

(b)

Figure 3.5: (a) Fits of the spot profile for 7 different wavelengths in the WLC corresponding to the slits of the calibration mask and their center position (b) Horizontal (x, red) and vertical (y, blue) profile center position as function of wavelength.

While the positions along the horizontal (x) axis almost coincide, the profiles show a strong dispersion (on the order of 100 μm) along the vertical (y) axis. In reference [170], Martinez shows the effects of a finite beam size on the transmitted amplitude across a grating compressor for the plane of diffraction (defined as x,z plane with z being the propagation direction). He demonstrates that a Luttinger configuration is required for avoiding astigmatic aberrations. Furthermore, he stresses the importance of recollimation of the beam to avoid temporal distortion of the pulse after it leaves the compressor. No effects are considered along the y-z plane. However, in order to exit the compressor the beam needs to be tilted down, which can lead to aberrations and coma from the focusing mirror, even for optimally aligned optics. Kane and Squier state in [171] "most stretchers require that the beam be tilted out of the plane of diffraction, which

puts an *uncompensatable spatial chirp* on the beam". Much effort was put at the beginning of this work to minimize this spatial chirp, that results especially detrimental for the non-linear optical experiments, where the intensity scales quadratic with the radius of the spot. Assuming that the spot profile of the *RegA* output does not affect the shape of the filaments in the sapphire [172, chap. 14], we tried to identify the relevant parameters in the compressor alignment. One first critical point is the alignment of the off-axis parabolic mirror, whose mount does not have a fine tuning for the vertical position. A second point is given by the tilting of the grating and its azimuthal rotation. The latter can be fine tuned by looking at the dispersed stripe in the far field. The position of the grating with respect to the focal plane of the mirror controls the

recollimation of the beam and thus the introduction of spatial chirp on the horizontal direction. Finally, we tried to minimize the vertical chirp by reducing the overall size of the beam into the compressor with an iris at the entrance, in a trade-off between imaging properties and transmitted intensity. A further step to reduce the vertical aberrations would be to increase the overall length of the 4-f compressor by reducing the groove density of the grating and accordingly increasing the focal length of the focusing mirror.

3.3   Sample preparation

This work investigates the exciton and charge relaxation dynamics in ZnO and in the model hybrid inorganic organic system (HIOS) composed by the spirobifluorene derivative 2,7-bis(biphenyl-4-yl)-2',7'-ditertbutyl-9,9'-spirobifluorene (SP6) and ZnO. This section describes the preparation of the samples used.

ZnO   Chapter 5 presents the results obtained on a hydrothermally grown ZnO single crystal purchased from MaTeck GmbH and cut along the non-polar $(10\overline{1}0)$ surface, which has been used without further preparation. Its defect energetics and dynamics have been compared with those of a 125 nm ZnO film grown by molecular beam epitaxy (MBE) on the $(10\overline{1}0)$ surface of an unprepared single crystal [3]. The growth is performed with a substrate temperature of 330 K and the Zn is evaporated by an effusion cell with a deposition rate of 5.5 nm min^{-1}. The oxygen is provided as plasma in front of the sample substrate and the plasma brightness is such that it ensures oxygen rich growth atmosphere. The base pressure in the chamber is of 10×10^{-10} mbar and increases to 10×10^{-6} mbar during deposition. After deposition the samples are further annealed to 700 K.

SP6 on ZnO($10\overline{1}0$)   The exciton dynamics in the HIOS have been investigated on SP6 films deposited on ZnO $(10\overline{1}0)$ and, for comparison, on an inert glass substrate. The samples have been prepared by sublimation in UHV environment with base pressure below 1×10^{-10} mbar [173]. The previously described hydrothermally grown ZnO single crystal was used as semi-conducting substrate. It has been prepared by repeated cycles of Ar$^+$ sputtering at 0.75 keV for

---

[3]The thin films were grown by Mino Sparenberg in the group of Prof. F. Henneberger at the Humboldt Universität zu Berlin.

10 min and annealing at 850 K with heating and cooling rates of 20 K/min [107]. The glass substrate, instead, was a microscope cover slip which has been sonicated in ethanol and used without further preparation. The molecules are sublimated with a Knudsen-type effusion cell at a base temperature of 570 K and the substrates are kept at 300 K during deposition.

To ensure that SP6 does not fragment upon sublimation, proton nuclear magnetic resonance (NMR) was performed on a solution of SP6 molecules in deuterated benzene before and after evaporation respectively and compared with the predicted NMR spectrum. All spectra show identical peak positions, confirming that no chemical change occurs to the molecules when heated [173]. We deposit 20 nm thick films on ZnO and 25 nm on glass. The thickness is monitored during deposition by a quartz microbalance.
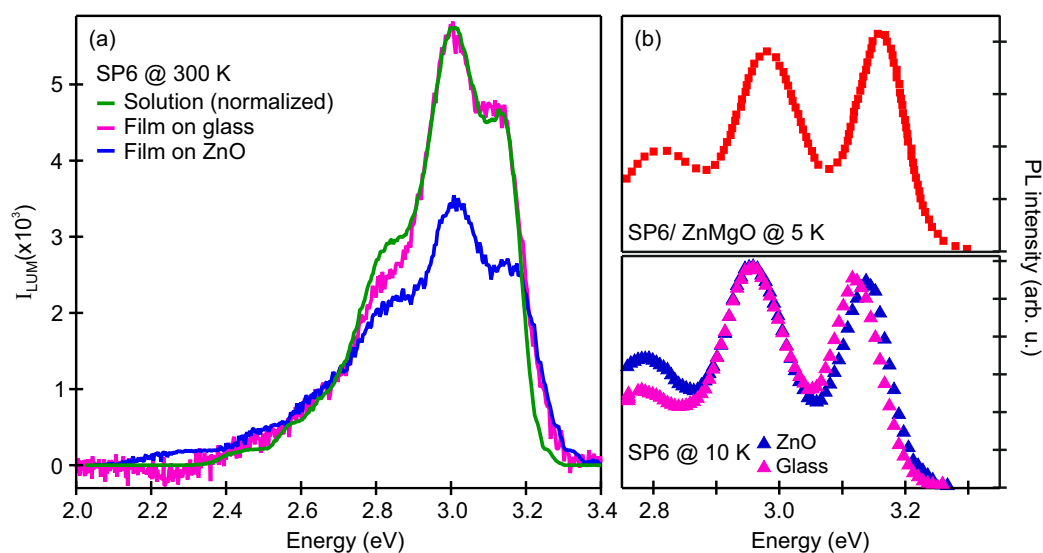

Figure 3.6: (a) Comparison of the luminescence spectra at 300 K of the SP6 film on glass (pink), ZnO (blue) and a diluted solution in toluene (green). (b) Comparison of the luminescence spectra at 10 K (*bottom*) with the data presented in reference [7] (*top*). All spectra are in good agreement, showing the same ground state progression and relative peak intensity.

The films have been characterized by photoluminescence (PL) spectroscopy after excitation at 3.7 eV. Panel (a) of figure 3.6 compares the emission spectrum of the films (in pink for the glass substrate and in blue for the ZnO) with the one of a very diluted solution in toluene [4] at 300 K, while panel (b) compares the emission at 10 K (bottom) with the data presented in

---

[4]The luminescence measurements in solution have been performed thanks to Pierre Schwach and Annette Trunschke at the department of inorganic chemistry of the Fritz Haber Institute

reference [7] and measured at 5 K for a SP6 film on ZnMgO. All the spectra coincide, both in energy position and in the relative intensity of the emission lines, suggesting that the molecules are not strongly influenced by the different environments.

3.4 Sample environment

For most of the experiments presented here the samples needed to be kept under controlled temperature and pressure conditions. To achieve this, a continuous flow optical cryostat (*Oxford Intruments* Optistat CF-V) is used. The cryostat is fixed to and x,y,z translational stage with micrometer screws via an in-house-made support such that all the translational degrees of freedom can be precisely controlled. The rotation of the cryostat is defined when mounting it into the holder.

The sample is kept in vacuum and the cryostat is pumped with a turbomolecular pumping station from Pfeiffer (HiCube ECO 80) that allows to achieve base pressures of 1×10^{-7} mbar. The cryogenic liquid is guided to the heat exchanger through a vacuum-insulated transfer tube. The returning gas is used to cool the radiation shield of the cryostat and the flexible part of the transfer tube, thus shielding the incoming liquid from thermal radiation. The sample can be cooled with either liquid nitrogen, to achieve temperatures around 90 K, or liquid helium, with which it is possible to reach 4.2 K if the transfer tube is continuously pumped. The temperature is measured and controlled with an external controller, the Mercury ITC, that also regulates the heating and the coolant flow. Both heater and temperature sensor are directly attached to the cold finger of the cryostat. Figure 3.7 shows the custom-designed sample holder, which allows measuring simultaneously two different samples. The principal sample is glued onto a circular mask (3) which allows to change the azimuthal orientation (see chapter 4). The plate is then held against the main part (1) by a screwed down retaining plate (4). A reference sample can be clamped between two retaining
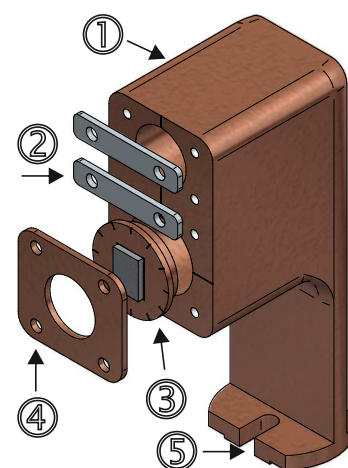

Figure 3.7: Custom-designed sample holder to allow simultaneous measurement of two samples and azimuthal rotation for non-linear optical experiments

slabs (2) and the main part. The whole holder is fixed to the cold finger by a retaining screw through a slit (5). The sample can be placed from 3 to 5 mm apart from the cryostat window, to allow for the maximum acceptance angle of the laser beams.

4. Proof of principle

Time-resolved electronic sum frequency generation

4.1 Motivation

The efficiency of hybrid inorganic organic systems (HIOS) is determined by multiple factors, as discussed in section 1.2. The most relevant ones are summarized in figure 4.1. Here (1) indicates exciton formation, (2) exciton radiative recombination, (3) exciton diffusion towards and away from the interface, (4) formation of a charge transfer exciton or an interface electronic state and (5) charge separation at the interface. Clearly some of these processes, as exciton formation and diffusion, are bulk properties of either the organic or inorganic semiconductor which can be addressed by linear optical techniques such as time-resolved excited state transmission (tr-EST). Others, like charge separation and energy transfer, or the formation of new hybrid electronic states as charge transfer excitons, are instead interface specific processes.
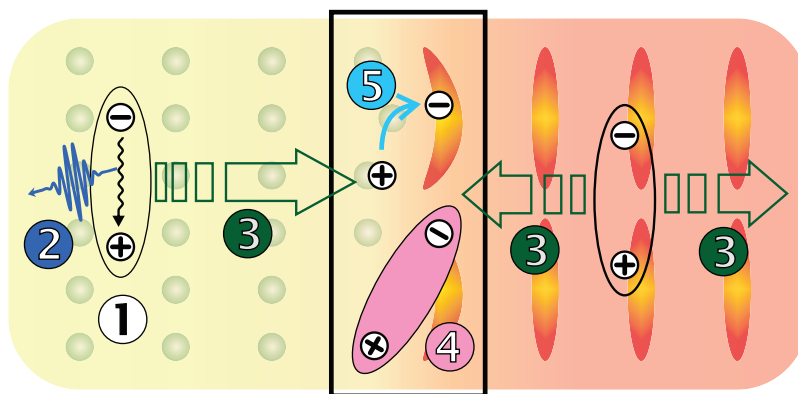

Figure 4.1: Processes at a hybrid organic inorganic interface. (1) Exciton formation, (2) Exciton recombination, (3) Exciton diffusion to or away from the interface, (4) Formation of charge transfer exciton and (5) Charge separation.

In time-resolved linear optical spectroscopies the spatial resolution along the propagation direction is determined by the penetration depth of the pump and the probe beams in the material. As depicted in figure 4.2 (a), systems as SP6 and ZnO with a band gap of 3.4 to 3.6 eV

are transparent to visible light that passes-through the whole bulk of the organic and inorganic semiconductors. The intensity of the ultraviolet (UV) pump pulse decays exponentially along the propagation axis, due to absorption, and the ratio of photons absorbed in the first 10 nm is approximately 20 times larger than that absorbed in the last nm before the interface, for an exemplary penetration depth of 25 nm. Therefore, the pump-induced signal originating from the interface may be buried under the bulk contribution, which itself may not be affected at all by the presence of the interface. Thus, to access interface-specific processes with linear optical spectroscopies requires tricks such as comparing the properties of the HIOS with those of the single constituents or reduce the thickness of the layer in order to limit the bulk contribution. Nevertheless, when it comes to the investigation of a realistic device, where the thickness of the layers is designed in order to optimize light absorption or emission, the disentanglement of the interfacial signal from the bulk signal can become as hard as looking for a needle in a haystack.

The situation would be substantially different if it was possible to exclusively investigate the interface with a specific technique. In this second case, shown in panel (b), it would be still necessary to reach the interface with a sufficiently intense pump beam to drive the excitation, but the probe signal would arise only from the few layers of material at the interface.
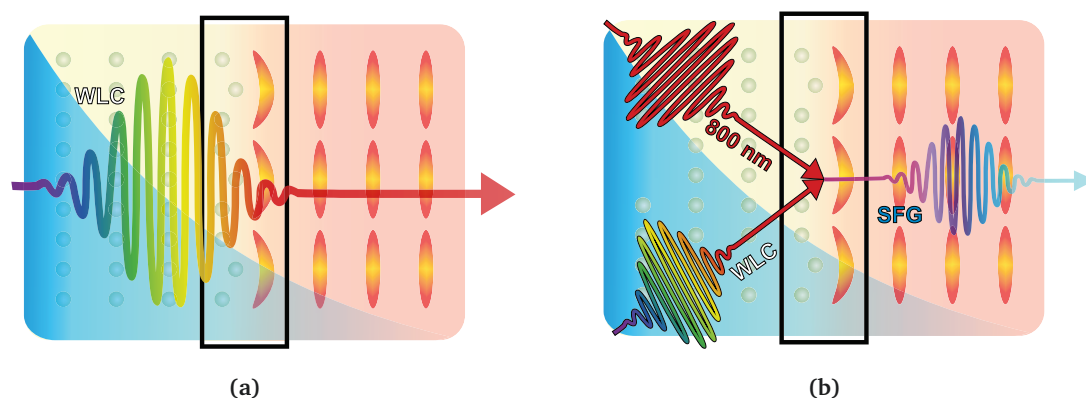

(a) **(b)**

Figure 4.2: (a) Linear optical probe: the probe beam is transmitted through the whole sample and the signal is mostly generated at the surface, i.e. far away from the interface due to the larger pump intensity. (b) Interface-specific technique: the probe signal is generated at the interface and is free from any bulk background.

The most common surface-specific spectroscopies are either based on electrons, such as photoelectron spectroscopy and electron scattering, or work at grazing incidence. The surface

specificity is in both cases a consequence of the short penetration (or escape) depth of the probe. Neither of them is, however, suited for addressing electronic states that arise at an interface buried by a thick layer of material. Section 2.3 presented non-linear optical processes as a powerful instrument to investigate the optical properties of a material with interface specificity, being forbidden, in the dipole approximation, for crystals with inversion symmetry and amorphous solids. Indeed, vibrational sum frequency generation is an established technique to look at the interface-specific vibrational modes of molecules, an thereby gain an insight on the molecular structure and orientation at the interface, which can substantially differ from the bulk structure. Electronic transitions have been mostly investigated with second harmonic generation by tuning the photon energy across an electronic resonance. Besides not being able to distinguish between intermediate and final state resonances as discussed in section 2.3, this technique requires to repeatedly tune the photon energy and the spectra consist of discrete points around the resonance. Furthermore, kinetic traces, and thus information about the dynamics, are often measured only at the resonance energy and are seldomly frequency resolved [174]. Electronic sum-frequency generation (eSFG) spectroscopy results, both static and time-resolved, have been published by only one group which looked at various dyes at the air water interface [148, 174] by using an uncompressed white-light continuum (WLC) generated in water as resonant beam and the fundamental of a Ti:Sa laser at 800 nm for upconversion and a second setup is currently under development in the Saykally group at the University of California Berkeley, again for the investigation of liquid interfaces.

There are several technical difficulties that need to be addressed in a time-resolved electronic sum-frequency generation (tr-eSFG) experiment:

1. In order to measure electronic transitions, typically in the visible (VIS) or near-infrared (IR), the resonant beam has to be in the visible range of the spectrum. Therefore, the sum frequency beam is in the UV spectral range and an efficient and almost flat detector response in this region is required.

2. Second order susceptibilities are 9 to 11 orders of magnitude smaller than linear susceptibilities, leading to signals of merely hundreds of photons per second. The detector quantum efficiency and noise floor needs to be optimized for low photon fluxes.

3. When aiming at time resolved measurements, the expected pump induced change is usually 10 to 20 % on top of an already small signal. In other words the change of the number

of photons impinging on the detector is on the order of few tens of photons. As a consequence tr-eSFG requires detectors with high dynamic range.

4. The group velocity dispersion of light usually increases with increasing frequency. Consequently a broadband visible pulse is much more strongly dispersed in time than a broadband infrared pulse. Since sum-frequency generation (SFG) requires the resonant and upconverting beams to be overlapped in time, acquiring an eSFG spectrum entails to vary the arrival time of the resonant pulse with respect to the upconverting one.

This chapter describes how these issues have been addressed in this work and demonstrates the first tr-eSFG experiment on a solid state sample. ZnO was used for the characterization of the setup for three reasons. First, it is expected to give high second order signal from the bulk since it does not possess inversion symmetry. Second, there is extensive linear absorption spectroscopy data to compare the energetic positions of the resonances observed. Third, as discussed in section 1.3, ZnO is an ideal candidate for a cheap, abundant and optically transparent inorganic semiconductor for HIOS and, therefore, the substrate of choice for the hybrid systems studied in the group. Since its bulk signal will contribute to the SFG spectra of any future complex system, it is necessary to characterize its response as a first step. At this point, it is relevant to stress that the intensity of the SFG signal is modulated by the azimuthal crystal symmetry. As shown in appendix A, the azimuthal dependence for the non-polar surface of ZnO is different than the one of the bulk crystal and this allows the separation of surface and bulk contributions.

4.2   Experimental Setup

The time-resolved electronic sum-frequency generation experiment is based on the compressed white-light continuum (WLC) setup described in section 3.2.1. The experiments have been performed at a repetition rate of 40 kHz to minimize contributions from long-lived in-gap states (IGS) as will be discussed in section 5.2. The left panel of figure 4.3 shows the experimental setup. The output of the RegA at 1.55 eV (= 800 nm) is split in two beams by a 50/50 beamsplitter (BS). 50 % is used to drive the OPA. Its output at 2.05 eV (=604 nm) is frequency-doubled to 4.1 eV (=302 nm) and serves to pump ZnO well above the band gap. It is sent across a motorized delay stage which controls the relative path length with respect to the WLC, i.e. the pump-probe delay. The remaining half of the RegA output is further divided by a 90/10 BS .
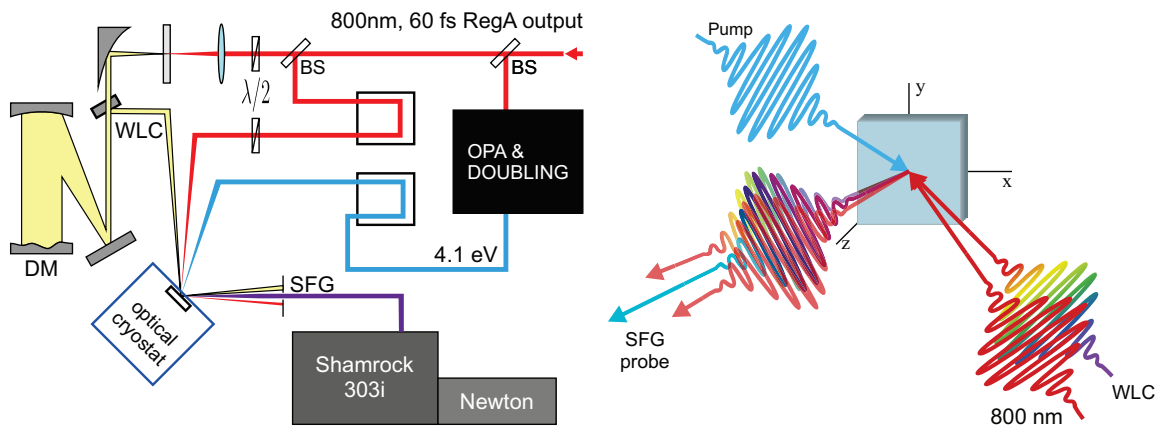
Figure 4.3: (*Left*)Experimental setup. The RegA output is divided in two parts by a 50/50 BS. One part drives the optical parametric amplifier (OPA) which output is frequency-doubled to 4.1 eV and used as pump beam. It goes across a motorized delay stage to control the pump probe delay. The remaining part is further divided by a 90/10 BS: 10 % is rotated to s-polarization with a $\lambda/2$ plate and generates the WLC, which is compressed before reaching the sample. The rest is sent across a delay stage to control the delay with the WLC and is used for upconversion, with either s- or p-polarization. (*Right*) Scheme of the pulse trajectories, with the sample surface on the $x-y$ plane. The fundamental beams propagate along the $x-z$ plane at a separation angle of $1°$. The WLC impinges at 45° on the sample. The 4.1 eV pump propagates along the $y-z$ plane at a 45° angle with the sample surface. Due to momentum conservation the eSFG field is emitted between the reflected fundamental beams.

The 90 % transmitted beam is used as upconverting beam and goes across another delay stage to control the relative delay with the WLC. The procedure for time integration of the SFG signal in order to take into account the group velocity dispersion (GVD) of the WLC is described in detail in section 4.2.3. The remaining 10 % is rotated to s-polarization with a $\lambda/2$ wave plate and generates the WLC. The experiments have been performed with both s- and p- polarized upconverting beam by rotating the polarization with another $\lambda/2$ plate. In the following the WLC, i.e. the resonant beam, and the 800 nm upconverting beam are called the *fundamental beams*.

The right panel in figure 4.3 schematizes the beam geometry at the sample. The fundamental beams propagate along the $x-z$ plane, while the sample surface defines the $x-y$ plane. The white-light is focused onto the sample at 45° with a spherical mirror of 250 mm focal length. The upconverting beam forms an angle of 1° with the WLC and is focused with a 300 mm focal
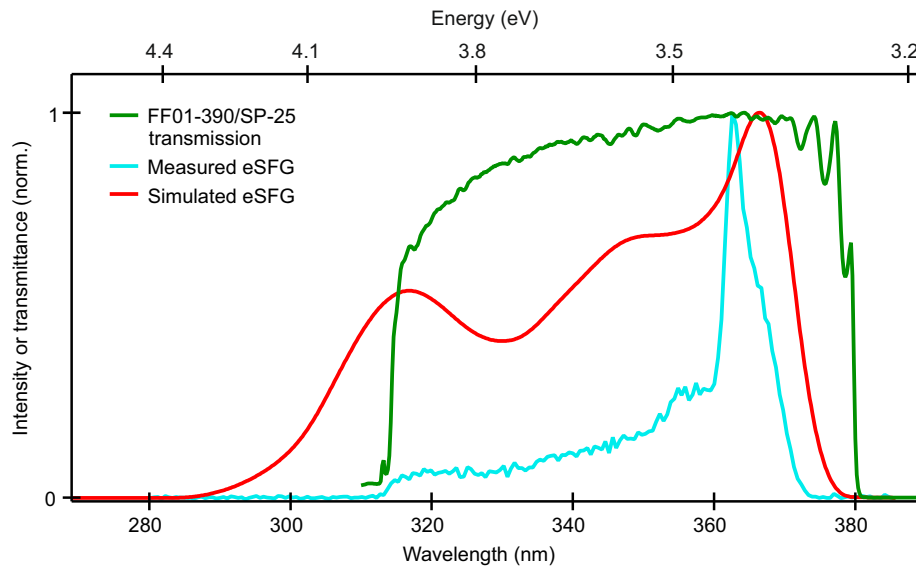
Figure 4.4: Measured transmission curve of the Semrock-FF01-390/SP-25 filter [175] (green) compared with the calculated (red) and measured (light blue) eSFG spectra. All traces are normalized at maximum for clarity.

length lens. The pump, instead, propagates along the $y - z$ plane and impinges on the sample after being focused with a 300 nm focal length lens at an angle of 45° from above. This way its reflection goes towards the laser table, where it is blocked by a beam dump, and the scatter of the pump light in the detector is minimized. The eSFG is measured in reflection and the beam is emitted between the reflected fundamental beams due to momentum conservation. All three beams are recollimated with a 100 mm focal length lens and the fundamental beams are used as a guide to align the eSFG output into the detector. In order to avoid scattering of the fundamental beams into the detector, and in particular from the second harmonic of the 800 nm, they are blocked with a mechanical slit which allows the eSFG to pass through. A spectral filter, the short pass filter FF01-390/SP-25 from Semrock, is used to further block both the visible beams and the pump scatter light. Its measured transmission curve, obtained from the company's website [175], is shown by the green line in figure 4.4, together with the theoretical prediction of the eSFG spectrum (red), calculated by convolving the spectrum of the WLC with the spectrum of the upconverting 800 nm beam, and the measured spectrum (light blue). All curves are normalized to one for clarity. For a WLC spectrum ranging from 480 to 700 nm (1.8–2.6 eV) we expect an SFG spectrum ranging from 303 to 379 nm (3.3–4.2 eV). From the transmission curve of the filter it is already clear that it cuts some of the SFG spectrum as well, as can be seen at

the high-energy edge of the measured spectrum. Unfortunately, the high-energy cut off of the short pass filter is not due to the multilayer coating, but to the substrate and no alternative filter with comparably large transmission bandwidth could be found on the market. Since the SFG scales linearly with the intensity of the WLC and the 800 nm pulses, respectively and the second harmonic scales quadratic with the 800 nm beam intensity, the latter is one order of magnitude more intense and, despite blocking it geometrically, the scattered 400 nm light is sufficient to saturate the detector if no spectral filter is used. The discrepancies between the low-energy tail of the theoretical and the measured SFG spectrum are discussed in section 4.2.3.

Before being focused onto the detector entrance, the SFG beam is sent to a galvanometer mirror rotationally oscillating at a frequency of 500 Hz. An optical chopper situated in the pump beam is synchronized to the galvanometer mirror such that it is possible to measure the perturbed and unperturbed eSFG spectra simultaneously as two vertically separated stripes on the detector. The referencing to the unpumped eSFG is treated in detail in section 4.2.4.

4.2.1 Spectrometer

SFG detection requires to frequency resolve the emitted signal. In order to do so, the beam is aligned into the entry slit of a spectrometer, to which an imaging detector is attached. Even though the imaging chip is the most critical component of the detection setup, as discussed in section 4.2.2, the importance of the spectrometer should not be underestimated. One of the requirements at the moment of choosing the spectrometer was to find the right compromise between energy resolution and transmission through the spectrometer.

Figure 4.5 shows the design of the used spectrometer. The light is focused onto the entry slit, from which it is recollimated by a spherical mirror to a dispersive grating and from there refocused to the detector with another spherical mirror. The focal lengths of the two mirrors determine the magnification of the spectrometer, which in our case is specified to be 1, i.e. the focal lengths are equal ($f_1 = f_2 = 300$ mm). The spectral resolution of a spectrometer, defined as the ability of the system to separate two closely spaced spectral lines, is determined by the groove density of the grating (the more dispersive the grating the higher the angular separation of two spectral components), the length of the spectrometer (the longer the spectrometer the wider the spatial separation on the detector) and the width of the wider slit between entrance and exit one (the resolution decreases as the width increases). A longer focal length spectrom-
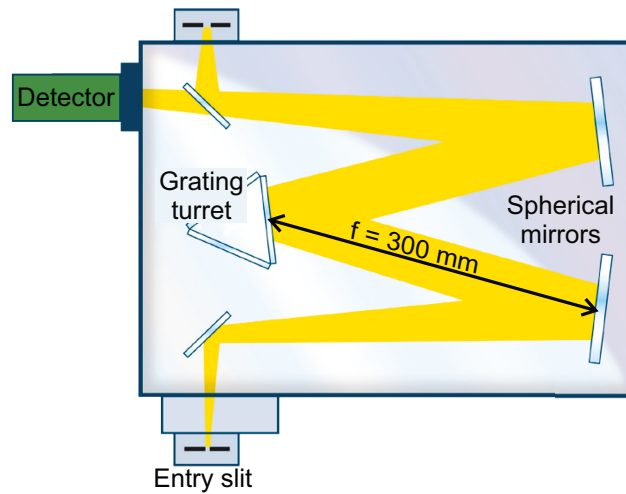
Figure 4.5: Design of the spectrograph: the SFG signal is focused onto the entry slit, reflected to a dispersive grating and from there reflected again to the detector. Image adapted from [176].

eter improves the spectral resolution at the expense of the intensity of light transmitted and the spectral bandwidth that actually illuminates the detector. Since the aim of the experiment is to image the whole SFG spectrum at once, the best compromise was found by using a 303 mm focal length spectrometer (Andor Shamrock 303i) with a 300 lines/mm grating blazed at 300 nm. The spectrograph is equipped with an electron multiplying charge coupled device (EMCCD) for simultaneous detection of the whole SFG spectrum with a pixel size of 16 µm. The EMCCD technology and the reason for this choice is discussed in the next section. For the minimal aperture width of the entrance slit and the width of the exit slit defined by the pixel size of the detector the manufacturer specifies an energy resolution of 3.4 to 6.3 meV (corresponding to about 0.4 nm), in the eSFG energy region.

However, the SFG signal has a natural angular divergence of the single colors due to momentum conservation at the generation. Furthermore, the signal is focused at the entrance slit with a lens, which introduces a chromatic aberration and, in practice only one color is optimally focused on the slit. This results in a finite width of the spot and the entrance slit needs to be kept open to 100 µm. Thereby, the entrance slit becomes the dominant one in the calculation of the spectral resolution, which becomes nominally 10 meV at an energy of 3.4 eV (in wavelength the resolution is of 1.08 nm).

In the case of sum frequency generation, the ability of distinguishing two adjacent spectral lines in a material is ultimately determined by the spectral bandwidth of the upconverting pulse.

Since the bandwidth also determines the time resolution in the inverse way (cf. sec. B.1), a compromise needs to be done between the temporal and the energy resolution. For the 800 nm pulse used, it results in an energy resolution of 66 meV for the measurements performed at a pulse duration of 40 fs and 40 meV for those performed at 60 fs duration.

Finally, figure 4.6 shows the efficiency of the grating in percent for both s- and p-polarized light as function of wavelength for the region of interest. The data has been digitized from [177]. Both spectra are almost flat in this energy region, while the grating is evidently more efficient for light polarized perpendicular to the grooves.
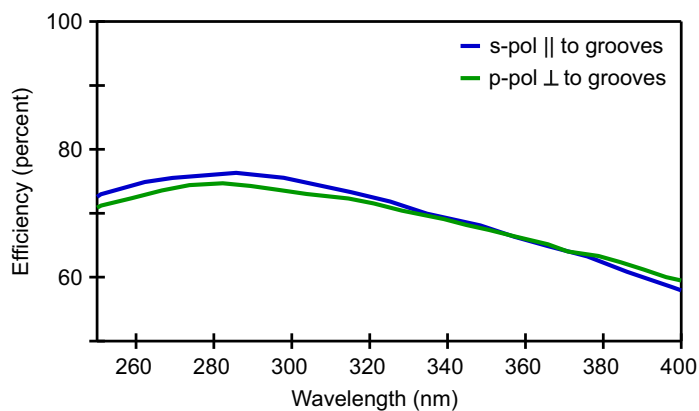

Figure 4.6: Efficiency of the used grating with 300 lines/mm and blazed at 300 nm in the eSFG spectral region. The data has been digitized from [177].

4.2.2 Detection

The most critical aspect in setting up the tr-eSFG experiment has been to find the optimal detector, which should fulfill the following requirements:

1. Second order susceptibilities are roughly 9 to 11 orders of magnitude smaller than the linear ones. Therefore, the expected signals are on the order of few tens to hundreds photons per second. Indeed, as a first test, we measured the SFG signal of GaAs at 375 nm with a photomultiplier voltage of 800 V, obtaining a countrate of 80×10^3 photons /s. This corresponds to a 30 % probability of having one SFG photon per pulse. Therefore, the detector needs to have almost single photon sensitivity.

2. Each kinetic trace consists roughly of 150 points and a single measurement is estimated to take at least 90 minutes. Furthermore, the expected signal changes are roughly 10 to 20 % of the static SFG spectrum and, given the low photon flux, many spectra need to be averaged for good statistics. Therefore, it is crucial to minimize the acquisition time for a single delay point.

3. During such a long scan the laser output intensity may fluctuate and drift. As a consequence it is important to have a reference for each single data point. We solve this issue by taking both perturbed and unperturbed spectra for every delay point, as described in section 4.2.4. This dictates the shape of the detector, which needs to accommodate two vertically separated spectra.

Every detector pixel is in principle a photodetector transforming a photon into current. The common technologies differ in how this current is extracted and can be divided into three main technologies: charge coupled device (CCD), complementary-metal-oxide-semiconductor (CMOS) and photodiode arrays. The latter are available only as single stripes and thus incompatible with requirement number 3. The others are described in the following.

Before doing so, however, it is important to consider what is relevant when trying to measure such low signals. There are two parameters which need to be taken into account: detector sensitivity and signal-to-noise ratio (SNR).

The sensitivity is itself determined by two fundamental parameters: the system noise floor and the quantum efficiency. The first dictates the intrinsic limit that needs to be overcome by the number of photons in order to be detectable, while the second is a measure of the ability of a detector to convert photons. These parameters vary largely among different detectors.

The overall noise of a measurement is given by the sum in quadrature of the *read*, the *darkcurrent* and the *shot* noise, i.e. overall noise $= \sqrt{(\text{ read })^2 + (\text{ darkcurrent })^2 + (\text{ shot })^2}$. The read noise is the noise introduced in the read-out process and increases for faster read-out rates, while dark current is mostly due to thermally excited electrons in the semiconducting detector. Together they result in the system noise floor. Shot noise instead is a measure of the intensity variation in the signal itself, i.e. the fluctuations of the signal due to the corpuscular nature of photons.

Charge coupled device (CCD) Camera

In a conventional CCD camera the active element (i.e. pixel) is typically a silicon diode photosensor. If this diode is irradiated with photons of sufficient energy it emits an electron. This electron is transferred through a series of parallel registers to a linear serial register (imagine a drain in a bathtub) and the resulting current is then amplified and read out. The CCD is a serial read out device (it essentially measures row by row) and, as such, it is not possible to

read out an entire sensor rapidly without significant sacrifices in SNR. The noise floor is directly given by the *read-out noise*: the unavoidable spurious current that occurs in the final read-out/amplification step by the charge to voltage conversion. This factor is a constant depending only on the read-out speed and the SNR is improved in CCD cameras by increasing the exposure time and decreasing the read out speed. Note that, if the exposure time is increased the dark current noise also increases and therefore the CCD needs to be cooled down to minimize the effect of thermal electrons, usually done by Peltier elements.

Complementary-metal-oxide-semiconductor (CMOS) Camera

Recently an increasing number of scientific applications have utilized CMOS cameras. The sensors in CMOS devices differ from those in CCDs because they are active: in general, both amplification and the conversion of current to voltage occurs on the chip itself. This requires CMOS sensors to have smaller features than those of CCD cameras which results in many benefits, such as the possible spatial resolution (for imaging applications), ruggedness, image acquisition time and cost. Unfortunately, current generation CMOS detectors have significantly lower sensitivity for weak signals. To overcome the low sensitivity problem in both classes of devices,

one would like to amplify the signal without amplifying noise floor. Currently this is done with two different approaches: iCCDs and EMCCDs.

Intensified charge coupled device (iCCD) Camera

In an intensified charge coupled device (iCCD) camera, incident photons first impinge on a photocathode where they cause the emission of electrons. These electrons are then accelerated under a high voltage towards a series of electron multiplying tubes (called micro-channel plates). The resulting cloud of emitted electrons can then be detected directly by an electron bombardment CCD or indirectly using a fluorescent phosphor screen and CCD. The degree of amplification is determined by the gain voltage applied to the micro-channel plates. iCCD cameras can sample smaller time windows than CCD or EMCCDs because the high voltage necessary to generate the signal can be rapidly switched on and off, thereby functioning as a gate or rapid shutter. This is often used in conjunction with kHz laser systems, which can directly trigger the camera such that one single image is acquired per laser pulse and the background photon noise

can be minimized. While iCCD cameras offer superior time resolution over CCDs and EMCCDs the increased time resolution comes at the expense of quantum efficiency. Also, the spectral response of an iCCD is primarily determined by the photocathode material. On a per photon basis CCDs and EMCCDs are approximately twice as efficient as iCCDs.

Electron multiplying charge coupled device (EMCCD) Camera

EMCCD cameras overcome the signal amplification problem by adding an additional amplification register to the conventional CCD: an amplification step before the signal is read off the sensor. This on-chip amplification means that signals can be straightforwardly made larger than the read out electrical noise. The idea behind the EMCCD is to keep the quantum efficiency of a conventional CCD, but at much higher read-out speeds by using a frame transfer structure, as shown in figure 4.7. It features two areas: an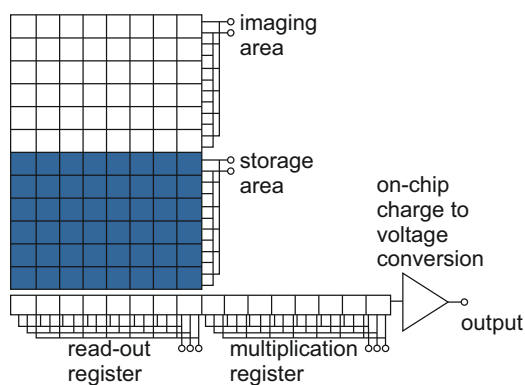 imaging area where the image is captured and a storage area where the image is stored while a new image is acquired. This stored image is then shifted at conventional read-out speeds to the read-out register and to a multiplication register, before, finally, the charge is converted to voltage. The amplification step in an EMCCD takes advantage of a process which is intrinsic in read-out registers and is commonly considered a source of noise: clock-induced, or spurious, charge. This occurs when an electron with sufficient energy creates additional electron-hole pairs by impact ionization. EMCCDs increase the probability of impact ionization by clocking the charge through the register with higher voltage. Furthermore, the length of the register is increased to increase the number of cells where amplification can occur. Thanks to the amplification step the EMCCD technology completely eliminates the limitation of read-out noise. The greatest source of noise in this kind of detector is multiplicative noise, related to the uncertainty inherent to the

Figure 4.7: The architecture of an electron multiplying charge coupled device detector. It consist of an imaging area where the image is captured, a storage area where the image is transferred in parallel, a read-out register and a multiplication register. This last register is used to amplify the signal before charge to voltage conversion by impact ionization.

amplification process and the statistical variation of the probability of amplification to occur. This type of noise is not affecting the noise floor of the instrument, but rather increases the shot noise, i.e. the fluctuations of the signal around the main value. These fluctuations have been estimated to be a factor $\sqrt{2} * (\text{shot noise})$. However, multiplicative noise is the most relevant only if dark current has been eliminated. Otherwise, thermally generated electrons can also be amplified in the gain register and appear in the image as noise spikes. Therefore, when the CCD is used in the electron multiplying mode, it is essential to cool it down to temperature values of about $-80\,°$C. Cooling, which is usually thermoelectric with Peltier elements, is fundamental even for low exposure times, since significant dark current can be generated even in the read-out register. Evidently, for relatively low signals, EMCCDs can be run at much smaller exposure times than conventional CCDs at the equivalent SNR. Assuming an adequate SNR, the smallest possible exposures in an EMCCD are given by the amount of time necessary to shift the charges off the chip.

This discussion makes clear that, working at 40 to 200 kHz where no gating is possible in an iCCD and requiring fast acquisition and read-out times to minimize the overall measurement time, the best-suited detector for time-resolved electronic sum-frequency generation is an EMCCD. Our setup uses the Newton 970 from Andor Technologies with the BV sensor, whose quantum efficiency in the spectral region of interest is plotted in figure 4.8. It has 1600×200 active pixels of $16 \times 16\,\mu\mathrm{m}^2$ size. The rectangular-shaped detector is advantageous over other imaging sensor for spectroscopy since it reduces the number of unexposed pixels contributing to the noise, while it still allows to accommodate the two vertically separated spectra.
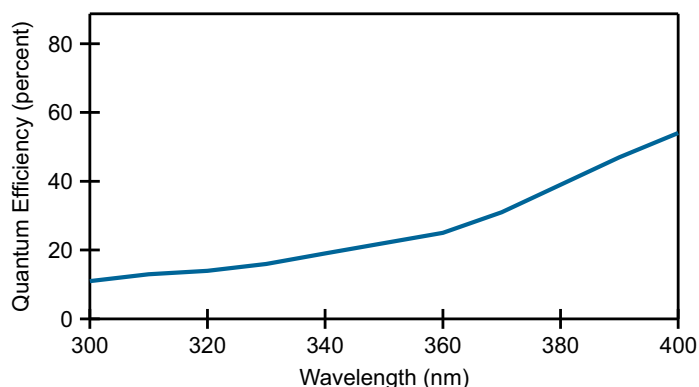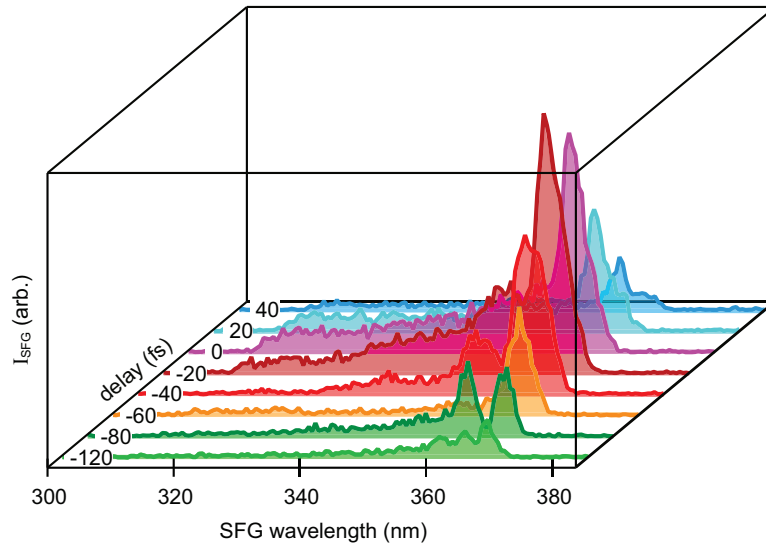

Figure 4.8: Quantum efficiency curve of the backthinned EMCCD sensor used in the tr-eSFG experiments for the wavelength region of the SFG signal.

Figure 4.9: eSFG spectra as a function of time delay between WLC and upconverting pulse. Clearly the spectral shape depends on the time delay and reflects the group velocity dispersion of the WLC.

4.2.3 Time integration of the static eSFG signal

Static eSFG is acquired with two fundamental pulses and, ideally, both are transform-limited Gaussian pulses. In that case, the upconverting pulse, being spectrally narrower, is necessarily temporally longer. Consequently, it is sufficient to center both pulses in time to obtain the whole SFG spectrum and the time resolution of the experiment is given by the temporal width of the longest pulse between the pump and the upconverting pulse. In reality the situation is quite different. As discussed in section 3.2.1, the temporal structure of the white-light continuum is strongly affected by third- and higher-order GVD. This results in the appearance of wings and oscillations in the temporal intensity, even if the full width half maximum (FWHM) of the main peak coincides with the one of the transform limited intensity profile. One of the consequences is that the spectral components appearing in the eSFG spectrum depend strongly on the relative delay between WLC and upconverting pulse, as shown in figure 4.9. The figure shows the eSFG spectra for different delays in the range from -120 to 40 fs. Analogous to the bottom panel of figure 3.4(a), at large negative delays, only the red edge of the spectrum is visible, while the blue edge is relatively more intense for positive delays. If one would restrict the measurement to only one delay point, some of the wavelength components would not be captured at all. This is clarified further in figure 4.10. The top panel plots the SFG intensity as a function of wavelength and delay Δt between the WLC and the upconverting pulse, measured with the very same mirror deformation as used for the bottom panel of figure 3.4(a). The replica at negative time delays, due to the cutting of the WLC spectrum at 700 nm on the deformable mirror, are
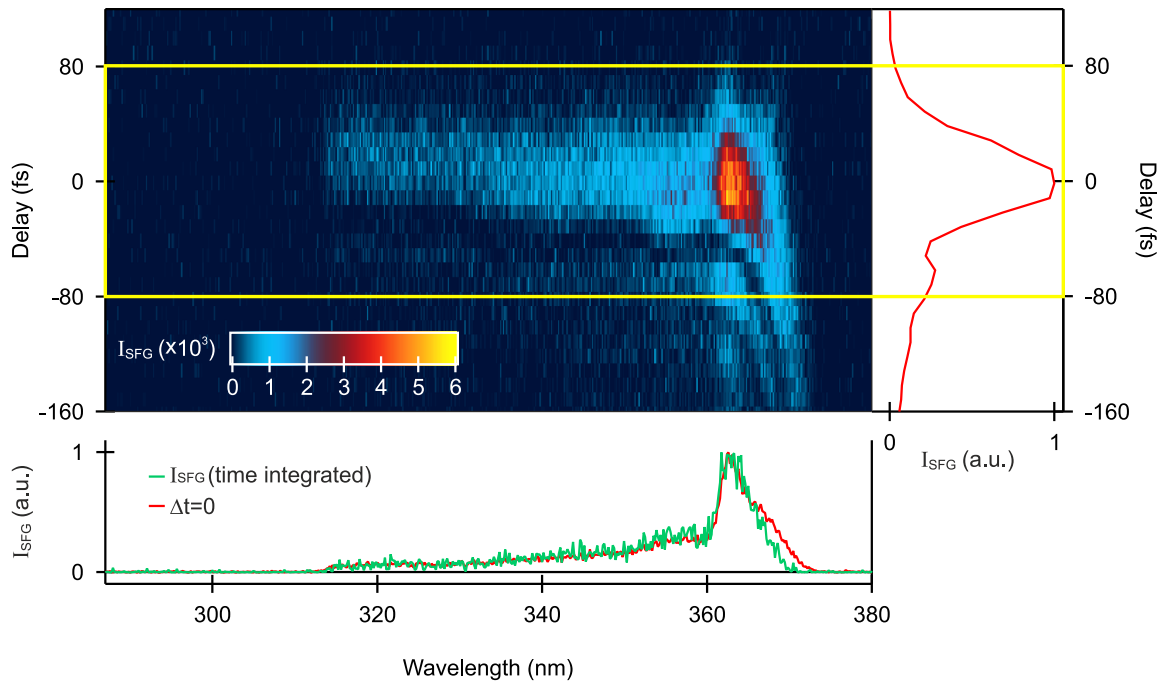
Figure 4.10: (*Top*) 2D plot of the eSFG intensity as a function of wavelength and time delay Δt. The replica due to the cutting of the spectrum at the 700 nm edge on the deformable mirror are clearly visible. The uncompressed red edge of the white light, due to the fixed end of the mirror membrane, affects the lower energy edge of the eSFG. (*Right*) Spectrally integrated eSFG intensity as function of delay. (*Bottom*) Comparison of the SFG spectrum at $\Delta t = 0$ and the spectrum integrated over the time delay in the yellow lines, differing only at the low energy edge.

again clearly visible. Moreover, the lower energy region of the spectrum is evidently affected by the uncompressed red edge of the WLC. This is presented in the bottom panel, where the spectrum taken for a delay $\Delta t = 0$ is compared with an eSFG spectrum integrated over the time span indicated by the yellow lines at $-80\,\text{fs} < \Delta t < 80\,\text{fs}$. Clearly, the spectra overlap perfectly over the whole spectral range except for the low-energy edge. Since this part of the spectrum corresponds to energies of about 3.3 eV, i.e. in the energy region expected for the ZnO excitons, it is not sufficient to fix the time delay at the time origin but it is necessary to integrate over a window of time. The right panel in figure 4.10 shows the total eSFG intensity vs. delay, obtained by spectrally integrating the two-dimensional of the top panel. It corresponds to the shape of the reconstructed time envelope of the WLC shown in figure 3.4b when convoluted with the upconverting pulse. The FWHM of the main peak is obtained by fitting with a Gaussian curve, which results in 61 fs, in good agreement with the duration of the 800 nm pulse for that
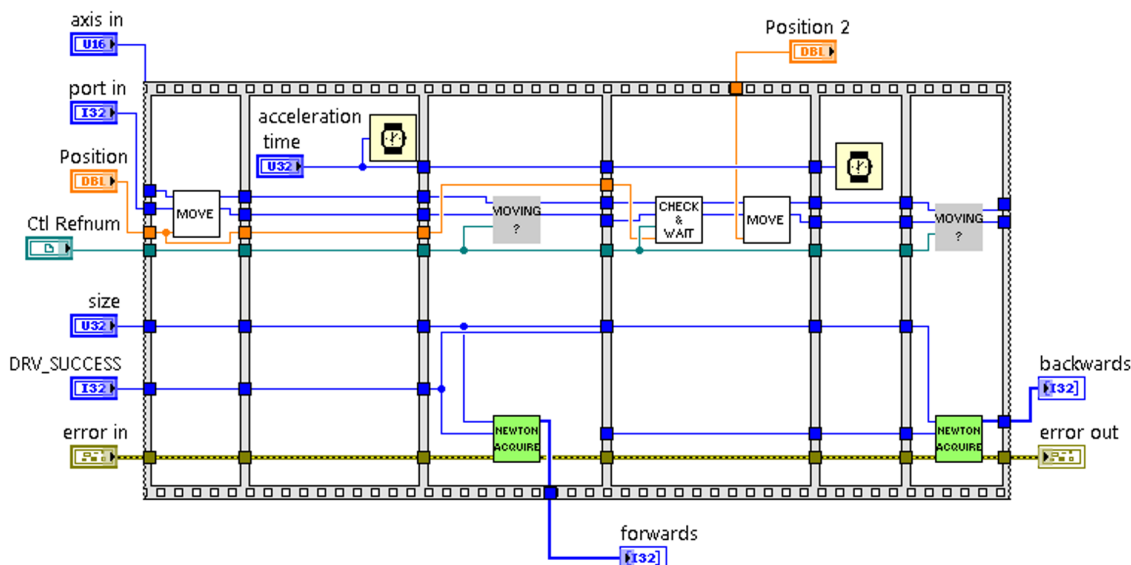
Figure 4.11: Labview implementation of the on-chip time integration of the eSFG signal. The "MOVE" subvi sets the stage to move at the velocity set previously ($0.0024\,\mathrm{mm\,s^{-1}}$), the program waits the "acceleration time" then the camera starts acquiring for $10\,\mathrm{s}$ during which the stage is moving at constant velocity and the SFG spectrum is integrated directly on the EMCCD chip. "Check & wait" controls that at finished acquisition the stage is indeed at the final position and then it is set to move again in backward direction, while another spectrum is acquired.

experiment.

One of the requirements when measuring tr-eSFG, is not to change the spectral shape by exposing the detector to different spectral regions for a different amount of time. This has to occur for each point of the UV pump - SFG probe delay and the overall exposition time has to be minimized in order to minimize the measurement time. This is accomplished by integrating the eSFG spectra for the time window indicated above *directly* on the EMCCD chip. Figure 4.11 shows how I have implemented the scanning procedure in labview. The exposition time on the EMCCD is set to $10\,\mathrm{s}$ and the delay stage of the upconverting pulse is moved to a delay of $-80\,\mathrm{fs}$. The velocity of the stage is set to $0.0024\,\mathrm{mm\,s^{-1}}$, which corresponds to traveling in 10 seconds exactly the distance of $160\,\mathrm{fs}$[1] and is set to move (both operations are performed by the "MOVE" subvi). The stage is only allowed to accelerate and reach the constant velocity for $200\,\mathrm{ms}$ before starting the aquisition. The distance traveled in the meantime of

---

[1]The beam travels twice the distance of the stage, since it gets on the stage, is retroreflected and goes out again.

0.48 µm corresponds to a time interval of 3.2 fs. At this point, the stage travels with constant speed and the camera starts acquiring ("NEWTON ACQUIRE"). This way, the eSFG spectrum is automatically integrated on the chip, with the same exposure time for every wavelength. Once the stage reaches the delay $\Delta t = 80$ fs and the camera has stopped to acquire (both controlled by the "CHECK & WAIT" subvi), another measurement is started, this time with the stage moving backwards. This procedure is repeated for every pump-probe delay and the two spectra, which are identical, are then averaged and give the spectrum at the corresponding delay. Comparison of the spectra acquired with the stage moving forward and backward is used at the beginning of a measurement series to make sure that the velocities are set correctly for the required 800 nm-WLC delay range.

4.2.4 Referencing

Due to the required long integration time, a tr-eSFG scan takes approximately 90 minutes, for a typical value of 100 delay points acquired. Since the pump-induced variations of the signal are about 10 to 20 %, an average of at least four scans is needed to acquire sufficiently good statistics. This results in an overall measurement time of six hours. Such a long time is comparable with potential power drifts and fluctuations of the RegA output, which, in turn, result in even stronger fluctuation of the UV pump and of the WLC intensities due to the nonlinear optical processes. Therefore, it is crucial to simultaneously acquire a reference of the unpumped signal, which can be subtracted from the pumped spectrum in order to obtain the pump-induced SFG intensity variations. Acquiring background spectra of the pump and of the unpumped SFG signal at the beginning of each scan is not sufficient for a reliable compensation of the WLC fluctuations and thus it is necessary to take the reference for every delay point. We achieve this by using a galvanometer scanner similar to the one depicted in figure 4.12. A galvanometer scanner, or in short galvanoscanner, is based on the principle that a current flowing through a small pivoting coil in the field of a permanent magnet, generates a magnetic field that acts against the permanent magnetic field and induces the coil motion. If an alternating current is applied, the coil will oscillate perpendicular to its axis. If a mirror is connected to the rotation axis of the coil, then a laser beam incident on the mirror will be scanned continuosly from the minimum position of the deviation to the maximum, with the deviation amplitude and frequency set by those of the current. In order to achieve high frequencies and limit the friction and consequent

Figure 4.12: Galvanometer scanner: *yellow*: permanent magnet rotor, *blue*: coil, *gray*: magnetic core. The current applied to the coils generates a magnetic field that sets the rotor to move and the mirror connected to the rotor rotates around the axis. If an AC current is applied the mirror is set to rotationally oscillate, with amplitude and period dictated by those of the current.
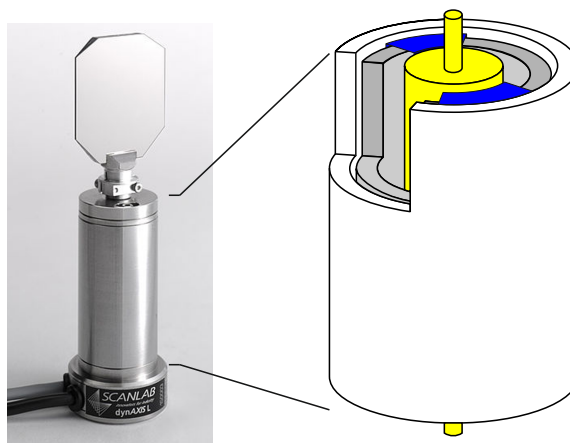
heating up of the coil, current galvanoscanners are designed in the so-called rotating magnet configuration, as shown on the right panel of figure 4.12. Here the coil (in blue) is fixed around a magnetic core (gray) while the permanent magnet (yellow) rotates as a consequence of the current circulating through the coils.

Usually, galvanoscanners are driven by an alternating sinusoidal current and the mirror oscillates between the maximum and minimum rotation. With laser systems running at a repetition rate of 1 kHz, the mirror and the chopper are both driven at half the frequency of the laser in a synchronized fashion. Every second laser pulse results in, for example, an unpumped SFG spectrum that reaches the mirror when it is at the minimum angular deviation, and vice versa for the next pulse (chopper open and mirror at the maximum deviation), which generates the pumped SFG spectrum. This is schematized in panel (a) of figure 4.13, where the red curve represents the oscillation of the mirror and the green and blue arrows the arrival times of the pumped and unpumped eSFG photons respectively. The resulting image on the CCD detector consists of two horizontal stripes (pumped and unpumped spectra) which are vertically offset, as shown in panel (c). At 40 or 200 kHz the situation is rather different. These frequencies are too high to be achieved with the current galvanoscanners and choppers, and much more than two pulses would hit the mirror during the oscillation period, leading to a vertically quasi-continuous stripe. In order to resolve two separate stripes, the sinusoidal wave driving the galvanoscanner needs to be replaced by a square wave. The mirror switches from one position to the other, and hundreds of pulses are integrated at each extremum. The switching time between maximum and minimum is dictated by the inertia of the rotor and by the bandwidth of the function generator and amplification circuitry. The rotor inertia also determines the ampli-
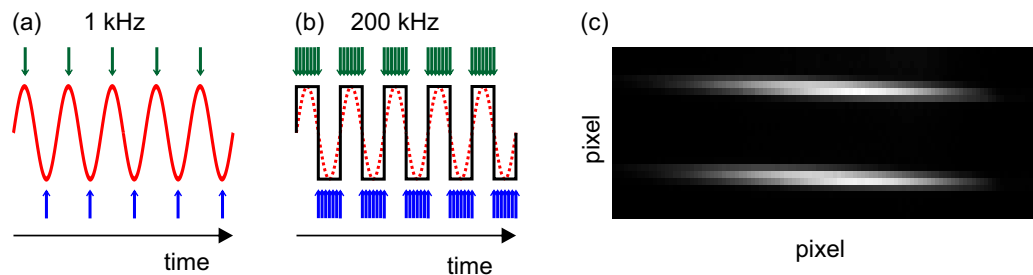
Figure 4.13: Shape of the current wave necessary to obtain two discrete stripes on the detector, as in panel (c). (a) For low repetition rate (e.g. 1 kHz) the mirror can be driven by a sinusoidal wave synchronized with the laser such that each pulse coincides with the deviation extrema. (b) For high repetition rate synchronization with the laser is not possible and the sinusoidal wave would lead to a vertically quasi-continuous stripe. A square wave is required to separate the spectra.

tude of the oscillations around the extremal positions. We use the dynAxis®-XS scanner from the company SCANLAB and operate it at a frequency of 500 Hz. The driving electronics and the control interface were built at the electronic workshop of the Fritz Haber Institute.

At the high repetition rates used in the experiments neither scanner nor chopper are synchronized with the laser and the chopper receives the trigger from the same frequency generator that drives the scanner. Still they need to be set in phase with each other, such that contributions from pumped and unpumped spectra are not mixed. This is realized by monitoring the luminescence signal, which originates exclusively from the pump and setting the phase delay between the mirror oscillation and the chopper such that on one of the regions of interest on the detector (lower or upper line) the luminescence is not visible.

### 4.2.5 Intensity of the upconverting pulse

As discussed in equation (2.22) of section 2.3, the intensity of the SFG signal is linearly proportional to the intensity of the white-light continuum and the upconverting 800 nm beam, respectively. The pulse energy of the WLC is very low, typically on the order of 10 pJ nm^{-1} [164]. In order to increase the SFG intensity it is thus only possible to increase the intensity of the upconverting 800 nm beam. However, it is fundamental not to trigger any dynamics with multiple-photon processes induced by the 800 nm beam. In the case of ZnO the origin of these dynamics can be twofold:

1. one and two photon absorption from IGS, such as populated defect states.

2. three photon excitation of valence band (VB) electrons across the gap.

A linear transient reflectivity experiment was performed to characterize the dependence of the ZnO dynamics on the power of the 800 nm beam. Here, the changes in reflectivity induced by the excitation at 800 nm were measured integrating over all white-light pulse frequencies. The results are plotted in figure 4.14.

Figure 4.14: Dependence of the transient visible reflectivity of ZnO on the 800 nm pulse fluence. The figure clearly shows a threshold behavior for an 800 nm power of 40 mW ($3.66\,\mathrm{mJ\,cm^{-2}}$). At this power a non-zero signal appears before the cross correlation of the pulses, indicative of a pump-induced dynamics surviving the repetition rate of the laser.
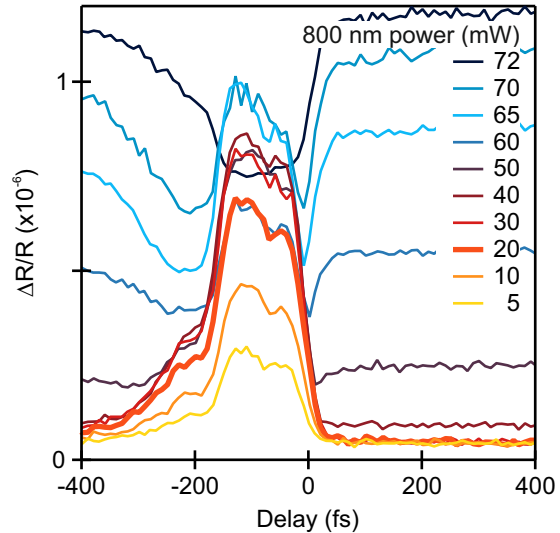
The figure shows the reflectivity changes induced by the 800 nm pump pulse as a function of pump-probe delay and of pump power. Clearly, the pump-induced reflectivity changes show a threshold behavior for pump powers above 40 nm, corresponding to a fluence of $3.66\,\mathrm{mJ\,cm^{-2}}$. At lower fluences the changes in the reflectivity have a temporal duration that is comparable to the cross-correlation between the 800 nm pulse and the white-light continuum shown in figure 4.10, thus indicating that no population is created by the upconverting pulse. At higher fluences instead the traces show a non zero offset at negative delays, indicative of a population living longer than the inverse of the repetition rate of the laser. For a repetition rate of 200 kHz, this population lives longer than $5\,\mu s$. In ZnO, this kind of dynamics, as will be discussed in detail in section 5.2, can originate only from intra-gap (i.e. defect) states.

Thus, to avoid the creation of a population with the 800 nm upconverting pulse, for all the performed experiments its fluence was kept to $1.83\,\mathrm{mJ\,cm^{-2}}$ at most, corresponding to a power of 20 mW in figure 4.14.

4.3 Proof of principle:
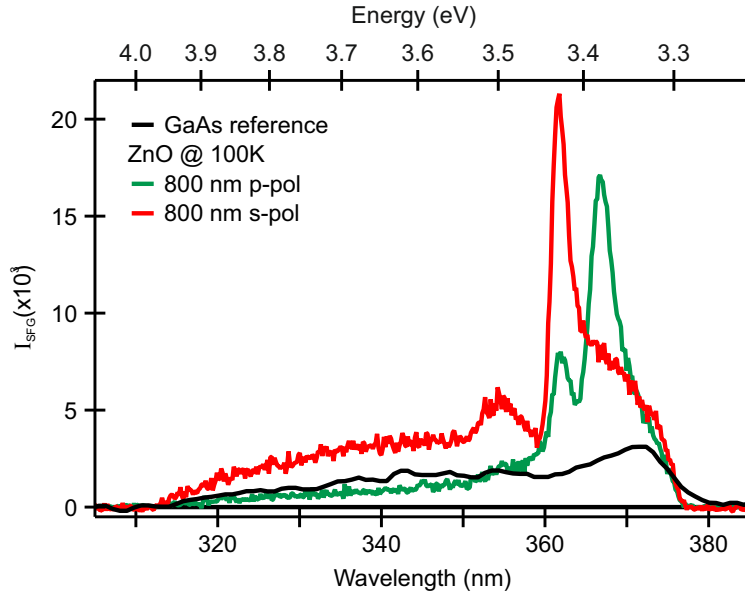
First eSFG measurement on ZnO

Figure 4.15: eSFG spectrum of ZnO for two polarizations of the upconverting beam, p-polarized in green and s-polarized in red. In black for comparison the eSFG spectrum of GaAs (p-polarized 800 nm). Clearly the two ZnO spectra differ from the reference spectrum, exhibiting two resonances around 3.4 eV, whose origin is explained in chapter 5.

The first eSFG spectrum of a solid is shown in figure 4.15. Here, the eSFG spectrum of ZnO is plotted for the two different polarizations of the 800 nm upconverting beam, while the polarization of the WLC is kept perpendicular to the plane of incidence, i.e. s-polarized. GaAs was used as reference and its spectrum is given by the black line in the graph. GaAs has a zincblende structure, which is also non-centrosymmetric in the bulk, and was chosen as reference because it does not exhibit resonant transitions at the WLC and eSFG energies. Thus, its eSFG spectrum reflects the shape of the convolution of the fundamental beams. All the spectra have been measured with an electron multiplication gain of 200 and exhibit count rates on the order of 20×10^3 counts per 10 s exposure time, leading to an average of 10 photons per second per pixel at the maximum resonance. Comparing the three spectra, two resonances are clearly visible for ZnO at an energy of about 3.4 eV, corresponding to the band gap energy. This section focuses on the technical aspects of the experiment and the nature of the resonances will be discussed in detail in chapter 5.

Figure 4.16 shows the proof of principle of time-resolved electronic sum-frequency generation. The static eSFG spectrum of ZnO and the luminescence background due to the UV pumping only are plotted in green and blue respectively in the left panel as function of SFG
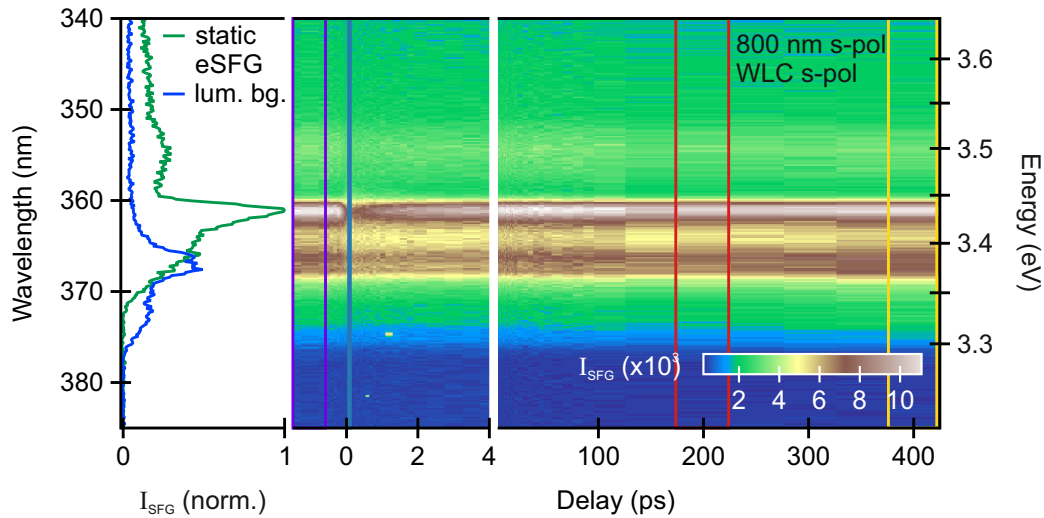
Figure 4.16: Proof of principle of the time-resolved electronic sum-frequency generation for both upconverting pulse and WLC s-polarized. The left panel shows the static SFG spectra and the luminescence of ZnO. The right panel shows the false color plot of the tr-eSFG intensity measured at 100 K as function of SFG wavelength on the y-axis and the pump-probe delay on the x-axis. The plot clearly shows that dynamics are visible at the eSFG resonance (3.43 eV) and at the maximum of the luminescence (3.38 eV). The spectra in the areas held by the coloured rectangles have been averaged and compared in figure 4.17.

wavelength (left y-axis) and SFG energy (right y-axis). Both traces are normalized to the maximum SFG intensity. The right panel shows the pump-induced eSFG changes in false colors as a function of pump-probe delay after photoexcitation at 4.1 eV. The spectrum is obtained with the time integration procedure explained in section 4.2.3, with an exposure time of 10 s and an EMCCD gain of 200, and by averaging over four scans. Clearly, dynamics are visible at the eSFG resonance at 3.43 eV (361 nm) and the luminescence maximum around 3.38 eV (367 nm).

Figure 4.17 shows the eSFG spectra integrated over four selected delay ranges, delimited by the colored lines in figure 4.16. The spectra have been binned in wavelength, such that each data point is averaged over two EMCCD pixels. In violet the averaged background at negative delays between −1.5 to 0.6 ps, in blue the averaged spectrum between 71 to 111 fs, corresponding to the maximum pump-induced variation, in red the spectrum at a pump-probe delay of 200 ps and in yellow the one at 400 ps. The black line results from the sum of the two static eSFG and the luminescence spectra depicted in the left panel of figure 4.16, and defines the static background intensity $I_{BG}(\lambda)$.
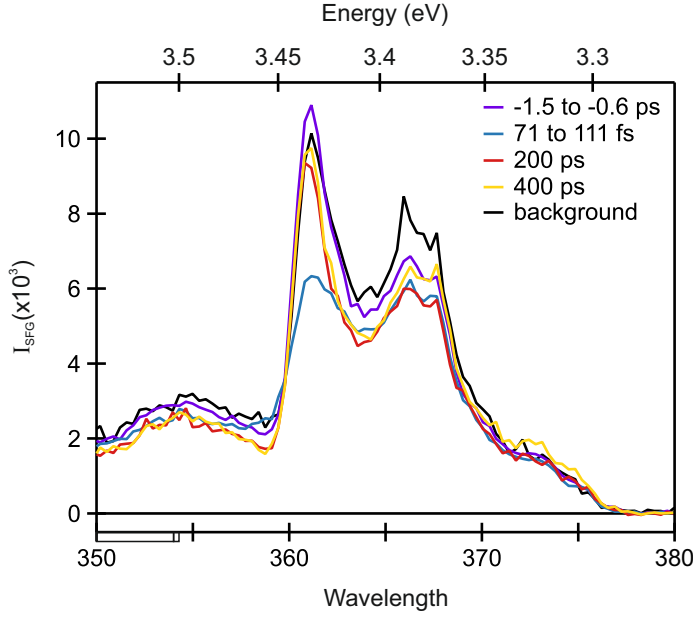
Figure 4.17: eSFG variation for four selected pump-probe delays, with respect to the background given by the sum of the static eSFG spectrum and the luminescence. The traces clearly show a pump-induced variation, both at positive and negative delays, for both the eSFG resonance at 3.43 eV and the maximum of the luminescence at 3.38 eV.

The traces clearly show a pump-induced variation at the eSFG resonance and at the maximum of the luminescence. We define the variation of the eSFG signal at a time delay t as:

$$\frac{\Delta I_{\text{eSFG}}(t,\lambda)}{I_{\text{BG}}(\lambda)} = \frac{I_{\text{eSFG}}(t,\lambda) - I_{\text{BG}}(\lambda)}{I_{\text{BG}}(\lambda)} \quad , \tag{4.1}$$

Where $I_{\text{eSFG}}(t,\lambda)$ is the measured eSFG intensity. To calculate the variation of the resonant eSFG peak we average the value over 6 points, corresponding to the interval (361 ± 1) nm. We observe a maximum variation of -30.6% at time zero and a minimum variation of -4.7% at 400 ps, in line with the expected values discussed in section 4.1. The intensity of the luminescence peak around 367 nm has also been averaged on the interval (367 ± 2) nm. Its variation ranges between -20% and -12%. Finally we observe a variation of 18.6 % at the lowest energy shoulder of the luminescence, integrated over the interval between 370 nm and 375 nm. This, due to the width of the peak, constitutes the smallest ΔI_{eSFG} variation we are able to resolve per nm.

Despite the low signals and the long integration times, these results demonstrate that time-resolved electronic sum-frequency generation is a feasible experiment and chapter 5 will discuss the results obtained.

Next steps towards the application of eSFG as *interface* specific technique at an HIOS interface with ZnO require the full characterization of its azimuthal dependence and the identification of the azimuthal angles at which the bulk eSFG contribution is zero, as described in

appendix A. This was, however, not possible since in the setup used it is not possible to rotate the sample without opening the cryostat. Since the resonances are visible at low temperatures only (cf. chapter 5), the error introduced on the position of the measured spot by heating up the sample, opening, rotating and cooling down again is too large for a precise azimuthal characterization.

5. Impurity

Effects of defect-related in-gap states on charge and exciton dynamics in ZnO

With its 3.4 eV bandgap and an exciton binding energy of 60 meV, ZnO could potentially represent an ideal candidate both as transparent electrode as well as substrate for resonant energy transfer in hybrid inorganic organic systems. The efficiency of charge and energy transfer processes between semiconductors depends strongly on the timescales of charge carrier and exciton relaxation processes. Furthermore, exciton lifetimes and diffusion as well as free carrier conductivity can be strongly affected by the presence of defects; their density and energetic position strongly depends on the sample growth conditions. Also, as discussed in section 1.3, the literature values for relaxation timescales in ZnO are quite divergent. Here, energy and charge carrier relaxation pathways in the bulk of ZnO are investigated with complementary all-optical techniques: static and time-resolved photoluminescence spectroscopy, time-resolved excited state transmission and the newly developed time-resolved electronic sum-frequency generation (tr-eSFG). Two excitation densities, one above and one below the Mott density, have been used in order to discern between the electron-hole-plasma and exciton dynamics. Moreover, defect-related dynamics have been tackled by comparison of the response of a single crystal with the one of a thin film deposited by molecular beam epitaxy on a single crystal substrate. The energy levels landscape of both samples are investigated by static spectroscopy (section 5.1) and show the presence of a defect band 1.7 to 2.7 eV below the conduction band. The optical response of these defect states prevails the pump-induced linear optical response after excitation above the Mott limit (section 5.2), both for light emission and transmission, and their dynamics strongly influence the relaxation timescales of the electron-hole plasma. In the low excitation regime, investigated by tr-eSFG and discussed in sections 5.3.2 and 5.3.3, the exciton-polariton resonances are initially affected by the free carriers relaxation in the conduction band (CB) and the formation of excitons is observed on a hundreds of picoseconds timescale.

5.1 The ZnO: visible and near-UV spectral features

A first fundamental step towards the characterization of charge and exciton relaxation pathways is the determination of the energy position of the relevant electronic states in the near band gap region and the identification of their spectral signatures. These signatures have been inspected by photoluminescence (PL) and electronic sum-frequency generation (eSFG) spectroscopy and are presented in this section. As discussed in section 1.3, the exciton-polariton lines of the three split valence bands are observed in reflection at 77 K at 3.371 eV, 3.378 eV and 3.418 eV for the A,B and C valence band (VB) respectively [87]. The first two are visible with light polarized perpendicular to the *c*-axis and the latter for light parallel to it. The PL spectrum at 10 K shows the ground state emission of the A and B free excitons at 3.377 eV and 3.39 eV respectively and longitudinal optical phonon (LOP) replicas for energies below the free exciton emission, with an average separation of 72 meV [23]. All these emission lines are observed to merge together in a single broad peak with a red-shift of roughly 60 meV at room temperature, which is attributed to the temperature induced narrowing of the band gap [90, 91].

As presented in section 3.3, this work investigates a ZnO single crystal and compares its energetics and dynamics with those of a homoepitaxially grown 125 nm film, both cut along the (10$\bar{1}$0) non-polar surface. Unless otherwise stated, all experiments have been performed in an optical cryostat at a base pressure of $\sim 1 \times 10^{-6}$ mbar and at a temperature of 100 K.

Figure 5.1 compares the PL spectrum of the ZnO single crystal, in black, with the one of the thin film, in red. The experiments have been performed together with Francesco Bianchi in the group of Sylke Blumstengel at the Humboldt University. The samples were excited at 354 nm (= 3.5 eV) by doubling the output of a Coherent Mira oscillator (repetition rate of 76 MHz) tuned to 709 nm. The static spectra have been acquired with an excitation density of 3×10^{17} cm^{-3}, well below the average literature value of the Mott density of 3×10^{18} cm^{-3} (cf. section 1.3). The left panel shows the emission spectrum in an energy region from 1.5 to 3.5 eV measured with a grating of 300 lines/cm, resulting in an energy resolution of 1.2 meV at 1.5 eV and of 6 meV at 3.4 eV. The two spectra are normalized at maximum emission, with the single crystal intensity being a factor 1.5 lower than the one of the thin film. Both substrates manifest a well-defined emission at 3.36 eV with clear vibronic replica at an average separation of (66 ± 15) meV. This transition energy is associated to the emission of the free exciton and the replica separation is
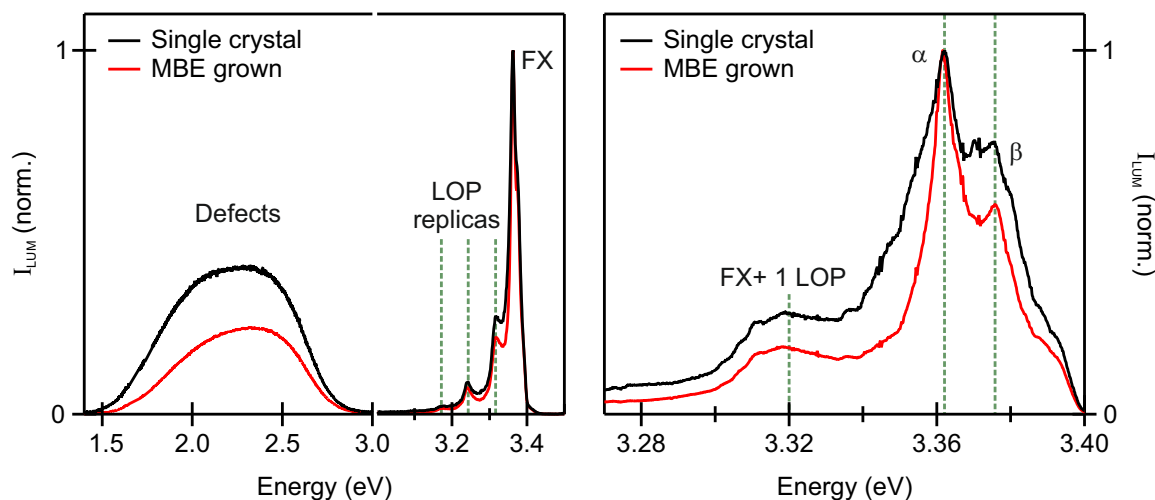
Figure 5.1: Comparison of the luminescence spectrum of a single crystal and a MBE grown film in the visible and near-UV spectral range. The spectra are normalized to maximum for clarity. (*Left*) Both samples show free excitonic emission and LOP replicas starting at 3.36 eV. The emission band in the visible is assigned to the recombination of defect-trapped excitons related to the presence of oxygen vacancies and interstitials. (*Right*) High resolution spectrum in the exciton emission region. The spectra show two shoulder, labeled α and β and discussed below and the first LOP replica. The broader single crystal emission suggests the higher probability of non-radiative decay with respect to the thin film.

in good agreement with the one of the prevailing LOP replica of 72 meV [92]. Furthermore, both samples exhibit an emission band in the visible, starting at 1.6 eV and ending at 2.8 eV. However, these bands differ in the energy position of the maximum intensity: the single crystal shows a rather homogeneous band over the whole energy window while the thin film emits predominantly at higher energies. From the results of references [95, 99, 100] presented in section 1.3, three kind of defects are responsible for this emission: oxygen vacancies centered around 2.46 eV, oxygen interstitials around 2.28 eV and defect complexes involving oxygen excess for the red emission shoulder centered at 1.8 eV. The relative weight of the bands in the emission spectra differs for the two samples, suggesting that the single crystal has a higher oxygen vacancy and defect complex to interstitial ratio than the molecular beam epitaxy (MBE) sample. Moreover, the ratio of the FX to defect emission in the single crystal is 2.5 compared with the 4.2 of the thin film, suggesting an overall higher density of defects in the former. The right panel of figure 5.1 expands the spectrum in the energy region of the exciton emission.

Again, the energy position of the PL lines is independent of the sample. The main emission line consists of two peaks labeled α and β and centered at 3.363 eV and 3.376 eV respectively, with a separation of 13 meV, in good agreement with the separation observed in reference [23] for the A and B exciton emission. The emission at 3.31 eV is attributed to the first LOP replica and its energy position agrees well with the literature values reported in section 1.3. The free exciton emission from the single crystal is much wider than the one of the MBE film, suggesting that defect trapping and other decay channels in the single crystal are more competitive to luminescence than in the thin film.
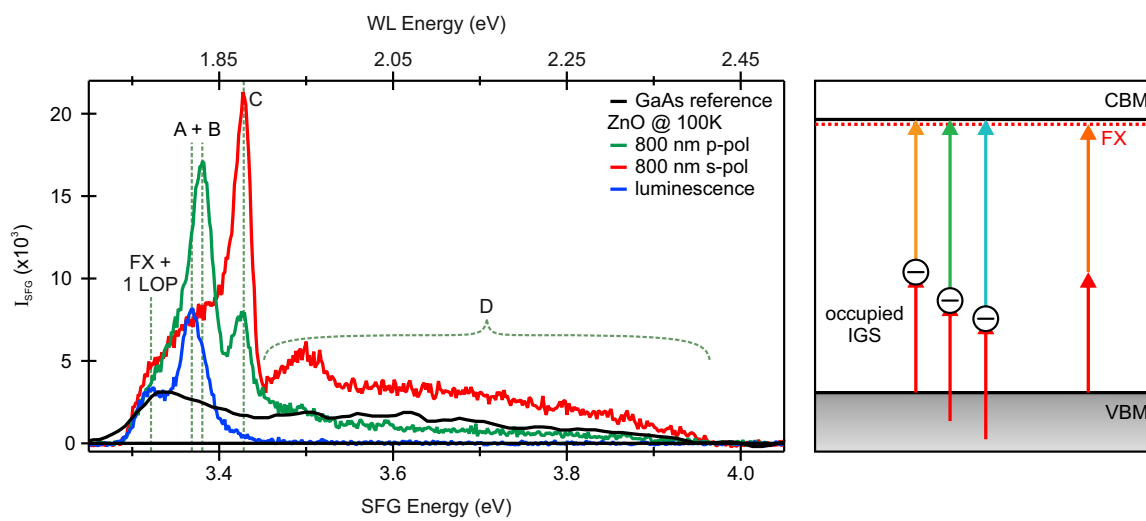

Figure 5.2: (*Left*) Static eSFG spectrum of the ZnO single crystal for two polarizations of the up-converting beam (green p- and red s-polarized), compared to the photoluminescence spectrum. Two clear resonances are observed around the onset of the CB and a broad feature, predominantly in the s-polarized spectrum, at higher energies. The resonances are attributed to final state eSFG transitions associated to the A,B and C exciton-polaritons, and the broad feature to intermediate state resonances from the defect band. (*Right*) Cartoon of intermediate eSFG transitions for IGS at energies corresponding to the emission band observed in the photoluminescence. For comparison, the scheme of the final state transition occurring at the free exciton (FX) resonance.

The left panel of figure 5.2 compares the single crystal emission after excitation at 4.1 eV, depicted in blue, with the the static eSFG spectrum measured for two different polarizations of the upconverting beam, s-polarized in red and p-polarized in green [1]. All the spectra have been

---

[1] eSFG spectra of the MBE sample were found to be strongly affected by the interference with the signal arising at the interface between the thin film and the underlying single crystal substrate and are therefore not considered in the following.

measured with eSFG setup presented in chapter 4 and the RegA tuned at 40 kHz. The energy resolution of the eSFG experiment is limited to 66 meV by the width of the upconverting pulse, while for the PL it is 10 meV and limited only by the spectrometer. The luminescence spectrum shows a broad peak centered at 3.37 eV without a clear structure, and the first LOP replica at 3.1 eV. The broad emission is attributed to both peaks α and β, which cannot be resolved due to the lower energy resolution of this spectrometer compared with the one used previously.

Two resonances are observed in the eSFG spectra: a broader resonance around 3.37 eV, visible only for p-polarized 800 nm beam and a narrower one at 3.43 eV, observed for both polarizations. The $(10\bar{1}0)$ surface of ZnO is parallel to the c-axis, such that s-polarized light has only components parallel to the c-axis while p-polarized light has both components parallel and perpendicular. The energy positions and polarization dependence of the spectral features are in good agreement with the observations of Thomas [87]. Therefore these transitions are assigned to the exciton-polaritons associated with the three split VBs of ZnO at the Γ point: the lower energy arises from the two almost degenerate VBs A and B and the higher one from VB C. All these transitions are final sum-frequency generation (SFG) transitions, as schematized by the free exciton (FX) resonance in the right panel of figure 5.2. The apparent shift of the A and B peak with respect to the luminescence spectrum is attributed to a different relative ratio between the contributions of A and B in the two probing methods.

Finally, one additional broad feature, labeled D, is observed in the s-polarized spectrum at energies above 3.45 eV, while the p-polarized spectrum coincides with the GaAs reference. The similarity of the GaAs and the p-polarized response strongly suggests that both arise from non-resonant contributions, which are sample-independent. The s-polarized response, however, can correspond either to final state transitions well within the ZnO CB, i.e. in the UV, or to intermediate state transitions from populated in-gap states (IGS) to the CB, with a transition energy given by the white-light continuum (WLC) photon energy and ranging from 1.9 to 2.4 eV, well within the emission band attributed to defect states in figure 5.1. The latter process is schematized in the right panel of figure 5.2 for three exemplary energies of 1.9 eV, 2.3 eV and 2.5 eV. Due to the good energetic agreement with the defect band observed in the luminescence spectra, the feature is associated to IGS which appear to couple better with the s-polarized geometry .

The excitonic nature of the A,B and C eSFG resonances is confirmed in figure 5.3. The
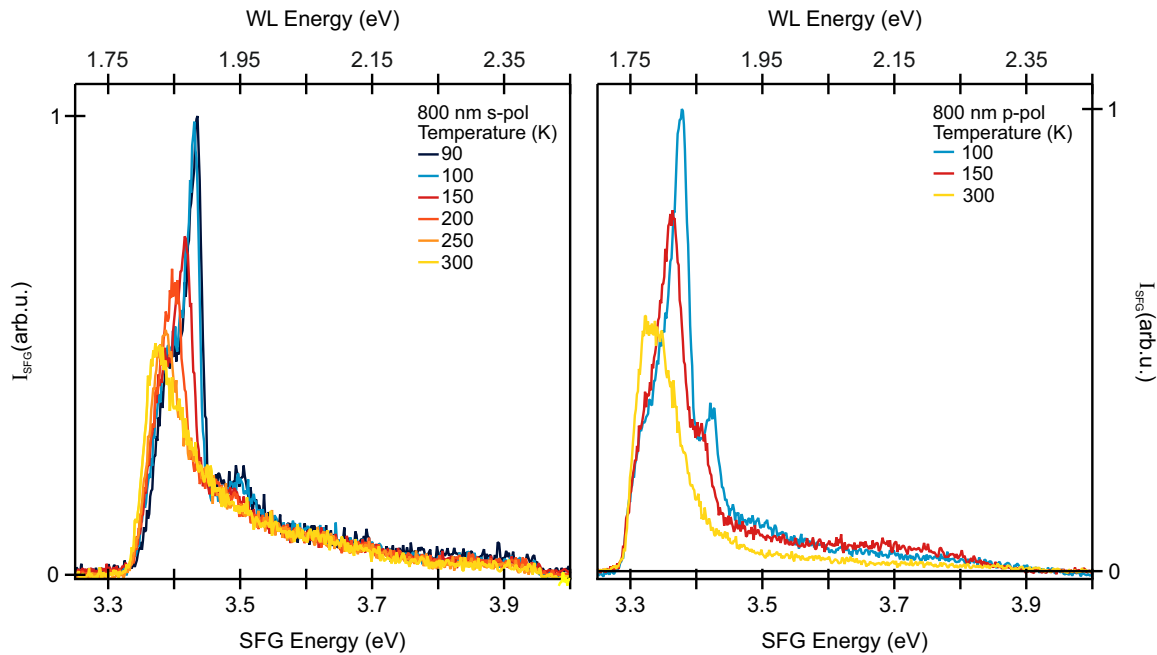
Figure 5.3: Temperature dependence of eSFG spectral signature for (*Left*) s-polarized and (*Right*) p-polarized 800 nm beam. The spectra all show a similar trend with the energy positions shifting to lower values and the width increasing for increasing temperature, confirming the excitonic nature of the transition lines.

figure presents the temperature dependence of the eSFG resonances for s-polarized (*Left*) and p-polarized (*Right*) 800 nm beam. The trends are similar for both polarizations: the peaks widen and shift to lower energies for increasing temperatures. The shift of the peak is attributed to the band gap narrowing with increasing temperature and the widening to homogeneous broadening. Our observations are in agreement with references [90] and [91], where the exciton binding energy for the FX associated with the valence band A has been determined not to depend on the temperature.

The combination of multiple techniques allows to identify the spectral features of the relevant energy levels in the band gap region of the ZnO single crystal. Three resonances associated with the exciton-polaritons corresponding to the three crystal field split VBs are observed at about 3.37 eV (A), 3.38 eV (B) and 3.42 eV (C). Furthermore, the first LOP replica is visible at 3.31 eV and a band related to transitions from and to in-gap states at energies from 1.6 to 2.8 eV is detected both in emission and s-polarized eSFG spectra. The energy level alignment for the near band-gap region is summarized in figure 5.4.
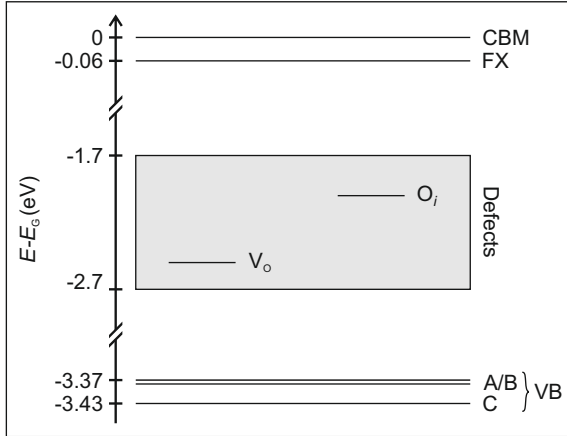
Figure 5.4: Energy level position with respect to the CB minimum of the features observed in the PL and SFG spectra. (1) The defect band between $-1.7\,\text{eV}$ and $-2.7\,\text{eV}$, where the position of oxygen vacancies (V_O) and interstitials (O_i) (2) the three valence bands A,B,C respectively at $-3.37\,\text{eV}$, $-3.38\,\text{eV}$ and $-3.43\,\text{eV}$

The next sections are devoted to get further insight on the dynamics associated to each of these components after non-resonant excitation across the band gap.

5.2 High excitation regime: Influence of defect dynamics on ZnO optical properties

Firstly, the charge carrier dynamics are investigated for excitation densities above the average nominal Mott density of $\simeq 3 \times 10^{18}\,\text{cm}^{-3}$, reported in section 1.3. At these densities, the presence of free carriers in the conduction and valence band is expected to screen the Coulomb attraction of the electron-hole pairs, such that no bound excitons can form. However, the literature values of the Mott density are ranging over two orders of magnitude and a clear Mott transition from bound excitons to free charges was never observed experimentally for direct band gap bulk semiconductors [27]. As repeatedly mentioned throughout the text, the literature reports multiple values for the timescales associated to exciton and charge carrier relaxation processes. For excitation densities comparable to the ones used in this section (0.9 to $1 \times 10^{19}\,\text{cm}^{-3}$), table 1.1 reports (1) charge carrier thermalization in the CB to occur within $1\,\text{ps}$ [112] predominantly via Auger recombination processes [19], which probability steeply increases for densities above 2×10^{18}–$3 \times 10^{18}\,\text{cm}^{-3}$, (2) exciton radiative and non-radiative recombination in $900\,\text{ps}$ and $200\,\text{ps}$ respectively [89], (3) exciton-exciton scattering in a time range from instantaneously to $12\,\text{ps}$ [119, 120] and (4) electron-hole-plasma (EHP) decay in $1.2\,\text{ns}$ [19]. Furthermore, recombination of IGS is observed in hundreds of ps to tens of ns.

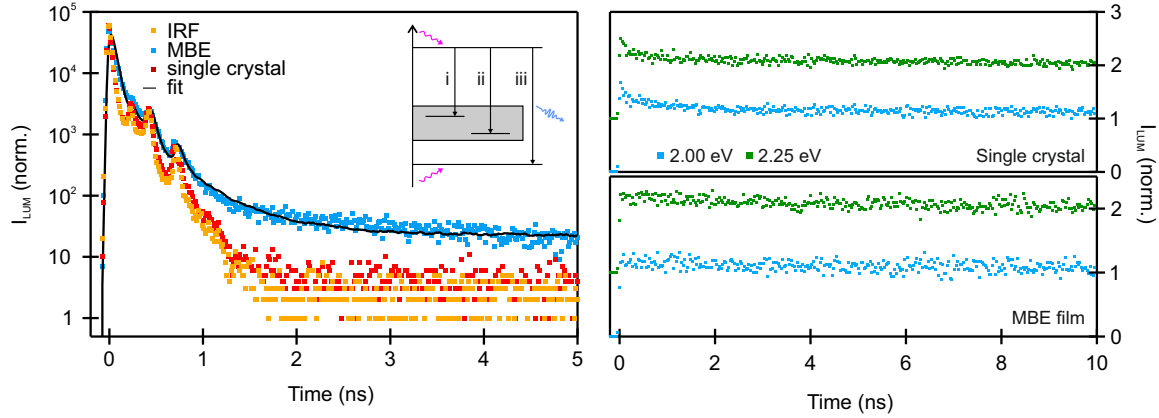Figure 5.5 shows time-resolved photoluminescence (tr-PL) measured on both the ZnO single

Figure 5.5: (*Left*) tr-PL of the ZnO syngle crystal, in red, and of the MBE film in blue at the emission energy of 3.37 eV, compared with the instrument response function (IRF) of the single photon counter spectrometer. Clearly, the excitons in the single crystal decay within the IRF of 30 ps, while the MBE film shows a triple exponential decay. (*Right*) tr-PL at two energies in the defect band of 2.25 eV and 2.00 eV. Both samples show a lifetime much longer than 12 ns, with the single crystal exhibiting also a fast decay component, on the order of 100 ps.

crystal and the MBE film. Analogously to the static luminescence, the samples were excited at 354 nm (= 3.5 eV) with a repetition rate of 76 MHz, this time with an excitation density of 1×10^{19} cm^{-3}. The excitation density was estimated from the pump fluence F as

$$ N_0 = \frac{F}{l_0 \hbar \omega} \left| \left(\frac{2}{1 + \sqrt{\varepsilon_r}} \right)^2 \right| \quad , \tag{5.1} $$

where l_0 is the light penetration depth and is 50 nm for photonenergies above 3.3 eV [178] and $\hbar \omega$ is the photon energy of the excitation beam. The second multiplier takes into account the surface reflectivity and ε_r is the dielectric constant of (4.3+1.9i), extracted from [178].

In the left panel, the emission decay at an energy of 3.37 eV, corresponding to the emission energy of A at low excitation densities, is plotted as a function of time after excitation for the single crystal (red) and for the MBE film (blue). Both are compared to the instrument response function (IRF) of the single photon counting spectrometer, depicted in yellow. Emission is clearly observed at this energy but, due to the high excitation density, it is to be attributed to free carrier recombination from the conduction band rather than to bound excitons. In the single crystal it decays within the IRF, which is less than 30 ps, while the emission decay in the MBE film can be fitted with a triple exponential decay leading to time constants of 39 ps, 523 ps and 33 ns, after deconvolution of the IRF. Several processes could be potentially responsible for

the multiple decay constants observed, and no concrete assignment can be made without further investigations. Nevertheless, one plausible hypothesis is that the fast constants are related to charge trapping by the defect band, as schematized in the inset of the figure. At equilibrium, these IGS are populated levels that can be depleted by the excitation beam and, once empty, act as traps for the electrons in the conduction band (processes i and ii), thus reducing the amount of electrons that can radiatively recombine. The long time constant, instead, can indeed be related to radiative recombination of CB electrons and VB holes (iii), and is consistent with the nanoseconds lifetime of the conducting EHP measured by Hendry et al. [19]. The much shorter lifetime observed on the single crystal, smaller than the instrument resolution of 30 ps, suggests that, there, the electron trapping by IGS could be an extremely efficient process and represent the predominant decay channel. The right panel of the figure shows the emission decay as a function of time at two energies within the defect band, 2.00 eV and 2.25 eV. In both samples, and independently on the energy, no dynamics can be resolved over the whole range and the radiative lifetime of the defect states is longer than the inverse repetition rate at 12 ns. Qualitatively, however, the decay traces for the single crystal show a superimposed fast dynamics which is compatible with the above described IGS re-population, both radiatively or not.

To address the nature of the charge carrier decay channels and thus explain the observed time scales, the emission dynamics are compared with the changes in visible light transmission, i.e. at energies smaller than the band gap energy. In an ideally pure semiconductor with band gap higher than the highest probe photon energy, the transmission before photoexcitation is expected to be maximum and the promotion of electrons in the conduction band should lead to an increase in absorption and therefore a decrease in transmission. On the other hand, for a semiconductor rich in impurities the situation is rather different, as schematized in the right panel of figure 5.6. Here, before photoexcitation, the IGS can absorb in the visible and photoexcitation leads to their depletion and a resulting increase in transparency. It is important to remark that the time-resolved excited state transmission response results from the sum of these induced absorption and transparency components. Depending on whether a given decay pathway affects more strongly the hole population in the IGS or the electron population in the conduction band, it results in an overall rise or decay of the time-resolved transmission (tr-T) signal.

The samples are photoexcited at 3.8 eV photon energy with a fluence of 0.15 mJ cm^{-2}, cor-

responding to a density of $8.6 \times 10^{18}\,cm^{-3}$ excited electrons. The experiments are performed with a repetition rate of 200 kHz and the WLC is used as probe pulse. The small pump-induced transmission changes do not allow broadband detection in the spectrometer and a lock-in amplifier is required. Thereby, the probe-energy is selected after interaction with the sample by a series of nine color filters with bandwidth of 10 nm and central wavelength in steps of 20 nm from 540 to 680 nm plus one at 694 nm.
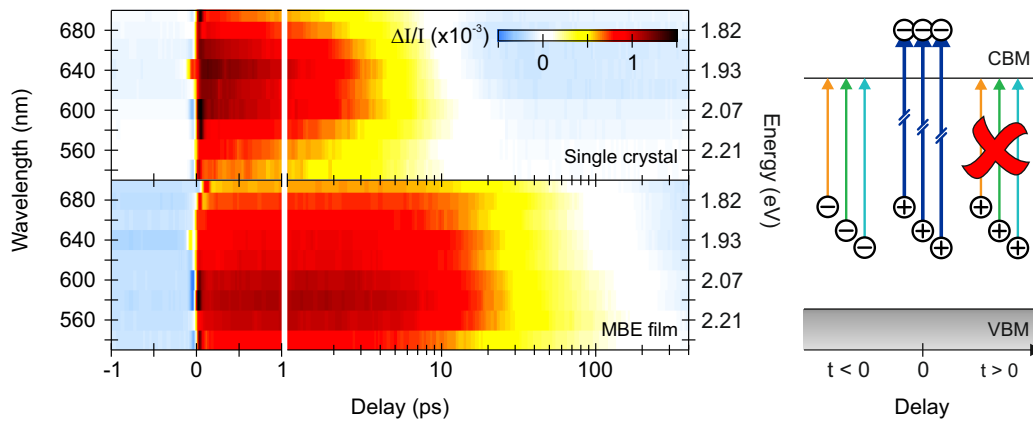

Figure 5.6: (*Left*) tr-EST of both the single crystal and the MBE ZnO sample when pumped at 3.6 eV. Both samples show a pump-induced increase of transmission over the whole visible range. (*Right*) This increase is explained with a depletion of the populated IGS by the pump pulse such that they can no longer absorb.

The pump-induced transmission changes are plotted as false color plot in the left panel of figure 5.6 as function of filter central wavelength and pump-probe delay, for the single crystal on the upper and for the MBE film on the lower panel. The delay axis is linear in the -1 to 1 ps range and logarithmic from 1 to 400 ps. The energy axis on the right y-axis is obtained by conversion of the filter central wavelengths and serves only as a visual reference.

Both samples show an abrupt increase in visible (VIS) transmission at the time overlap of pump and probe beams, i.e. both samples become more transparent after photoexcitation. The maximum transmission change occurs at 640 nm (~ 1.9 eV) in the single crystal and at 580 nm (~ 2.14 eV) in the thin film. Already at a first qualitative glance, the two samples manifest different recovery dynamics, with the decay of the induced transparency being longer for the MBE film. At longer time delays, where the induced transparency has fully recovered, the transmission of both samples becomes slightly negative, indicating an increased absorption in
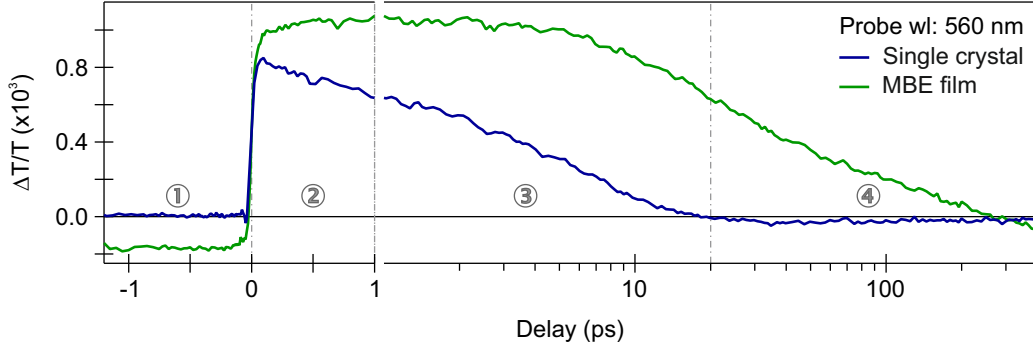
the visible range.

Figure 5.7: Comparison of the tr-EST at a probe wavelength of 560 nm (2.2 eV) for the two ZnO samples. See text for discussion.

To get a quantitative insight on how relevant the two expected induced transparency and absorption components are in each sample, the kinetic traces are analyzed individually for each probe wavelength. Figure 5.7 exemplarily shows the transient transmission changes for a probe wavelength of 560 nm, corresponding to a probe photon energy of 2.2 eV. The dynamics can be qualitatively divided in four time ranges, indicated in the figure: (1) a non-zero signal at negative delays, more evident at this wavelength for the MBE film, (2) a fast component in a time range of 1 to 2 ps, which is observed as rise exclusively in the MBE film, (3) a slower double exponential decay for both samples and (4) a long time negative component.

The pump-induced transmission changes in both samples can be fitted by the empirical fit function

$$\Delta T/T(t > 0) = A_0 + A_1 * \exp\left(\frac{-t}{\tau_1}\right) + A_2 * \exp\left(\frac{-t}{\tau_2}\right) + A_3 * \left(1 - \exp\left(\frac{-t}{\tau_3}\right)\right) \quad . \tag{5.2}$$

Here A_0 is the amplitude at negative delays and is extracted directly from the data, i.e. independently of the fit. This signature is present for all wavelengths in the thin film and only at long wavelengths in the single crystal. It is indicative of an excitation that is created by a pump-pulse reaching the sample at least an inverse repetition rate of the laser before the interaction with the probe. This excitation, thus, survives for longer than 5 μs and constitutes a quasi-stationary background to the measurements. The fit function is the same for both samples but the single summands are not describing the same processes. For the single crystal, the first and second addends describe the double exponential decay (range 3) and the third one the long time recovery in (4), i.e. the decay of the absorption. For the MBE sample, instead, the third addend

fits the initial fast rise of (2). The time-constants averaged over the whole wavelength interval are summarized in table 5.1, where they are compared with the PL timescales.

Sample		Hot carriers	defect trapping		PL	IGS PL
		(ps)	IGS 1 (ps)	IGS 2 (ps)		
Single	tr-PL		< 30.0 ps			> 12.0 ns
crystal	tr-EST	–	1.2 ± 0.5	6.5 ± 0.4	100s of ps to ns	–
MBE	tr-PL	–	39.0	523.0	33.0 ns	> 12.0 ns
film	tr-EST	2.3 ± 0.4	26 ± 3	210 ± 10	–	–

Table 5.1: Time constants for the four different recovery components in the tr-EST traces for the single crystal and MBE film.

Strikingly, in the case of the MBE crystal, for which time constants could be extracted from the tr-PL at 3.37 eV, strikingly, they are observed to agree in order of magnitude with the time-resolved excited state transmission (tr-EST) results. The time constants obtained by tr-EST on the single crystal are both below 10 ps, thus in agreement with the timescale observed in the tr-PL experiment, where the charge carriers relaxed on less than 30 ps. This suggests that the relaxation mechanisms leading to the decay of the CB electron emission are the same that lead to a recovery of the VIS transmission in both samples.

As mentioned previously, an increased transmission (positive variation) is related to the depletion of the IGS and a consequent induced transparency, and a decreased transmission (negative variation) is related to the absorption due to the charge carriers in the CB. The photoinduced transmission dynamics observed at early time delays are, for both samples, clearly dominated by the IGS related induced transparency. The negative component, related to the absorption from CB electrons is detected only at long time delays, once the relative ratio of defect-localized holes and CB electrons is such that the hole response no longer dominates the sample optical properties. Despite the qualitative similarities, the time scales observed for the two samples are significantly different, suggesting that the multiple decay pathways, discussed in figure 5.8, are differently relevant in each sample.

The fast 1 to 2 ps rise observed exclusively on the MBE sample, can be also viewed as fast decay of a negative transmission variation, which can be related to the cooling of hot charge
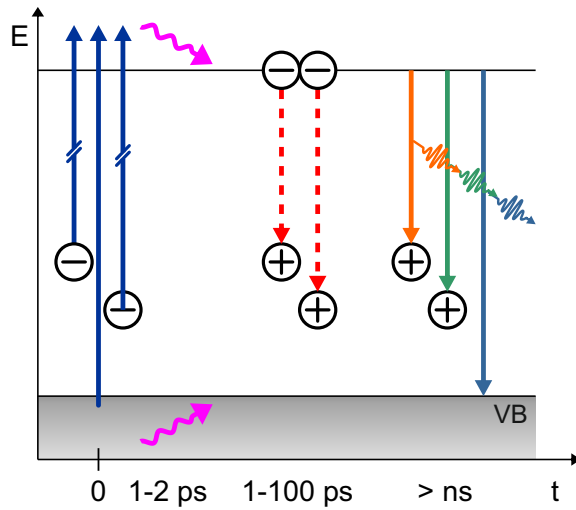
Figure 5.8: Summary of the relaxation processes in ZnO after excitation above the Mott density. The photoexcited hot carriers relax to the band edges via electron-electron scattering mechanisms (pink), the electrons are trapped in the empty IGS (red dashed arrows) and finally, on timescales of several ns to μs, the optical properties come to full recovery via radiative recombination.

carriers in the conduction and valence band, as schematized by the pink wiggling arrow. At these electron densities, well above the Mott density, electron-electron scattering can become a relevant scattering mechanism [19]. Hot carriers, thus, relax to the respective band edges predominantly via many-body Auger-like relaxation mechanisms and indeed the obtained time scale is comparable to the one assigned to many body charge annihilation by Hendry et al. [19].

The slow components (IGS 1 and 2), schematized by the dashed arrows, lead to a full decay of the induced transparency and therefore are related to a process that substantially refills the IGS. Thus, similar to the hypothesis discussed previously for the tr-PL data, they are associated to electron trapping in the empty defect states. This defect trapping is additionally supported by the fast decay of the IGS luminescence in the single crystal, which can be associated to a reduction of both the electrons in the CB and the holes in the IGS. The multiple timescales observed are most probably due to different trapping probabilities for the various kinds of defects and the generally longer relaxation times of the MBE film response are due to a lower density of defect states, thus supporting the observations made in the static luminescence spectra. Moreover, the involvement of two distinct defect distributions in the two samples is supported by the different wavelength position of the maximum transmission change, which suggests that the dynamics of the single crystal could be dominated by those of the defect complexes at 1.85 eV and in the MBE sample by oxygen interstitials at 2.24 eV.

Finally, the unperturbed optical properties of ZnO are recovered on nanosecond to microsecond timescales. The radiative recombination from CB and VB (blue arrow) is estimated to be 33 ns and in agreement with the persistence of a conducting EHP over nanosecond time scales

as observed by Hendry et al. [19]. Moreover, the long-lived recombination dynamics of the IGS PL and the non-zero quasi-stationary background, indicative of a process surviving the inverse laser repetition rate at $5\,\mu s$, set the time scales necessary for a complete recombination of electron-hole pairs strongly localized on the defect states (orange and green arrows) to be longer than what can be resolved with either of the used experimental setups.

Summarizing, excitation of ZnO with photon doses that lead to an excited electron density larger than the Mott density, also strongly depopulates IGS. Their presence severely affects the pump-induced optical response and their re-population dynamics via electron trapping dictates the early relaxation timescales observed in both tr-EST and tr-PL. Therefore, IGS are identified to be the predominant energy loss channel in ZnO. Only in the MBE sample, where the defect density is smaller, an additional negative component relaxing within 1 to 2 ps is detectable and is related to the cooling of hot carriers in the conduction and valence bands. The full recovery of the optical properties takes times on the order of nanoseconds to microseconds.

5.3 Intermediate excitation regime

The previous section identified IGS as a relevant relaxation pathway for the charge carriers in ZnO when the excitation density is high. As a next step, it is relevant to investigate if, and how, they instead affect exciton dynamics. To do so, the newly developed tr-eSFG experiment, where all A, B and C exciton-polariton resonances are directly resolved, is used and the excitation density n_e is reduced to 1.5×10^{18}–3×10^{18} cm^{-3}. These excitation densities are slightly lower than, or equal to, the average Mott density reported in section 1.3 (3×10^{18} cm^{-3}) and excitons are expected to form. Since excitons are presumed to decay on ns to μs timescales, the repetition rate of the laser is decreased to 40 kHz, which also minimizes the quasi-stationary effects of the long-lived defect populations detected in the linear optical measurements. The samples are excited with a photon energy of 4.1 eV, generated by doubling the output of the optical parametric amplifier tuned at 605 nm.

The tr-eSFG spectra are depicted in figure 5.9, for two polarizations of the 800 nm upconverting beam: p-polarized ($n_e = 1.5 \times 10^{18}$ cm^{-3}) in panel (a) and s-polarized ($n_e = 3 \times 10^{18}$ cm^{-3}) in panel (b). As for the static spectra, the polarization of the WLC is kept perpendicular to the plane of incidence, i.e. s-polarized, for all the measurements. The
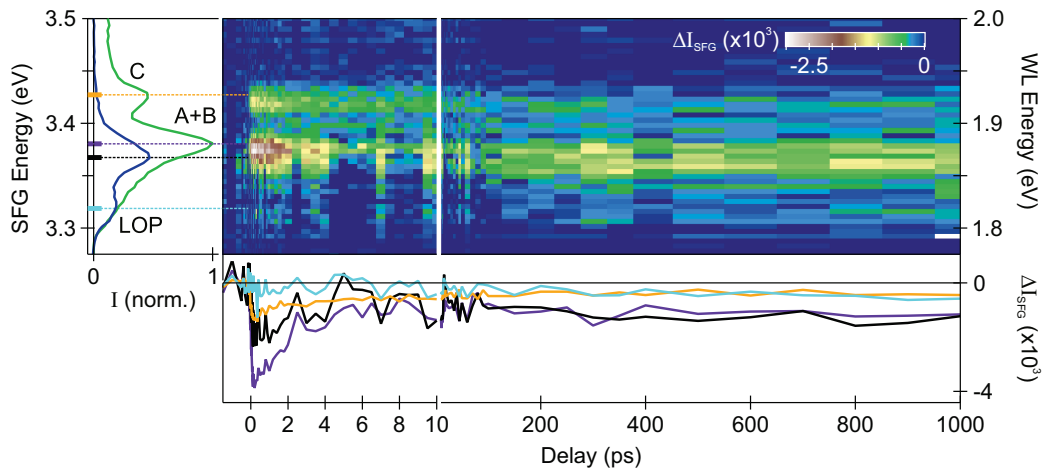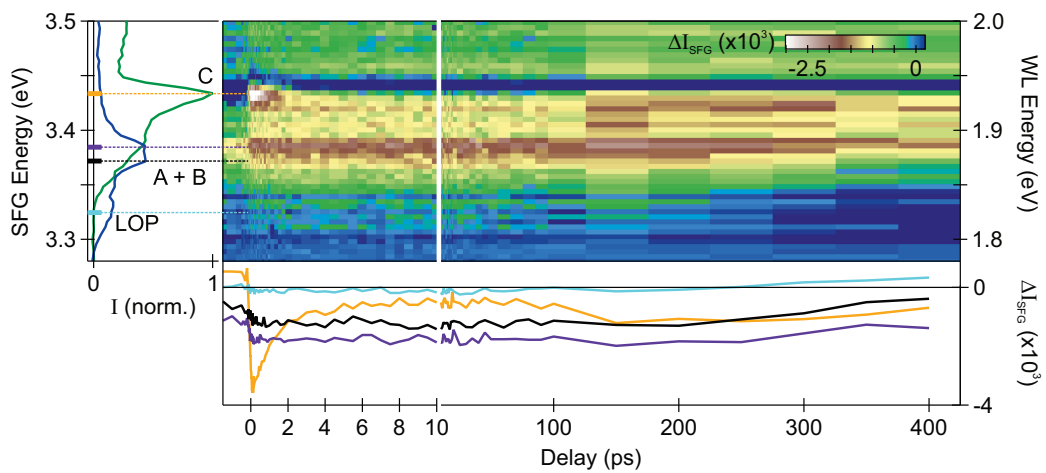
Figure 5.9: False color plots of the pump-induced variation of eSFG intensity as function of pump-probe delay and eSFG energy for (a) p- and (b) s-polarized upconverting beam. The left panels report the respective static eSFG and PL spectra as well as the energy positions of the kinetic traces depicted in the bottom panels. The cuts are taken in correspondence of the A (black) ,B (violet) and C (yellow) resonances at 3.37 eV, 3.38 eV and 3.43 eV respectively and at the LOP replica at 3.31 eV. Dynamics are clearly observed for both polarizations and can be divided in 3 different processes. The intensity of all final-state resonances abruptly decreases at time zero and recovers on a fast (1–2 ps) timescale. Step-like dynamics are seen at the energy of A and B in (b). A decrease of the intensity of resonance A and B in (a) and an intensity increase at the energy of A and of the LOP replica in (b) are detected on a long (200 ps) timescale.

105

eSFG intensity variation, defined as $\Delta I_{SFG} = I_{SFG}(\Delta t) - I_{BG}$, is shown as a false color plot as a function of SFG final state energy and delay between the maximum amplitudes of the eSFG and pump pulse electric fields (cf. section 4.2.3). The right y-axis reports the WLC photon energy for reference. The background intensity I_{BG} is given by the sum of the static eSFG and PL spectra, which are depicted respectively in green and blue in each of the left panels of the figures. Both the static and the time resolved spectra have been binned in energy for better clarity with a bin width of three pixels[2]. As discussed above for the static eSFG spectra, two resonances are detected for p-polarization: a wider one at around 3.37 eV due to the transitions from the valence band (VB) A (3.37 eV) and B (3.38 eV) exciton-polaritons and a narrower one at 3.43 eV for the C exciton-polariton. The latter is the only visible resonance for the s-polarized beam configuration. The two-dimensional plots clearly exhibit pump-induced dynamics at the energies corresponding to all the spectral features, as further clarified by the kinetic traces depicted in the bottom panels. The color code, indicated by the lines in the static plot, is the following: resonance A in black, resonance B in violet, resonance C in orange and the LOP replica in the luminescence in light-blue. The dynamics can be divided into three main time regimes: (1) a fast relaxation, observed in all eSFG final state resonances, (2) a long time dynamics, visible as intensity decrease for resonance A and B in panel (a) and as an increase for resonance A and the LOP replica in the (b) and (3) a non zero intensity at negative delays in panel (b).

From the literature values reported in table 1.1 and the results of the static spectroscopy, three different processes are expected to affect the ZnO response at these excitation densities. In the first place, the exciton-polariton resonance energies are quasi degenerate with the onset of absorption from the CB and the exciton-polariton continuum of states is indeed overlapping with the CB continuum (see section 1.1.1). Therefore, the electron dynamics in the CB are expected to affect the early response of the eSFG final state transitions to A, B and C. According to the results reported in table 1.1 these dynamics occur on timescales of fs to few ps and are related to the relaxation of the hot photoexcited carriers. At these excitation densities Auger recombination is not a relevant scattering mechanism [19] and electron relaxation through the continuum has been predicted theoretically to occur via electron-phonon scattering, first mainly with LOPs (tens of fs) and then, when the excess energy is lower than ~ 10 meV, with acoustical

---

[2]The binning does not reduce the energy resolution, which is in any case limited by the bandwidth in energy of the upconverting 800 nm pulse of 66 meV.

phonon (AP) (picoseconds dynamics) [110]. In agreement with the theory, Deinert et al. and Tisdale et al. [109, 111] observed ultrafast (20 to 40 fs) dynamics for excess energies larger than 0.2 eV, which are substantially slowed down at lower energies.

Secondly, at excitation densities below the Mott density, the Coulomb screening in the CB is not sufficient to contrast the electrostatic attraction of free electrons and holes and bound excitons are formed. Two formation timescales are reported in the literature, depending on whether the exciton is a surface or a bulk exciton. The first is formed on timescales as fast as 200 fs [109], while the second on timescales of hundreds of ps [19], i.e. one order of magnitude larger. In both cases, the excitons are formed in excited states and the relaxation to the 1-s ground state is observed to take several tens of ps [115, 179]. This relaxation occurs via phonon emission and consequently is found to accelerate for increasing temperature [180].

Finally, the previous section (5.2) demonstrated that IGS can severely affect the dynamics of charge carriers and excitons acting as trap levels. Section 5.1 showed that, at least when both the fundamental beams are s-polarized, eSFG transitions involving IGS are observed as intermediate state eSFG resonances. These resonances can thus allow to directly address the IGS dynamics and their interplay with other electronic populations.

The next sections address the influence of these three aspects on the dynamics observed in figure 5.9, starting from the latter in section 5.3.1.

5.3.1 In-gap states dynamics

A clear signature of IGS dynamics, which as seen in section 5.2 can be as long as several µs, is visible in the pump-induced eSFG variation for s-polarized upconverting beam plotted in panel (b) of figure 5.9. The eSFG variation ΔI_{SFG} shows a non zero background at negative delays indicative, as discussed previously, of a population excited by a pump pulse reaching the sample at least one inverse of the repetition rate (25 µs) before the eSFG probe. Figure 5.10 (a) compares the background intensity I_{BG} (black), given by the sum of the static eSFG and PL spectra, with the tr-eSFG intensity at negative delays (light blue). The static eSFG response (green), to which the time-resolved eSFG intensity should converge for sufficiently long time delays when the system is fully relaxed, shows, as discussed in section 5.1, a single resonance corresponding to the exciton-polariton C. On top of this, the background intensity includes as well the PL peaks of A and B and the first LOP. The eSFG intensity at negative delays, i.e. the

Figure 5.10: (a): Comparison of the tr-eSFG spectrum at negative delays with the static spectrum and the background intensity. The discrepancy with the latter indicates the presence of excited populations surviving the inverse laser repetition rate. (b): eSFG variation for negative delays and at time-zero clearly peaks at the energy of resonance B, which is forbidden by symmetry in the static case, as schematized in (c). (d): The pump induced depletion of the IGS leaves them as available intermediate states for a double resonance with B.
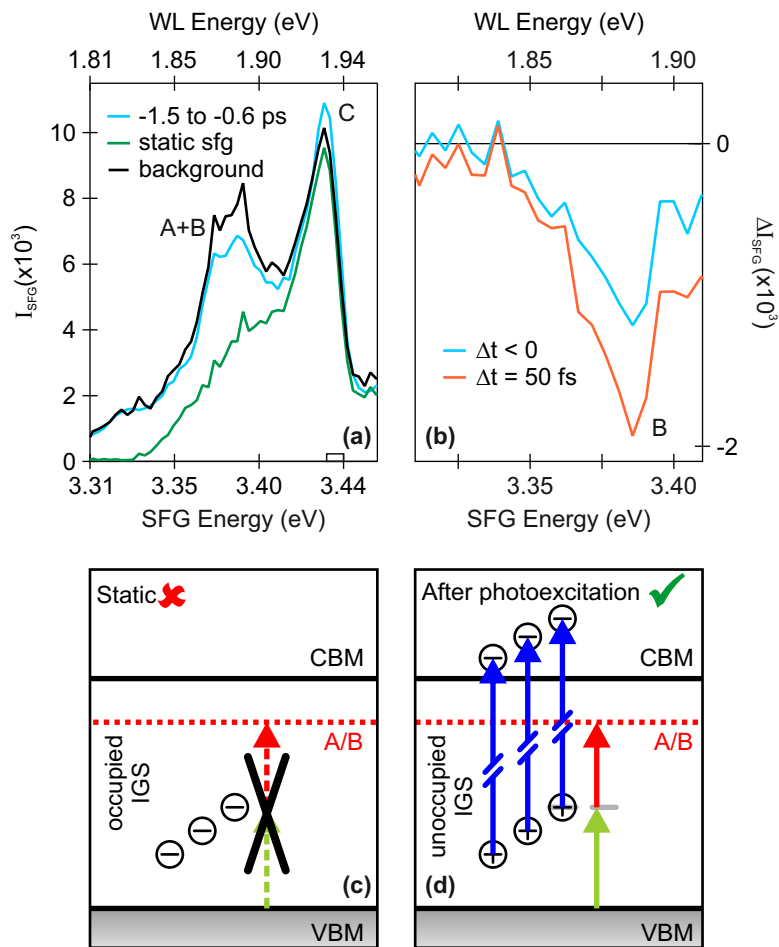
long-lived response, clearly differs from the static background for all three exciton-polariton lines, even for those which are *not* detected as static eSFG resonances. Moreover, the eSFG variation ΔI_{SFG}, i.e. the background-subtracted eSFG intensity, peaks in correspondence of the exciton-polariton B at 3.38 eV for all delays, as exemplary shown in panel (b) of figure 5.10 for time zero (50 fs, in orange) and at negative delays (light blue). Indeed, as it is visible in the black and violet kinetic traces of figure 5.9 (b), the dynamics detected at the energy of A and B are rather peculiar: the signal drops at time zero and then remains constant over the whole measurement window.

The flat and long-lived dynamics, not even fully recovering after 25 μs, are a clear signature that the A and B exciton polariton resonances are visible in the tr-eSFG spectra, contrary to the static one, thanks to a long-lived pump-induced effect that couples to them. This effect is associated with the depletion of the IGS, which couple to the exciton-polariton resonance through the mechanism illustrated in panel (c) and (d) of figure 5.10. Before photoexcitation,

panel (c), the IGS are fully occupied and the eSFG transition to the exciton-polariton A or B is blocked by symmetry. After photoexcitation, panel (d), a number of IGS is depleted by the pump-pulse and can act as intermediate SFG resonant levels. The eSFG transition to the exciton-polariton becomes an allowed *double* resonance. The observed dynamics, however, do not reflect the exciton-polariton dynamics but rather those of the defect levels.

5.3.2   Conduction band dynamics

As discussed above, all final state exciton-polariton resonances, i.e. all resonances but those discussed in the previous section, are isoenergetic to final state resonances within the CB. With the band gap energy of ZnO ranging from 3.37 eV at room temperature to 3.44 eV at low temperature [76], the excitonic resonances are at most 60 meV higher than the onset of absorption to the CB continuum. Thus, in the eSFG spectra, they overlap with the CB region where the expected predominant scattering mechanism is with acoustic phonons and the relaxation should occur on timescales of tens of picoseconds.

The kinetic traces measured at all these resonances are compared in the delay range -1 to 5 ps in figure 5.11. The figure includes the kinetic traces extracted at resonance A and B for p-polarized upconverting beam, in pink, the one extracted at resonance C for the same polarization, in light green, and two traces for resonance C measured with s-polarized beam obtained from two different data-sets and plotted in gray and light-blue respectively. These last two measurements differ in density of excited electron, being 1.5×10^{18} cm^{-3} for the gray one and 3×10^{18} cm^{-3} for the light blue, with the latter corresponding to the experiment shown in figure 5.9 (b).

All traces have been fitted with a single exponential decay multiplied by an error function which takes into account the rise of the signal at the time overlap between pump and probe pulses t_0:

$$\Delta I_{SFG} = \Theta(t - t_0) \cdot \left[M_i \cdot \exp\left(-\frac{t - t_0}{\tau}\right) + M_f \right] , \text{ with } \quad \Theta(t - t_0) = \frac{1}{2}\left[1 + \text{erf}\left(\frac{t - t_0}{\tau_p}\right)\right] \quad (5.3)$$

Here τ is the decay time of the signal and τ_p is the cross correlation of the eSFG field and the pump field. M_i and M_f are respectively the initial and final amplitude of the signal. The fits are plotted in figure 5.11 as dash-dotted lines of darker colors than the data. The time constants extracted from the fit are summarized in table 5.2.
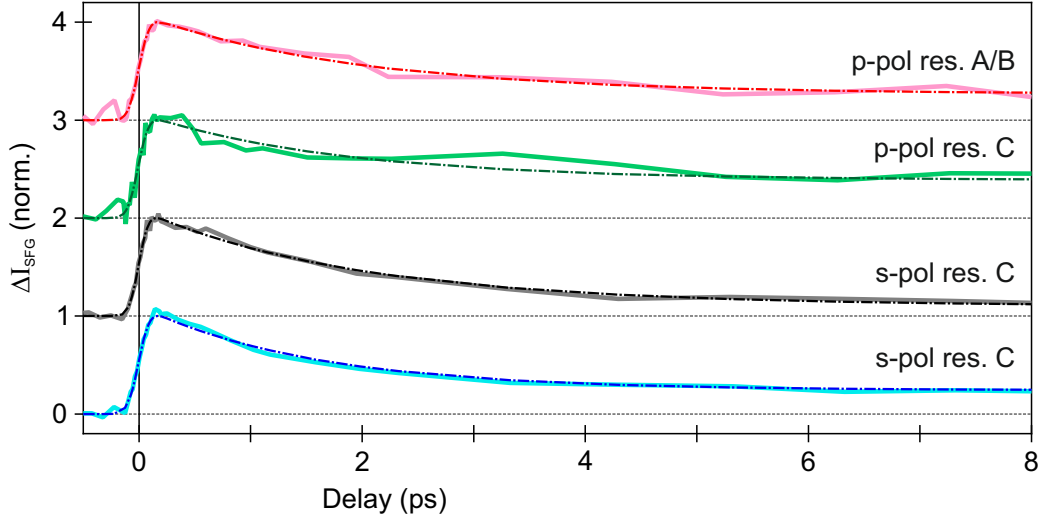
Figure 5.11: Dynamics measured at the three resonances A, B and C for different upconverting polarization. All traces are normed to 1 for clarity and have been fitted (darker lines) with a single exponential decay, obtaining similar timescales for all resonances and polarizations.

Resonance	A/B p-pol	C p-pol	C s-pol	n_e cm^{-3}
τ (ps)	2.1 ± 0.5	1.8 ± 0.6	1.9 ± 0.2	1.5×10^{18}
			1.3 ± 0.2	3×10^{18}

Table 5.2: Signal decay constants extracted from exponential fit to the data for the traces presented in figure 5.11

All resonances exhibit a comparable decay time, with the data point at higher excitation density exhibiting a slightly shorter timescale. At excited electron densities of 1.5×10^{18} cm^{-3}, all timescales range between 1.8 ps and 2.1 ps, with the slower relaxation time corresponding to the lowest energy resonance. This is in agreement with the predicted ps timescales for electron-phonon scattering, which are expected to increase for energies approaching the CB minimum. Despite exciting at energies well above the proposed energy for the transition from picosecond to femtosecond dynamics of 10 meV, no femtosecond dynamics are observed, due to the limited (160 fs) time resolution of the experiment.

Finally, the slightly faster relaxation for the higher excitation density is most probably to be attributed to an interplay of electron-phonon scattering and Auger relaxation, since the probability of the latter steeply increases for electron densities larger than 2×10^{18} to 3×10^{18} cm^{-3}
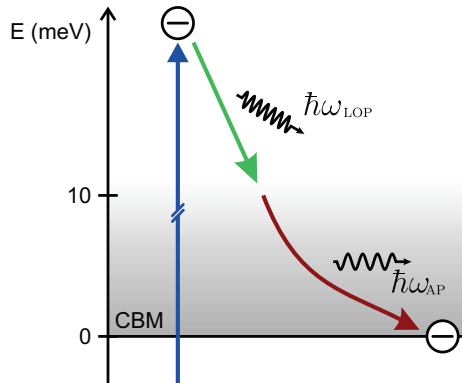
[19].

Figure 5.12: Relaxation processes in the ZnO CB at low excitation density. Electrons with excess energy above 10 meV scatter with LOPs within femtoseconds. Below this excess energy they instead scatter with AP with picoseconds relaxation timescales that increase for decreasing excess energy.

The discussed relaxation processes are summarized in figure 5.12. The electrons, excited with excess energy of 600 meV, relax to about 10 meV excess energy via emission of longitudinal optical phonons. This process, occurring on tens of femtoseconds in reference [109], cannot be resolved with the time resolution of the tr-eSFG experiment. Below this excess energy, the relaxation occurs via emission of acoustical phonons and couples to the continuum of the exciton-polariton resonances, for which relaxation timescales of 1 to 2 ps are observed.

5.3.3 Exciton formation

As mentioned in the introduction to this section, at these excited electrons densities excitons are expected to form, since the Coulomb attraction to the holes in the VB is no longer screened by the other free carriers. In ZnO, the surface exciton (SX) has been observed to form within 200 fs in a highly exited state at the non polar $(10\bar{1}0)$ surface [109], while, both on the oxygen-terminated surface and on nanowires, the luminescence transients for the SX emission show rise times on the order of several tens of picoseconds [115, 179]. This timescale difference is related to the time the excitons need to relax from the highly excited electronic states to the 1-s ground state, from which they recombine radiatively. A slightly different picture was presented by Hendry et al. for bulk excitons: their THz spectroscopy experiments show that electron and holes remain uncorrelated for most of the cooling process, i.e. the cooling occurs through the electron-hole continuum, where the uncorrelated electron and holes have, on average, no net center of mass momentum. Only after about 50 ps the imaginary part of the conductivity switches from positive to negative indicating that a fraction of the free carriers is bound into correlated excitons and at 200 ps all electron-holes pairs are bound excitons.

Clearly, light emission from the ground state is thus a sufficient but not necessary evidence for the existence of bound excitons and the emission rise-time can only give an upper limit for the exciton formation timescales. Therefore, the investigation of exciton formation requires the use of complementary techniques to PL, such as for example resonant absorption experiments, that can directly look at higher excited excitonic levels with zero momentum. If these levels become populated, i.e. excitons are formed, the transition is expected to be blocked and thus the absorption intensity to decrease. Something similar should occur for resonant eSFG, which can be interpreted as a sort of two-photon absorption process. Here, the intensity of the excion-polariton resonances is expected to decrease after exciton formation, due to the blocking of the final state SFG transition.

However, considering an exciton binding energy of 60 meV, the separation of the 1-s from the 2-s excitonic level in ZnO is about 45 meV. Thus, they cannot be distinguished with the energy resolution (66 meV) of the eSFG experiment and both contribute to the same eSFG peak. If excitons are bound in hot states that successively decay to the ground emitting level, the eSFG transients are thus expected to show the formation of excitons earlier than what is observed in tr-PL. Otherwise, if the cooling occurs in the electron-hole continuum, the timescales should coincide.

Panel (a) of figure 5.13 shows, in red, the temporal evolution of the pump-induced eSFG variation averaged over the exciton-polariton resonances A and B (3.36 to 3.4 eV) and, in blue, the variation integrated over the first LOP replica (3.29 to 3.35 eV) for the p-polarized upconverting beam. Both traces are normalized at the maximum variation of the A/B line. At this energy, after the initial fast relaxation discussed in the previous section, the eSFG intensity remains constant for approximately 70 ps after which it decreases again, , i.e. ΔI_{SFG} becomes more negative. A similar behavior is observed at the energy of the first LOP replica, where no initial dynamics are observed but only the signal decrease after about 70 ps. Radically different dynamics are visible in panel (b), which reports the pump-induced signal at the same energies as above but for the s-polarized configuration, where the eSFG does not couple directly, as final state transition, with the excitonic levels. Instead, as discussed in section 5.3.1, A and B are only observed in the tr-eSFG as a consequence of the pump-induced change in the IGS population. Thus, their transients are expected to be dominated by the IGS dynamics. However, after the initial step-like dynamics associated with IGS depletion, a steep *rise* is observed around 100 to
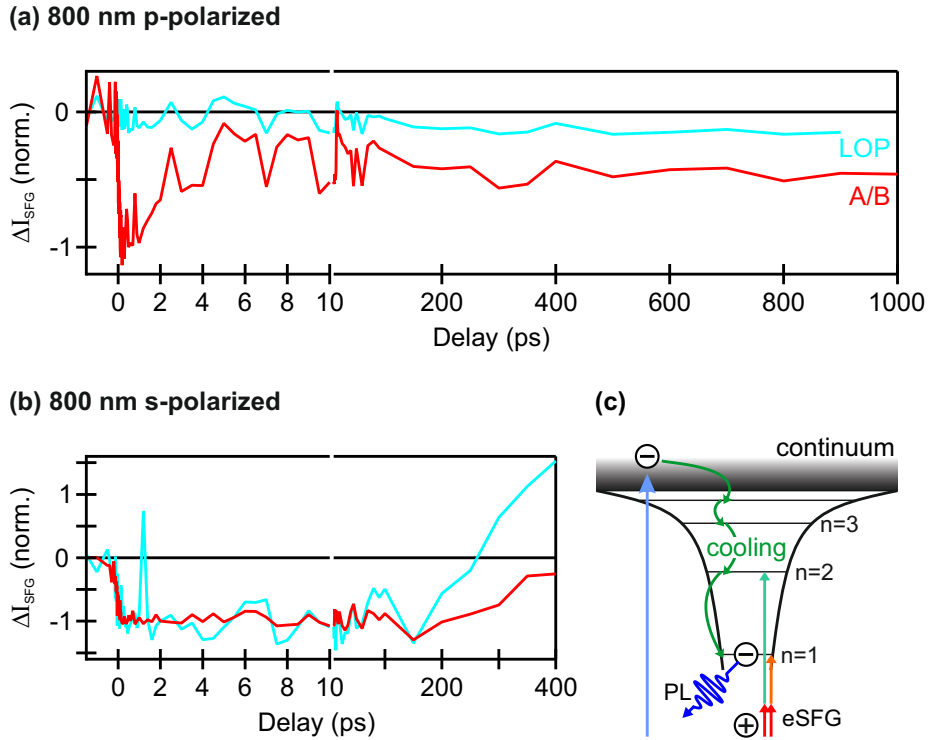
Figure 5.13: (a) Pump-induced eSFG variation for p-polarized upconverting beam integrated over the energy of the A and B exciton-polariton (red) and of the first LOP replica (blue). In both energy regions the eSFG intensity decreases around 70 ps, indicative of exciton formation. (b) tr-eSFG transients for s-polarized upconverting beam, where the intensity increases for long time delays. These increase is interpreted as the onset of stimulated emission (see text.) (c) Exciton relaxation processes. After photoexcitation, charge carrier cooling occurs through the e-h continuum until bound excitons of quantum number $n > 1$ are formed. These excitons can be probed by eSFG. Only excitons in n=1 recombine radiatively and are probed by PL

200 ps for both the energy of the exciton-polaritons and of the first LOP replica, which variation even changes from negative to positive. The low signal to noise ratio, unfortunately, does not allow to extract quantitative values for the rise time of these late dynamics in either of the two polarization combinations.

In order to get a deeper insight in the origin of the signal rise in the s-polarization, figure 5.14 depicts the spectral shape of this signal variation. The spectrum at time zero (orange), previously discussed in figure 5.10, shows the peak correspondent to the exciton-polariton B that arises as double eSFG resonance involving the IGS.

At long positive delays (400 ps - violet trace) the eSFG variation ΔI_{SFG} becomes less negative

Figure 5.14: (*Top*) Comparison of the eSFG variation at 50 fs and at 400 ps. At long positive delays, a positive variation of eSFG intensity is clearly detected over the energy range of excitonic emission. (*Bottom*) Difference between the eSFG variation at long positive delays and at time zero compared with the luminescence spectrum. Both traces are normalized at maximum and evidently show the same spectral shape, indicative of stimulated emission due to the presence of the eSFG photons.
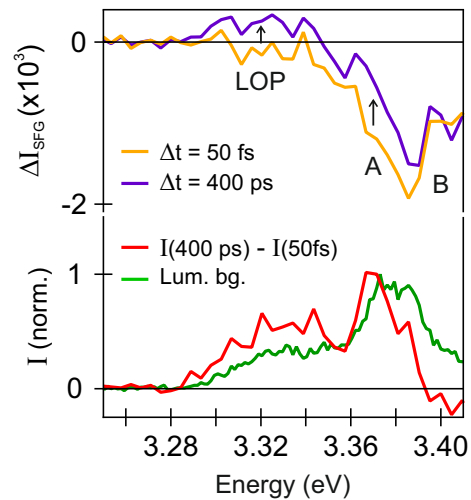
at the energy of resonance A and positive at the energy of the LOP. Subtraction of the first from the latter leads to the red curve in the bottom panel, showing a narrower peak centered at 3.37 eV and a broader one at 3.2 eV. This spectral shape coincides with the one of the static PL spectrum, shown in green for comparison, suggesting that the signal variation observed in the s-polarized tr-eSFG spectrum is not related to a variation of the eSFG intensity but rather to an increase in photoluminescence. Luminescence, however, is a spontaneous process and therefore its detection is not time-resolved in a common pump-probe scheme, where it usually appears as a constant background. Other methods, such as gating with another synchronized pulse or time-correlated single photon counting, are required to measure PL transients. Here, the gating is naturally provided by the presence of the eSFG photons, which trigger stimulated light emission. The process can be understood as follows: the ultraviolet (UV) eSFG photons, generated either non-resonantly or double resonantly by involvement of IGS, can induce the radiative decay of excitons in the $n = 0$ level, as soon as it is populated. This is no longer a spontaneous effect and consequently the exciton formation is resolved in time.

Thus, even though only qualitatively, eSFG allows to detect the exciton formation in ZnO. The findings are summarized in panel (c) of figure 5.13. Just after photoexcitation the electron-hole cooling occurs partially through the continuum and at about 70 ps bound excitons are formed and lead to a decrease of the eSFG resonance. The excitons further cool down to the $n = 0$ state and, at about 100 to 200 ps, the onset of stimulated emission is observed. Thus the cooling mechanism proposed is neither a "hot exciton cascade", i.e. with the electron and holes as correlated quasi particle, nor fully through the electron-hole continuum. Instead it

involves the creation of excitons with zero momentum but higher electronic quantum number. Nevertheless, all timescales are in good agreement with those reported by Hendry et al. for the bulk exciton of ZnO [19].

5.4 Summary and discussion

Multiple linear and non-linear time-resolved optical techniques have been used to investigate the charge carrier and exciton dynamics in ZnO, after excitation across the optical band gap at 3.6 eV and 4.1 eV. The role of IGS in the charge carrier and exciton relaxation has been addressed by comparison of a ZnO single crystal and a MBE grown thin film. In both samples, photoluminescence spectroscopy identifies excitonic emission centered at 3.36 eV, with clear vibronic replicas, with a separation compatible with the literature value of the longitudinal optical phonons energy of 71 meV and 72 meV. Furthermore, a defect band in the energy range between 1.7 eV and 2.7 eV has been observed.

The dynamics of these in-gap states dominate the early-time transmission changes at photon energies in the visible range. After photoexcitation with densities above the Mott density, the samples become more transparent, indicating a depletion of the defect levels, which can no longer absorb visible light. The induced transparency exhibits multiexponential decay, related to the trapping of the charge carriers by at least two different kinds of defect states. The single crystal, which among the two samples shows the higher defect to exciton emission ratio, also exhibits faster recombination rates, due to the larger defect density. Once a sufficient number of defects has been repopulated, a sign change of the sample response is observed, due to the predominance of light absorption from electrons in the conduction band. The MBE film also shows fast (1–2 ps) charge carrier relaxation dynamics in CB and VB, which, due to the high electron densities, are attributed to many-body electron-electron scattering events, such as for example Auger recombination. The equilibrium population is restored by radiative recombination of both charge carriers and IGS on nanosecond to microsecond timescales.

Electronic sum-frequency generation spectra show two resonances that depend on the polarization of the upconverting 800 nm beam. For electric field parallel to the incidence plane, i.e. p-polarized light, eSFG detects a narrow resonance centered at 3.43 eV and a broad one at 3.37 eV. For s-polarized light, the first is the only resonance observed. The electric field configu-

rations and the energy positions are compatible with earlier absorption measurements [87] and the resonances are accordingly assigned to the A, B and C exciton-polaritons associated with the split ZnO valence bands. Furthermore, the s-polarized configuration couples more strongly with IGS, which act as intermediate SFG resonances and are detected at energies higher than 3.45 eV. Since it directly couples to excitons and IGS, tr-eSFG is used to investigate if, and how, IGS affect exciton dynamics and to determine the rates of exciton formation and relaxation pathways.

After photoexcitation with densities of $1.5 \times 10^{18} \, \text{cm}^{-3}$ and $3 \times 10^{18} \, \text{cm}^{-3}$, i.e. below and equal to the nominal Mott density, all A,B and C exciton-polaritons exhibit initial fast dynamics on a 1.8 to 2 ps timescale that increases with decreasing energy, i.e. approaching the bottom of the CB, which are attributed to the initial relaxation of charge carriers in the conduction and valence bands. At these lower excitation densities, Auger recombination rates decrease and the decay is rather assigned to the relaxation of the carriers to the band edges via scattering with acoustic phonons, in agreement with the calculations from reference [110]. For the slightly higher excitation density, electron-electron scattering probabilities increase and the relaxation timescale is observed to decrease.

As intermediate states for eSFG resonances, IGS lead to a *double* resonance with the exciton-polaritons A and B even for the s-polarization, for which they are forbidden by symmetry in the static spectrum. The dynamics observed at these energies, though, are mainly related to IGS dynamics and are compatible with the IGS response seen in the PL at high fluences.

Finally, excitons are formed on a 70 ps timescale in higher electronic excited states, leading to a decrease of the direct eSFG transition to the exciton-polariton and at the energy of the first LOP replica. Once the exciton has cooled to the 1-s ground state, within 100 to 200 ps, the presence of the UV eSFG photons results in stimulated emission, which is observed as an increase of the intensity at energies corresponding to the A and B exciton-polaritons and to the phonon replica.

The exciton formation mechanism proposed is thus the following: after photoexcitation electron-hole cooling occurs mostly in the uncorrelated continuum by scattering with acoustic phonons, in agreement with reference [19]. However, bound excitons are not directly formed in the lowest state, but rather in higher electronic excited states from which they further cool to $n = 1$.

These results identify IGS as the main energy loss channel in ZnO, not only affecting the charge carrier dynamics but also the optical properties of the material. Their presence thus turns out to be detrimental for any possible optoelectronic application that uses ZnO either as a near UV emitter or as an electrode. Therefore, the control and minimization of IGS densities in the crystal growth is a fundamental step towards the realization of efficient ZnO-based devices. Moreover, the probability of charge trapping by IGS depends on the square of the excitation density since absorption of a photon is required to create the free carrier in the CB and of another to deplete the IGS, before trapping can occur. Consequently, and contrary to the common expectation, a reduction of the excitation density should lead to higher device efficiency.

6. A tale of two states
The influence of long-lived excited states on charge separation at the SP6/ZnO(10$\bar{1}$0) interface

While the functionality of a hybrid semiconducting system is typically determined by the interfacial properties, its efficiency is also strongly dependent on energy relaxation processes occurring in the bulk of the semiconductor, which lead to energy dissipation and decrease energy or charge transfer rates across the interface. These processes include for example intramolecular vibrational relaxation (IVR), (radiative) decay to the electronic ground state, transfer to long-lived triplet states via intersystem crossing (ISC) and exciton diffusion to or away from the interface. They are investigated in this chapter for the model hybrid inorganic organic system formed by the spirobifluorene derivative 2,7-bis(biphenyl-4-yl)-2',7'-ditertbutyl-9,9'-spirobifluorene (SP6) and ZnO by time-resolved excited state transmission (tr-EST) and photoluminescence (PL) spectroscopy. These complementary experiments allow the disentanglement of the multiple relaxation processes that follow exciton formation in the organic dye and compete with charge separation (CS) at the ZnO interface. Within 1 to 2 ps after photoexcitation, IVR leads to the population of two long-lived states localized on the two π-systems of SP6: a singlet exciton X_{6P} and an intramolecular charge-transfer exciton X_{2P}. Additionally, ISC to a triplet state X_T with microsecond lifetime is identified as an efficient relaxation channel. Comparison of the excited state dynamics of SP6 in the hybrid system (sec. 6.1) with those on an inert substrate (sec. 6.2) reveals that only the X_{6P} population is affected by CS to ZnO, most probably due to a longer exciton diffusion length. Also, only X_{6P} excitons radiatively recombine and the PL spectrum coincides with the one of sexiphenyl (6P), strongly suggesting that this lowest energy excited state is localized in the sexiphenyl backbone (sec. 6.3). The X_{2P} population, on the contrary, decays only by ISC. Thus, the formation of X_{2P} constitutes the largest loss channel in the hybrid inorganic organic system (HIOS). The CS efficiency can be calculated from the difference in PL intensity on both subtrate and, for the thick films investigated, is found to decrease with increasing temperature due to the arising of competing decay channels that reduce the diffusion length (sec. 6.4).

6.1   Excited state dynamics at the hybrid SP6/ZnO interface

Section 1.4 presented the hybrid system formed by 2,7-bis(biphenyl-4-yl)-2',7'-ditertbutyl-9,9'-spirobifluorene (SP6) and ZnO as a candidate model hybrid inorganic organic system (HIOS). The molecular dye is characterized by a high emission yield, showing even stimulated emission for sufficient excitation densities [6], and forms a type II energy level alignment with the non polar ($10\bar{1}0$) surface of ZnO [7, 8]. Blumstengel and coworkers have demonstrated that this energy level alignment favors the electron separation from a molecular electronic excited state to the conduction band of ZnO, with transfer times that can become as short as 10 ps but are limited by the exciton diffusion rate to the ZnO surface [7]. Fitting the charge separation (CS) efficiencies extracted from time-resolved photoluminescence (tr-PL) experiments as a function of layer thickness and temperature with a linear diffusion model, they extract an exciton diffusion length of 10 nm at room temperature and an S_1 lifetime of 300 ps.

The first step towards a deeper understanding of the relevant energy coupling and loss mechanisms in the hybrid system is the characterization of the lifetime and dynamics of the population in the electronic excited states and the comparison with those of the semiconducting compounds when taken separately. Efficient charge separation at the SP6/ZnO interface is possible only if the probabilities of the multiple exciton relaxation pathways in the bulk of the organic layer are balanced favorably. In other words, the excitons generated at the surface of the molecular layer need to reach the interface with ZnO and charge separate before they decay via other channels or get trapped. To get an insight into the mechanisms that compete with charge separation and determine its efficiency, therefore, requires the direct measurement of the excited state and diffusion dynamics in the bulk of thick films. This is achievable by the combination of complementary static and time-resolved linear optical spectroscopies, such as photoluminescence (PL) and time-resolved excited state transmission (tr-EST) (see sec. 3.1). After resonant photoexcitation of the system and consequent population of the electronic excited states, the former addresses the radiative recombination from the lowest excited state into the ground state, while the latter monitors the transitions to higher excited states, as a function of pump-probe delay. This first section of the chapter reports tr-EST experiments performed on a 20 nm film deposited on the non polar surface of a ZnO single crystal and, for comparison, on a 25 nm film deposited on an inert glass substrate. The sample preparation is described in detail

in section 3.3. The experiments, unless otherwise stated, have been performed in the optical cryostat (Oxford instruments Optistat CF-V, section 3.4) with a base pressure of $\sim 10^{-6}$ mbar, cooling down the sample to 100 K with liquid nitrogen.

SP6 was excited with photon energies of 3.7 eV, slightly above the absorption maximum, while probing with the white-light continuum (WLC), which is resonant to higher excited state transitions, such as $S_1 \rightarrow S_2$ or $T_1 \rightarrow T_2$. The experiments have been performed at a repetition rate of 200 kHz. Due to the very low pump-induced transmission change, the transmitted white-light beam is filtered with bandpass filters of 10 nm width in the 540 to 700 nm range and detected with a lock-in amplifier. To avoid photo damage, the maximum photon energy is kept to 0.15 nJ per pulse. At 3.7 eV the absorption coefficient of SP6 is $\alpha_{SP6} = 4 \times 10^5$ cm^{-1} and 40 % of the incident intensity is absorbed in the 20 nm film, resulting in an average of 1.8×10^{18} photons /cm^3 absorbed per pulse. Considering a molecular density of 1.15×10^{21} molecules/cm^3, 0.1 to 0.2 % of the molecules are photoexcited.
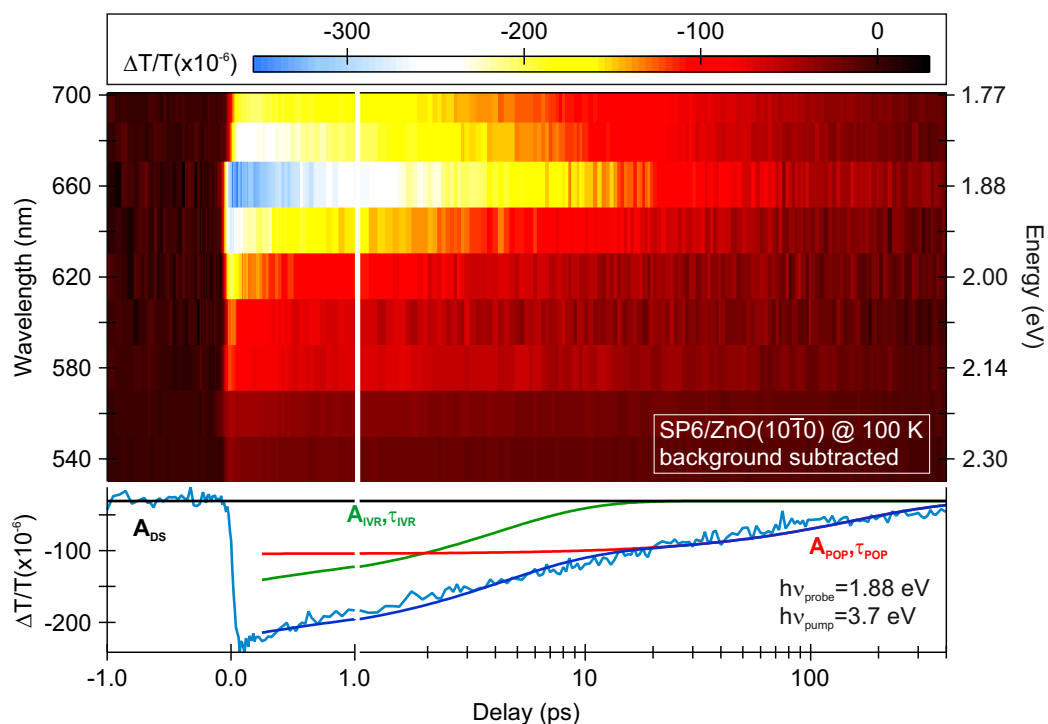
Figure 6.1: False color plot of the background subtracted transient excited state transmission of a 20 nm film of SP6 on ZnO . Please note the logarithmic x-axis in the range from 1 to 400 ps. Below: Transmission change at 660 nm (1.94 eV) in light blue. Dark blue: Double exponential fit. Green: fast component. Red: Slow component. Black: baseline

The top panel of figure 6.1 shows a background-subtracted false color plot of the excited state transmission of SP6 on ZnO after photoexcitation, versus pump-probe delay (x-axis) and central wavelength of the color filters (left y-axis, corresponding energy on the right y-axis). Note the split x-axis: linear in the -1 to $1\,\text{ps}$ range and logarithmic from 1 to $400\,\text{ps}$.

At the time of overlap between the pump and the probe pulse, the signal abruptly drops in the whole measured wavelength range, with a distinct maximum pump-induced change at $640\,\text{nm}$ $(1.94\,\text{eV})$. This drop in intensity is indicative of the onset of excited state absorption (ESA) across the $S_1 \rightarrow S_2$ transition, which then decays double exponentially for positive time delays. The relaxation dynamics are analyzed separately for every probe wavelength. The bottom panel of figure 6.1 exemplary shows the normalized change of transmission $\Delta T/T$ probed at $660\,\text{nm}$ $(1.88\,\text{eV})$. The whole trace is offset by a negative constant amplitude A_{DS} at negative time delays, which, as discussed in section 3.1, is indicative of an excited state absorption (ESA) lasting longer than the inverse of the laser repetition rate, $5\,\mu\text{s}$. The origin of this ESA is discussed in more detail below. At early time delays, 0 to $250\,\text{fs}$, the electric field of pump and probe pulse temporally overlap on the sample and generate coherent electronic polarizations which, due to the complex structure of the WLC, interfere with each other [181]. This time and frequency-dependent interference pattern is reflected in the so-called coherent artifacts, as discussed in section 2.2.2. Therefore, the recovery of the excited state transmission (EST) is fitted with an empirical double exponential decay starting at $\Delta t = 250\,\text{fs}$, where we can assume the coherences to have decayed and the amplitude of the signal to be related only to the oscillator strength of the transition and the evolution of the excited state population distribution[1]. The summands of the empirical fit function

$$\frac{\Delta T}{T} = A_{IVR} \cdot e^{-(t-t_0)/\tau_{IVR}} + A_{POP} \cdot e^{-(t-t_0)/\tau_{POP}} + A_{DS} \tag{6.1}$$

are plotted in the bottom panel of figure 6.1 together with the overall fit. A_{IVR} and τ_{IVR}, in green, are respectively the amplitude and the time constant of the fast decay component. A_{POP} and τ_{POP}, in red, those of the slow decay and A_{DS}, in black, the amplitude of the offset at negative delays, which is determined independently of the fit.

Figure 6.2 shows the fit results for the fast exponential recovery as a function of probe photon energy (bottom axis) or wavelength (top). The fit amplitude A_{IVR} is plotted in panel (a),

---

[1] According to the discussion in section 2.2.1, for dephasing times at least one order of magnitude shorter than the recombination times, this approach introduces an error of about $1\,\%$ in the extracted decay times.
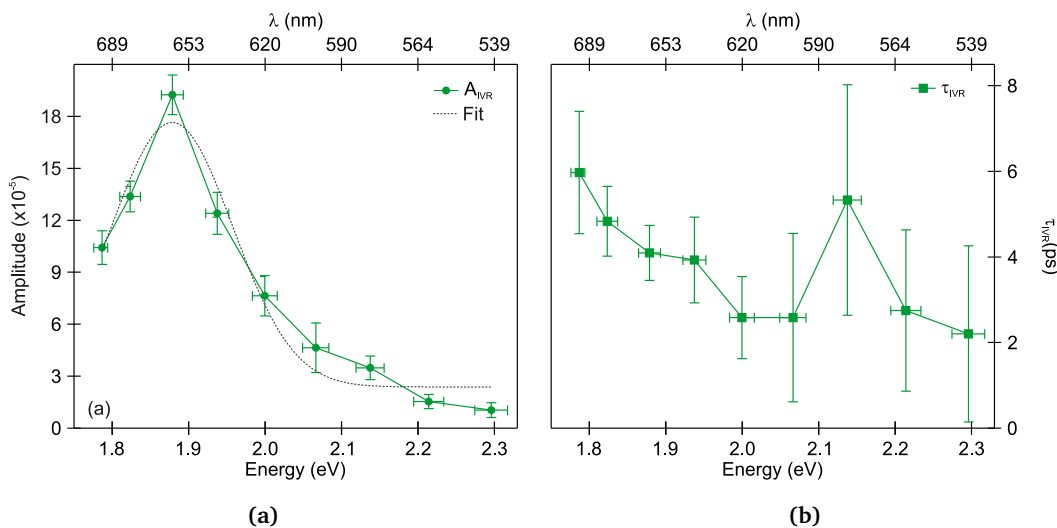
Figure 6.2: Fit results for the fast exponential recovery as a function of probe photon energy. (a) The amplitude exhibits a broad resonance centered at 1.85 nm. (b) The time constant is strongly dependent on the probe photon energy and ranges from 6 to 2 ps.

while the time constant τ_{IVR} in (b). The amplitude shows a broad energy distribution and a Gaussian fit (gray dashed line) yields a maximum energy of (1.87 ± 0.05) eV. The time constant strongly depends on the probe photon energy: it spans from 2 ± 2 to 6 ± 2 ps, becoming faster for higher resonance energies. This fast exponential recovery characterizes the response of the sample shortly after the pump laser has populated the first electronic excited state by vertical projection of the ground state population, within the bandwidth of the pump pulse. The lifetime measured in an optical experiment, where the probe photons are mapping vertical transitions in the potential energy landscape, is related to the population distribution in the initial state of the transition. Thus, a broad amplitude distribution and a strongly energy dependent lifetime are indicative of a population spread over multiple levels that relaxes to the bottom of the multiplicity, such as an initially vibronically excited electronic population undergoing intramolecular vibrational relaxation (IVR).

The fit parameters of the slow exponential recovery are plotted in figure 6.3. Panel (a) shows the amplitude A_{POP} and panel (b) the time constant τ_{POP}. The amplitude distribution is narrower and has a clear double peak structure with maxima at (1.85 ± 0.03) eV and (2.12 ± 0.03) eV, labeled respectively X_{6P} and X_{2P} for reasons that will become clear in section 6.3, separated by (270 ± 60) meV. The time constants show a similar energy dependence,
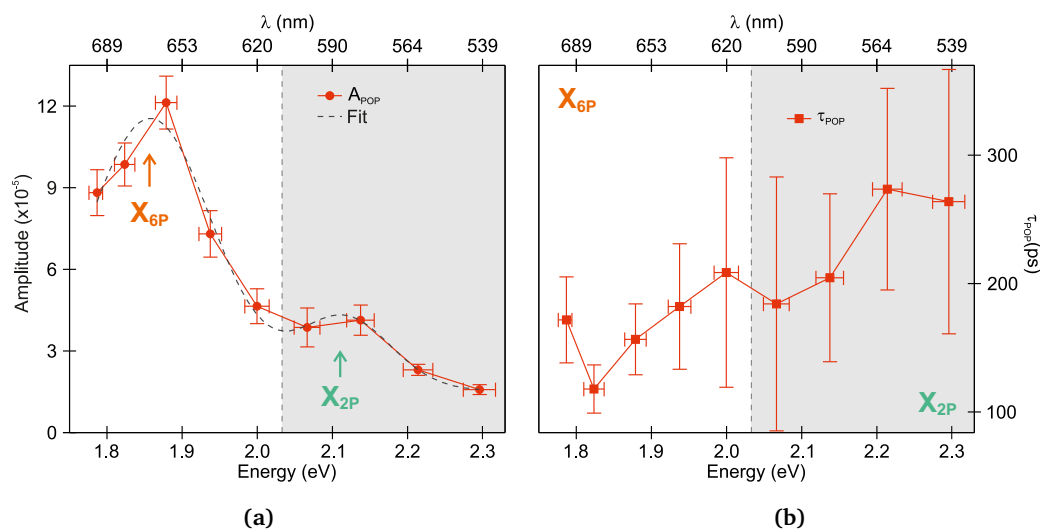
Figure 6.3: Fit results for the slow exponential recovery as a function of probe photon energy. (a) Two clear resonances are visible in the energy dependence of the amplitude. (b) The resonances show clearly distinct time constants.

with the two resonances having two clearly distinct lifetimes of (140 ± 30) ps for X_{6P} and (230 ± 50) ps for X_{2P}. Both lifetimes are on the order of magnitude of the S_1 lifetime of 300 ps estimated for an isolated molecule in reference [7]. As discussed above, the timescales measured in a tr-EST experiment depend directly on the population of the initial state of the transition and two resonances having different time constants must originate from two distinct initial levels, i.e. they must map two different electronic or vibrational populations.

Regardless of their origin, these excited state populations can decay via multiple pathways of given probability. Charge separation to the ZnO , with a rate limited by the diffusion of the excitons to the interface, and luminescence have been identified as an efficient decay channels in this system by reference [7], as discussed above.

Additionally, the presence of a pump-induced, non-zero offset at negative delays points at the formation of a very long-lived excitation. This excitation has been generated by a pump pulse perturbing the sample at least one inverse of the repetition rate before the probe is interacting with it. In other words, working at 200 kHz, the excitation was generated at least 5 μs before it was probed. Therefore, this long-lived excitation has to be a so-called dark state, i.e. an excited state that does not decay radiatively, such as a charge transfer exciton or a triplet state, formed via intersystem crossing (ISC) from X_{6P} and X_{2P}. Figure 6.4 shows the amplitude

of the baseline at negative delays for the different probe photon energies, on the bottom axis, or wavelengths, on the top axis. Similar to the slow exponential recovery term, this amplitude peaks at 1.94 eV (corresponding to 640 nm). The magnitude A_{DS} is comparable to A_{IVR} and A_{POP}, which suggests that ISC is a competitive process to luminescence and charge separation. With a radiative lifetime estimated to be on the order on hundreds of ps (see section 1.4 and references [7, 8]), an upper limit for the intersystem crossing (ISC) timescale can be set to hundreds of ps as well.

Figure 6.4: Baseline amplitude as a function of probe photon energy (top) or wavelength (bottom).

Photoemission studies performed on this interface in our group show that the signature of this long-lived state is only reduced when tuning the laser to 40 kHz, corresponding to a lifetime of 25 μs [173]. Moreover, these experiments, individuate a relevant contribution of triplet-triplet annihilation to the photoelectron dynamics. This implies that, in the experiments presented here, the baseline at negative delays is a signature of a quasi stationary contribution that accumulates over multiple pulse trains and that it most probably originates from a triplet state population with microsecond lifetime, labeled X_T in the following.

The analysis of the amplitudes and decay constants gives a complete picture of the relaxation processes at the hybrid SP6/ZnO ($10\bar{1}0$) interface, which are summarized in figure 6.5. Photoexcitation projects an electronic population from the electronic ground state to highly excited states. This vibrationally excited electronic population relaxes via intramolecular vibrational relaxation in 2 to 6 ps, as indicated by the green arrow. Once the population is relaxed, two long-lived ESA resonances are observed, named X_{6P} and X_{2P}, both with a lifetime on the order of the S_1 literature lifetime [7]. This two resonances originate from two distinct excited states, since they have clearly different decay times of 140 ps and 230 ps. The electronic population in these levels can decay via multiple pathways. On one hand the measurements presented here directly detect the occurrence of intersystem crossing (ISC), black arrow, as an efficient decay channel, as discussed above. On the other hand, reference [7] indicates both lumines-
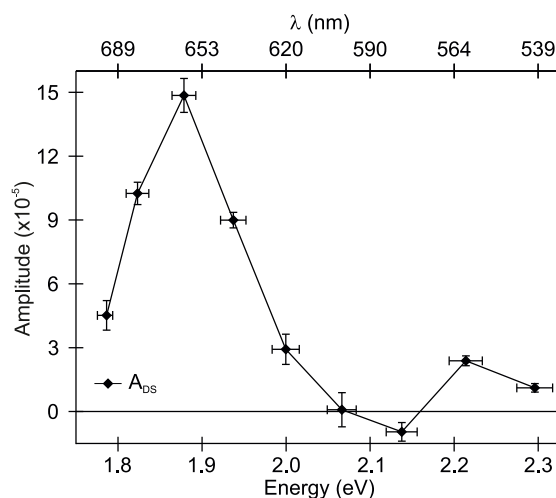
cence (blue arrow) and charge separation (red arrow) at the hybrid interface as relevant decay pathways in this system.

Figure 6.5: Competing elementary relaxation processes at the SP6/ZnO (10$\bar{1}$0) interface after photoexcitation: Intramolecular vibrational relaxation (IVR, 2–6 ps) to two long-lived excited states X_{6P} and X_{2P}, radiative recombination (PL) to the ground state ($\sim$300 ps from Ref. [7]), intersystem crossing (ISC, hundreds of ps) and charge separation to the ZnO (diffusion limited from Ref. [7]).
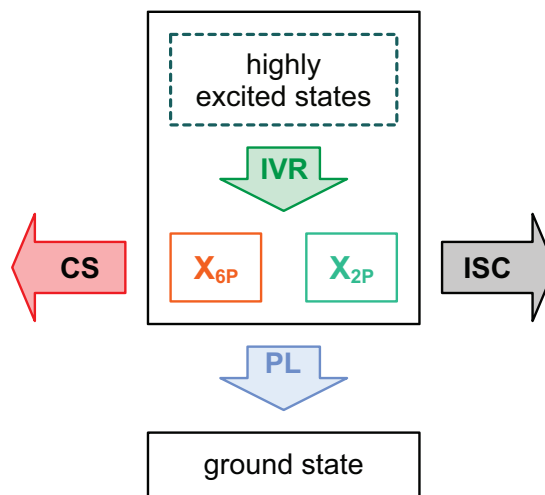
6.2 Tuning the balance of elementary relaxation processes: The role of the interface

Direct determination of the relevance of one specific relaxation pathway with respect to the others in optical spectroscopy is complicated by the fact that, even assuming the recovery of the excited state transmission to be directly related to a decay of the population in the electronic excited state of the molecule, the decay rates of the multiple pathways sum up in one overall decay rate. Disentanglement of the contributions is made possible by a modification of the balance of the relaxation processes in a targeted way. For example, CS at the interface could be avoided by a change of the substrate, such that type I energy level alignment is achieved, i.e. the first excited state lies within the band gap of ZnO. This can be realized by substitution of ZnO with a microscope cover glass. If charge separation to the ZnO is indeed a competitive process at this interface, thus occurring on time scales comparable or even shorter than the other relaxation channels, the life time for the population in the excited states is expected to increase when charge separation is switched off.

Repetition of the transient transmission experiments for all probe wavelengths with the 25 nm thick SP6 layer deposited on glass yields qualitatively similar dynamics to those obtained on ZnO. Figure 6.6 shows the background subtracted pump-induced transmission change as a
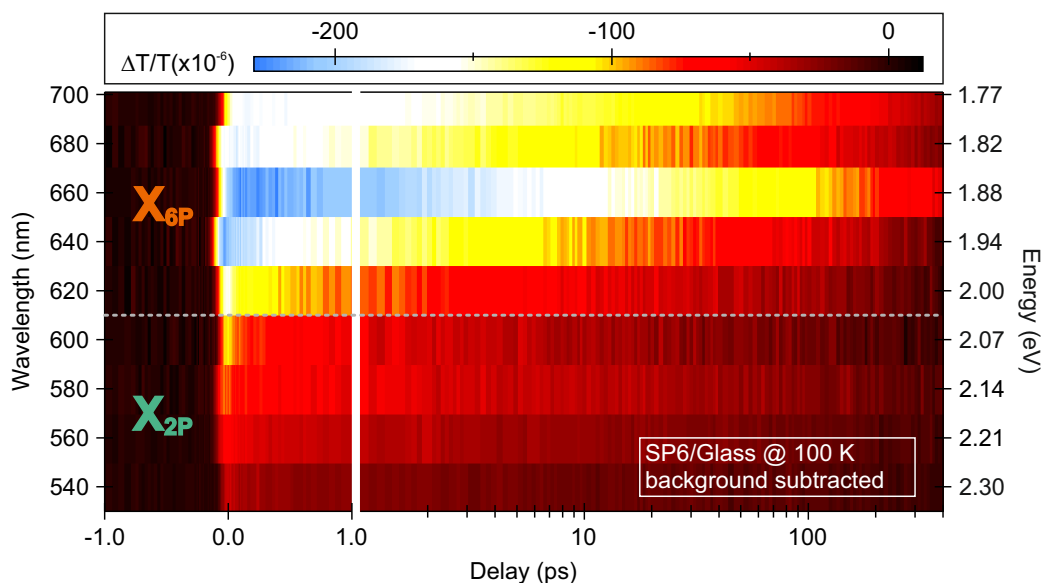
Figure 6.6: False color plot of the background-subtracted transient excited state transmission of a 25 nm film of SP6 on glass. Note the logarithmic x-axis in the range from 1 to 400 ps. The orange and light green rectangles indicate the energy region of resonance A and B, respectively. Compared to figure 6.1, resonance A clearly shows a longer lifetime.

function of probe wavelength (left axis) and photon energy (right) and of pump-probe delay (bottom). Again, note the logarithmic delay axis from 1 to 400 ps. As for the hybrid interface, the transmission drops abruptly at time zero and recovers double exponentially. Furthermore, the background at negative delays, indicative of the existence of a long-lived excited state, is also observed. The energy regions of the X_{6P} and X_{2P} resonance are separated by the dashed line. A qualitative comparison of this figure with figure 6.1 evidently reveals that the X_{6P} resonance lives longer on glass. This observation is in agreement with what is expected if charge separation occurs at the SP6/ZnO interface. In a rate equation picture, the lack of the CS decay channel on glass removes an addend from the exponent denominator, making the decay rate smaller and therefore the lifetime longer.

A systematic fit to the transmission traces at every probe photon energy with equation (6.1) results in a full set of fit parameters for the amplitudes and the decay times that can be compared to the one of section 6.1 and allows to extract the relative importance of charge separation among the relaxation pathways in the dye. The obtained amplitudes A_{IVR}, A_{POP} and A_{DS} show the same energy dependence as on ZnO and have a comparable magnitude. The time constants
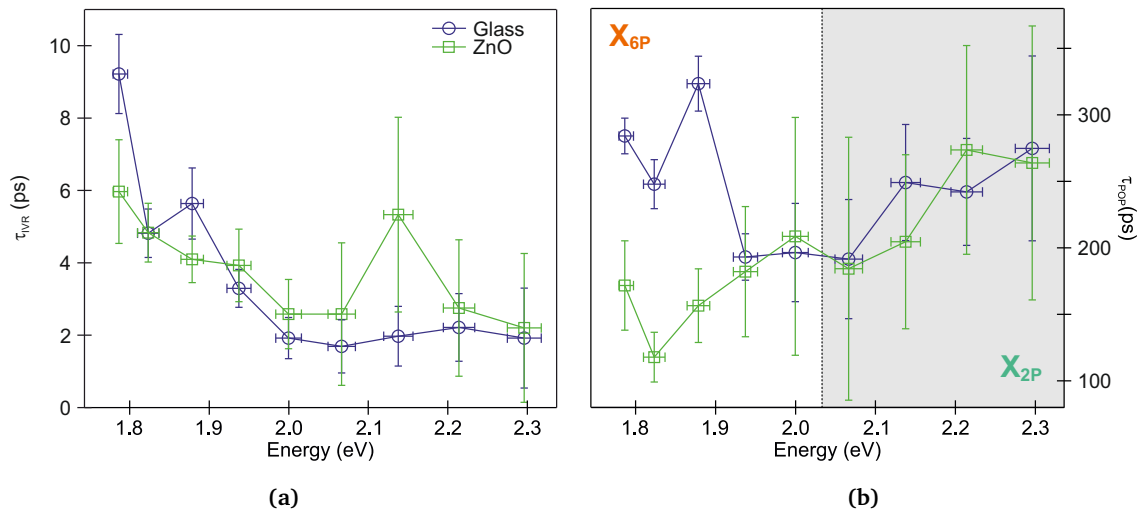
Figure 6.7: Comparison of the time constants for exciton decay in SP6 on glass (blue) and on ZnO (green). (a) intramolecular vibrational relaxation. (b) S_1 population decay resulting from luminescence and intersystem crossing. Charge separation at the hybrid interface strongly reduces the lifetime of resonance A but leaves resonance B unaffected.

τ_{IVR} and τ_{POP} are compared to those on ZnO in figure 6.7. Panel (a) depicts the fast relaxation time constant τ_{IVR} for SP6 on glass, in blue, and on ZnO $(10\bar{1}0)$, in green, as a function of probe photon energy. Indubitably, this fast time scale is not affected by the change of substrate. On the other hand, panel (b) evidences that changing the substrate to an insulating one leads to an increase in lifetime of the X_{6P} resonance, as qualitatively remarked for figure 6.6. The fit results in a lifetime of (250 ± 30) ps, compared with the 140 ps observed on ZnO. Remarkably, however, the lifetime of the X_{2P} resonance remains unaffected, being (230 ± 50) ps.

As far as IVR is concerned, its substrate independence is consistent with the diffusion limited charge separation scenario presented in [7]. Diffusion occurs on a much slower timescale and thus cannot compete with IVR. Furthermore, although these are bulk sensitive transmission measurements, almost 50 % of the light intensity is absorbed in the first 10 nm of the film which, in turn, dominate the signal. As a consequence, the eventual small increase in the time constant due to the thin layer adjacent to the interface is buried in the rather large error bars of the analysis.

In the case of the X_{6P} resonance, interfacial charge separation can indeed compete with luminescence and ISC and this is reflected in the shorter lifetime observed on ZnO. The X_{6P}

excitons diffuse to the interface and charge separate. A first estimate of an average time constant for the diffusion of (300 ± 100) ps, thus on the same order of magnitude than the lifetime of the state, can be given from the difference in time constants extracted on the ZnO and on the glass substrate

$$\frac{1}{\tau_{POP}(Glass)} - \frac{1}{\tau_{POP}(\text{ZnO})} = \frac{1}{\tau_{DIFF}} \quad . \tag{6.2}$$

It is remarkable that the charge separation decay channel is open only for X_{6P} excitons, without affecting X_{2P} excitons. Indeed, as mentioned in section 1.4 and at the beginning of this chapter, charge transfer was found to be limited by exciton diffusion to the interface and, as long as the excited state is resonant with the conduction band (CB), to be extremely efficient for excitons that are sufficiently close to the interface [7]. From this, clearly, there are two possible reasons to explain the absence of CS signatures for the X_{2P} population: either the state is energetically *not* resonant with the CB or the diffusion length for excitons in this level is too short for them to reach the interface. Either way, the formation of X_{2P} population represents an important loss channel for the CS process.

Summarizing, tr-EST experiments reveal, after a fast intramolecular vibrational relaxation (IVR), the formation of two excited states with picosecond lifetime, labeled X_{6P} and X_{2P}. Furthermore, a triplet state X_T with nanosecond lifetime is efficiently formed via ISC. CS to the ZnO CB, which was indicated as an efficient relaxation channel in reference [7], has been confirmed *only* for the X_{6P} population, while the dynamics of X_{2P} are unaffected by the change of substrate. Since Blumstengel et al. [7] observed the signatures of CS in the tr-PL spectra, the next session investigates more deeply the emission properties of the films, in order to gain further insight in the nature of state X_{6P} and X_{2P}.

6.3   The nature of the excited states: emission properties

State X_{6P} and X_{2P} can have several origins:

1. They could actually be the same SP6 electronic state but located in two kind of molecules that differ by a slight chemical or morphological modification occurred during sublimation. This scenario was ruled out by the proton nuclear magnetic resonance (NMR) experiments presented in section 3.3, which exhibited no difference in the position of the peaks for previously sublimated and non-sublimated molecules when compared to the theoretical spectrum [173].

2. X_{6P} and X_{2P} could belong to two different spin multiplicities, i.e. one is a singlet and the other a triplet exciton. This scenario can be excluded due to the comparable lifetime of the two states, with neither of them being comparable with the much longer lifetime observed for the triplet.

3. The molecules could aggregate upon deposition. While the three-dimensional shape of SP6 and the high density of the films should prevent the formation of extended aggregate chains, smaller dimers or multimers cannot be excluded. As discussed in section 1.1.2, molecular aggregates exhibit clear spectral signatures in the absorption and emission spectra. J-aggregates have blue-shifted emission with respect to the monomer and their spectra are characterized by a very narrow 0-0 line. The emission of H-aggregates, instead, has a rich vibronic structure and overlaps energetically with the monomer emission. In either case, the emission shape depends on the exciton delocalization, which rapidly decreases for increasing temperature due to an increased disorder and exciton-phonon coupling [54]. Therefore, aggregate peaks exhibit a strong temperature dependence, differing from the one of the monomer emission lines, and rapidly increase with decreasing temperature.

4. The last possibility is that X_{6P} and X_{2P} are two distinct electronic states of the SP6 molecules. SP6 is constituted by two π-systems, one on the sexiphenyl backbone and the other on the biphenyl, that are separated by a non-conjugated bridge, the spiro-link. As explained in section 1.4, similar systems exhibit excited state localization in the separated π-groups, with a consequent enhancement of their lifetime. The Kohn-Sham orbitals depicted in figure 1.10, with the LUMO and LUMO+1 localized in the sexiphenyl and the LUMO+2 in the biphenyl, suggest that a similar situation could be possible in SP6 as well. A strong localization could be reflected by an emission spectrum resembling either the sexiphenyl or the byphenil one, depending on where the lowest energetic state is localized and how strongly it interacts with the environment.

While the first and second possibilities are excluded, up to this point both scenarios 3 and 4 are possible. One way of distinguishing between them is to look at the PL spectra, since both of them have a well defined emission signature.

The most direct way to exclude the formation of aggregates is the measurement of the PL spectra as a function of temperature, since, as just discussed, the aggregate lines show a different temperature dependence than the monomer emission. The experiments have been performed
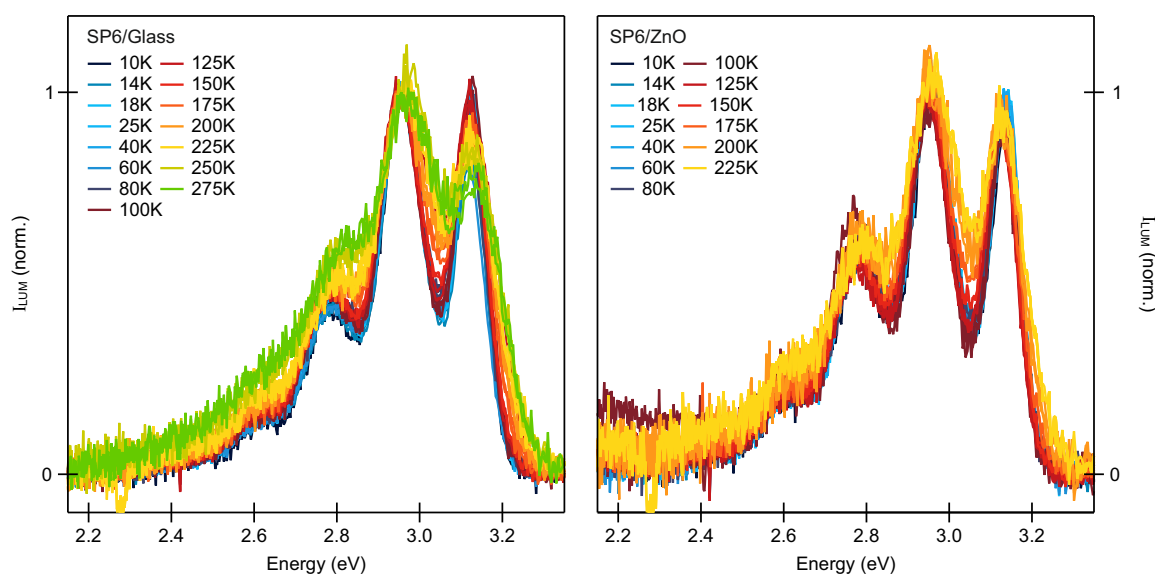
Figure 6.8: Temperature dependence of SP6 luminescence on glass (left) and ZnO (right). The spectra have been normalized at the (0-1) transition and do not show any clear signature of an aggregate emission line showing a different temperature dependence than the rest of the progression.

at a repetition rate of 40 kHz to minimize any possible contribution of the long-lived triplet state and temperatures below 90 K are achieved by cooling with liquid helium. Figure 6.8 shows the temperature dependence of the photoluminescence spectra of SP6 on glass, on the left, and on ZnO, on the right. The spectra have been normalized with respect to the (0-1) vibronic transition. The energy positions and the relative intensity of the peaks remain unchanged for almost the whole temperature range from 10 to 275 K, with broadening of the peaks and a slight change in the amplitude ratios arising at around 150 K on both substrates. Obviously, no signature of a line having a distinct temperature dependence is present in the spectra, which therefore show no clear signature of the presence of aggregates.

Once the formation of aggregates has been excluded, the SP6 PL can be analyzed in more detail in order to identify any possible signature of exciton localization, such as for example any strong similarity of the spectral features with those associated to either one between biphenyl and sexiphenyl.

The luminescence spectrum of SP6 on glass at 100 K is plotted in the left panel of figure 6.9. The spectrum exhibits four distinct vibronic peaks, which can be fitted with a sum of Gaussian functions, as shown by the violet line and the gray dashed curves, obtaining an energy separation of (160 ± 15) meV. This energy, that corresponds to about $1290 \, \text{cm}^{-1}$, matches the energies
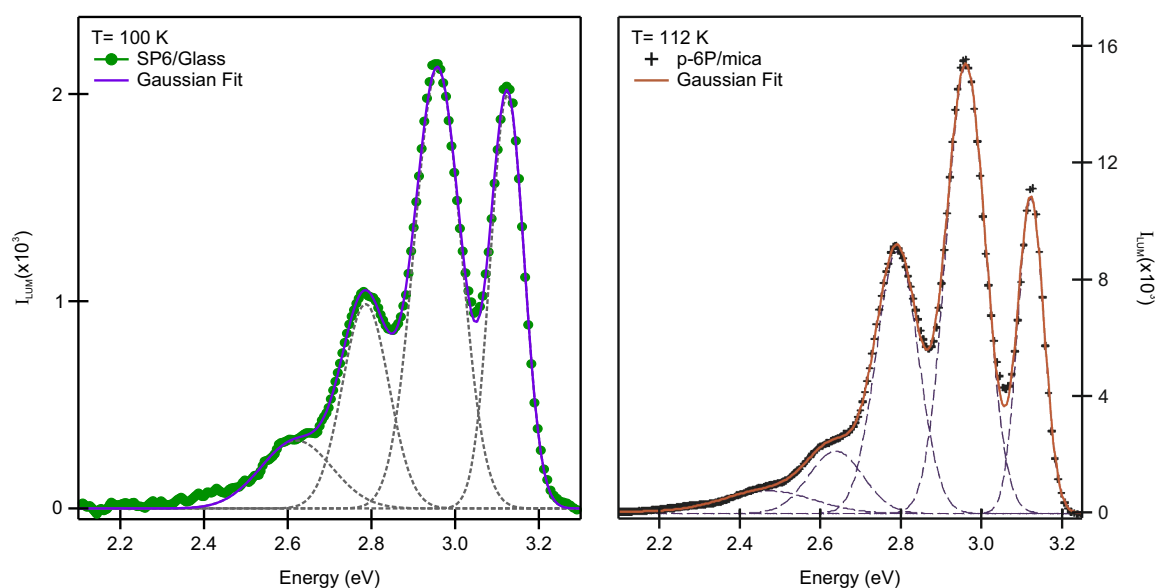
Figure 6.9: (*Left*) Luminescence spectrum of SP6 on glass at 100 K, in green. The spectra shows four vibrational lines that have been fitted (violet line) with a sum of Gaussian peaks, indicated by the dashed gray curves. (*Right*) Luminescence spectrum of 6P adapted from reference [182]. The spectrum shows five vibrational lines, with the same progression as the spectrum of SP6.

of the CC stretching modes in the Raman spectra of reference [126] discussed in section 1.4. The same energy separation also dominates the emission spectra of the majority of phenylenes, where it has been assigned to the symmetric inter-ring CC stretch at about 1280 cm^{-1} [183].

For comparison, the right panel of figure 6.9 depicts the emission of sexiphenyl (6P) as adapted from reference [182], showing a nearly exact vibrational progression of five peaks with the same energy separation of (160 ± 10) meV. Table 6.1 compares the energy position and full width half maximum (FWHM) of the peaks resulting from the Gaussian fit with the fit results of Balzer et al. in reference [182].

The energy positions and the separation coincide within the experimental error, as qualitatively observed above. In both SP6 and 6P films the (0-0) line is narrower than the higher progressions. According to reference [182], this is to be attributed to selfabsorption due to the partial overlap with the steep onset of the absorption spectra visible on both molecules. The two emission spectra differ only in the width of the peaks, which are systematically larger in SP6, and on the relative intensity of the (0-0) line. Both differences can be attributed to the different crystallinity of the two organic films. On the one hand, in the films measured in refer-

|	0-0 line	0-1 line	0-2 line	0-3 line	Ref.
Energy (eV)	3.12	2.96	2.79	2.62	This work
FWHM (meV)	94.47	131.27	131.15	200.23	
Energy (eV)	3.14	2.97	2.79	2.62	[182]
FWHM (meV)	75.00	112.00	120.00	——	

Table 6.1: Energy position and FWHM of the vibrational progression of the SP6 luminescence spectrum at 100.00 K obtained from the fit with a sum of four Gaussian peaks and comparison to the fit results on 6P from [182].

ence [182], 6P formed a crystalline, well ordered, needle like structure. On the other hand, the shape of SP6 prevents crystallization and the films are amorphous, which naturally increases the disorder and thus the width of the emission lines. Moreover, the (0-0) line is forbidden in perfectly ordered 6P crystals but becomes allowed due to structural defects [184], which are naturally present in the amorphous SP6 film, where the (0-0) line is more intense.

From this comparison it is evident that the emission spectrum of SP6 and 6P coincide, despite the substantial differences in the molecular structure, with the presence of the spiro-link and the tert-butyl decorated biphenyl in SP6. This coincidence of the two spectra strongly suggests that the lowest energetic excited state of SP6, from which emission occurs according to Kasha's rule (see. sec. 1.1.2), is localized in the sexiphenyl backbone and it is *not* affected by the presence of the second π-system in the biphenyl. Since reference [7] observes signatures of CS in the tr-PL, this emitting state needs to be associated to the X_{6P} resonance. Consequently, X_{2P} is assumed to be most probably localized on the biphenyl, and the decoupling due to the spiro-link could support the comparably long lifetime. Furthermore, again as a consequence of Kasha's rule, X_{2P} is higher in energy than X_{6P} and the absence of CS from X_{2P} to the CB cannot be attributed to a lack of energy overlap with the CB but is rather related to a shorter diffusion length, as suggested at the end of section 6.2.

Having determined that only X_{6P} excitons are emitting, all possible relaxation pathways are identified. This allows to write a full set of rate equations for the system, which describe the time evolution of the population in the excited states. To do so, it is useful to summarize the observations up to this point, which are schematized in figure 6.10.

Figure 6.10: Summary of the relaxation pathways at the SP6/ZnO interface. Two states A and B are detected in addition to a long-lived triplet state. A can decay via photoluminescence (PL), charge separation (CS) to the ZnO and intersystem crossing (ISC) to the triplet. B decays only via ISC and a weak, if any, coupling to A.
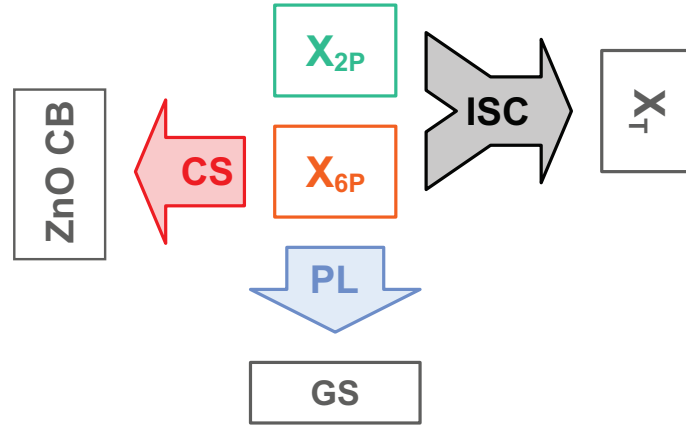
1. tr-EST reveals two excited states X_{6P} and X_{2P} with a lifetime of about 250 ps on the inert glass substrate.

2. A triplet state X_T with a lifetime of at least 5 μs is formed within comparable timescales to radiative recombination.

3. Only the X_{6P} population is affected by charge separation to the ZnO CB, and its lifetime is decreased to 140 ps.

4. The luminescence occurs from only one state, localized on the sexiphenyl backbone. Since Blumstengel et al. [7] observe an effect of the charge separation on the luminescence lifetime, this state is associated to X_{6P}.

5. Consequentely, according to Kasha's rule, X_{6P} is the lowest singlet excited state.

6. The coupling between the states cannot be excluded, but no clear rise time is visible in the tr-EST of either resonance, suggesting that the coupling rate, if any, is small. In any case, the coupling goes from state X_{2P} to X_{6P} and not vice versa, otherwise both populations, and consequently their lifetimes, would be affected by CS.

These observations define the following rate equations for the population in A and B

$$
\begin{cases}
\dot{n}_{6P}(t) + \left(\Gamma_{ISC}^{(6P)} + \Gamma_{L}^{(6P)} + \Gamma_{CS}^{(6P)} \right) n_{6P}(t) = \Gamma_C n_{2P}(t) & \text{(6.3a)} \\
\dot{n}_{2P}(t) + \left(\Gamma_{ISC}^{(2P)} + \Gamma_C \right) n_{2P}(t) = 0 & \text{(6.3b)}
\end{cases}
$$

Here $\Gamma_{ISC}^{(6P)}$ and $\Gamma_{ISC}^{(2P)}$ are the respective rates of intersystem crossing, $\Gamma_{L}^{(6P)}$ and $\Gamma_{CS}^{(6P)}$ are the rates of luminescence and charge separation to the ZnO , occurring only for state X_{6P}, and Γ_C is the rate of coupling from X_{2P} to X_{6P}. The integration of (6.3) is presented in appendix C, and results in

$$\begin{cases} n_{6P}(t) = n_{6P}(0) \cdot \exp\left[-\left(\Gamma_{ISC}^{(6P)} + \Gamma_{L}^{(6P)} + \Gamma_{CS}^{(6P)}\right)t\right] + \\ \qquad\qquad -n_{2B}(0) \cdot \dfrac{\Gamma_C \exp\left[-\left(\Gamma_{ISC}^{(2P)} + \Gamma_C\right)t\right]}{\left(\Gamma_{ISC}^{(2P)} + \Gamma_C\right) - \left(\Gamma_{ISC}^{(6P)} + \Gamma_L^{(6P)} + \Gamma_{CS}^{(6P)}\right)} \\ n_{2P}(t) = n_{2P}(0) \cdot \exp\left[-\left(\Gamma_{ISC}^{(2P)} + \Gamma_C\right)t\right] \end{cases}$$

$$(6.4a)$$

$$(6.4b)$$

In equation (6.4a), the first summand represents the decay of the population n_{6p} in state X_{6P} via ISC, PL and the CS to the ZnO conduction band. The second summand, instead, indicates the rise of X_{6P} population due to the coupling with X_{2P}. Equation (6.4b) describes the decay of the population in state X_{2P} via the coupling to X_{6P} and ISC to the triplet X_T.

As mentioned previously, the tr-EST traces at X_{6P} resonance do not show any rise ascribable to the transfer of population from X_{2P}. The long lifetime of X_{2P} excludes a strong coupling regime, where the transfer could occur on times faster than the time resolution of the experiment. Therefore, the absence of the rise can be attributed to a weak coupling regime, that mathematically corresponds to a vanishing Γ_C. In this limit the rate equations for the X_{6P} and X_{2P} populations reduce to

$$\begin{cases} n_{6P}(t) = n_{6P}(0) \cdot \exp\left[-\left(\Gamma_{ISC}^{(6P)} + \Gamma_L^{(6P)} + \Gamma_{CS}^{(6P)}\right)t\right] \\ n_{2P}(t) = n_{2P}(0) \cdot \exp\left[-\left(\Gamma_{ISC}^{(2P)}\right)t\right] \end{cases}$$

$$(6.5a)$$

$$(6.5b)$$

from which it is evident that the X_{2P} population relaxes exclusively via triplet formation. The intersystem crossing timescale can be thus equaled to the X_{2P} lifetime of (230 ± 50) ps.

Summarizing, two singlet excited states have been identified in SP6, labeled X_{6P} and X_{2P}, which exhibit comparably long lifetimes on the order of 250 ps on the insulating glass substrate. Upon change of substrate to the semiconducting ZnO only X_{6P} excitons have been found to charge separate and the population lifetime decreases to 140 ps. Finally, the coincidence of the emission spectrum of SP6 with the one of 6P, strongly suggests that the lowest energetic state, which is identified with X_{6P}, is localized on the sexiphenyl backbone. X_{2P}, that is most probably an intramolecular charge transfer exciton with the electron localized on the biphenyl, can only decay via ISC, which timescale can be set to 250 ps. The formation of X_{2P} population represents thus a loss channel for the efficiency of the CS process. Nevertheless, the energy remains stored in the triplet state X_T and, as observed in photoemission spectroscopy [173], triplet-triplet annihilation is an efficient process in SP6. The thereby generated highly excited

singlet excitons could still contribute to CS if they would efficiently relax back into X_{6P}. This relaxation pathway could potentially be identified by the observation of delayed emission.

The relaxation processes listed have different temperature dependencies. Blumstengel et al. have shown that, for films up to 12 nm thickness, the charge separation efficiency increases with increasing temperature (cf. figure 1.11), due to an increase of exciton diffusion probability [7], similarly to what observed in [185]. Instead, luminescence and intersystem crossing rates are expected to decrease with increasing temperature. Indeed, both of them depend on the wavefunction overlap between the states, which is decreased by the increasing exciton-phonon coupling and disorder in the system. Consequently, temperature-dependent measurements can give further insight in the relative importance of the decay channels, as shown by the PL temperature dependence presented in the next section.

6.4 Temperature dependence and charge separation efficiency
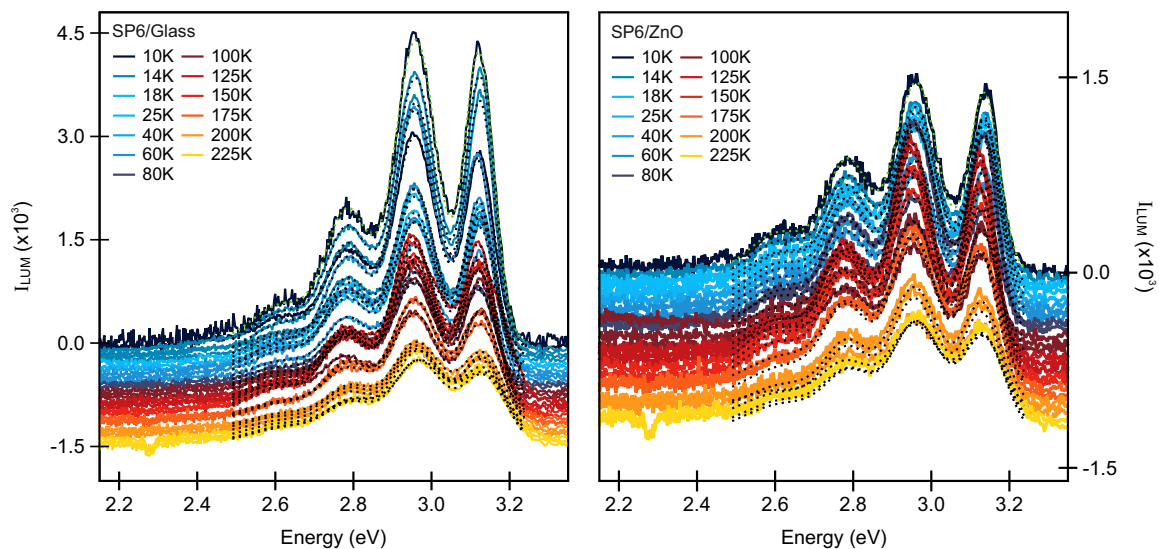
Figure 6.11: Fits of the temperature dependence of SP6 luminescence on glass (left) and on ZnO (right) for a temperature range from 14 to 250 K. The traces have been fitted with a sum of four gaussian peaks in a global way and are plotted as black dashed lines (green for the fit at 14 K to achieve contrast with the black background).

The temperature dependent luminescence spectra of two freshly-prepared films of 25 nm thickness are plotted in a waterfall plot in figure 6.11, where the results for glass are depicted

in the left and the ones for ZnO in the right panel. The curves have been all fitted with a sum of four Gaussian fits, similar to the analysis performed in section 6.3, with a global fit. This allows to extract the temperature dependence of the intensity, FWHM and energy position of all four vibrational lines. The fits are superimposed to the data as black dashed lines and exhibit good agreement with the experimental data on both substrates.

The energy position and the FWHM of the Gaussian peaks show the same temperature dependence for both substrates and all emission lines. Figure 6.12 (a) and (b), show exemplarily the trend for the most intense progression line, the 0-1 line.
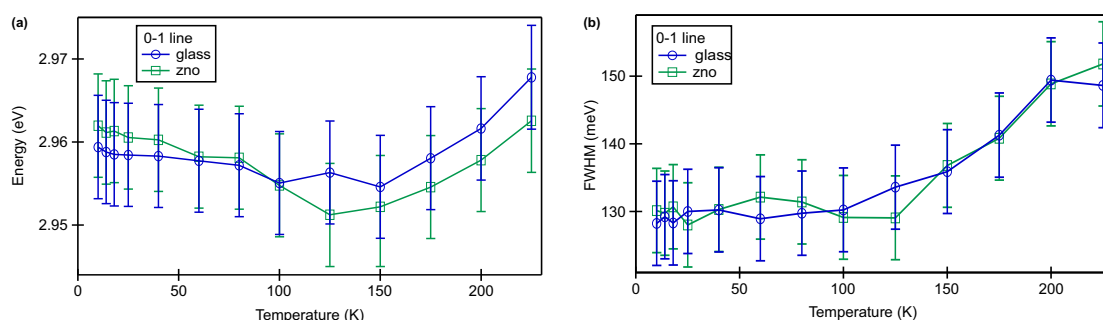
Figure 6.12: Temperature dependence of the energetic position and FWHM of the 0-1 line. The same trend is observed on both substrates. See text for discussion. (a) Energy position: : the peaks shift to the red from 14 to 125 K and then back to the blue for higher energies. (b) FWHM: the peak width remains constant until 125 K and then increases non-linearly with increasing temperatures.

The energy position shifts to the red for temperatures from 14 to 125 K and then strongly back to the blue. The FWHM remains constant for temperatures below 125 K and then non-linearly increases for increasing temperatures. Both effects can be attributed to an increased electron-phonon coupling, which probability increases with increasing temperature, as discussed above. Indeed, the broadening of the peaks can be directly related to phonon scattering and consequent increase of homogeneous broadening, while a similar trend to the one reported in figure 6.12 was observed in reference [182] for 6P and associated to the coupling with phonons and consequent increase of disorder.

The identification of the temperature range where the luminescence starts to be affected by electron-phonon coupling is fundamental in order to interpret the PL intensity variations as a function of temperature. The emission intensity is related to the integral of the population in the lowest excited state X_{6P}, over the whole time window. As shown in appendix C, integration

of equation (6.4a) results in

$$I_{LUM} = \frac{n_{6P}(0)}{\Gamma_{ISC}^{(6P)} + \Gamma_L^{(6P)} + \Gamma_{CS}^{(6P)}} + \frac{\Gamma_C n_B(0)}{\left(\Gamma_{ISC}^{(B)} + \Gamma_C\right) \cdot \left[\left(\Gamma_{ISC}^{(6P)} + \Gamma_L^{(6P)} + \Gamma_{CS}^{(6P)}\right) - \left(\Gamma_{ISC}^{(B)} + \Gamma_C\right)\right]} \qquad (6.6)$$

and for the weak coupling limit ($\Gamma_C \to 0$) discussed in the previous section, the intensity of the luminescence for SP6 on glass and ZnO becomes

$$I_G(T) \propto \frac{n_{6P}(0)}{\Gamma_{ISC}^{(6P)}(T) + \Gamma_L^{(6P)}(T)} \quad \text{and} \quad I_Z \propto \frac{n_{6P}(0)}{\Gamma_{ISC}^{(6P)}(T) + \Gamma_L^{(6P)}(T) + \Gamma_{CS}^{(6P)}(T)} \qquad . \qquad (6.7)$$

The luminescence intensity is commonly observed to decrease with increasing temperature [182, 186, 187]. According to equation (6.7) this would imply an increase of ISC and PL probability. However, both rates are observed at most to weakly *decrease* with increasing temperature [188, 189]. Thus the reduction of the luminescence intensity has to be attributed to additional relaxation channels that lead to a non-radiative decay of X_{6P} population and which probability increases with increasing temperature. To take this into account equation (6.7) is changed into

$$I_G(T) \propto \frac{n_{6P}(0)}{\Gamma_{ISC}^{(6P)}(T) + \Gamma_L^{(6P)}(T) + \Gamma_S^{(6P)}(T)} \quad \text{and} \quad I_Z \propto \frac{n_{6P}(0)}{\Gamma_{ISC}^{(6P)}(T) + \Gamma_L^{(6P)}(T) + \Gamma_{CS}^{(6P)}(T) + \Gamma_S^{(6P)}(T)}$$
$$(6.8)$$

where $\Gamma_S^{(6P)}(T)$ is the rate of the additional vibrational scattering processes. Therefore, the luminescence intensity of the film deposited on glass is expected to decrease with increasing temperature, with a dependence that reflects the one of $\Gamma_S^{(6P)}(T)$. The difference in temperature dependence on glass and ZnO is then to be attributed to the temperature dependence of the CS.

Figure 6.13 shows the temperature dependence of the PL intensity on both substrates (blue on glass and green on ZnO) for the four progression lines. The photoluminescence intensity on ZnO is systematically smaller than on glass. At low temperatures, the PL intensity on glass shows a fast decrease with increasing temperature while the one on ZnO stays almost constant. Instead, above 100 K the temperature dependence is almost identical on both substrates. The first observation confirms the relevance of CS as decay channel on the semiconducting substrate. The second suggests that the temperature dependence of the PL yield on glass is dominated by a process that is counter-arrested by CS on the ZnO. At about 100 K, however, the temperature dependence is dominated by a process that is not substrate dependent. The experiments presented here do not allow to pinpoint the corresponding processes. Nevertheless, the coincidence
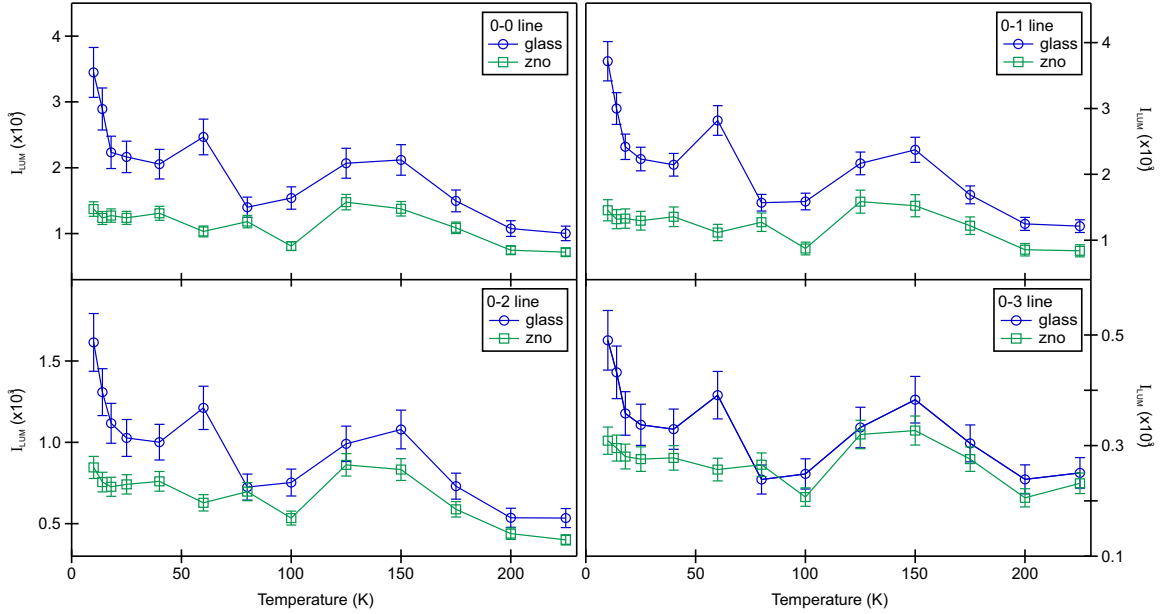
Figure 6.13: Comparison of the temperature dependence of the luminescence intensities for SP6 on glass and on ZnO.

of the temperature at which the behavior becomes substrate independent with the one observed for the change in peak width and energy, strongly suggests the higher temperature regime to be dominated by the activation of electron-vibron coupling. Therefore, the additional scattering channel with rate $\Gamma_S^{(6P)}(T)$ is probably associated with inter- and intramolecular vibrational scattering that depletes the X_{6P} population via non-radiative decay.

From this discussion, clearly, several factors may substantially influence the energy and charge loss channels at hybrid interfaces, and all this factors, in turn, affect the charge separation efficiency. The relative CS rate per initial excitation can be calculated as the difference of the inverse PL intensity on ZnO and on glass (cf. eq. (6.8)) and is plotted as a function of temperature on the left panel of figure 6.14, after being averaged over the four progression lines. The gray dashed line serves as guide to the eyes. It is evidently dominated at very low temperatures by the strong temperature dependence observed on the glass substrate and afterwards remains almost constant over the measured temperature range.

A similar temperature dependence is observed for the charge separation efficiency η_{CS}, which is defined as $\eta_{CS} = (I_G - I_Z)/I_G$ [7] and is plotted in the right panel of figure 6.14. The efficiency decreases from 0.6 at 10 K to 0.2 at 225 K. For a purely diffusion-limited CS process, and if diffusion was indeed temperature assisted as discussed above, the CS efficiency would in-
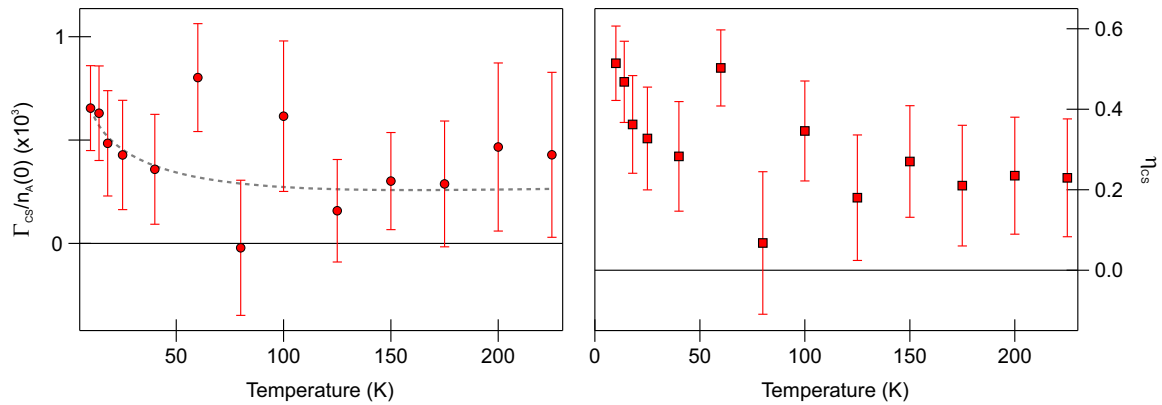
Figure 6.14: (*left*) Temperature dependence of the ratio of charge separation rate and initial exciton population. (*right*) Temperature dependence of the charge separation efficiency.

crease with increasing temperature. The trend observed here, instead, suggests that additional scattering channels become progressively more relevant and compete with the temperature assisted increase of diffusion length by reducing the exciton lifetime. In other words, while CS remains a diffusion-limited process, its efficiency is reduced by competing decay channels that shorten the effective diffusion length with increasing temperature.

Figure 6.15: Layer thickness dependence of the charge separation efficiency compared with the values of reference [7].
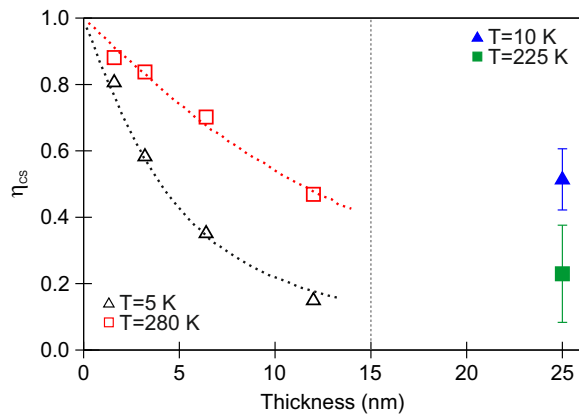
Figure 6.15 compares the efficiency obtained in this work for a layer thickness of 25 nm at 10 K and 225 K respectively, with the one extracted from reference [7] at 5 K and 280 K. Clearly, they differ in two main aspects: the absolute value and the temperature dependence. The efficiency from reference [7] can be extrapolated to range from 0.1 to 0.2 at a film thickness of 24 nm, while in this work it ranges from 0.2 to 0.6. Besides the layer thickness, the only other difference between the two experiments is that Blumstengel et al. have measured at 80 MHz. At this repetition rate, as seen in the tr-EST measurements of section 6.1 and in reference [173],

triplet states play a crucial role in the excited state dynamics. With roughly one excitation pulse every 12 ns and a triplet lifetime on the microsecond timescale, X_T population accumulates over multiple pulses. Once they undergo triplet-triplet annihilation, however, they produce highly excited singlet excitons that can again relax to X_{6P} and radiatively decay, increasing the PL intensity. This process is expected to be more efficient on glass, since the lack of the CS channel increases the probability for triplets to form, and ultimately leads to a reduction of the I_Z to I_G ratio that determines the efficiency η_{CS}. Moreover, triplet and highly excited singlet excitons could themselves act as scattering centers that decrease the exciton diffusion length by directly inducing non-radiative decay of the X_{6P} population and consequently reducing CS efficiency.

The difference in temperature dependence is instead most probably related to the interplay of the increase of diffusion rate and scattering probabilities with increasing temperatures. For sufficiently low layer thicknesses, on the order of the exciton diffusion length or thinner, the increase of scattering events does not severely affect the CS, since the distance from the substrate remains sufficiently short for the excitons to reach the ZnO. In this regime the temperature induced increase of diffusion probability remains the dominating factor. For thicker layers, however, the reduction of exciton lifetime via scattering events becomes indeed detrimental because it stops the excitons from reaching the interface at all and the efficiency decreases with increasing temperature.

6.5   Summary and discussion: Multiple excited states and loss channels at the hybrid interface

The nature and the dynamics of the excited states of the organic dye 2,7-bis(biphenyl-4-yl)-2',7'-ditertbutyl-9,9'-spirobifluorene (SP6) and how they affect the efficiency of charge separation (CS) at the hybrid inorganic-organic interface with ZnO have been extensively studied by means of complementary linear optical techniques such as time-resolved excited state transmission (tr-EST) and photoluminescence spectroscopy. Their combination allows to investigate different aspects of the excited state dynamics and thus provide access to all relevant decay pathways. The findings are summarized in the left of figure 6.16.

After photoexcitation at the absorption maximum of 3.7 eV, the molecules undergo intramolecular vibrational relaxation (IVR) on a timescale of 2 to 6 ps, which strongly depends on
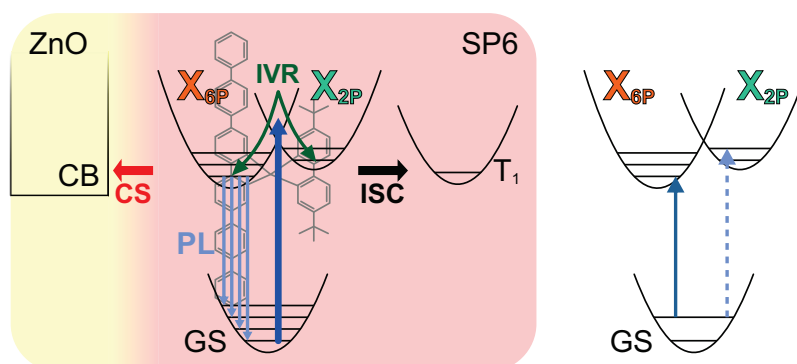
Figure 6.16: (*Left*) Summary of the excited state dynamics in SP6 and at the hybrid interface to ZnO. See text for the discussion. (*Right*) A possible pathway to avoid the population of state X_{2P} is to excite the molecule at the *onset* of absorption, leading to the population of X_{6P} only.

the photon energy of the probe pulse. The excitonic population is found to cool down into two distinct excited states, labeled X_{6P} and X_{2P}, with comparable lifetime of about 250 ps on the insulating substrate. Furthermore, a triplet state X_T that lives longer than 5 µs, corresponding to the inverse repetition rate of the laser, is formed by intersystem crossing (ISC) on a timescale of about 250 ps, i.e. comparable to the excited states lifetime. The excitons in X_{6P} are the only ones that radiatively recombine and, from the coincidence of the emission spectrum of SP6 with the one of sexiphenyl (6P), X_{6P} is found to be strongly localized on the 6P backbone of the molecule. Also, upon change of substrate to ZnO, the X_{6P} excitons are the only diffusing to the ZnO interface and separating. These process results in the reduction of the X_{6P} lifetime to 140 ps. The CS efficiency can be extracted from the difference of the emission intensities on both substrates and ranges from 0.6 at 10 K to 0.2 at 225 K. The efficiency is thus observed to decrease with increasing temperatures, opposite to the results of reference [7]. The observed temperature dependence is attributed to the onset of inter- and intramolecular vibrational scattering events, which probability is increasing with temperature and which decrease the effective diffusion length of the excitons. The contrasting behavior of this work observations compared to reference [7] is most probably due to the different thickness regime for the investigated films. Indeed, the reduction of the exciton diffusion length by competing scattering events becomes relevant only for films which thickness exceeds or equals the exciton diffusion length.

Instead, excitons in state X_{2P} are found to decay only via formation of the triplet state X_T by ISC. The results suggest that state X_{2P} is likely to be an intramolecular charge transfer exciton

with the electrons localized on the biphenyl group and the decoupling due to the non-conjugated spiro-link explains the comparably long lifetime. Due to the strong localization, X_{2P} represents therefore an exciton trap state and its population constitutes the predominant loss channel for the CS process at the hybrid interface. Nevertheless, the energy can remain stored in the triplet, which, as known from reference [173] is likely to undergo triplet-triplet annihilation. It is plausible that the highly excited singlet excitons resulting from the annihilation process could relax to X_{6P} and contribute to CS at later times. Further details on this process could be obtained by looking at any signature of delayed fluorescence from X_{6P}.

The results reported in this chapter evidence how the decoupling of π-systems in conjugated molecules severely reduces internal conversion between excited states and consequently increases the lifetime of higher excited states. Moreover, the determination of the relaxation pathway towards X_{6P}, which leads to efficient interfacial charge separation, or towards X_{2P}, ad the consequent exciton trapping, happens on the ultrafast timescale of intramolecular vibrational relaxation. A reasonably approach to avoid the population of X_{2P} is suggested in the right panel of figure 6.16. Instead of exciting the molecules at the maximum absorption it should be possible to excite at the *onset* of absorption, thus populating only X_{6P}. This would obviously reduce the amount of absorbed photons but should in principle lead to a higher efficiency per photon. Again, as it was for ZnO, *less is more*.

7. Summary and outlook

The exciton and charge carrier relaxation pathways in hybrid inorganic organic systems (HIOS) were investigated in this thesis with particular focus on energy loss channels. Indeed, when aiming at the design of functional interfaces, all dynamical processes that occur in the system and do not contribute to the intended charge or energy transfer process at the interface are to be considered energy loss processes. Thus, these processes include (1) vibrational relaxation, both in the conduction band (CB) of inorganic semiconductors or within the excited states manifold of the molecules, (2) localization and trapping of excitons and charge carriers, (3) formation of triplet or charge transfer excitons or (4) exciton recombination through radiative and non-radiative pathways, among others. Since all these energy loss mechanisms determine the efficiency of the interfacial processes and consequently of any hybrid-based device, understanding to which extent their probability is affected by, for example, defect-related in-gap states (IGS) in the inorganic semiconductor or long-lived excited states such as intramolecular charge transfer or triplet excitons in the organic semiconductor represents a cardinal objective for fundamental science. Moreover, external factors such as layer thickness, temperature or excitation density can affect the balance of relaxation processes and alter their influence on the functionality of the device.

In this thesis, these issues have been investigated with a combination of complementary all-optical time-resolved spectroscopies that access the evolution of the excited electronic states of the system as a function of time elapsed after photoexcitation, including time-resolved photoluminescence (PL) spectroscopy and time-resolved excited state transmission (tr-EST). Additionally, a novel non-linear optical technique, time-resolved electronic sum-frequency generation (tr-eSFG) was applied for the first time to the investigation of a solid state system, the non-centrosymmetric crystal of ZnO, in the context of this work. tr-eSFG is potentially an *interface specific* technique, since it is based on second order non-linear optical effects that arise only where inversion symmetry is broken, and allows for the spectroscopy of interfacial electronic states in *real* devices, where the active interface is buried under layers of matter. Exciton

dynamics and energy loss processes were investigated for the spirobifluorene derivative 2,7-bis(biphenyl-4-yl)-2',7'-ditertbutyl-9,9'-spirobifluorene (SP6) and the inorganic semiconductor ZnO, both separately and in a combined model HIOS.

The combination of complementary all-optical techniques allows to obtain a comprehensive picture of the exciton and charge relaxation processes in the model HIOS: the dominant energy loss channels in both material classes are related to the presence of long-lived strongly localized excited states, such as defect levels and charge transfer or triplet excitons. These excited states act as electron or exciton traps, limiting the probability of radiative recombination or charge separation at the hybrid interface. Furthermore, in both systems, the relaxation pathway is exclusive, i.e. either the charges or excitons get trapped or not, and is determined already on an ultrafast timescale immediately after photoexcitation.

The optical properties of ZnO were found to be affected by the presence of a defect-related IGS band from 1.7 to 2.7 eV below the CB, which is partially depleted by the photoexcitation. While in the low excitation regime, i.e. below the Mott density, the empty IGS only act as intermediate states for electronic sum-frequency generation (eSFG) transitions, their influence becomes much more extreme above the critical density. Here, the depleted IGS act as trap states for the excited excitons in the CB, reducing their lifetime. In the specific case of the single crystal, this trapping channel is even so efficient that no radiative recombination from the CB could be observed. These results suggest that a successful device design based on ZnO requires the ability of growing ZnO in a controlled way, such that the density of IGS is minimized. However, this is not the only way to control the effects of defects states on the optical properties of ZnO. Indeed, reducing the excitation density should limit the IGS influence on the ZnO optical properties and excited state lifetime. This because, contrary to exciton formation, electron trapping by IGS is a second order process that requires one photon to promote the electrons from the valence band (VB) to the conduction band and another to deplete the IGS, before the free carrier can be trapped. Therefore, the probability for this process to occur depends on the square of the excitation density. The reduction of excitation density is achievable without reducing the overall amount of absorbed photons by exciting over a wider, uniformly illuminated surface. In fact the experiments presented here show that, at lower excitation densities, the trapping channel is no-longer detrimental and excitons are observed to form on a hundreds of picoseconds timescale.

In the organic dye SP6, the experiments revealed two long-lived excited states of compa-

rable lifetime ($\sim 250\,\mathrm{ps}$), X_{6P} and X_{2P}, localized in the two π-systems of the molecule. These two states are populated by intramolecular vibrational relaxation (IVR) within 2 to 6 ps. The excitons in state X_{6P}, which is localized in the sexiphenyl (6P) backbone, decay efficiently by radiative recombination, intersystem crossing (ISC) to a microsecond-lived triplet state X_T, and charge separation to the ZnO CB. The efficiency of the charge separation (CS) process ranges from 0.2 to 0.6 and decreases for increasing temperature. This behaviour, which contrasts with the observation of reference [7], is attributed to the onset of thermally assisted intra- and inter-molecular vibrational scattering events that, by reducing the X_{6P} exciton lifetime, shorten the effective exciton diffusion length. The excitons in X_{2P}, instead, are found to decay *exclusively* by ISC. X_{2P}, which is associated to an intramolecular charge transfer exciton with the electron localized in the biphenyl group, constitutes therefore an exciton trap and represents the main energy loss channel for the CS process in the HIOS.

The localization of X_{2P} is ascribed to the presence of the spiro-link between the two π-systems. Non-conjugated bridges are included in conjugated systems in order to reduce aggregation probability and thus preserve the optical properties of the monomers in the film. The findings reported in this work, however, evidence how the decoupling of π-systems in conjugated molecules can severely reduce internal conversion between excited states, increasing the lifetime of higher excited singlet states. Additionally, the reduced coupling of the excited states implies that the relaxation pathway of a given exciton is determined already on an ultrafast timescale, namely at the IVR stage. Therefore, the suggested approach in order to reduce the population in X_{2P} and increase the CS efficiency per absorbed photon is to excite the molecules at the onset of the absorption such that only X_{6P} population is created. Additionally, it is worth to consider that the energy dissipated into the formation of X_{2P} excitons remains stored in the triplet state and that triplet-triplet annihilation is an efficient mechanism in this system [173]. Thus, it is plausible to hypothesize that part of the highly energetic singlets resulting from the annihilation process could relax back into X_{6P} and contribute to the CS at a later time. The existence of this additional relaxation pathway could be proven by looking at the appearance of delayed fluorescence from X_{6P} excitons.

The identified energy loss channels, defect states and highly localized long-lived excited states, are not exclusive of the investigated system. Accordingly, despite having been acquired for a very specific model HIOS, these results are considered to be rather general and apply to

other semiconducting systems. Both identified energy loss channels are strongly localized states and their population occurs already during an initial ultrafast timescale. This finding suggests that alternative relaxation pathways need to be considered in order to increase the efficiency of hybrid based optoelectronic and light harvesting devices.

The results presented in this thesis lead to the conclusion that a full step-by-step map of localization mechanisms and of the involved electronic states is ultimately required in order to reach the goal of designing hybrid based devices in a top-down approach. The achievement of this comprehensive picture requires further theoretical and experimental investigation, as little literature regarding localization mechanisms in both organic and inorganic compounds is available. Molecular dynamics and density functional theory simulations could give, for example, further insight on how the introduction of non-conjugated bridges alters the electronic structure and the dynamics of complex molecular systems. Experimentally, these theoretical studies could be complemented using techniques that provide chemical and orbital specificity, as in, for example, X-ray based spectroscopy. Now that free electron lasers in the X-ray regime give sufficient time resolution for time-resolved X-ray spectroscopies, it should be possible to pinpoint the electronic states that are involved in molecular charge transfer processes by investigating the dynamics at X-ray absorption edges, with timescales as fast as the ones observed in this work. For the specific case of SP6, a different response at the Carbon K-edge absorption should be observed for the 6P backbone and for the spiro-linked biphenyl. The chemical specificity of X-ray spectroscopy is also potentially attractive for the study of electron trapping dynamics due to IGS, since, for example, an interstitial oxygen is expected to have a different response than the oxygen covalently bond in the lattice.

A. Second order non-linear susceptibility tensor of ZnO

ZnO has wurtzite crystal structure and belongs to the symmetry class $6mm$, for which there are four non-vanishing $\chi^{(2)}$ tensor elements. From references [131] and [128], in the crystal axes frame chosen in figure 1.6, where the c-axis is perpendicular to the polar surfaces and the non-polar ones lie on the plane formed by c- and a-axis, this elements are:

$$\chi_{aca} = \chi_{bcb}, \quad \chi_{aac} = \chi_{bbc}, \quad \chi_{caa} = \chi_{cbb} \quad \text{and} \quad \chi_{ccc}. \tag{A.1}$$

From which the tensor can be written as

$$\chi^{(2)}_{abc} = \begin{bmatrix} 0 & 0 & 0 & 0 & 0 & aca & aac & 0 & 0 \\ 0 & 0 & 0 & aac & aca & 0 & 0 & 0 & 0 \\ caa & caa & ccc & 0 & 0 & 0 & 0 & 0 & 0 \end{bmatrix} \tag{A.2}$$

In the laboratory frame the plane of incidence is given by the $x-z$ plane and, for an angle of incidence of 45°, the incident fields are defined as

$$E_{1,p} = \begin{bmatrix} E_{1,x}, 0, E_{1,z} \end{bmatrix} \quad \text{and} \quad E_{1,s} = \begin{bmatrix} 0, E_{1,y}, 0 \end{bmatrix}$$

$$E_{2,p} = \begin{bmatrix} E_{2,x}, 0, E_{2,z} \end{bmatrix} \quad \text{and} \quad E_{2,s} = \begin{bmatrix} 0, E_{2,y}, 0 \end{bmatrix}$$

where p and s indicate the polarizations.

The generated sum-frequency generation (SFG) electric field is given by the general expression

$$E_{\text{SFG},i} = \sum_{jk} \chi_{ijk} E_{1,j} E_{2,k} \quad \text{where} \quad i, j, k \text{ are the cartesian indices.} \tag{A.3}$$

The crystal symmetry is reflected in the azimuthal rotation dependence. For a rotation around the c-axis, corresponding as well to an azimuthal rotation of the polar surfaces, it results, independently of the polarization of the incoming beams, in a constant value: p-polarized and given by χ_{caa} for both incoming beams s-polarized and s-polarized and given respectively by χ_{aac} or χ_{aca} for the cross-polarizations $E_{1,s}E_{2,p}$ and $E_{1,p}E_{2,s}$. Since in bulk ZnO the symmetry is already broken along the c-axis, the azimuthal dependence of surface and bulk coincides.

The situation is different for the non-polar surface. Here we obtain for the bulk the following azimuthal rotation dependencies:

For ss-input

$$E_{\text{SFG}} = \begin{pmatrix} E_{1,y}E_{2,y}\sin(\phi)\left((\chi_{aac} + \chi_{aca} - \chi_{ccc})\cos^2(\phi) - \chi_{caa}\sin^2(\phi)\right) \\ -E_{1,y}E_{2,y}\cos(\phi)\left(\chi_{ccc}\cos^2(\phi) + (\chi_{aac} + \chi_{aca} + \chi_{caa})\sin^2(\phi)\right) \\ 0 \end{pmatrix} \qquad \text{(A.4)}$$

For sp-input

$$E_{\text{SFG}} = \begin{pmatrix} E_{1,y}E_{2,x}\cos(\phi)\left(-\chi_{aca}\cos^2(\phi) + (\chi_{aac} + \chi_{caa} - \chi_{ccc})\sin^2(\phi)\right) \\ E_{1,y}E_{2,x}\sin(\phi)\left((\chi_{aca} + \chi_{caa} - \chi_{ccc})\cos^2(\phi) - \chi_{aac}\sin^2(\phi)\right) \\ -E_{1,y}E_{2,z}\chi_{aca}\cos(\phi) \end{pmatrix} \qquad \text{(A.5)}$$

For ps-input

$$E_{\text{SFG}} = \begin{pmatrix} E_{1,x}E_{2,y}\cos(\phi)\left(-\chi_{aac}\cos^2(\phi) + (\chi_{aca} + \chi_{caa} - \chi_{ccc})\sin^2(\phi)\right) \\ E_{1,x}E_{2,y}\sin(\phi)\left((\chi_{aac} + \chi_{caa} - \chi_{ccc})\cos^2(\phi) - \chi_{aca}\sin^2(\phi)\right) \\ -\chi_{aac}E_{1,z}E_{2,y}\cos(\phi) \end{pmatrix} \qquad \text{(A.6)}$$

Figure A.1 shows the azimuthal dependence of the SFG intensity for p- and s-polarized output, obtained as $I_P = |E_P|^2 = E_x^2 + E_z^2$ and $I_S = |E_y|^2$. The plots are simulated with the following values for the non-zero $\chi^{(2)}$ components, all within the values presented in [78]:

$$\chi_{aca} = \chi_{bcb} = -1.2, \quad \chi_{aac} = \chi_{bbc} = -0.5, \quad \chi_{caa} = \chi_{cbb} = -1 \quad \text{and} \quad \chi_{ccc} = 2.$$

The plots clearly show that the electronic sum-frequency generation (eSFG) intensity has six maxima and several zero intensity points. Furthermore, the sp and ps configurations exhibit different response. This, as can be seen in equations (A.5) and (A.6), is due to the fact that in SFG an exchange of fields requires an exchange of tensor indices, allowing SFG to address much more tensor components than SHG.

The $(10\bar{1}0)$ surface further reduces the symmetry by breaking it along the b-axis of the crystal frame. The $\chi^{(2)}$ tensor thus becomes:

$$\chi^{(2)}_{abc} = \begin{bmatrix} 0 & 0 & 0 & 0 & 0 & aca & aac & aab & aba \\ baa & bbb & bcc & bbc & bcb & 0 & 0 & 0 & 0 \\ caa & cbb & ccc & cbc & ccb & 0 & 0 & 0 & 0 \end{bmatrix} \qquad \text{(A.7)}$$
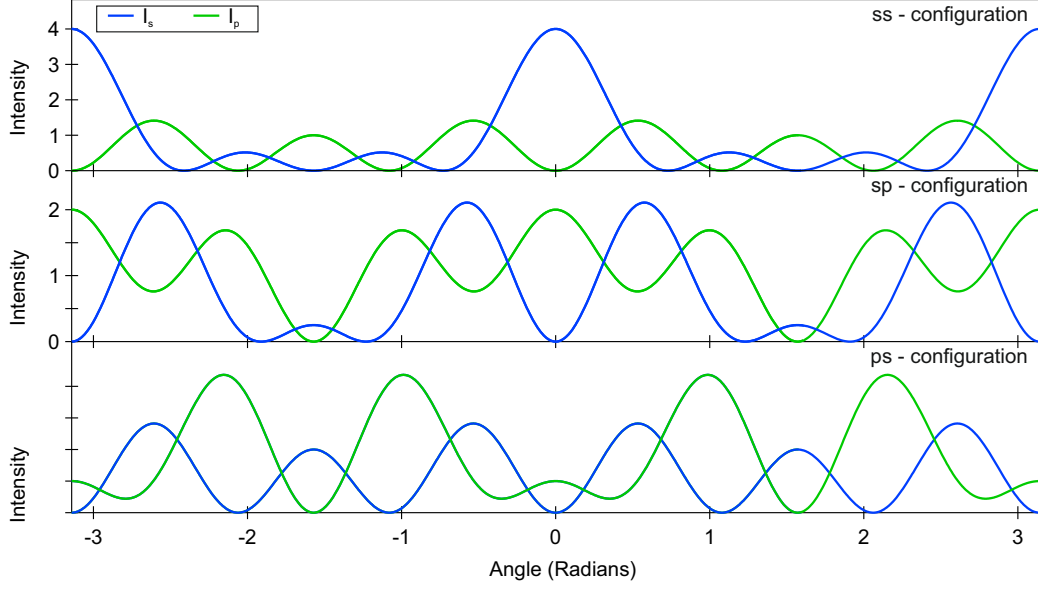
Figure A.1: Azimuthal dependence of eSFG intensity of bulk ZnO in the $[10\bar{1}0]$ direction. Plotted are in green and blue respectively the p- and s- polarized intensities of the outgoing signal for the three incoming polarization combinations ss (top), sp (middle) and ps (bottom). Clearly several zero crossing points are observed. Furthermore, sp and ps configurations show the same azimuthal dependence but different intensity, due to the coupling to different tensor components. See text for discussion.

Exemplarily we calculate the electric field components for ss-configuration, which result in

$$E_{\text{SFG}} = \begin{pmatrix} E_{1,y}E_{2,y}\sin(\phi)\big((\chi_{aac} + \chi_{aca} - \chi_{ccc})\cos^2(\phi) - \chi_{caa}\sin^2(\phi)\big) \\ -E_{1,y}E_{2,y}\cos(\phi)\big(\chi_{ccc}\cos^2(\phi) + (\chi_{aac} + \chi_{aca} + \chi_{caa})\sin^2(\phi)\big) \\ E_{1,y}E_{2,y}\big(\chi_{bcc}\cos^2(\phi) + \chi_{baa}sin^2(\phi)\big) \end{pmatrix} \quad (A.8)$$

Clearly, the breaking of the symmetry due to the surface truncation introduces an E_z component which is not present in the bulk. Figure A.2 compares the bulk response, in green, with the surface response, in red, for a pss-geometry. The surface induced z-component modifies the bulk eSFG intensity such that there no longer is any point where the intensity is zero and at the previous zero-points of the bulk response, the eSFG intensity is fully given by the surface response. Thus, being able to measure the azimuthal dependence of bulk and surface allows to separate the two contributions and be surface sensitive even for non-centrosymmetric bulk. The effect, obviously, depends on the magnitude of the tensor components and the image was simulated with values of $baa = 0.4$ and $bcc = 0.3$ to make the effect evident. However, surface

151
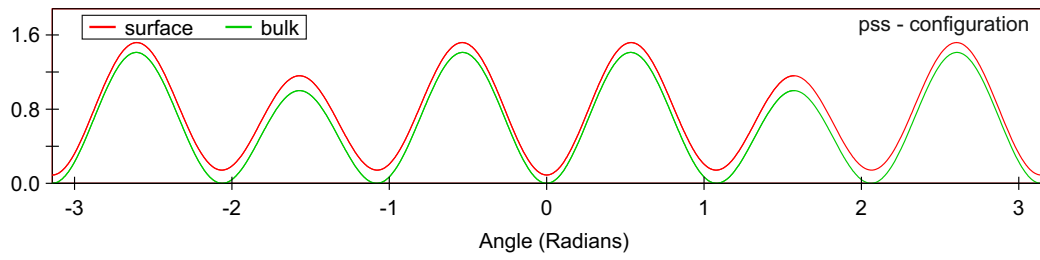
Figure A.2: Comparison of bulk and surface azimuthal dependence for pss-configuration. Clearly the surface induced E_z field leads to a shift of the SFG intensity such that it no loger has zero points. At the bulk zero points the signal is fully due to the surface response.

SFG signals tend to be two orders of magnitude smaller than bulk ones, such that in reality the effect will be noticeable just at the zero intensity points of the bulk response.

B. (Non-)Linear effects of beam propagation on the temporal shape of pulses

This appendix summarizes the concepts of light pulse propagation that are relevant to the discussions in chapter 3 and chapter 4. It is based on [190, chap. 2], [191, sec. 2] and [132]. The fields are treated as complex scalar quantities.

B.1 Time-bandwith relation

The general formulation for the electric field of a laser pulse is given by

$$E(t) = \mathrm{Re}\left(\left| E(t) \right| \exp\left[i\Phi(t) \right] \exp(-i\omega_0 t) \right) \tag{B.1}$$

where $\left| E(t) \right|$ and $\Phi(t)$ are the time-dependent envelope and phase and ω_0 is the carrier frequency. For a Gaussian pulse this results in

$$E(t) = \mathrm{Re}\left(E_0 \exp(-\Gamma t^2 - i\omega_0 t) \right). \tag{B.2}$$

Its spectral amplitude can be obtained by Fourier transformation

$$E(\omega) = \frac{1}{\sqrt{2\pi}} \int_{-\infty}^{\infty} E(t)\exp(-i\omega t)dt = \frac{1}{\sqrt{2\pi}} \int_{-\infty}^{\infty} E_0 \exp(-\Gamma t^2 - i\omega_0 t)\exp(-i\omega t)dt \tag{B.3}$$

$$\propto E_0 \exp\left(-\frac{(\omega - \omega_0)^2}{4\Gamma} \right) \tag{B.4}$$

being also a Gaussian function of finite width Γ. The temporal and spectral full width half maximum (FWHM) are given by

$$\Delta t = 2\sqrt{\frac{\ln 2}{2\Gamma}} \quad \text{and} \quad \Delta\omega = 2\sqrt{2\Gamma \ln 2}$$

and the product yields

$$\Delta t \Delta\omega = 4\ln 2 \quad \text{or} \quad \Delta t \Delta\nu = \frac{2}{\pi}\ln 2$$

In fact, the presented example of non-chirped, i.e. $\Phi(t) = 0$, Gaussian pulses represents the limiting case (Fourier-Limit) of this time-bandwidth relation. In general it holds that

$$\Delta t \Delta\nu \geq \frac{2}{\pi}\ln 2 \,. \tag{B.5}$$

B.2   Group velocity dispersion and the effect of dispersive media

A propagating wave in a linear medium must satisfy

$$\left(\frac{\partial^2}{\partial z^2} - \mu_0 \omega^2 \varepsilon(\omega)\right) E(\omega, z) = 0 \quad \text{with} \quad \varepsilon(\omega) = \varepsilon_0(1 + \chi) \tag{B.6}$$

and thus

$$E(\omega, z) = \exp\left(-\frac{(\omega - \omega_0)^2}{4\Gamma}\right) \exp\left[-ik(\omega)z\right] \quad \text{with} \quad k(\omega) = \frac{n\omega}{c}. \tag{B.7}$$

where $\varepsilon(\omega)$ is the dielectric function, χ the linear susceptibility, n the index of refraction and $k(\omega)$ the absorption coefficient.

If $k(\omega)$ is expanded in a Taylor series up to the second order the pulse spectrum becomes [190]

$$E(\omega, z) = \exp\left(-ik(\omega_0)z - ik'z \cdot (\omega - \omega_0) - \left(\frac{1}{4\Gamma} + \frac{i}{2}k''\right)(\omega - \omega_0)^2\right) \tag{B.8}$$

and the pulse's temporal evolution is proportional to

$$E(t, z) \propto \exp\left[i\omega_0\left(t - \frac{z}{v_\phi(\omega_0)}\right)\right] \cdot \exp\left[-\Gamma(z)\left(t - \frac{z}{v_g(\omega_0)}\right)^2\right] \tag{B.9}$$

As a consequence of propagation in a linear medium:

1. the phase of the central frequency is delayed by an amount of time $\frac{z}{v_\phi(\omega_0)}$ where $v_\phi(\omega_0) = \left(\frac{\omega}{k(\omega)}\right)_{\omega_0} = \frac{c}{n(\omega)}$ is the phase velocity.

2. the pulse keeps a gaussian envelope which is delayed by a time $\frac{z}{v_g(\omega_0)}$ being $v_g(\omega_0) = \left(\frac{\partial \omega}{\partial k}\right)_{\omega_0}$ the group velocity

3. the pulse envelope is distorted since its form factor $\Gamma(z)$ depends on ω from $\frac{1}{\Gamma(z)} = \frac{1}{\Gamma} + 2ik''z$ with the second derivative $k'' = \frac{d^2k(\omega)}{d\omega^2}$ known as the group velocity dispersion.

If the field is written in the form $E(t, z) = \tilde{E}(t, z)\exp[i\Phi(t)]$ it can be shown that propagation leads to a quadratic term in the time-dependent phase. The instantaneous frequency is defined as $\omega(t) = \partial\Phi/\partial t$. Figure B.1 (b) shows the effects of constant, quadratic and cubic phase (respectively yellow, red, blue and black trace in panel (a)) on a Gaussian pulse (black trace in panel (a)) . For the case of the Gaussian pulse with linear phase $\Phi(t) = \omega_0 t$ the instantaneous frequency coincides with the carrier frequency. The pulse is said to be transform limited and
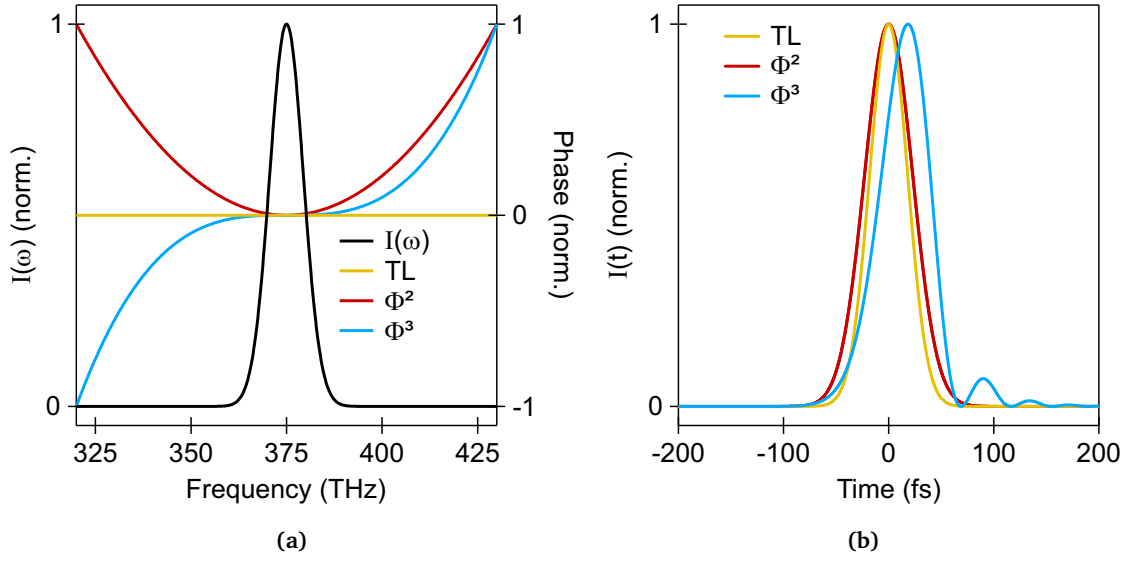
Figure B.1: (a) Black: Spectral intensity of a gaussian pulse centered at 375 THz (= 800 nm) with a bandwidth of 4.4 THz. Yellow, red and blue indicate a constant (transform-limited), quadratic and cubic time-dependent phase, respectively. (b) Temporal pulse shape calculated for the reported spectrum with the phases indicated by the corresponding color in (a)

it holds the equality in eq. (B.5). When a quadratic term at^2 is added to the phase, then $\omega(t) = \omega_0 + at$ varies linearly with time and the pulse is said to be "chirped". Media with normal dispersion, such as optical glasses in the visible range, lead to a positive quadratic term and the instantaneous frequency is smaller in the leading part of the pulse than in the trailing pulse. The pulse spreads in time, as illustrated by the red curve of figure B.1 (b). The effect of a third-order term in the phase, i.e. a instantaneous frequency increasing quadratic with time, is visible in the blue curve. Third- and higher-order terms in the phase induce oscillations in the temporal intensity.

B.3 Higher order non linear effects

When the electric field strength approaches the strength of the atomic fields (i.e. on the order of $10^{11}\,\mathrm{V\,m^{-1}}$) the dielectric polarization starts depending non-linearly on $E(\mathbf{x}, t)$, i.e.

$$P(\mathbf{x}, t) = \varepsilon_0 \left(\chi^{(1)} E(\mathbf{x}, t) + \chi^{(2)} E^2(\mathbf{x}, t) + \chi^{(3)} E^3(\mathbf{x}, t) + \cdots \right) \tag{B.10}$$

$$= P^{(1)}(\mathbf{x}, t) + P^{(2)}(\mathbf{x}, t) + P^{(3)}(\mathbf{x}, t) + \cdots \tag{B.11}$$

155

The second-order term in eq. (B.10), occurring for non-centrosymmetric media or where inversion symmetry is broken, has been discussed in detail in section 2.3. Here we focus on the first higher-order term occurring in centrosymmetric media, the third-order $P^{(3)}(\mathbf{x}, t)$.

For the sake of simplicity we discuss the effects for a gaussian beam with radial symmetry for which it is convenient to use polar coordinates.

The dielectric function $\varepsilon(r, t)$ can be written as $\varepsilon(r, t) = \varepsilon + \frac{1}{2}\varepsilon_2 |E(r, t)|^2$ and the index of refraction $n(r, t) = \sqrt{\varepsilon(r, t)}$ becomes

$$n(r, t) = n_0 + \frac{1}{2}n_2 I(r, t) \quad \text{where} \quad I(r, t) = |E(r, t)|^2 \text{ is the intensity of the field.} \qquad \text{(B.12)}$$

Eq. (B.12) states that the temporal and spatial dependence of the pulse intensity affect the refractive index of the medium as the pulse propagates through it. The two most relevant effects arising from these index changes are discussed in the following, assuming a normally dispersive medium ($n_2 > 0$).

The Kerr lens effect

The spatial intensity dependence of a Gaussian pulse propagating through a $\chi^{(3)}$ material leads to the so-called Kerr lens effect. The intensity of such a beam can be written as $I(r) = I_0 \exp(-\Gamma r^2)$ where r is the radial distance and $n(r) = n_0 + \frac{1}{2}n_2 \exp(-\Gamma r^2)$. In words, the index of refraction has a gaussian profile and is maximum at the center of the beam.

The effects of light propagation through an optical medium are governed by the optical path, defined as $d = nl$ where n is the refractive index and l the propagation length in the medium. For example, the focusing effect of a convex lens is given by the fact that the beam travels a longer distance l in the center than at the edges such that the optical path at the center is larger. In analogy, a gaussian beam traveling a constant length trough a $\chi^{(3)}$ medium experiences a gaussian focusing lens since the propagation distance is constant but the refraction index, and thus the optical paht, is higher in the center. In turn this focusing leads to an increased intensity at the center of the beam which further enhances the focusing effect. This self-focusing effect stops only when the diameter of the beam is small enough that the linear diffraction is sufficiently large to balance it.

Self-phase-modulation

The temporal intensity dependence $I(t) = \exp(-\Gamma t^2)$ induces a temporal modulation of the refractive index $\Delta n(t) \propto n_2 \exp(-\Gamma t^2)$. As a consequence, the wavevector k of a pulse propagating along z

$$E(z,t) = \sqrt{I(t)} \exp\left[i\left(\omega_0 t - kz\right)\right]$$

also depends on time since $k = \frac{\omega_0}{c} n(t)$. The instantaneous frequency is then $\omega(t) = \omega_0 - \frac{\omega_0}{c}\frac{\partial n(t)}{\partial t}z$. The frequency variation $\Delta\omega = \omega(t) - \omega_0$ is thus given by

$$\Delta\omega = -\frac{\omega_0 n_2}{2c}\frac{\partial I(t)}{\partial t}z \; . \tag{B.13}$$

New lower frequencies are created at the leading edge of the pulse, where the temporal derivative of the intensity is positive, and higher frequencies emerge at the trailing edge. These new frequencies are generated within the pulse temporal envelope but are not synchronized. In fact, self-phase modulation leads to a quadratic term in the phase that further enhances the natural group velocity dispersion (GVD) of a beam propagating in a dispersive medium.

C. Rate equations

The populations in the two excited states of 2,7-bis(biphenyl-4-yl)-2',7'-ditertbutyl-9,9'-spirobi-fluorene (SP6) can be expressed in terms of rate equations, where the decay of the populations is determined by the rates of the different decay channels. Following the discussion of section 6.1 and 6.2 we need to take into account the following observations:

1. There are two excited states with comparable lifetime
2. The luminescence coincides with the sexiphenyl luminescence (6P), such that only one of the two states luminesce
3. Only one state is affected by the change of substrate

Regarding this last observation we need to add that reference [7] observes the influence of charge separation in the luminescence, from which we conclude that the state diffusing to the interface is also the state luminescing. Furthermore, for the most general case in which the two states are coupled, the coupling needs to be from the state that does not luminesce and diffuses to the other state. Otherwise the diffusion would affect the decay of both populations in the time-resolved excited state transmission (tr-EST).

We define a state with population $n_2(t)$ which decays by intersystem crossing (ISC) and coupling to the other state of population $n_1(t)$, decaying by ISC, luminescence and diffusion to the ZnO . Thus the system of rate equations becomes:

$$
\begin{cases}
\dot{n}_2(t) + \left(\Gamma_{ISC}^{(2)} + \Gamma_{12} \right) n_2(t) = 0 & \text{(C.1a)} \\
\dot{n}_1(t) + \left(\Gamma_{ISC}^{(1)} + \Gamma_{L}^{(1)} + \Gamma_{CS}^{(1)} \right) n_1(t) = \Gamma_{12} n_2(t) & \text{(C.1b)}
\end{cases}
$$

This coupled rate equation system can be solved for t as follows :

Equation (C.1a) is an homogeneous differential equation of the form $\dot{y} + ay = 0$, which is solved as

$$
n_2(t) = n_2(0) \cdot \exp\left[-\left(\Gamma_{ISC}^{(2)} + \Gamma_{12} \right) t \right] . \tag{C.2}
$$

Equation (C.1b) instead is a non-homogeneous differential equation of the form $\dot{y} + a(t)y = g(t)$, where $a(t)$ and $g(t)$ are arbitrary functions of time. Its general solution is given by solving

$$y(t) = e^{-A(t)}\left[c_1 + \int g(t) \cdot e^{A(t)} dt\right]$$

where

$$A(t) = \int a(t) dt$$

Substituting (C.2) in (C.1b) one obtains:

$$\dot{n}_1(t) + \left(\Gamma_{ISC}^{(1)} + \Gamma_L^{(1)} + \Gamma_{CS}^{(1)}\right)n_1(t) = \Gamma_{12}n_2(0) \cdot \exp\left[-\left(\Gamma_{ISC}^{(2)} + \Gamma_{12}\right)t\right] \tag{C.3}$$

and the general solution is given by

$$
\begin{aligned}
n_1(t) &= \exp\left[-\left(\Gamma_{ISC}^{(1)} + \Gamma_L^{(1)} + \Gamma_{CS}^{(1)}\right)t\right] \cdot \\
&\quad \cdot \left[c_1 + \int \Gamma_{12}n_2(0) \cdot \exp\left[-\left(\Gamma_{ISC}^{(2)} + \Gamma_{12}\right)t\right] \cdot \exp\left[+\left(\Gamma_{ISC}^{(1)} + \Gamma_L^{(1)} + \Gamma_{CS}^{(1)}\right)\right]dt\right] = \\
&= n_1(0) \cdot \exp\left[-\left(\Gamma_{ISC}^{(1)} + \Gamma_L^{(1)} + \Gamma_{CS}^{(1)}\right)t\right] + \frac{\Gamma_{12}n_2(0)\exp\left[-\left(\Gamma_{ISC}^{(2)} + \Gamma_{12}\right)t\right]}{\left(\Gamma_{ISC}^{(1)} + \Gamma_L^{(1)} + \Gamma_{CS}^{(1)}\right) - \left(\Gamma_{ISC}^{(2)} + \Gamma_{12}\right)}
\end{aligned} \tag{C.4}
$$

where the initial condition $n_1(t=0) = n_1(0)$ was introduced.

Summing up the population in the two states is given by

$$
\begin{cases}
n_2(t) = n_2(0) \cdot \exp\left[-\left(\Gamma_{ISC}^{(2)} + \Gamma_{12}\right)t\right] & \text{(C.5a)} \\[2mm]
n_1(t) = n_1(0) \cdot \exp\left[-\left(\Gamma_{ISC}^{(1)} + \Gamma_L^{(1)} + \Gamma_{CS}^{(1)}\right)t\right] + \frac{\Gamma_{12}n_2(0)\exp\left[-\left(\Gamma_{ISC}^{(2)} + \Gamma_{12}\right)t\right]}{\left(\Gamma_{ISC}^{(1)} + \Gamma_L^{(1)} + \Gamma_{CS}^{(1)}\right) - \left(\Gamma_{ISC}^{(2)} + \Gamma_{12}\right)} & \text{(C.5b)}
\end{cases}
$$

Finally, the luminescence intensity is related to the integrated population in state 1, which is the only one emitting and given by the integral of (C.5b)

$$I_1 = \frac{n_1(0)}{\Gamma_{ISC}^{(1)} + \Gamma_L^{(1)} + \Gamma_{CS}^{(1)}} + \frac{\Gamma_{12}n_2(0)}{\left(\Gamma_{ISC}^{(2)} + \Gamma_{12}\right) \cdot \left[\left(\Gamma_{ISC}^{(1)} + \Gamma_L^{(1)} + \Gamma_{CS}^{(1)}\right) - \left(\Gamma_{ISC}^{(2)} + \Gamma_{12}\right)\right]} \tag{C.6}$$

Bibliography

[1] NCPV efficiency chart. Available online: http://www.nrel.gov/ncpv/images/efficiency_chart.jpg. Last accessed: 17/09/2015.

[2] Heliatek. Available online: http://www.heliatek.com/en/heliafilm/technical-data. Last accessed: 17/09/2015.

[3] K. Vandewal, S. Albrecht, E. T. Hoke, K. R. Graham, J. Widmer, J. D. Douglas, M. Schubert, W. R. Mateker, J. T. Bloking, G. F. Burkhard, A. Sellinger, J. M. J. Fréchet, A. Amassian, M. K. Riede, M. D. McGehee, D. Neher, and A. Salleo. *Efficient charge generation by relaxed charge-transfer states at organic interfaces*. Nat Mater, **13(1)**, 63–68, 2014. DOI: 10.1038/nmat3807.

[4] C. Silva. *Organic photovoltaics: Some like it hot*. Nat Mater, **12(1)**, 5–6. DOI: 10.1038/nmat3523. 10.1038/nmat3523.

[5] D. Schneider, T. Rabe, T. Riedl, T. Dobbertin, O. Werner, M. Kröger, E. Becker, H.-H. Johannes, W. Kowalsky, T. Weimann, et al. *Deep blue widely tunable organic solid-state laser based on a spirobifluorene derivative*. Applied Physics Letters, **84(23)**, 4693–4695, 2004. DOI: 10.1063/1.1760227.

[6] D. Schneider, T. Rabe, T. Riedl, T. Dobbertin, M. Kröger, E. Becker, H.-H. Johannes, W. Kowalsky, T. Weimann, J. Wang, et al. *Organic solid-state lasers based on sexiphenyl as active chromophore*. Journal of applied physics, **98(4)**, 3104, 2005. DOI: 10.1063/1.1991967.

[7] S. Blumstengel, S. Sadofev, C. Xu, J. Puls, R. L. Johnson, H. Glowatzki, N. Koch, and F. Henneberger. *Electronic coupling in organic-inorganic semiconductor hybrid structures with type-II energy level alignment*. Phys. Rev. B, **77**, 085323, Feb 2008. DOI: 10.1103/PhysRevB.77.085323.

[8] S. Blumstengel, S. Sadofev, and F. Henneberger. *Electronic coupling of optical excitations in organic/inorganic semiconductor hybrid structures*. New Journal of Physics, **10(6)**, 065010, 2008. DOI: 10.1088/1367-2630/10/6/065010.

[9] P. Sen, S. Yamaguchi, and T. Tahara. *Ultrafast dynamics of malachite green at the air/water interface studied by femtosecond time-resolved electronic sum frequency generation (TR-ESFG): an indicator for local viscosity*. Faraday Discuss., **145**, 411–428, 2010. DOI: 10.1039/B908097J.

[10] Ashcroft and Mermin. *Festkörperphysik*. Oldenbourg Wissenschaftsverlag, 2007.

[11] C. Kittel. *Introduzione alla fisica dello stato solido*. Bollati Boringhieri, 2nd edition, 2007.

[12] H. J. Queisser and E. E. Haller. *Defects in Semiconductors: Some Fatal, Some Vital*. Science, **281**, 945–950, 1998. DOI: 10.1126/science.281.5379.945.

[13] B. Pajot and B. Clerjaud. *Optical absorption of Impurities and Defects in Semiconducting Crystals*. Springer, 2013.

[14] M. Klessinger and J. Michl. *Lichtabsorption und photochemie organischer Moleküle*. VCH, 1989.

[15] W. Brütting (Ed.). *Physics of Organic Semiconductors*. Wiley-VCH, 2008.

[16] C. Klingshirn. *Semiconductors Optics*. Springer-Verlag Berlin Heidelberg, 2012.

[17] P. Yu and M. Cardona. *Fundamentals of semiconductors*. Springer, 2010.

[18] R. A. Kaindl, M. A. Carnahan, D. Hägele, R. Lövenich, and D. S. Chemla. *Ultrafast terahertz probes of transient conducting and insulating phases in an electron–hole gas*. Nature, **423(6941)**, 734–738, 2003. DOI: 10.1038/nature01676.

[19] E. Hendry, M. Koeberg, and M. Bonn. *Exciton and electron-hole plasma formation dynamics in ZnO*. Phys. Rev. B, **76**, 045214, Jul 2007. DOI: 10.1103/PhysRevB.76.045214.

[20] G. Wannier. *The Structure of Electronic Excitation Levels in Insulating Crystals*. Phys. Rev., **52**, 191–197, 1937. DOI: 10.1103/PhysRev.52.191.

[21] N. F. Mott. *Conduction in polar crystals. II. The conduction band and ultraviolet absorption of alkali-halide crystals*. Trans. Faraday Soc., **34**, 500–506, 1938. DOI: 10.1039/TF9383400500.

[22] R. J. Elliott. *Intensity of Optical Absorption by Excitons*. Phys. Rev., **108**, 1384–1389, Dec 1957. DOI: 10.1103/PhysRev.108.1384.

[23] M. R. Wagner. *Fundamental properties of excitons and phonons in ZnO: A spectroscopic study of the dynamics, polarity, and effects of external fields*. PhD thesis, Technische Universität Berlin, 2010. Available online: https://opus4.kobv.de/opus4-tuberlin/frontdoor/index/index/docId/2727.

[24] Y. Toyozawa. *On the Dynamical Behavior of an Exciton*. Progress of Theoretical Physics Supplement, **12**, 111–140, 1959. DOI: 10.1143/PTPS.12.111.

[25] N. Mott. *Metal-Insulator Transition*. Reviews Of Modern Physics, **40**, 677–683, 1968. DOI: 10.1103/RevModPhys.40.677.

[26] G. Mahan. *Excitons in degenerate semiconductors*. Phys. Rev., **153**, 882, 1966. DOI: 10.1103/PhysRev.153.882.

[27] A. Schleife, C. Rödl, F. Fuchs, K. Hannewald, and F. Bechsted. *Optical absorption in degenerately doped semiconductors: Mott transition or Mahan excitons?* Phys. Rev. Lett., **107**, 236405, 2011. DOI: 10.1103/PhysRevLett.107.236405.

[28] M. Feneberg, J. Däubler, K. Thonke, R. Sauer, P. Schley, and R. Goldhan. *Mahan excitons in degenerate wurtzite InN: Photoluminescence spectroscopy and reflectivity measurements*. Phys. Rev. B, **77**, 245207, 2008. DOI: 10.1103/PhysRevB.77.245207.

[29] M. Kira, F. Jahnke, and S. Koch. *Microscopic theory of Excitonic Signatures in Semiconductor Photoluminescence*. Phys. Rev. Lett., **81**, 3263, 1998. DOI: 10.1103/PhysRevLett.81.3263.

[30] U. Bovensiepen, H. Petek, and M. Wolf (Ed.). *Dynamics at Solid State Surfaces and Interfaces*, volume 2: Fundamentals, *Quasi-Particles and Collective Excitations*, p. 41–46. Wiley-VCH, 2012.

[31] S. Koch, M. Kira, G. Khitrova, and H. Gibbs. *Semiconductor excitons in new light*. Nature materials, **5(7)**, 523–531, 2006. DOI: 10.1038/nmat1658.

[32] D. Hägele, J. Hübner, W. Rühle, and M. Oestreich. *When do excitons really exist?* Physica B, **272**, 328–330, 1999. DOI: 10.1016/S0921-4526(99)00384-1.

[33] M. Oestreich, D. Hägele, J. Hübner, and W. Rühle. *Excitons, or No Excitons, That is the questions*. Phys. Stat. Sol. (a), **178**, 27, 2000. DOI: 10.1002/1521-396X(200003)178:1<27::AID-PSSA27>3.0.CO;2-X.

[34] G. Hayes and B. Deveaud. *Is Luminescence from Quantum Wells Due to Excitons?* Physica Status Solidi (a), **190(3)**, 637–640, 2002. DOI: 10.1002/1521-396X(200204)190:3<637::AID-PSSA637>3.0.CO;2-7.

[35] S. Chatterjee, C. Ell, S. Mosor, G. Khitrova, H. M. Gibbs, W. Hoyer, M. Kira, S. W. Koch, J. P. Prineas, and H. Stolz. *Excitonic Photoluminescence in Semiconductor Quantum Wells: Plasma versus Excitons*. Phys. Rev. Lett., **92**, 067402, Feb 2004. DOI: 10.1103/PhysRevLett.92.067402.

[36] W. Hoyer, C. Ell, M. Kira, S. W. Koch, S. Chatterjee, S. Mosor, G. Khitrova, H. M. Gibbs, and H. Stolz. *Many-body dynamics and exciton formation studied by time-resolved photoluminescence*. Phys. Rev. B, **72**, 075324, Aug 2005. DOI: 10.1103/PhysRevB.72.075324.

[37] R. P. Smith, J. K. Wahlstrand, A. C. Funk, R. P. Mirin, S. T. Cundiff, J. T. Steiner, M. Schafer, M. Kira, and S. W. Koch. *Extraction of Many-Body Configurations from Nonlinear Absorption in Semiconductor Quantum Wells*. Phys. Rev. Lett., **104**, 247401, Jun 2010. DOI: 10.1103/PhysRevLett.104.247401.

[38] R. H. M. Groeneveld and D. Grischkowsky. *Picosecond time-resolved far-infrared experiments on carriers and excitons in GaAs-AlGaAs multiple quantum wells*. J. Opt. Soc. Am. B, **11(12)**, 2502–2507, Dec 1994. DOI: 10.1364/JOSAB.11.002502.

[39] M. Kira, W. Hoyer, T. Stroucken, and S. W. Koch. *Exciton Formation in Semiconductors and the Influence of a Photonic Environment*. Phys. Rev. Lett., **87**, 176401, Oct 2001. DOI: 10.1103/PhysRevLett.87.176401.

[40] R. Huber, F. Tauser, A. Brodschelm, M. Bichler, G. Abstreiter, and A. Leitenstorfer. *How many-particle interactions develop after ultrafast excitation of an electron–hole plasma*. Nature, **414(6861)**, 286–289, 2001. DOI: 10.1038/35104522.

[41] P. Atkins and R. Friedman. *Molecular quantum mechanics*. Oxford university press, 4th edition, 2011.

[42] M. Kasha. *Characterization of electronic transitions in complex molecules*. Discuss. Faraday Soc., **9**, 14–19, 1950. DOI: 10.1039/DF9500900014.

[43] M. Muntwiler and X. Zhu. *Exciton formation and decay at surfaces and interfaces*. In: U. Bovensiepen, H. Petek, and M. Wolf (Ed.), *Dynamics at solid state surfaces and interfaces*, p. 325. Wiley-VCH, 2010.

[44] J. Frenkel. *On the Transformation of light into Heat in Solids. I*. Phys. Rev., **37**, 17–44, Jan 1931. DOI: 10.1103/PhysRev.37.17.

[45] J. Frenkel. *On the Transformation of Light into Heat in Solids. II*. Phys. Rev., **37**, 1276–1294, May 1931. DOI: 10.1103/PhysRev.37.1276.

[46] M. Knupfer. *Exciton binding energies in organic semiconductors*. Appl. Phys. A, **77**, 623, 2003. DOI: 10.1007/s00339-003-2182-9.

[47] T. Förster. *Zwischenmolekulare Energiewanderung und Fluoreszenz*. Annalen der Physik, **437(1-2)**, 55–75, 1948. DOI: 10.1002/andp.19484370105.

[48] M. Kasha. *Energy transfer mechanisms and the molecular exciton model for molecular aggregates*. Radiation Research, **20**, 55, 1963. DOI: 10.2307/3571331.

[49] E. Jelley. *Spectral absorption and fluorescence of dyes in the molecular state*. Nature, **138**, 1009, 1936. DOI: 10.1038/1381009a0.

[50] G. Scheibe. *Über die Veränderlichkeit der Absorptionsspektren in Lösungen und die Nebenvalenzen als ihre Ursache*. Angewandte Chemie, **50(11)**, 212–219, 1937. DOI: 10.1002/ange.19370501103.

[51] B. Norden. *Linear and circular dichroism of polymeric pseudoisocyanine*. The Journal of Physical Chemistry, **81(2)**, 151–159, 1977. DOI: 10.1021/j100517a011.

[52] S. K. Saikin, A. Eisfeld, S. Valleau, and A. Aspuru-Guzik. *Photonics meets excitonics: natural and artificial molecular aggregates*. Nanophotonics, **2(1)**, 21, 2013. DOI: 10.1515/nanoph-2012-0025.

[53] C. Spitz and S. Daehne. *Architecture of J-aggregates studied by pressure-dependent absorption and fluorescence measurements*. Berichte der Bunsengesellschaft für physikalische Chemie, **102(5)**, 738–744, 1998. DOI: 10.1002/bbpc.19981020506.

[54] E. Da Como, M. A. Loi, M. Murgia, R. Zamboni, and M. Muccini. *J-Aggregation in α-Sexithiophene Submonolayer Films on Silicon Dioxide*. Journal of the American Chemical Society, **128(13)**, 4277–4281, 2006. DOI: 10.1021/ja056060s. PMID: 16569002.

[55] F. C. Spano. *Temperature dependent exciton emission from herringbone aggregates of conjugated oligomers*. The Journal of Chemical Physics, **120(16)**, 7643–7658, 2004. DOI: http://dx.doi.org/10.1063/1.1676250.

[56] X.-Y. Zhu, Q. Yang, and M. Muntwiler. *Charge-Transfer Excitons at Organic Semiconductor Surfaces and Interfaces*. Acc. Chem. Res., **42(11)**, 1779–1787, 2009. DOI: 10.1021/ar800269u.

[57] A. E. Jailaubekov, A. P. Willard, J. R. Tritsch, W.-L. Chan, N. Sai, R. Gearba, L. G. Kaake, K. Williams, K. Leung, P. J. Rossky, and X. Y. Zhu. *Hot charge-transfer excitons set the time limit for charge separation at donor/acceptor interfaces in organic photovoltaics*. Nat. Mater., **12(1)**, 66–73, 2013. DOI: 10.1021/ar800269u.

[58] D. Dexter. *Two ideas on energy transfer phenomena: Ion-pair effects involving the OH stretching mode, and sensitization of photovoltaic cells*. Journal of luminescence, **18/19**, 779, 1979. DOI: 10.1016/0022-2313(79)90235-7.

[59] W. Shockley and H. J. Queisser. *Detailed Balance Limit of Efficiency of p-n Junction Solar Cells*. Journal of Applied Physics, **32(3)**, 510–519, 1961. DOI: http://dx.doi.org/10.1063/1.1736034.

[60] S. Blumstengel, S. Sadofev, C. Xu, J. Puls, and F. Henneberger. *Converting Wannier into Frenkel Excitons in an Inorganic/Organic Hybrid Semiconductor Nanostructure*. Phys. Rev. Lett., **97**, 237401, Dec 2006. DOI: 10.1103/PhysRevLett.97.237401.

[61] G. Itskos, G. Heliotis, P. G. Lagoudakis, J. Lupton, N. P. Barradas, E. Alves, S. Pereira, I. M. Watson, M. D. Dawson, J. Feldmann, R. Murray, and D. D. C. Bradley. *Efficient dipole-dipole coupling of Mott-Wannier and Frenkel excitons in (Ga,In)N quantum well/polyfluorene semiconductor heterostructures*. Phys. Rev. B, **76**, 035344, Jul 2007. DOI: 10.1103/PhysRevB.76.035344.

[62] Q. Zhang, T. Atay, J. R. Tischler, M. S. Bradley, V. Bulovic, and A. V. Nurmikko. *Highly efficient resonant coupling of optical excitations in hybrid organic//inorganic semiconductor nanostructures*. Nat Nano, **2(9)**, 555–559, 2007. DOI: 10.1038/nnano.2007.253.

[63] R. Schlesinger, F. Bianchi, S. Blumstengel, C. Christodoulou, R. Ovsyannikov, B. Kobin, K. Moudgil, S. Barlow, S. Hecht, S. R. Marder, F. Henneberger, and N. Koch. *Efficient light emission from inorganic and organic semiconductor hybrid structures by energy-level tuning*. Nat Commun, 6, 2015. DOI: 10.1038/ncomms7754.

[64] N. Bansal, L. X. Reynolds, A. MacLachlan, T. Lutz, R. S. Ashraf, W. Zhang, C. B. Nielsen, I. McCulloch, D. G. Rebois, T. Kirchartz, M. S. Hill, K. C. Molloy, J. Nelson, and S. A. Haque. *Influence of Crystallinity and Energetics on Charge Separation in Polymer-Inorganic Nanocomposite Films for Solar Cells*. Sci. Rep., 3, 2013. DOI: 10.1038/srep01531.

[65] C. K. Renshaw and S. R. Forrest. *Excited state and charge dynamics of hybrid organic/inorganic heterojunctions. I. Theory*. Phys. Rev. B, **90**, 045302, Jul 2014. DOI: 10.1103/PhysRevB.90.045302.

[66] A. Panda, C. K. Renshaw, A. Oskooi, K. Lee, and S. R. Forrest. *Excited state and charge dynamics of hybrid organic/inorganic heterojunctions. II. Experiment*. Phys. Rev. B, **90**, 045303, Jul 2014. DOI: 10.1103/PhysRevB.90.045303.

[67] I. Haeldermans, K. Vandewal, W. D. Oosterbaan, A. Gadisa, J. D'Haen, M. K. Van Bael, J. V. Manca, and J. Mullens. *Ground-state charge-transfer complex formation in hybrid poly(3-hexyl thiophene):titanium dioxide solar cells*. Applied Physics Letters, 93(22):223302, 2008. DOI: http://dx.doi.org/10.1063/1.3041633.

[68] Y. Vaynzof, A. A. Bakulin, S. Gélinas, and R. H. Friend. *Direct Observation of Photoinduced Bound Charge-Pair States at an Organic-Inorganic Semiconductor Interface*. Phys. Rev. Lett., **108**, 246605, Jun 2012. DOI: 10.1103/PhysRevLett.108.246605.

[69] F. Piersimoni, R. Schlesinger, J. Benduhn, D. Spoltore, S. Reiter, I. Lange, N. Koch, K. Vandewal, and D. Neher. *Charge Transfer Absorption and Emission at ZnO/Organic Interfaces*. The Journal of Physical Chemistry Letters, **6(3)**, 500–504, 2015. DOI: 10.1021/jz502657z.

[70] V. M. Agranovich, Y. N. Gartstein, and M. Litinskaya. *Hybrid Resonant Organic-Inorganic Nanostructures for Optoelectronic Applications*. Chem. Rev., **111(9)**, 5179–5214, 2011. DOI: 10.1021/cr100156x.

[71] V. M. Agranovich, D. M. Basko, G. C. La Rocca, and F. Bassani. *Excitons and optical nonlinearities in hybrid organic-inorganic nanostructures*. J. Phys.: Condens. Matter, **10**, 9369, 1998.

[72] O. Roslyak and J. L. Birman. *Theory of enhanced second-harmonic generation by the quadrupole-dipole hybrid exciton*. J. Phys.: Condens. Matter, **20(23)**, 235238, 2008. DOI: 10.1088/0953-8984/20/23/235238.

[73] P. Peumans, A. Yakimov, and S. R. Forrest. *Small molecular weight organic thin-film photodetectors and solar cells*. Journal of Applied Physics, **93(7)**, 3693–3723, 2003. DOI: http://dx.doi.org/10.1063/1.1534621.

[74] D. C. Reynolds, D. C. Look, B. Jogai, C. W. Litton, G. Cantwell, and W. C. Harsch. *Valence-band ordering in ZnO*. Phys. Rev. B, **60**, 2340–2344, Jul 1999. DOI: 10.1103/PhysRevB.60.2340.

[75] C. Klingshirn, J. Fallert, H. Zhou, J. Sartor, C. Thiele, F. Maier-Flaig, D. Schneider, and H. Kalt. *65 years of ZnO research - old and very recent results*. Phys. Stat. Sol. (b), **247 (6)**, 1424–1447, 2010. DOI: 10.1002/pssb.200983195.

[76] A. Janotti and C. G. V. de Walle. *Fundamentals of zinc oxide as a semiconductor*. Reports on Progress in Physics, **72(12)**, 126501, 2009. DOI: 10.1088/0034-4885/72/12/126501.

[77] Ü. Özgür, Y. I. Alivov, C. Liu, A. Teke, M. A. Reshchikov, S. Doğan, V. Avrutin, S.-J. Cho, and H. Morkoç. *A comprehensive review of ZnO materials and devices*. Journal of Applied Physics, 98(4):041301, 2005. DOI: 10.1063/1.1992666.

[78] H. Morkoç and U. Özgür. *Zinc Oxide*. Wiley-VCH, 2009.

[79] X. Q. Zhang, Z. K. Tang, M. Kawasaki, A. Ohtomo, and H. Koinuma. *Resonant exciton second-harmonic generation in self-assembled ZnO microcrystallite thin films*. J. Phys.: Condens. Matter, **15**, 5191, 2003. DOI: 10.1088/0953-8984/15/30/301.

[80] C. Liu, B. Zhang, N. Binh, and Y. Segawa. *Second harmonic generation in ZnO thin films fabricated by metalorganic chemical vapor deposition*. Optics Communications, **237**, 65 – 70, 2004. DOI: 10.1016/j.optcom.2004.03.064.

[81] D. Look, D. Reynolds, J. Sizelove, R. Jones, C. Litton, G. Cantwell, and W. Harsch. *Electrical properties of bulk ZnO*. Solid State Communications, **105(6)**, 399 – 401, 1998. DOI: 10.1016/S0038-1098(97)10145-4.

[82] E. Ohshima, H. Ogino, I. Niikura, K. Maeda, M. Sato, M. Ito, and T. Fukuda. *Growth of the 2-in-size bulk ZnO single crystals by the hydrothermal method*. Journal of Crystal Growth, **260**, 166 – 170, 2004. DOI: 10.1016/j.jcrysgro.2003.08.019.

[83] D. C. Reynolds, C. W. Litton, D. C. Look, J. E. Hoelscher, B. Claflin, T. C. Collins, J. Nause, and B. Nemeth. *High-quality, melt-grown ZnO single crystals*. Journal of Applied Physics, **95(9)**, 4802–4805, 2004. DOI: 10.1063/1.1691186.

[84] T. Ive, T. Ben-Yaacov, C. V. de Walle, U. Mishra, S. DenBaars, and J. Speck. *Step-flow growth of ZnO(0001) on GaN(0001) by metalorganic chemical vapor epitaxy*. Journal of Crystal Growth, **310**, 3407 – 3412, 2008. DOI: 10.1016/j.jcrysgro.2008.04.032.

[85] S. Blumstengel, S. Sadofev, H. Kirmse, and F. Henneberger. *Extreme low-temperature molecular beam epitaxy of ZnO-based quantum structures*. Appl. Phys. Lett., 98(3): 031907, 2011. DOI: 10.1063/1.3544575.

[86] W. R. L. Lambrecht, A. V. Rodina, S. Limpijumnong, B. Segall, and B. K. Meyer. *Valence-band ordering and magneto-optic exciton fine structure in ZnO*. Phys. Rev. B, **65**, 075207, Jan 2002. DOI: 10.1103/PhysRevB.65.075207.

[87] D. Thomas. *The exciton spectrum of zinc oxide*. J. Phys. Chem. Solids, **15**, 86–96, 1959. DOI: 10.1016/0022-3697(60)90104-9.

[88] Y. S. Park, C. W. Litton, T. C. Collins, and D. C. Reynolds. *Exciton spectrum of ZnO*. Phys. Rev., **143**, 512, 1966. DOI: 10.1103/PhysRev.143.512.

[89] A. Teke, U. Özgür, S. Doğan, X. Gu, H. Morkoç, B. Nemeth, J. Nause, and H. O. Everitt. *Excitonic fine structure and recombination dynamics in single-crystalline* ZnO. Phys. Rev. B, **70**, 195207, Nov 2004. DOI: 10.1103/PhysRevB.70.195207.

[90] L. Wang and N. C. Giles. *Temperature dependence of the free-exciton transition energy in zinc oxide by photoluminescence excitation spectroscopy*. Journal of Applied Physics, **94 (2)**, 973–978, 2003. DOI: 10.1063/1.1586977.

[91] R. Hauschild, H. Priller, M. Decker, J. Brückner, H. Kalt, and C. Klingshirn. *Temperature dependent band gap and homogeneous line broadening of the exciton emission in ZnO*. Physica Status Solidi (c), **3(4)**, 976–979, 2006. DOI: 10.1002/pssc.200564643.

[92] T. C. Damen, S. P. S. Porto, and B. Tell. *Raman Effect in Zinc Oxide*. Phys. Rev., **142**, 570–574, 1966. DOI: 10.1103/PhysRev.142.570.

[93] D. C. Reynolds, D. C. Look, B. Jogai, C. W. Litton, T. C. Collins, W. Harsch, and G. Cantwell. *Neutral-donor-bound-exciton complexes in ZnO crystals*. Phys. Rev. B, **57**, 12151, 1998. DOI: 10.1103/PhysRevB.57.12151.

[94] M. R. Wagner, G. Callsen, J. S. Reparaz, J.-H. Schulze, R. Kirste, M. Cobet, I. A. Ostapenko, S. Rodt, C. Nenstiel, M. Kaiser, A. Hoffmann, A. V. Rodina, M. R. Phillips, S. Lautenschläger, S. Eisermann, and B. K. Meyer. *Bound excitons in ZnO: Structural defect complexes versus shallow impurity centers*. Phys. Rev. B, **84**, 035313, Jul 2011. DOI: 10.1103/PhysRevB.84.035313.

[95] S. Vempati, J. Mitra, and P. Dawson. *One-step synthesis of ZnO nanosheets: a blue-white fluorophore*. Nanoscale research letters, **7(1)**, 1–10, 2012. DOI: 10.1186/1556-276X-7-470.

[96] K. Vanheusden, C. H. Seager, W. L. Warren, D. R. Tallant, and J. A. Voigt. *Correlation between photoluminescence and oxygen vacancies in ZnO phosphors*. Appl. Phys. Lett., **68 (3)**, 403–405, 1996. DOI: 10.1063/1.116699.

[97] F. Leiter, H. Alves, A. Hofstaetter, D. Hofmann, and B. Meyer. *The Oxygen Vacancy as the Origin of a Green Emission in Undoped ZnO*. Phys. Stat. Sol. (b), **226(1)**, R4–R5, 2001. DOI: 10.1002/1521-3951(200107)226:1<R4::AID-PSSB99994>3.0.CO;2-F.

[98] D. Reynolds, D. Look, B. Jogai, J. V. Nostrand, R. Jones, and J. Jenny. *Source of the yellow luminescence band in GaN grown by gas-source molecular beam epitaxy and the green luminescence band in single crystal ZnO*. Solid State Communications, **106(10)**, 701 – 704, 1998. DOI: 10.1016/S0038-1098(98)00048-9.

[99] A. F. Kohan, G. Ceder, D. Morgan, and C. G. Van de Walle. *First-principles study of native point defects in ZnO*. Phys. Rev. B, **61**, 15019–15027, Jun 2000. DOI: 10.1103/PhysRevB.61.15019.

[100] A. B. Djurišić, Y. H. Leung, K. H. Tam, Y. F. Hsu, L. Ding, W. K. Ge, Y. C. Zhong, K. S. Wong, W. K. Chan, H. L. Tam, K. W. Cheah, W. M. Kwok, and D. L. Phillips. *Defect emissions in ZnO nanostructures*. Nanotechnology, **18(9)**, 095702, 2007. DOI: 10.1088/0957-4484/18/9/095702.

[101] K. Bandopadhyay and J. Mitra. *Zn interstitials and O vacancies responsible for n-type ZnO: what do the emission spectra reveal?* RSC Adv., **5**, 23540–23547, 2015. DOI: 10.1039/C5RA00355E.

[102] S. B. Zhang, S.-H. Wei, and A. Zunger. *Intrinsic n-type versus p-type doping asymemetry and the defect physics in ZnO*. Phys. Rev. B, **63**, 075205, 2001. DOI: 10.1103/PhysRevB.63.075205.

[103] A. Janotti and C. G. Van de Walle. *Native point defects in ZnO*. Phys. Rev. B, **76**, 165202, Oct 2007. DOI: 10.1103/PhysRevB.76.165202.

[104] C. G. Van de Walle. *Hydrogen as a Cause of Doping in Zinc Oxide*. Phys. Rev. Lett., **85**, 1012–1015, Jul 2000. DOI: 10.1103/PhysRevLett.85.1012.

[105] Y. Wang, B. Meyer, X. Yin, M. Kunat, D. Langenberg, F. Traeger, A. Birkner, and C. Wöll. *Hydrogen Induced Metallicity on the* ZnO(10$\bar{1}$0) *Surface*. Phys. Rev. Lett., **95**, 266104, Dec 2005. DOI: 10.1103/PhysRevLett.95.266104.

[106] K. Ozawa and K. Mase. *Comparison of the surface electronic structures of H-adsorbed ZnO surfaces: An angle-resolved photoelectron spectroscopy study*. Phys. Rev. B, **83**, 125406, Mar 2011. DOI: 10.1103/PhysRevB.83.125406.

[107] J.-C. Deinert, O. T. Hofmann, M. Meyer, P. Rinke, and J. Stähler. *Local aspects of hydrogen-induced metallization of the* ZnO(10$\overline{1}$0) *surface*. Phys. Rev. B, **91**, 235313, Jun 2015. DOI: 10.1103/PhysRevB.91.235313.

[108] M. A. M. Versteegh, T. Kuis, H. T. C. Stoof, and J. I. Dijkhuis. *Ultrafast screening and carrier dynamics in ZnO: Theory and experiment*. Phys. Rev. B, **84**, 035207, Jul 2011. DOI: 10.1103/PhysRevB.84.035207.

[109] J.-C. Deinert, D. Wegkamp, M. Meyer, C. Richter, M. Wolf, and J. Stähler. *Ultrafast Exciton Formation at the ZnO (10$\overline{1}$0) Surface*. Phys. Rev. Lett., **113**, 057602, Jul 2014. DOI: 10.1103/PhysRevLett.113.057602.

[110] V. P. Zhukov, P. M. Echenique, and E. V. Chulkov. *Two types of excited electron dynamics in zinc oxide*. Phys. Rev. B, **82**, 094302, Sep 2010. DOI: 10.1103/PhysRevB.82.094302.

[111] W. A. Tisdale, M. Muntwiler, D. J. Norris, E. S. Aydil, and X.-Y. Zhu. *Electron Dynamics at the ZnO (10$\overline{1}$0) Surface*. The Journal of Physical Chemistry C, **112(37)**, 14682–14692, 2008. DOI: 10.1021/jp802455p.

[112] A. Yamamoto, T. Kido, T. Goto, Y. Chen, T. Yao, and A. Kasuya. *Dynamics of photoexcited carriers in ZnO epitaxial thin films*. Applied Physics Letters, **75(4)**, 469–471, 1999. DOI: 10.1063/1.124411.

[113] V. Travnikov, A. Freiberg, and S. Savikhin. *Surface excitons in ZnO crystals*. Journal of Luminescence, **47(3)**, 107 – 112, 1990. DOI: 10.1016/0022-2313(90)90006-W.

[114] T. Koida, S. F. Chichibu, A. Uedono, A. Tsukazaki, M. Kawasaki, T. Sota, Y. Segawa, and H. Koinuma. *Correlation between the photoluminescence lifetime and defect density in bulk and epitaxial ZnO*. Applied Physics Letters, **82(4)**, 532–534, 2003. DOI: 10.1063/1.1540220.

[115] S. Kuehn, S. Friede, S. Sadofev, S. Blumstengel, F. Henneberger, and T. Elsaesser. *Surface excitons on a ZnO (000-1) thin film*. Applied Physics Letters, 103(19):191909, 2013. DOI: 10.1063/1.4829466.

[116] F. Bertram, J. Christen, A. Dadgar, and A. Krost. *Complex excitonic recombination kinetics*

in ZnO: Capture, relaxation, and recombination from steady state. Applied Physics Letters, **90**, –, 2007. DOI: 10.1063/1.2432259.

[117] C. J. Cook, S. Khan, G. D. Sanders, X. Wang, D. H. Reitze, Y. D. Jho, Y.-W. Heo, J.-M. Erie, D. P. Norton, and C. J. Stanton. *Ultrafast carrier relaxation and diffusion dynamics in ZnO*. Proc. SPIE, **7603**, 760304–760304–14, 2010. DOI: 10.1117/12.845636.

[118] S. F. Chichibu, T. Onuma, M. Kubota, A. Uedono, T. Sota, A. Tsukazaki, A. Ohtomo, and M. Kawasaki. *Improvements in quantum efficiency of excitonic emissions in ZnO epilayers by the elimination of point defects*. Journal of Applied Physics, 99:093505, 2006. DOI: 10.1063/1.2193162.

[119] C. Bauer, G. Boschloo, E. Mukhtar, and A. Hagfeldt. *Ultrafast relaxation dynamics of charge carriers relaxation in ZnO nanocrystalline thin films*. Chemical Physics Letters, **387**, 176 – 181, 2004. DOI: 10.1016/j.cplett.2004.01.106.

[120] J. Takeda, N. Arai, Y. Toshine, H.-J. Ko, and T. Yao. *Ultrafast Dynamics of Exciton-Exciton and Exciton-Longitudinal Optical-Phonon Scattering Processes in ZnO Epitaxial Thin Films*. Japanese Journal of Applied Physics, **45**, 6961, 2006. DOI: 10.1143/JJAP.45.6961.

[121] W.-L. Yu, J. Pei, W. Huang, and A. J. Heeger. *Spiro-Functionalized Polyfluorene Derivatives as Blue Light-Emitting Materials*. Advanced Materials, **12**, 828–831, 2000. DOI: 10.1002/(SICI)1521-4095(200006)12:11<828::AID-ADMA828>3.0.CO;2-H.

[122] I. Franco and S. Tretiak. *Electron-Vibrational Dynamics of Photoexcited Polyfluorenes*. Journal of the American Chemical Society, **126(38)**, 12130–12140, 2004. DOI: 10.1021/ja0489285. PMID: 15382949.

[123] E. Zojer, P. Buchacher, F. Wudl, J. Cornil, J. P. Calbert, J. L. Brédas, and G. Leising. *Excited state localization in organic molecules consisting of conjugated and non-conjugated segments*. The Journal of Chemical Physics, **113(22)**, 10002–10012, 2000. DOI: 10.1063/1.1323263.

[124] F. Momicchioli, M. C. Bruni, and I. Baraldi. *Fluorescence and absorption spectra of polyphenyls. Theoretical study on the band shape*. The Journal of Physical Chemistry, **76(26)**, 3983–3990, 1972. DOI: 10.1021/j100670a017.

173

[125] S. Karabunarliev, E. R. Bittner, and M. Baumgarten. *Franck-Condon spectra and electron-libration coupling in para-polyphenyls*. The Journal of Chemical Physics, **114(13)**, 5863–5870, 2001. DOI: http://dx.doi.org/10.1063/1.1351853.

[126] J. Stähler, O. T. Hofmann, P. Rinke, S. Blumstengel, F. Henneberger, Y. Li, and T. F. Heinz. *Raman study of 2,7-bis(biphenyl-4-yl-)2',7'-ditertbutyl-9,9'-spirobifluorene adsorbed on oxide surfaces*. Chem. Phys. Lett., **584**, 74 – 78, 2013. DOI: 10.1016/j.cplett.2013.08.030.

[127] Oxford Dictionaries, 2015. Available online: http://www.oxforddictionaries.com/. Last accessed: 23/06/2015.

[128] P. Butcher and D. Cotter. *The elements of nonlinear optics*. Cambridge University Press, 1990.

[129] Y. B. Band. *Light and Matter*. Wiley, 2006.

[130] M. Bass (Ed.). *Handbook of Optics*, volume IV. Mc Graw Hill, 3rd edition, 2010.

[131] Y. R. Shen. *The principles of nonlinear optics*. John Wiley & sons, 1984.

[132] R. W. Boyd. *Nonlinear Optics*. Elsevier Academic Press, 3rd edition, 2008.

[133] H. Bruus and K. Flesnberg. *Many-Body Quantum Theory in Condensed Matter Physics: An Introduction*. Oxford Graduate Texts, 2004.

[134] A. Einstein. *Zur Quantentheorie der Strahlung*. Physikalische Zeitschrift, **18**, 121–128, 1917.

[135] R. Loudon. *The quantum theory of light*. Oxford university press, 3 edition, 2000.

[136] S. Mukamel. *Principles of nonlinear optical spectroscopy*. Oxford university press, 1995.

[137] R. Ernstorfer. *Spectroscopic investigation of photoinduced heterogeneous electron transfer*. PhD thesis, Freie Universität Berlin, 2004.

[138] A. L. Dobryakov, S. A. Kovalenko, and N. P. Ernsting. *Electronic and vibrational coherence effects in broadband transient absorption spectroscopy with chirped supercontinuum probing*. The Journal of Chemical Physics, **119(2)**, 988–1002, 2003. DOI: http://dx.doi.org/10.1063/1.1579672.

[139] R. W. Boyd and S. Mukamel. *Origin of spectral holes in pump-probe studies of homogeneously broadened lines*. Phys. Rev. A, **29**, 1973–1983, Apr 1984. DOI: 10.1103/PhysRevA.29.1973.

[140] M. Lorenc, M. Ziolek, R. Naskrecki, J. Karolczak, J. Kubicki, and A. Maciejewski. *Artifacts in femtosecond transient absorption spectroscopy*. Applied Physics B, **74(1)**, 19–27, 2002. DOI: 10.1007/s003400100750.

[141] E. Tokunaga, A. Terasaki, and T. Kobayashi. *Femtosecond continuum interferometer for transient phase and transmission spectroscopy*. J. Opt. Soc. Am. B, **13(3)**, 496–513, Mar 1996. DOI: 10.1364/JOSAB.13.000496.

[142] K. Ekvall, P. van der Meulen, C. Dhollande, L.-E. Berg, S. Pommeret, R. Naskrecki, and J.-C. Mialocq. *Cross phase modulation artifact in liquid phase transient absorption spectroscopy*. Journal of Applied Physics, **87(5)**, 2340–2352, 2000. DOI: http://dx.doi.org/10.1063/1.372185.

[143] M. Raschke, M. Hayashi, S. Lin, and Y. Shen. *Doubly-resonant sum-frequency generation spectroscopy for surface studies*. Chemical Physics Letters, **359**, 367 – 372, 2002. DOI: http://dx.doi.org/10.1016/S0009-2614(02)00560-2.

[144] P. Guyot-Sionnest, R. Superfine, J. Hunt, and Y. Shen. *Vibrational spectroscopy of a silane monolayer at air/solid and liquid/solid interfaces using sum-frequency generation*. Chemical Physics Letters, **144(1)**, 1 – 5, 1988. DOI: http://dx.doi.org/10.1016/0009-2614(88)87079-9.

[145] P. B. Miranda and Y. R. Shen. *Liquid Interfaces: A Study by Sum-Frequency Vibrational Spectroscopy*. The Journal of Physical Chemistry B, **103(17)**, 3292–3307, 1999. DOI: 10.1021/jp9843757.

[146] F. Vidal and A. Tadjeddine. *Sum-frequency generation spectroscopy of interfaces*. Reports on Progress in Physics, **68(5)**, 1095, 2005. DOI: 10.1088/0034-4885/68/5/R03.

[147] J. F. D. Liljeblad and E. Tyrode. *Vibrational Sum Frequency Spectroscopy Studies at Solid/Liquid Interfaces: Influence of the Experimental Geometry in the Spectral Shape*

and Enhancement. The Journal of Physical Chemistry C, **116(43)**, 22893–22903, 2012. DOI: 10.1021/jp306838a.

[148] S. Yamaguchi and T. Tahara. *Precise Electronic $\chi^{(2)}$ Spectra of Molecules Adsorbed at an Interface Measured by Multiplex Sum Frequency Generation*. The Journal of Physical Chemistry B, **108(50)**, 19079–19082, 2004. DOI: 10.1021/jp045306x.

[149] N. Bloembergen and P. S. Pershan. *Light Waves at the Boundary of Nonlinear Media*. Phys. Rev., **128**, 606–622, Oct 1962. DOI: 10.1103/PhysRev.128.606.

[150] DARPA Circuit Achieves Speeds of 1 Trillion Cycles per Second, Earns Guinness World Record. Available online: www.darpa.mil/news-events/2014-10-28. Last accessed: 21/09/2015.

[151] L. Foglia. *Transient reflectivity and coherent phonon excitation: An ultrafast probe of the metal-to-insulator transition in* VO_2. Diplomarbeit, Freie Universität Berlin, 2011. Available online: http://www.fhi-berlin.mpg.de/pc/electrondynamix/publications/diplom/foglia_diplom2011.pdf.

[152] R. L. Fork, O. E. Martinez, and J. P. Gordon. *Negative dispersion using pairs of prisms*. Opt. Lett., **9(5)**, 150–152, May 1984. DOI: 10.1364/OL.9.000150.

[153] O. Martinez. *Design of high-power ultrashort pulse amplifiers by expansion and recompression*. Quantum Electronics, IEEE Journal of, **23(8)**, 1385–1387, Aug 1987. DOI: 10.1109/JQE.1987.1073518.

[154] E. Treacy. *Optical pulse compression with diffraction gratings*. Quantum Electronics, IEEE Journal of, **5(9)**, 454–458, Sep 1969. DOI: 10.1109/JQE.1969.1076303.

[155] J. Stähler. *Freezing Hot Electrons - Electron Transfer and Solvation Dynamics at D_2O and NH_3 - Metal interfaces*. PhD thesis, Freie Univeristät Berlin, 2007.

[156] D. Wegkamp. *Schnelle Elektronendynamiken an Grenzflächen untersucht mit einer NOPA-basierenden Femtosekunden-Lichtquelle*. Diplomarbeit, Freie Universität Berlin, 2009.

[157] S. Gélinas, A. Rao, A. Kumar, S. L. Smith, A. W. Chin, J. Clark, T. S. van der Poll, G. C. Bazan, and R. H. Friend. *Ultrafast Long-Range Charge Separation in Organic Semicon-*

ductor Photovoltaic Diodes. Science, **343(6170)**, 512–516, 2014. DOI: 10.1126/science.1246249.

[158] D. Polli, P. Altoè, O. Weingart, K. M. Spillane, C. Manzoni, D. Brida, G. Tomasello, G. Orlandi, P. Kukura, R. A. Mathies, M. Garavelli, and G. Cerullo. *Conical intersection dynamics of the primary photoisomerization event in vistion*. Nature, **467**, 440–443, 2010. DOI: 10.1038/nature09346.

[159] J. Léonard, N. Lecong, J.-P. Likforman, O. Crégut, S. Haacke, P. Viale, P. Leproux, and V. Couderc. *Broadband ultrafast spectroscopy usinga photonic crystal fiber: application tothe photophysics of malachite green*. Opt. Express, **15(24)**, 16124–16129, Nov 2007. DOI: 10.1364/OE.15.016124.

[160] D. Wegkamp, D. Brida, S. Bonora, G. Cerullo, J. Stähler, M. Wolf, and S. Wall. *Phase retrieval and compression of low-power white-light pulses*. Appl. Phys. Lett., 99(10):101101, 2011. DOI: http://dx.doi.org/10.1063/1.3635396.

[161] D. Wegkamp. *Ultrafast electron dynamics and the role of screening*. PhD thesis, Freie Universität Berlin, 2015.

[162] R. R. Alfano and S. L. Shapiro. *Emission in the Region 4000 to 7000 Å Via Four-Photon Coupling in Glass*. Phys. Rev. Lett., **24**, 584–587, Mar 1970. DOI: 10.1103/PhysRevLett.24.584.

[163] A. L. Gaeta. *Catastrophic Collapse of Ultrashort Pulses*. Phys. Rev. Lett., **84**, 3582–3585, Apr 2000. DOI: 10.1103/PhysRevLett.84.3582.

[164] M. Bradler, P. Baum, and E. Riedle. *Femtosecond continuum generation in bulk laser host materials with sub-µJ pump pulses*. Appl.Phys. B, **97(3)**, 561–574, 2009. DOI: 10.1007/s00340-009-3699-1.

[165] O. Martinez. *3000 times grating compressor with positive group velocity dispersion: Application to fiber compensation in 1.3-1.6 µm region*. Quantum Electronics, IEEE Journal of, **23(1)**, 59–64, Jan 1987. DOI: 10.1109/JQE.1987.1073201.

[166] F. Cilento, C. Giannetti, G. Ferrini, S. Dal Conte, T. Sala, G. Coslovich, M. Rini, A. Cavalleri, and F. Parmigiani. *Ultrafast insulator-to-metal phase transition as a switch to measure*

the spectrogram of a supercontinuum light pulse. Appl. Phys. Lett., 96(2):021102, 2010. DOI: http://dx.doi.org/10.1063/1.3291105.

[167] R. Trebino. *Frequency-Resolved Optical Gating: The Measurement of Ultrashort Laser Pulses*. Kluwer Academic Publishers, 2000.

[168] M. Stern, J. Heritage, and E. Chase. *Grating compensation of third-order fiber dispersion*. Quantum Electronics, IEEE Journal of, **28(12)**, 2742–2748, Dec 1992. DOI: 10.1109/3.166468.

[169] E. Zeek, K. Maginnis, S. Backus, U. Russek, M. Murnane, G. Mourou, H. Kapteyn, and G. Vdovin. *Pulse compression by use of deformable mirrors*. Opt. Lett., **24(7)**, 493–495, Apr 1999. DOI: 10.1364/OL.24.000493.

[170] O. E. Martinez. *Grating and prism compressors in the case of finite beam size*. J. Opt. Soc. Am. B, **3(7)**, 929–934, Jul 1986. DOI: 10.1364/JOSAB.3.000929.

[171] S. Kane and J. Squier. *Grating compensation of third-order material dispersion in the normal dispersion regime: Sub-100-fs chirped-pulse amplification using a fiber stretcher and grating-pair compressor*. Quantum Electronics, IEEE Journal of, **31(11)**, 2052–2057, Nov 1995. DOI: 10.1109/3.469287.

[172] G. Fibich. *The Nonlinear Schrödinger Equation*. Applied Mathematical Sciences. Springer, 2015. Available online: http://link.springer.com/book/10.1007/978-3-319-12748-4.

[173] L. Bogner. *Electronic structure and excited state dynamics in π-conjugated organic systems on inorganic substrates*. PhD thesis, Freie Universität Berlin, 2015.

[174] S. Yamaguchi and T. Tahara. *Novel interface-selective even-order nonlinear spectroscopy*. Laser & Photonics Reviews, **2(1-2)**, 74–82, 2008. DOI: 10.1002/lpor.200710027.

[175] Semrock Filter specifications. Available online: http://www.semrock.com/FilterDetails.aspx?id=FF01-390/SP-25. Last accessed: 28/06/2015.

[176] Andor spectrometer specifications. Available online: http://www.andor.com/pdfs/specifications/Andor_Shamrock_303_Specifications.pdf. Last accessed: 27/06/2015.

[177] Specifications for Richardson grating 53 −* −090R. Available online: http://www.gratinglab.com/Products/Product_Tables/Efficiency/Efficiency.aspx?catalog=53-*-090R. Last accessed: 27/06/2015.

[178] G. E. Jellison and L. A. Boatner. *Optical functions of uniaxial ZnO determined by generalized ellipsometry*. Phys. Rev. B, **58**, 3586–3589, Aug 1998. DOI: 10.1103/PhysRevB.58.3586.

[179] L. Wischmeier, T. Voss, I. Rückmann, J. Gutowski, A. C. Mofor, A. Bakin, and A. Waag. *Dynamics of surface-excitonic emission in ZnO nanowires*. Phys. Rev. B, **74**, 195333, Nov 2006. DOI: 10.1103/PhysRevB.74.195333.

[180] J.-C. Deinert. *Zinc Oxide Surfaces and Interfaces: Electronic structure and charge carrier dynamics*. PhD thesis, Technische Universität Berlin, 2015.

[181] D. Polli, D. Brida, S. Mukamel, G. Lanzani, and G. Cerullo. *Effective temporal resolution in pump-probe spectroscopy with strongly chirped pulses*. Phys. Rev. A, **82**, 053809, 2010.

[182] F. Balzer, A. Pogantsch, and H.-G. Rubahn. *Temperature dependent analysis of three classes of fluorescence spectra from p-6P nanofiber films*. Journal of Luminescence, **129(8)**, 784 – 789, 2009. DOI: 10.1016/j.jlumin.2009.02.014.

[183] E. Faulques, J. Wéry, S. Lefrant, V. G. Ivanov, and G. Jonusauskas. *Transient photoluminescence of para -hexaphenyl layers*. Phys. Rev. B, **65**, 212202, Jun 2002. DOI: 10.1103/PhysRevB.65.212202.

[184] F. C. Spano. *Absorption and emission in oligo-phenylene vinylene nanoaggregates: The role of disorder and structural defects*. The Journal of Chemical Physics, **116(13)**, 5877–5891, 2002. DOI: 10.1063/1.1446034.

[185] O. V. Mikhnenko, F. Cordella, A. B. Sieval, J. C. Hummelen, P. W. M. Blom, and M. A. Loi. *Temperature Dependence of Exciton Diffusion in Conjugated Polymers*. The Journal of Physical Chemistry B, **112(37)**, 11601–11604, 2008. DOI: 10.1021/jp8042363. PMID: 18729397.

[186] V. V. N. Ravi Kishore, K. L. Narasimhan, and N. Periasamy. *On the radiative lifetime,*

quantum yield and fluorescence decay of Alq in thin films. Phys. Chem. Chem. Phys., **5**, 1386–1391, 2003. DOI: 10.1039/B211264G.

[187] R. Priestley, A. D. Walser, and R. Dorsinville. *Temperature dependence of transient photoluminescence in tris(8-hydroxyquinoline) aluminum (Alq3)*. Optics Communications, **158**, 93 – 96, 1998. DOI: 10.1016/S0030-4018(98)00569-0.

[188] J. Adolph and D. F. Williams. *Temperature Dependence of Singlet-Triplet Intersystem Crossing in Anthracene Crystals*. The Journal of Chemical Physics, **46(11)**, 4248–4251, 1967. DOI: http://dx.doi.org/10.1063/1.1840532.

[189] B. Meyer, L. Phillips, and J. Smith. *Temperature dependence of intersystem crossing: lifetime and intensity of SO2 phosphorescence in low-temperature solids*. Proceedings of the National Academy of Sciences of the United States of America, **61(1)**, 7, 1968.

[190] C. Rulliére. *Femtosecond laser pulses*. Springer, 2nd edition, 2005.

[191] I. A. Walmsley and C. Dorrer. *Characterization of ultrashort electromagnetic pulses*. Adv. Opt. Photon., **1(2)**, 308–437, Apr 2009. DOI: 10.1364/AOP.1.000308.

Acknowledgments

A thesis cannot be finished without acknowledging all the persons that contributed to it, both directly or indirectly. Therefore thanks to. . .

. . . in the first place Martin Wolf and Julia Stähler for giving me the possibility of working in such a fertile environment. Moreover, I am grateful to them for believing in me and assigning me to the eSFG project. Therewith they allowed me to develop an experiment from scratch and thereby learn how to deal with sales managers, how to plan in advance the required components and the laboratory space, and much more. The whole process was of course bound to many restless nights, feelings of helplessness and frustrations, but I would have never grown that much, as a scientist and as a person, without these challenges.

. . . the electrondynamiχ group as a whole: Jan, Lea, Daniel, Marc, Clemens, Sesha, Lukas and Selene. She deserves a special mention for becoming not only a great coworker, always enthusiastic to start stimulating discussions, but most importantly for becoming a good friend outside these walls. And last but not least, she increased the number of Italians in the group and convinced me to buy a moka.

. . . the many persons behind the curtains of the department: Manuel and Daria, Albrecht (not only for the IT support but also for the company in the many late evening breaks on the terrace), Sven (who always has a solution for everything) and of course Marcel, who taught me how to tear apart a laser if needed and made me loose the fear for those black boxes. And, very important, taught me how to make cocktails and thus gave me an emergency exit if science does not work out! Among the scientific coworkers, I am deeply indebted to Alex (what a pity you started working on non-linear optics so late in my PhD!), Kramer and Alexey for the stimulating discussions and the patience in helping me with any single silly problem. To all others thanks for making such a good working atmosphere!

. . . the technical workshops, without whom this work could have never be finished. A big thank goes to Petrick, who always found time for building my sample-holders on the very last minute, and to Patrick and Christian who made my galvano mirror work.

... the other side of the terrace (someone might call it the bright side): the MP department. There I found over the years fantastic persons with whom I shared many funny events, PhD defenses in Holland, and filming days: Nadja, Schewe and Christian, Johanna, Stefan and Isa, Simon and Gert. Among them a special thought goes to Matias and Alex. The first for being there and listen to me many many times, and I know I can be annoying when I whine. The second for the great friendship we developed over delicious dinners and incredibly good wines. And yes, thanks for organizing the wine tastings!

... the people who became my second family here in Berlin. First and foremost Daniele and Fabio, who have been there since our first erasmus day and simply are the best friends I could have asked for. Francesca and Rosaria joined the family shortly after and have always been like older sisters to me. Edoardo, who besides being a good buddy also helped with tensor calculations and rate equations solving, sometimes even drawing molecules on a napkin. "I furlans", Puppo and Giambo, and "i muloni", among which a special thanks goes to Ale, with whom, I bet, I'll cross paths again soon.

... Vale, Tony, Eli, Val, Sofi and Erica who, despite being 1500 km away, know exactly what to send over the chat to make me laugh as if I would be sitting next to them.

... my grandma, for being our little Atom Ant and literally flying here when I needed her.

... my parents. Mamá, thanks for helping me get this far and for being my example of passion and self-denial in research. Papà, thanks for investing that much time in my sport career. I would have probably never have made it to the Olympics but, as I was sitting here thinking this thesis would never come to an end, I reminded myself that upwind legs were much harder and I always made it to the end.

And finally, thanks to Enrico, who, willing or not, has endured all these months. And now that we made it, I hope to be able to demonstrate it was worth it.

Academic Curriculum Vitae

Laura Foglia

born 16.11.1986, Savona, Italy

2000-2005	**Maturità scientifica**, Liceo scientifico statale Leonardo da Vinci, Genova, Italy
09.2005-02.2009	**B. Sc. in Physics** Università degli studi di Genova, Italy
Thesis	*Isomerization of tetra-tert-butyl-azobenzene on Au(111) - Fluence and pulse length dependence of the cross section.*
Supervised by:	Prof. Mario Rocca
	Measurements performed in the 2PPE laboratory of
	Prof. Dr. Martin Wolf at the Freie universität Berlin, Germany.
04.2009-04. 2011	**Physik Diplom**, Freie universität Berlin, Germany
Thesis:	*Transient reflectivity and coherent phonon generation: an ultrafast probe of the metal-to-insulator transition in VO_2*
Supervised by:	Dr. Julia Stähler and Prof. Dr. Martin Wolf
15.04.2011-Now	**Doctoral studies**, Physical chemistry department,
	Fritz-Haber-Institut der Max-Planck-Gesellschaft, Berlin, Germany.
Thesis:	*Ultrafast dynamics and energy loss channels at an hybrid organic inorganic interface.*
Supervised by:	Dr. Julia Stähler and Prof. Dr. Martin Wolf

Laura Foglia

Berlin, den 20.Oktober 2015

List of Publications

Papers relating to this thesis

L. Foglia, L. Bogner, M. Wolf and J. Stähler

Exciton trapping in vibrationally excited organic molecules near a ZnO surface

arXiv:1412.0597, (2014)

Additional papers not related to this thesis

S. Wall, D. Wegkamp, L. Foglia, K. Appavoo, J. Nag, R.F. Haglund Jr, J. Stähler and M. Wolf,

Ultrafast changes in lattice symmetry probed by coherent phonons,

Nature Communications **3**, (2012), 721

S. Wall, L. Foglia, D. Wegkamp, K. Appavoo, J. Nag, R.F. Haglund Jr, J. Stähler and M. Wolf,

Tracking the evolution of electronic and structural properties of VO2 during the ultrafast photoinduced insulator-metal transition,

Physical Review B **87**, (2013), 115126

Eidestattliche Versicherung

Hiermit versichere ich, Laura Foglia, geboren am 16.11.1986 in Savona (Italien), an Eides statt die vorliegende Dissertation selbständig verfaßt zu haben. Sämtliche verwendeten Hilfsmittel, Hilfen und Quellen sind an der entsprechenden Stelle angegeben. Diese Arbeit wurde bisher weder in gleicher noch ähnlicher Form einer anderen Prüfungskomission vorgelegt oder veröffentlicht.

Die Angaben über meinen Eigenanteil meiner Veröffentlichungen in meiner Erklärung sind zutreffend.

Laura Foglia

Berlin, den 20. Oktober 2015